Uncertainty Analysis Procedures for Neutron-Induced Cross Section Measurements and Evaluations

by

Amanda Lewis

A dissertation submitted in partial satisfaction of the

requirements for the degree of

Doctor of Philosophy

in

Engineering – Nuclear Engineering

in the

Graduate Division

of the

University of California, Berkeley

Committee in charge:

Professor Lee Bernstein, Chair
Professor Jasmina Vujic
Dr. Devin Barry
Dr. Barbara Jacak

Spring 2020

Uncertainty Analysis Procedures for Neutron-Induced Cross Section Measurements and Evaluations

Abstract

Uncertainty Analysis Procedures for Neutron-Induced Cross Section Measurements and Evaluations

by

Amanda Lewis

Doctor of Philosophy in Engineering – Nuclear Engineering

University of California, Berkeley

Professor Lee Bernstein, Chair

The accuracy and precision of nuclear data is of great importance to many fields, including nuclear energy, nuclear medicine, non-proliferation, stockpile stewardship and fundamental physics. New Generation-IV nuclear reactor designs, which are a vital part of the solution to current climate change crisis, rely on nuclear data for their simulations. The nuclear energy community has developed sophisticated methods and codes to propagate uncertainties through the simulation and design process. There is still work to be done, however, on the nuclear data uncertainties that these methods aim to incorporate. In the newest release of the Evaluated Nuclear Data File (ENDF) library, the majority of the 557 individual isotopic evaluations do not even have associated uncertainties. For many isotopes, experimental data are available and the evaluations and their uncertainties are in part based on these data. In this dissertation, methods for improving the accuracy and consistency of the uncertainties on the experimental data are presented. Improving the quality of the reported experimental uncertainties is the first step in the vital process of improving the evaluated uncertainties in libraries such as ENDF.

In order to achieve this goal, templates of measurement uncertainties were created for total and capture cross section measurements. These templates can be used by evaluators to ensure that the uncertainties reported by experimentalists are complete and realistic. Templates are provided for total cross section measurements (utilizing transmission) and for capture cross section measurements (utilizing total absorption spectroscopy, total energy detection, activation analysis, partial gamma detection, or accelerator mass spectrometry). A large-scale literature review for the creation of the measurement uncertainties templates is introduced, which will help to ensure consistency between the estimated uncertainties and other data sets. One common and significant source of uncertainty—the efficiency of an HPGe detector—is studied in detail. The proper method for calculating a data covariance matrix is explained, and new intensity correlation matrices are presented which will allow for more realistic correlations between the measured data points. A new method for determining curve fitting uncertainties is developed, and future work that will allow for proper interpolation uncertainties is explored, with applications in many fields of the physical sciences. Finally, a new method to combine experiment and theory for partial gamma measurements is presented. This method focuses on the partial gamma cross sections that are the least discrepant with the experimental data to infer the total reaction cross section, and includes a simple method for putting uncertainties on the deduced reaction cross section. This uncertainty is a realistic measure of the discrepancies between the experimental data and the calculation. Using this method, an accurate ^{238}U inelastic scattering cross section, which is critical for accurately modeling some fast reactor systems, is calculated from a data set which has significant issues in the measurement of the strongest gamma. Together, these methods improve the experimental uncertainties that the evaluations rely on.

To everyone who has inspired me along the way

Contents

List of Figures

List of Tables

Acknowledgments

This thesis is the culmination of many years of work, but also of the inspiration, motivation and dedication of many people around me. Without this support I would not be where I am now, and I would not be nearly as happy. I can't possibly thank everyone who has influenced me, but I can cover the highlights.

To Dr. Danon and Nick, who were the first to believe that I could make it in this field, thank you for the opportunities. I'm here because of you guys. And to everyone at RPI and NNL, who inspired me to stay in the field, even through a quick flirtation with fusion. Amanda and Jesse, it won't be the same without you guys. And Devin, Zeke, Adam, Mike, Brian and Tim, I am so excited to come back and work with you again.

To Vlad, thank you for always encouraging me and providing opportunities for me to grow. To Dave and Gustavo, thank you for making my introduction to evaluations fun and interesting and for making me want to stay. And to Denise, Toshihiko and Wim, for making my summer in Los Alamos worth the terribly dry air. And especially to Denise, thank you for being a wonderful role model and mentor. You have changed my outlook on my career, and have honestly made me consider just buying a lot of humidifiers.

To my committee—Dr. Bernstein, Dr. Barry, Dr. Vujic and Dr. Jacak—thank you for your time, your feedback and your commitment. This work and I are better for it.

To Devin, for always being excited about something, and for encouraging my own interests. You're the reason I'm coming back.

To Lee, of course, who not only inspired, encouraged and guided me along the way, but who also made me feel like I really do belong here in this field, thank you.

Thank you to everyone who made Berkeley into my home these past four years—Mitch, Sami, Eric, Franziska, Jack, Alex, Kathy, Joanna, Mauricio, Justin, Rebecca—you're going to make me really miss this place. And to everyone in my group—Eric, Morgan, Ian, Darren, Andrew, Jon, Austin, Tyler, Catherine, Joey, Jason, Leo—working with you guys has been wonderful, and I'm excited to continue.

To Franziska, who ran away for my last year, thank you for being a great friend and constant source of laughter. I'm hoping you'll stay where you are so I can see you again and have more three hour coffee breaks. To Jack and Eric, who kept me sane through the global pandemic that marked my last months in Berkeley, thank you for being great roommates and great friends (but you're not in my will). And of course, people are saying that no one contributed as tremendously as Eric. I'm so glad I found you. And to Mitch, for keeping me sane through the last two years—you kept me going, kept me moving forward. I could not have done this without you.

To Uncle Paul and Aunt Gwen, to Aunt Karen, to Grandma, thank you all for your constant love and support and interest all of these years. To Aunt Pam, I'm sorry I wasn't there. To Grandma and Grandpa, I'm glad that we were close for so many years, and I'm sorry that you're not here.

To my parents, who have always been supportive of my dreams, even when it meant buying a lot of art supplies or not having time to clean my room—you've allowed me to

believe that I can be whatever I want to be. After all of this time I think I'm officially out of the car. And no matter what, I know I'll always have somewhere to come home to.

And finally, to Becky, the original Dr. Lewis. Thank you for being such an amazing role model in getting up, going in, and doing what you need to do to get where you want to be, no matter what. You're the strongest person I know. I've been following you my whole life and you've only ever led me to good things.

Chapter 1

Introduction

1.1 Overview of Nuclear Data

Nuclear phenomena including reactions, decay and structure, are important in many fields, including nuclear energy, nuclear medicine, non-proliferation, stockpile stewardship and fundamental physics. Analysis and quantification of these phenomena is the responsibility of the nuclear data community. This community is made up of people with backgrounds in theoretical physics, experimental physics, data evaluation, compilation, and validation who work to produce the best evaluated nuclear data possible. The evaluated nuclear data is then used in calculations and simulations for applications as wide-ranging as nuclear reactor design, anti-neutrino fundamental physics and cancer diagnosis and treatment.

1.1.1 Nuclear Data Observables

The nuclear data observable that is most commonly used is the cross section, which is a measure of the probability of an incident particle interacting with a target nucleus and producing a specific outcome. Cross sections are defined in units of area, and can be thought of as the areal representation of this probability. Cross sections for incident neutrons are the majority of nuclear data at present, but current applications are leading to increasing interest in charged particle reactions as well. Cross sections are energy and isotope dependent, creating the need for a vast amount of unique information. The total cross section of an isotope represents the probability that the incident particle will interact, in any nuclear process, with the target nucleus. Each possible reaction, such as elastic scattering, inelastic scattering, capture, etc., has its own cross section, all of which sum to the total cross section. Other observables of the reactions that are assessed include the angular and energy distributions of the outgoing particles, multiplicities of outgoing gammas, and in the special case of fission reactions, the probability distributions for the product nuclei. In addition to reaction observables, nuclear data includes information about the structure of nuclei, such as the mass, lifetime, static deformation, binding energy and excited levels.

1.1.2 Databases

The nuclear data community maintains many databases for the use of their members as well as the application communities. The evaluated libraries are the recommended values based on an evaluation performed by experts. Unevaluated libraries and databases also exist, where experimental data and calculations are compiled, which are available for use within and outside of the community without evaluation.

1.1.2.1 Evaluated Libraries

The primary product of the nuclear data community is the set of evaluated reaction libraries that are used in the simulations and calculations in other fields. There are many evaluated libraries, but the most commonly used are the Evaluated Nuclear Data File (ENDF) [1], the Japanese Evaluated Nuclear Data Library (JENDL) [2] and the Joint Evaluated Fission and Fusion File (JEFF) [3]. ENDF is maintained by the National Nuclear Data Center (NNDC) in the United States, JENDL by the Japan Atomic Energy Agency (JAEA) and JEFF by the Nuclear Energy Agency (NEA) within the Organisation for Economic Co-operation and Development (OECD). A separate library exists for evaluated resonance parameters, called the Atlas of Neutron Resonances [4]. These libraries represent our current best understanding of the nuclear data observables.

There are also application-specific evaluated libraries, which focus on certain reactions and observables that are of greater interest to their application. They may also make use of application-specific validation methods and measurements. These include the Fusion Evaluated Nuclear Data Library (FENDL) [5], a library of monitor reactions [6], the Evaluated Gamma-ray Activation File (EGAF) [7], and the International Reactor Dosimetry File (IRDF) [8] which has recently been superseded by the International Reactor Dosimetry and Fusion File (IRDFF-II) [9].

Structure information can be found in the Evaluated Nuclear Structure Data File (ENSDF) [10], which is also maintained by the NNDC. All of the known excited levels and gamma transitions are included in ENSDF, along with the binding energy, the Q-values for decays and separation energies.

The Reference Input Parameter Library (RIPL) [11] is a collection of information that is important for reaction calculations. This includes the evaluated structure information from ENSDF, and also reaction model inputs such as the optical potential and fission barriers. This library recommends values or models to use for reaction calculations, based on the evaluated structure information, experimental data, and theory work. This library is a single database that contains most of the nuclear data needed to run the reaction calculation codes, and enforces a minimum accuracy and consistency in these calculations.

Finally, the International Criticality Safety Benchmark Experiment Project (ICSBEP) [12], contains information about experiments that measure integral quantities, which have been evaluated and turned into benchmarks. The experimental integral quantity, such as k_{eff}, is presented along with the information necessary to simulate the experiment. This includes the geometry and setup of the experiment and the material characteristics, and in many cases input files for common simulation codes. These benchmarks provide precise experimental measurements of quantities that are integral over incident particle energy, reaction type, and/or target nucleus.

1.1.2.2 Unevaluated Databases

There are a series of unevaluated databases as well, which compile experimental data and calculations that are not put through an evaluation process. The EXFOR (EXchange FORmat) database [13] stores information about reaction experiments of cross sections, outgoing particles, multiplicities, fission product yields, and more. EXFOR started as a consistent format that was used to exchange nuclear measurement results between different data centers. It has since become a massive database of measurements, with information from over 23,000 experiments. The EXFOR compilation usually closely follows the published references, but occasionally includes additional information or corrections for issues discovered after publication.

There is an analogous database for structure experiments, the Experimental Unevaluated Nuclear Data List (XUNDL) [14]. This database contains measured structure information from over 3500 experiments, and also contains the information in the reference, without additional evaluation.

There is a similar database for reaction calculations, known as the TALYS Evaluated Nuclear Data Library (TENDL) [15]. This library is based on calculations of cross sections using tuned models. TENDL does contain some evaluations of nuclear data observables, for the cases where there are experimental data. However, striving for completeness has led to global theoretical calculations for many reactions, so this library on the whole should not be considered evaluated in the same way as ENDF, JENDL and JEFF.

1.1.3 The Nuclear Data Pipeline

The creation of evaluated nuclear data libraries such as ENDF follows a many-step process that has been coined the "Nuclear Data Pipeline" [16]. A schematic of the pipeline, from Reference [16], is shown in Figure 1.1. The pipeline starts with experimental data, as our current models of nuclear structure and reactions are not predictive at the level of accuracy needed for most applications. Experiments are performed, analyzed and published or released. The results are then compiled into the EXFOR and XUNDL databases, and the publication metadata is added to the Nuclear Science References (NSR) database. For structure data, the XUNDL experimental results are evaluated into the ENSDF library. For reactions, the evaluations include input from the EXFOR database, the ENSDF library (usually through RIPL), the Atlas of Neutron Resonances, and theory (in reaction calculation codes). These evaluations are based on experimental measurements that are differential in incident particle energy and in reaction. Integral quantities, which are usually higher precision than the differential data, are used to validate the library. The integral data come in

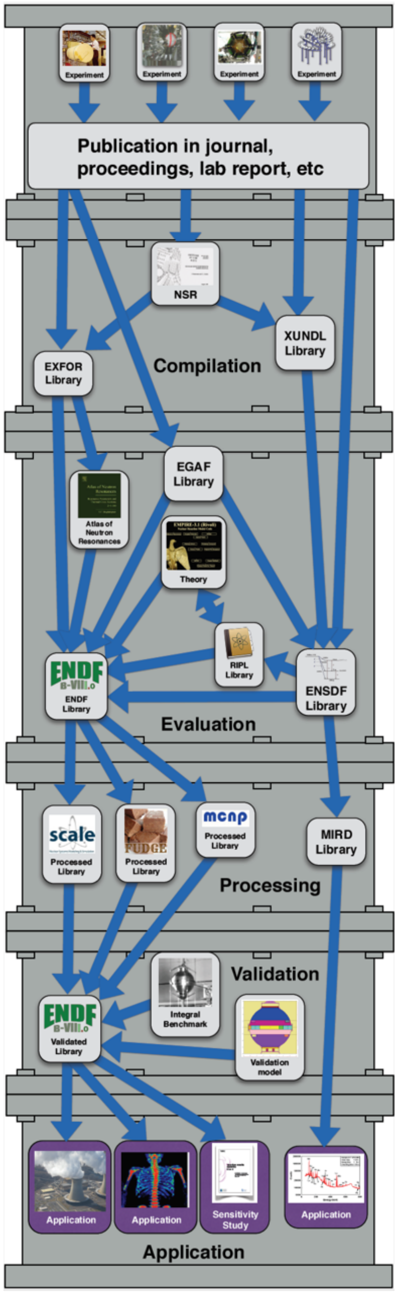

Figure 1.1: Schematic of the nuclear data pipeline, taken from Reference [1]. The pipeline describes the process by which the evaluated libraries are created, validated, and used. There is also feedback that comes from applications, as their use of the evaluated nuclear data can uncover inaccuracies that the benchmarks are not sensitive to and therefore were not found.

many forms, but shares the common characteristic that the measured quantity depends on multiple underlying components of nuclear data, such as fission cross sections, neutron yields and energy spectra etc. One example are measurements of k_{eff} for critical assemblies which depends on the fission parameters as well as neutron scattering and capture cross sections. The ICSBEP library is one of the largest sources of integral measurements used for this purpose. The library is first processed into a form that can be used for validation—specifically, into the formats used by the transport codes such as MCNP [17]. Finally, the validation is performed by comparing the simulated integral quantity with the measured integral quantity from the ICSBEP database. This comparison can find problems with the evaluated library, and the evaluators can correct them. The validated library is then available for use by the application communities.

1.1.4 Uncertainties in Nuclear Data

Currently, there is no accepted practice for estimating the uncertainties and correlations on evaluated data in the ENDF library. The Cross Section Evaluation Working Group (CSEWG) covariance committee prepared a report named “Guidance on Generating Neutron Reaction Data Covariances for the ENDF/B Library” [18], which is more focused on the documentation and formatting of covariance matrices than on how they are generated. One reason for this is that there are many evaluation methodologies used throughout the library, and the uncertainty estimation should be based on the evaluation method.

For Resolved Resonance evaluations, the covariances of the resonance parameters can be calculated with the fitting code used in the evaluation [19]. These codes use Generalized Least Squares or Bayesian updating procedures, both of which provide covariances for the outputs. For existing evaluations, a procedure has been developed to retroactively estimate covariances between resonance parameters [20]. The resonance parameters are used to simulate data, which can then be input into the fitting process that is typically used to generate covariances.

In the fast region, most evaluations are not the product of fitting processes, but rather of theoretical calculations that are tuned to match experimental data. There are many methods for quantifying model uncertainty, which are introduced briefly here. More detail on modeling uncertainties is given in Section 7.2.3. The two main sources of uncertainties in model predictions are the deficiencies in the model and the uncertainties in the parameters. Parametric uncertainties are much easier to study, by estimating a distribution and then determining the sensitivity of the calculation to each parameter. The model deficiency uncertainty can be estimated by comparing the calculation to experimental data. Evaluations can be performed by comparing calculations to the available data, and updating either the model parameters (Kalman Filter) or the nuclear data observable value itself (Unified Monte Carlo). In the Kalman Filter method [21] a Bayesian updating procedure is used to improve the model parameters, and then the model is used to generate the evaluated nuclear data. In the Unified Monte Carlo (UMC) method [22], a similar procedure is used but the nuclear data observable itself is updated, and the result of the updating procedure is the evaluation.

In the most recent ENDF library release (ENDF/B-VIII.0 [1]), some time was devoted to the status of the covariances in the library. The statistics on the evaluations that were updated in the new release, along with the numbers of evaluations with or without covariances are shown in Table 1.1. This shows that of the total 557 isotope evaluations, the majority (375) still do not have covariances associated with the evaluation. The lack of uncertainties means that the users of the data have no indication of the confidence in the evaluation. These statistics are improving, as all new evaluations are expected to have associated covariances as time goes on, but there is still work to be done.

Table 1.1: Evaluations in the ENDF/B-VIII.0 library based on whether or not the evaluation is new, modified, or unchanged in ENDF/B-VIII.0 (rows) and whether or not the evaluation has covariances (columns), from Reference [1].

ENDF/B-VIII.0 Status	Have Covariances	No Covariances	Total
New Evaluation	73	95	168
Modified Evaluation	34	102	136
Unchanged Evaluation	75	178	253
Total	186	375	557

1.2 Gen IV Reactor Nuclear Data Needs

The fields directly impacted by nuclear data are varied and diverse, including medical isotopes, safeguards, non-proliferation and nuclear energy. Nuclear power has the potential to be the most universally impactful, as an integral part of the fight against climate change. It is widely accepted in the scientific community that the effects of global warming are real, and that human-caused green-house gas emission has contributed to it [23]. A crucial step towards green-house gas reduction is to curtail the emissions from the energy production sector, which makes up about a third of the current emissions. Nuclear energy is the only emission-free source of electricity that is developed enough to replace our considerable fossil-fuel energy production in the short time frame necessary [24]. The current generation of nuclear reactors (Gen II and III) already provides sustainable energy, and new fast-spectrum Gen IV reactor designs will have a practically inexhaustible supply of fuel [25]. This is vital, as the only practical route forward is to acknowledge and meet the ever-increasing global power needs [26].

These Gen IV reactors are essential to the future of nuclear power, but many utilize different materials and neutron spectra from the current fleet of reactors. This leads to the use of nuclear data values that may have not been extensively validated by experience and often do not have uncertainties in the evaluated libraries. Quantified uncertainties on evaluated nuclear data values indicate a minimal level of consideration for that reaction—the missing uncertainties are likely larger than the quantified ones. The lack of uncertainties may become an issue for this generation of the reactors, as the designs are done mostly by simulation and little experimental time is devoted to validating the neutronics calculations. This could lead to the unfortunate situation of late-stage testing failures, for reasons that cannot be disentangled with the integral experiment results. Realistic uncertainties on the evaluated nuclear data would help provide realistic uncertainties on the design process and simulated quantities, and can point to where progress needs to be made before the designs can be finalized. Extensive work has been done in the nuclear power field to fully propagate the known uncertainties through the reactor simulations [27–30], including methods to propagate the nuclear data uncertainty [31–38]. The accuracy of the uncertainties on the simulated quantities, however, depends heavily on the accuracy of the input nuclear data uncertainties. As explained in Section 1.1.4, the current state of evaluated nuclear data uncertainties is patchwork at best. There are varied methods for calculating the uncertainties that are presented, and many reactions that have no uncertainty information at all.

Two of the major departures from the current fleet of reactors are the use of an epithermal or fast spectrum, and the use of new materials. An example of a Gen IV design is presented for each, along with at least one example of a nuclear data quantity that is important to the design and needs improvement.

1.2.1 Traveling Wave Reactor

One example of the new fast spectrum reactor designs is the Traveling Wave Reactor, currently under study by the company TerraPower, LLC [39]. The breeder reactor has a fast neutron spectrum due to the sodium coolant, and uses natural or depleted uranium fuel. An internal study on the reactor design sensitives uncovered a significant dependence on the inelastic scattering cross section of ^{238}U [38]. This cross section is of importance to the nuclear energy field in general, which has been noted in the final report for the NEA-WPEC Subgroup "Meeting Nuclear Data Needs for Advanced Reactor Systems" [40], and in a recent review on nuclear data needs [16].

In fissionable nuclei, it is difficult to directly measure the inelastically-scattered neutrons due to the continuous fission neutron background. There are a series of measurements, as recently as 2001, that perform direct measurements of the scattered neutrons. Due to the low energy resolution of neutron detectors, some present their measurements as a function of scattered neutron energy in bins [41, 42]. Other experiments present cross sections for individual excited levels, including one experiment that presented level cross sections for levels between 680 and 1290 keV [43] and several others that present cross sections for just the first excited state [44] or with a single neutron energy [45]. There is limited information available from these experiments, however, and these measurements suffer from large correction factors for multiple scattering and the fission neutron background. Most of the recent measurements instead utilize the characteristic gammas emitted by the de-exciting product nucleus [46–48]. Measurements are also underway at the GELINA facility [49], but results

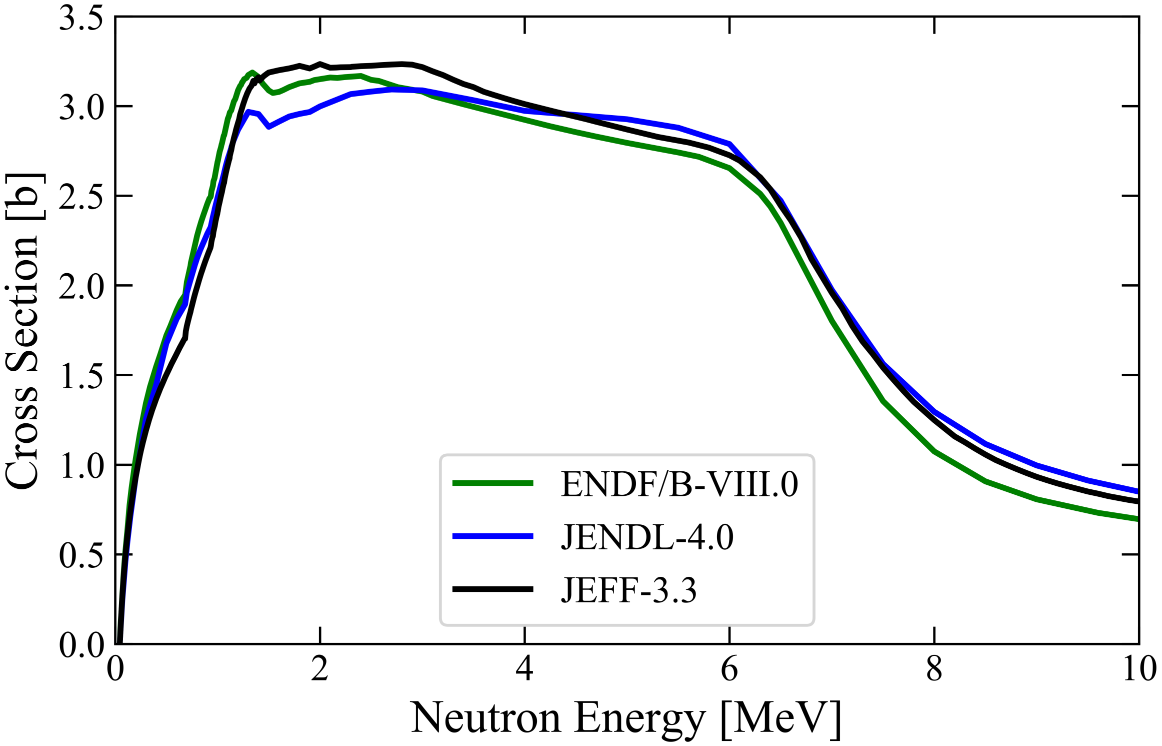

Figure 1.2: Evaluations of ^{238}U inelastic scattering from three major libraries. There are significant discrepancies between the libraries, especially in the energy regions between 1 and 2 MeV, and above 7 MeV. There is very little experimental data for the total inelastic reaction, allowing the libraries to diverge.

have yet to be published. The results of these experiments are often discrepant, with even larger differences seen between the measured cross sections and theoretical calculations.

There are also inconsistencies in the evaluations of the inelastic scattering cross section for ^{238}U, shown in Figure 1.2. The uncertainty on the recent CIELO evaluation [50] (adopted in ENDF/B-VIII.0) reflects the lack of understanding of this reaction, with uncertainties that are greater than 10% over most of the energy region. Even in the region of the most significant differences between the evaluations, around 1 to 2 MeV, the large uncertainty on the CIELO evaluation fully covers the range of the libraries, and accounts for uncertainties and biases common to all of the evaluations. This realistically large uncertainty was what drew attention to this reaction in the Traveling Wave Reactor simulations, and the nuclear data field has responded to improve our understanding of the reaction. Specifically in this work, the uncertainties in these measurements are addressed in Chapter 5, and a new method to combine the measured gamma cross sections with theoretical calculations is presented in

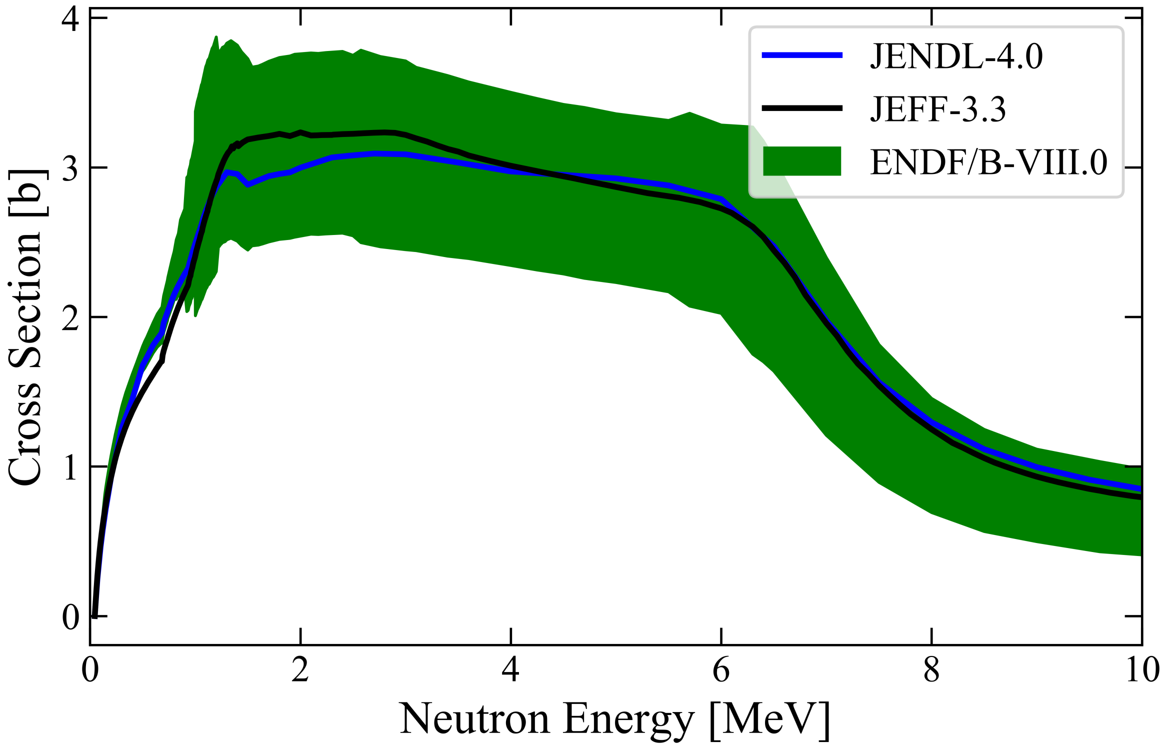

Figure 1.3: Evaluations of ^{238}U inelastic scattering from three major libraries, with the ENDF/B-VIII.0 uncertainties shown in the green band. The large uncertainties reflect the lack of data for the inelastic and elastic reactions for this isotope, and completely covers the discrepancies between the libraries.

Chapter 7.

1.2.2 Molten Salt Reactors

New materials are being utilized in Gen IV reactors as well, including fluoride and chloride salts in molten salt reactor systems [51]. There are multiple data sets for the total cross section of ^{19}F, but limited data for each reaction channel, a fairly common situation. Due to this, the locations of resonances in the inelastic cross section are known, but the magnitude of each must be modeled. The inelastic scattering cross section evaluations from ENDF/B-VIII.0 [1] and JENDL-4.0 [2] are shown in Figure 1.4, along with the one data set available in EXFOR for the inelastic reaction in this energy region [52]. The ENDF/B-VIII.0 evaluation follows the resonance shape of the well-constrained total cross section, but does not match the magnitude of the measurement. The JENDL-4.0 evaluation follows the data, and is much smoother as a result. The JENDL-4.0 evaluation will likely give a better result in the reactor simulation, but could be improved by including the information about resonance energies known from the other channels. Fluorine-Lithium-Beryllium (FLiBe) salts are being studied, but in most cases the focus is on the material and chemical properties [53–57]. The nuclear data uncertainty studies that have been done [58] focus on other reactions that the simulation is more sensitive to; but with an order of magnitude bias, this reaction does not require a high sensitivity to have a large impact. The ENDF/B-VIII.0 evaluation of ^{19}F does include uncertainties, but they are about 20% in this energy region, giving users no indication that this evaluation is up to an order of magnitude different from the available information. This discrepancy was recently discovered in the course of understanding integral benchmark simulations with machine learning techniques [59]. However, it was pointed out in earlier work [60], which discussed how the cross section discrepancies affect the neutron spectrum in the reactor.

Another reaction that has recently been discovered to have a large bias in the evaluation is ^{35}Cl(n,p). The evaluated cross sections are shown in Figure 1.5, along with a recent measurement at $\approx$2.5 MeV [61], and two older measurements at $\approx$14.5 MeV [62, 63]. The evaluations are about three times larger than the new experimental data, likely due to the lack of constraining data. Before this recent experiment, the EXFOR database contained only two (n,α) measurements and one partial inelastic scattering cross section measurement providing differential data between 1 and 4 MeV. The evaluation was therefore heavily based on theory, and does not have uncertainties.

The simulations that are aiding in the design of these Gen IV molten salt reactors are relying on these and many more reactions that have not been extensively studied or validated. Realistic uncertainties need to be estimated for the evaluations, which can then be propagated through the design process using the sophisticated techniques developed for this purpose. Estimating these uncertainties is not trivial, but requires first that the uncertainties on the available experimental data are consistent and complete. In Chapters 3, 4 and 5, the experimental uncertainties in three reactions are studied in detail, and a template is presented to allow for missing or underestimated sources of uncertainty to be accounted for. In Chapter 6, the efficiency of a gamma detector is studied in detail, since these detectors are often used to obtain the data that guides the evaluation process and the efficiency is often one of the most significant sources of uncertainty. The uncertainties in the curve fitting process used to obtain gamma intensities are also explored, with implications for curve fitting in the physical sciences. Finally, Chapter 7 presents a new method to estimate the uncertainty on a specific subset of cross section evaluations. These are cases where there are measurements only of specific gammas de-exciting the product nucleus, and the reaction cross section is deduced by combining the measured gamma cross sections with a theoretical calculation. The work presented here is a first step in improving the uncertainty analysis for evaluations that have constraining data.

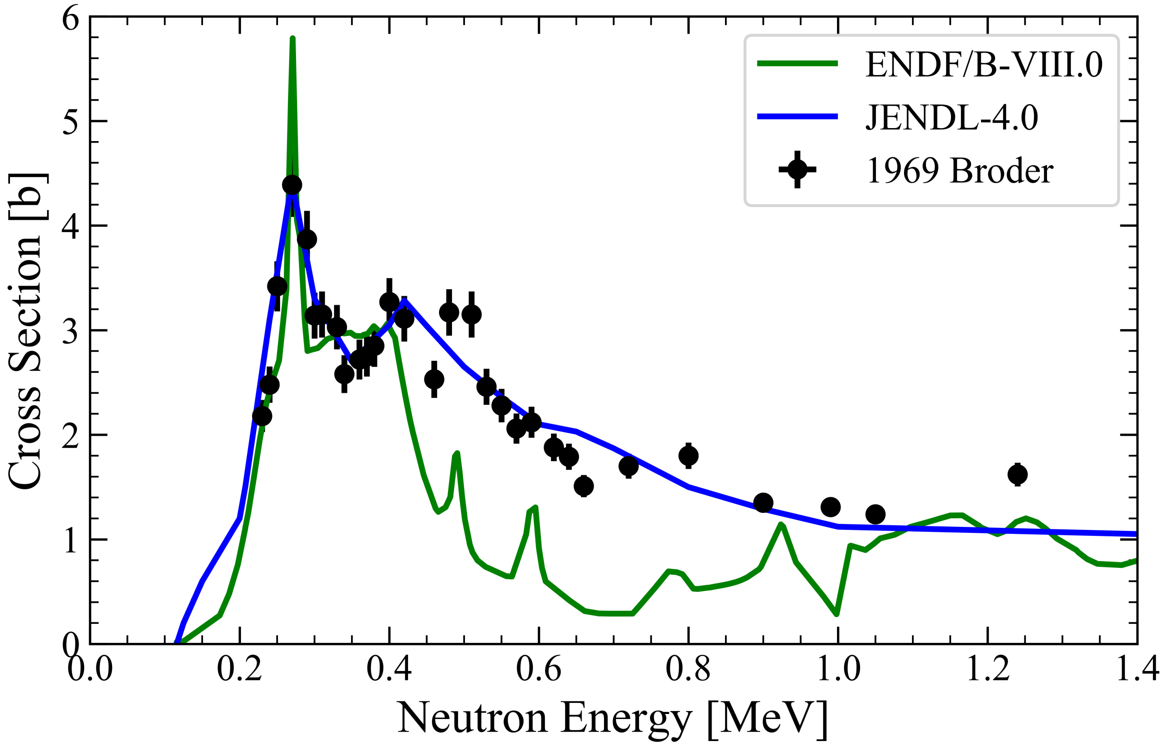

Figure 1.4: Inelastic scattering cross section of ^{19}F from ENDF/B-VIII.0 and JENDL-4.0, along with a data set from 1969. The ENDF/B-VIII.0 evaluation follows the energy dependence of the total cross section, but between 0.5 and 1 MeV, the magnitude is up to an order of magnitude lower than the available data. The JENDL-4.0 evaluation follows the data more closely, but does not include the resonance structure that is present at these energies.

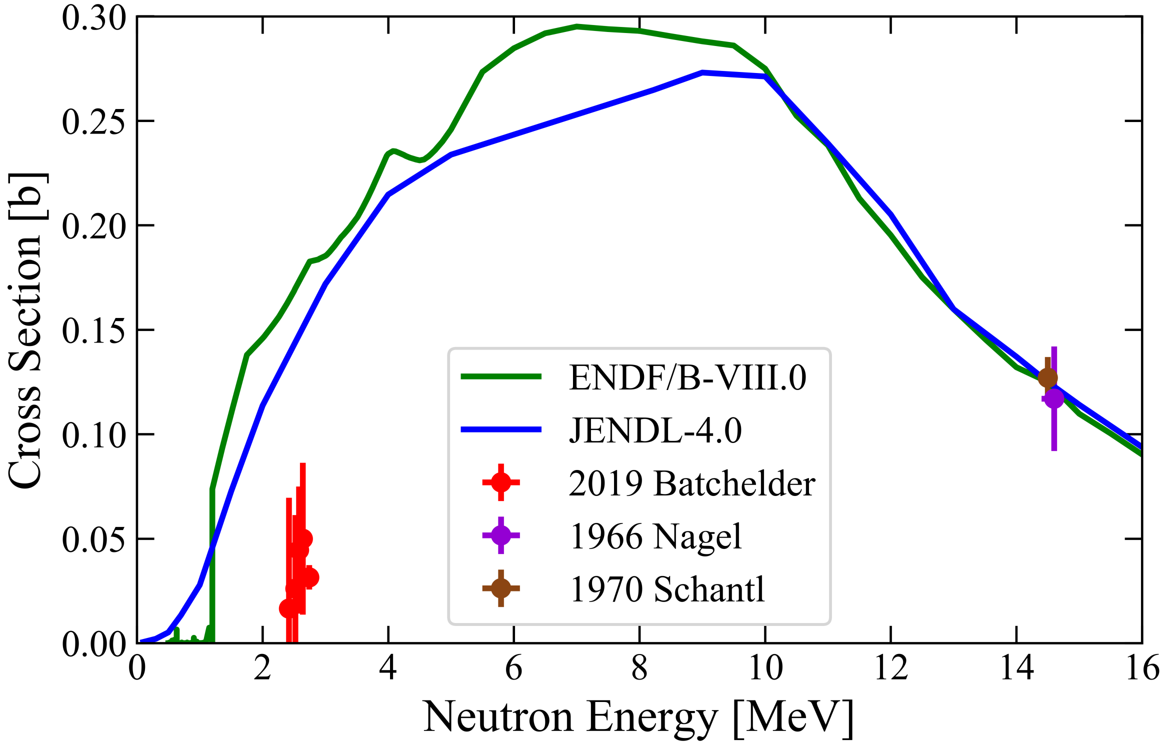

Figure 1.5: Evaluated cross section for ^{35}Cl(n,p) from the ENDF/B-VIII.0 and JENDL-4.0 libraries. Both evaluations match the older data sets at 14 MeV, but are significantly higher than the recent measurement between 2 and 3 MeV. There is little data on any ^{35}Cl reactions in this energy region, leading to this large discrepancy.

Chapter 2

Background

2.1 Nuclear Reaction Physics

2.1.1 Nucleons and the Strong Force

The nucleus is made up of protons and neutrons, which are spin-1/2 Fermi particles, and obey the Pauli Exclusion Principle, which states that no two identical fermions can share all of the same quantum numbers.

The dominant forces through which these particles interact are the nuclear strong force and the Coulomb force. The nuclear strong force is a short-range attractive force mediated by the exchange of mesons, particles with rest energy of about 140 MeV. This leads to an estimate of the range of the force of about 1.4 fm [64]. The force is attractive except at very short distances, when it becomes strongly repulsive to keep the particles from having completely overlapping quantum numbers. Between this repulsive core and the short range of the attractive force, the nucleons find an energy minimum at a distance of about 2.4 fm from each other [65]. Attempts to derive the nuclear strong force starting from the quarks and gluons are ongoing and in most applications phenomenological models of the effective nucleon-nucleon interaction are used.

The Coulomb force is mediated by the exchange of virtual photons. The massless photons give the force infinite range, but the strength falls off with distance as $1/\mathrm{r}^2$. It is repulsive between protons, reducing the overall strength of the force between them, and does not effect neutrons.

2.1.2 The Nucleus

The nucleus is made up of nucleons bound in an attractive potential well. The minimum energy distance between the nucleons, about 2.4 fm, leads to a system that is incompressible and therefore of constant density. The constant density leads to the nuclear size being directly dependent on the number of nucleons, A,

$$R = R_0 A^{1/3} \tag{2.1}$$

where R_0 is a constant that has been fit using radius measurements and is taken to be about 1.25 fm [66].

The ground state is the state where the nucleus is the lowest energy configuration possible, and it cannot reduce its energy by any means other than changing its constituent parts. The nucleus in its ground state is characterized by the mass, binding energy, stability against decay, deformation, angular momentum and parity.

The total mass of a nucleus is the sum of the masses of all constituent nucleons minus the binding energy,

$$m(Z, A) = Zm({}^1_1\mathrm{H}) + (A - Z)m({}^1_0\mathrm{n}) - B_E(Z, A). \tag{2.2}$$

The binding energy arises from the attractive potential. Each nucleon releases energy as it falls into the potential well, which comes from its effective mass.

The ground state of the nucleus has a set angular momentum and parity, which are defined by the orbitals of the nucleons. All even-even nuclei have a ground state spin-parity $\mathrm{J}^\pi = 0^+$, because of a strong residual pairing interaction that causes them to cancel out their angular momenta. Other nuclei can have a wide range of ground state J^π values, which in all but a few simple cases cannot be determined without measurement.

The nucleus is not always spherically symmetric, but may be deformed. Most deformed nuclei can be well-approximated as being axially symmetric in their ground state. The deformation of a nucleus in its ground state determines what type of excitations it can sustain. The deformation of the ground state is represented by β_2. A β_2 value around 0.1 or below indicates a spherically symmetric nucleus.

Each nucleus has a separation energy for each type of nucleon, which represents the amount of energy required to remove the least bound nucleon of that type. For nuclei close to or at the neutron drip line, the neutron separation energy becomes zero, meaning that any additional neutrons that tried to enter the system would not be bound to the nucleus.

These characteristics can be modeled with a combination of two complementary classes of models, spherical and deformed Shell Models and collective or generalized Liquid Drop Models.

2.1.2.1 Shell Model

The spherical shell model is based on a mean field approximation where there are no residual interactions between the nucleons, only a static, attractive central force with a repulsive core. The spatial dependence of the mean potential is described by the Woods-Saxon potential,

$$V(r) = -V_0 \left[1 + \exp\left(\frac{r - R}{a}\right)\right], \tag{2.3}$$

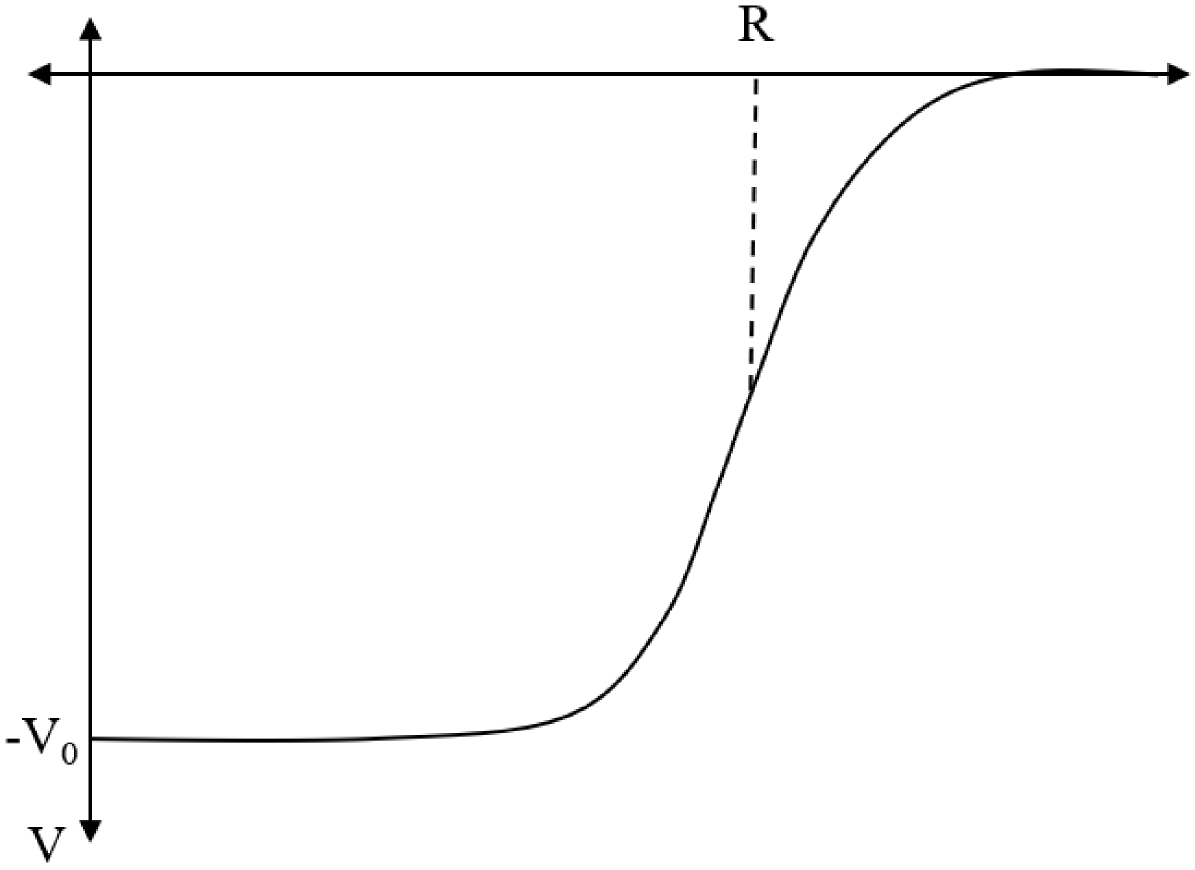

Figure 2.1: Schematic of the Woods-Saxon potential. The force is constant throughout most of the nucleus, due to the constant density of nucleons. Near the surface the strength of the force is reduced due to the lower density. The force is short range.

shown in Figure 2.1. The value of a is approximately 0.5 fm, V_0 is approximately 50 MeV, and R is calculated with Equation 2.1 [66]. At the center of the nucleus, the force is constant in order to reproduce the constant nuclear density. Near the surface of the nucleus the attractive force decreases smoothly, dropping to zero just beyond the average radius of the nucleus, Equation 2.1. The repulsive Coulomb force between protons shifts the whole potential well up in energy and slightly changes the shape, as can be seen in Figure 2.2. The neutron well is the strong nuclear force Woods-Saxon potential, whereas the proton well is a mix of the Woods-Saxon potential and the repulsive Coulomb potential [66]. The Coulomb potential creates a lip at the surface of the nucleus with a tail that asymptotically goes to zero. This lip is caused by the repulsion between the positively charged proton and nucleus, so if a proton were just touching the surface of the nucleus they would be accelerated away

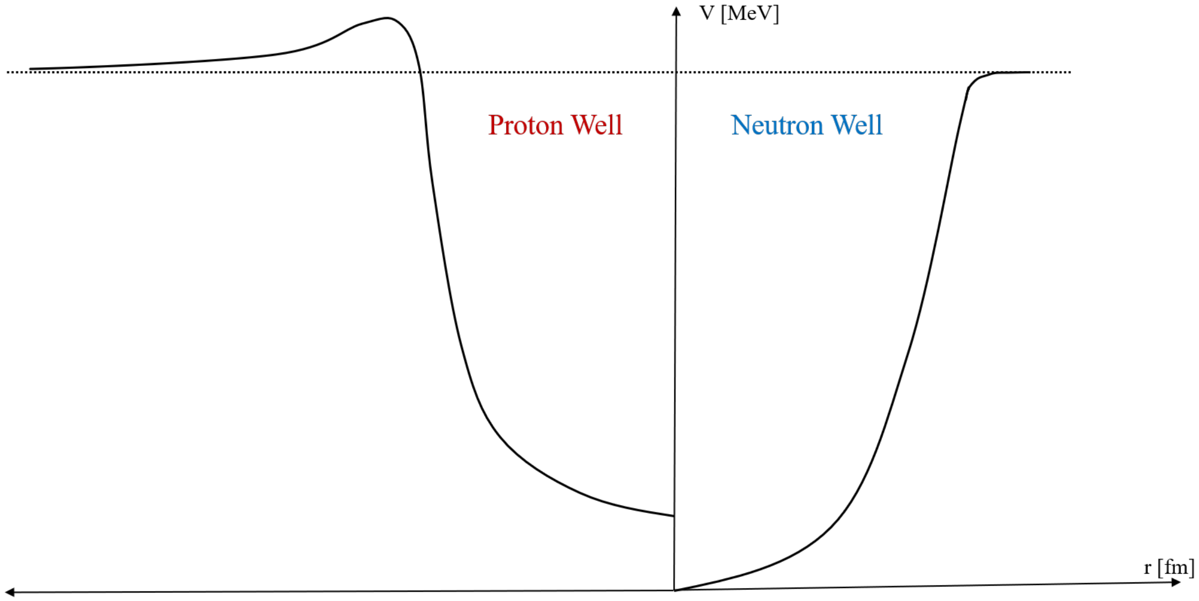

Figure 2.2: Schematic of the Woods-Saxon potential wells for the protons (on the left) and the neutrons (on the right). The dashed black line represents $V = 0$. The neutron well is the pure Woods-Saxon form, and the proton well is a combination of the Woods-Saxon potential representing the strong nuclear force, and the Coulomb potential representing the repulsive Coulomb force. This leads to a proton well that is not as deep as the neutron well and has a slight lip near $V = 0$ with a tail that extends to infinity. The actual difference in depth between the neutron and proton wells is dependent on the total charge of the nucleus. This diagram is not to scale, and the well depth differences are exaggerated for visual clarity.

from each other. This acceleration requires energy, so a proton cannot be removed from the nucleus with zero kinetic energy while a neutron can. The relative shift between the proton and neutron wells increases with increasing total charge in the nucleus, as it is dependent on Coulomb repulsion. This means that for light nuclei with low-Z, the difference between the depths of the proton and neutron wells is small, whereas for the actinides it is much larger. The proton and neutron potential wells are shown in the schematic diagram in Figure 2.2.

The nucleons are considered independent particles and move in unperturbed single-particle orbitals, which are eigenfunctions of the central force (which itself comes from all of the nucleons). The eigenfunctions of the Woods-Saxon potential cannot be determined in closed-form, so the approximations of the infinite square well and the infinite harmonic oscillator are used in some circumstances to understand the trends and general characteristics of the orbitals. However, they do not give the correct number of nucleons for shell closures, referred to as “magic numbers”, which have been determined experimentally by trends in the two-proton and two-neutron separation energies, capture cross sections and the nuclear charge radius [66]. Furthermore, a strong spin-orbit interaction needs to be added in to the

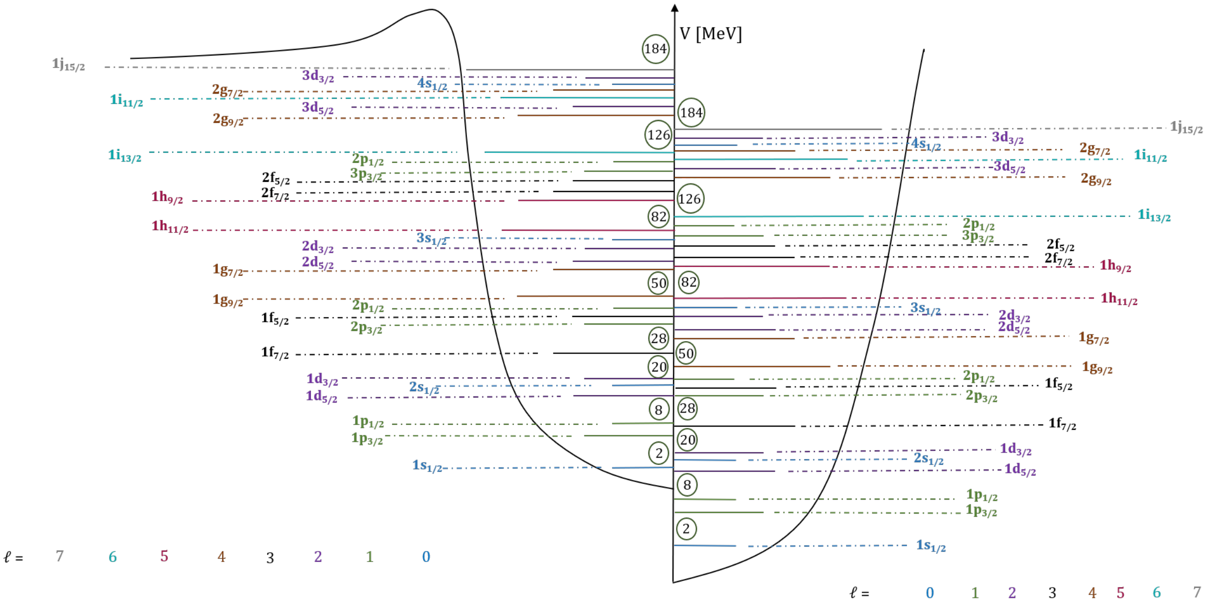

Figure 2.3: Schematic showing the single-particle orbitals calculated from the Woods-Saxon potential with spin-orbit coupling. The magic numbers, which come from large gaps between orbitals, are shown. The location of the proton and neutron orbitals and magic numbers are mass-dependent and are just shown here for a general reference. It can be seen that because of the shifted well, the magic numbers for the protons typically occur higher in energy (less bound) than those for the neutrons.

Woods-Saxon potential in order to accurately reproduce the observed magic numbers.

The spin-orbit coupling term, $\boldsymbol{\ell}\cdot\mathbf{s}$, is modeled after the spin-orbit coupling in atomic physics, only much stronger. The effect is large enough to change the order of the orbitals relative to the j-degenerate solutions. The orbitals for the Woods-Saxon potential with spin-orbit coupling are shown in Figure 2.3 for both protons and neutrons. Since protons and neutrons are distinguishable particles they fill separate orbitals. However, their similarity in mass and spin, and the fact that the strong force is not sensitive to charge, leads to identical orbitals schemes for protons and neutrons. The difference in the well depth due to the Coulomb repulsion of the protons leads to the orbitals occurring at different energies. The lower energies of the neutrons is seen in the chart of isotopes, where the valley of stability quickly falls away from the $Z = N$ line for heavier nuclei.

The nucleus must obey proper symmetrization—as a collection of identical fermions, the wavefunction must be anti-symmetric, with means that there is a sign change when particles are exchanged. The consequences of this requirement include that two identical particles in the same orbital can only couple to even values of angular momentum. Identical particles in different orbitals can couple to any value of angular momentum allowed by the vector addition. For two particles with angular momentum j_1 and j_2, the coupled angular momentum can range from $|j_1 - j_2|$ to $(j_1 + j_2)$. A special case of coupling is pairing of nucleus, which is two identical particles coupled in time reversed orbits with orbital angular momentum values that cancel each other.

The shell model can be used to calculate some properties of the nucleus in its ground state, such as the ground state J^π and static deformation. For nuclei near closed shells, angular momentum addition can be used to predict the ground state J^π. As the number of protons or neutrons beyond the largest closed shell increases, the number of possible combinations grows and this method soon loses its efficacy. Static deformation of the ground state can also be determined using this model, as it depends on the number of interactions between valence nucleons of different type. There is a simple equation to calculate the "promiscuity factor," P, that gives a good estimate of whether or not a nucleus will be deformed in its ground state,

$$P = \frac{N_n \times N_p}{N_n + N_p}, \tag{2.4}$$

where N_n is the number of neutrons from the nearest magic number (which can be either above or below) and N_p is the same for protons [67]. If P is above 4, the nucleus is sufficiently deformed in its ground state to have all the properties of deformed nuclei. This method is simplified and approximate, and the actual deformation values can be calculated with more sophisticated models.

When P is greater than 4, and the nucleus is sufficiently deformed, the spherical shell model is no longer predictive. This can be remedied by the use of the Nilsson model which accounts for the deformation by using a rotational ellipsoid central potential [66]. In this case, ℓ is no longer a "good" quantum number and different quantum numbers are used instead—the projection of the angular momentum on the axis of symmetry, called K.The spherical solutions have a degeneracy of (2j+1), as the orientation of the angular momentum is not important for a spherically symmetric potential. In the deformed model that degeneracy breaks and each value of K becomes a separate orbital, as can be seen in Figure 2.4, with degeneracy two (for spin). The shell model orbital diagrams can then be expanded into another dimension, with a deformation (β_2) axis. An example of such a Nilsson Diagram (also known as a "spaghetti plot") is shown in Figure 2.5. This figure shows only the orbitals between the N = 50 and N = 80 shell closures, and demonstrates how the orbitals overlap and cross each other with increasing deformation.

2.1.2.2 Liquid drop model

The liquid drop model sits at the other extreme from the shell model—it is a highly collective model that is mostly classical, and mostly ignores the individual constituent nucleons. The model is successful in describing behavior of the entire nucleus as nuclear matter is similar to a liquid drop in that it has similar saturation and low-compressibility properties, as well as a well-defined surface. The liquid drop, composed of charged water molecules, is held together by attractive van der Waals forces, which are not central.

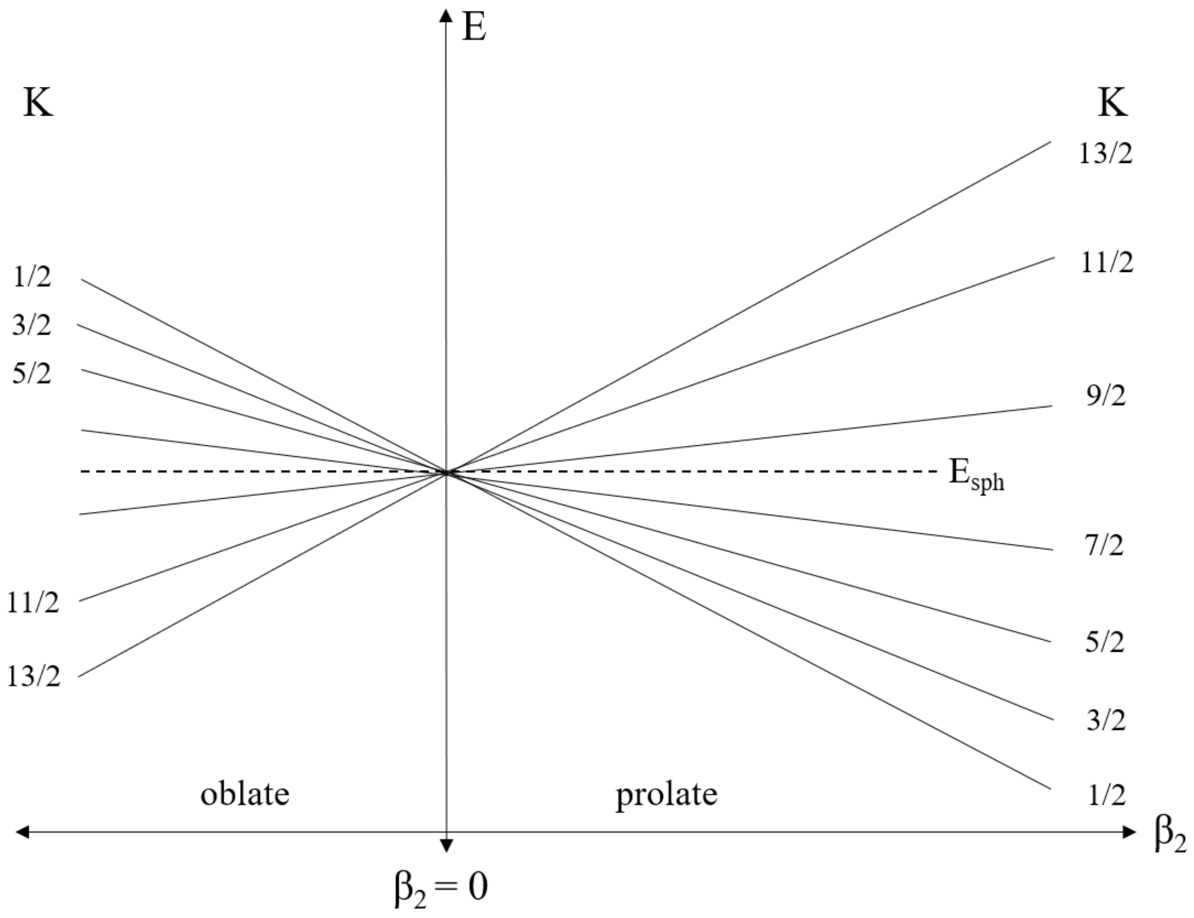

Figure 2.4: Schematic showing how an $i_{13/2}$ orbital splits into many individual orbitals, defined by the K quantum number, in the Nilsson model. For prolate nuclei (β_2 >0), orbitals with lower K values spend more time closer to other nuclei, so their energy decreases. For oblate nuclei, the higher K values have lower energies.

The liquid drop model is particularly successful in representing nuclear binding energies, with a few quantum corrections. The Bethe-Weizsäcker formula,

$$B(Z, A) = a_v A - a_s A^{2/3} - a_c \frac{Z(Z-1)}{A^{1/3}} - a_{sym} \frac{(A-2Z)^2}{A} + a_p \delta(A, Z), \tag{2.5}$$

predicts the binding energy, B, of nucleus with Z protons and mass number A [66]. The first term is the volume term, which has its basis in the liquid-drop model. The attractive force (whether the strong force or the van der Waals forces) comes from the nucleons or molecules themselves, so the binding energy should be proportional to the number of nucleons, A. The rest of the terms reflect other aspects of the nuclear mean-field model. The second term is the surface term, which corrects for the fact that nucleons on the surface do not interact with

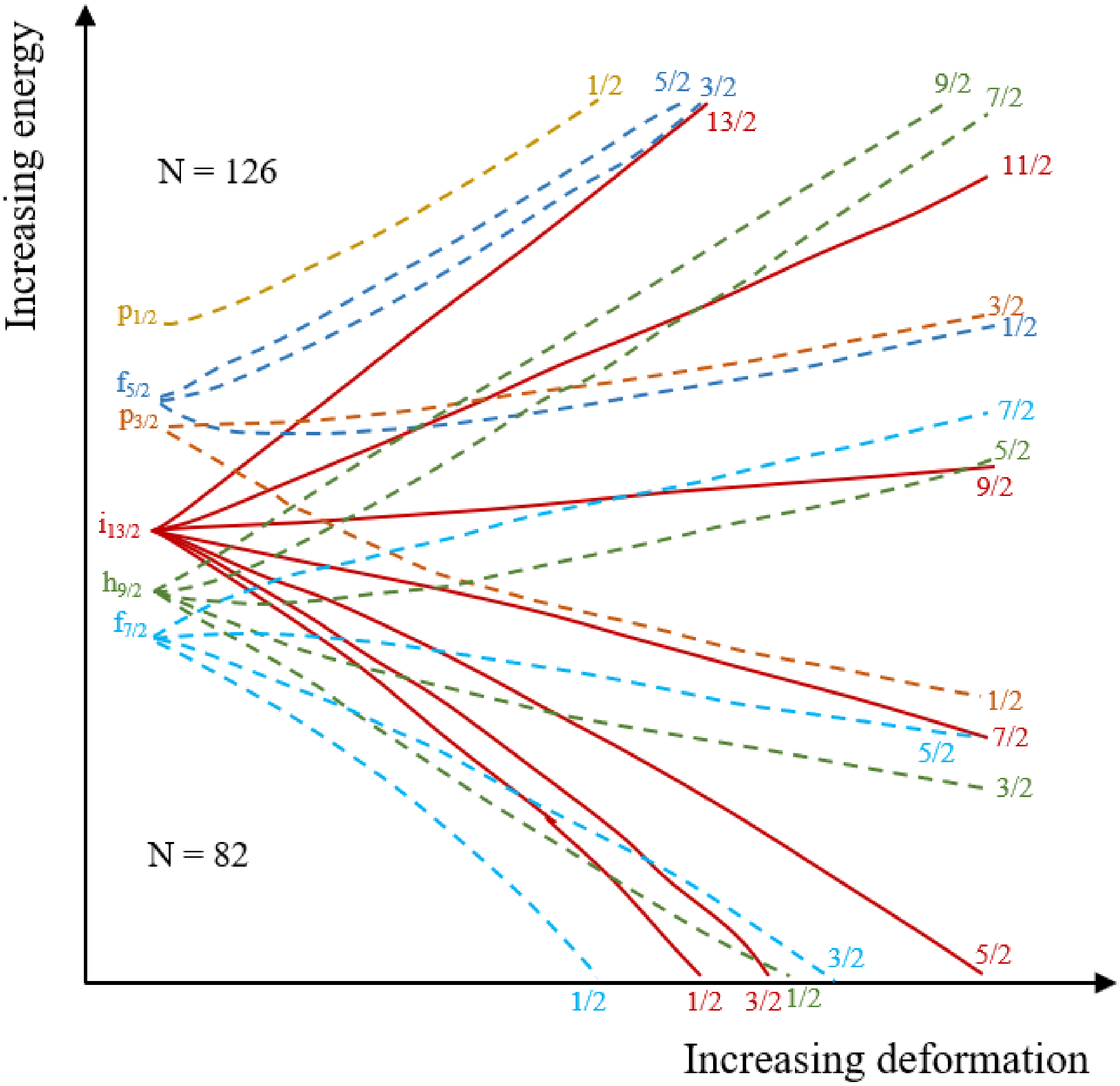

Figure 2.5: Example of part of a Nilsson diagram, showing only the orbitals originating between the N = 50 and N = 82 magic shell closures. The $i_{13/2}$ orbital is highlighted in red. As the deformation increases, the splitting increases and the shell model orbitals overlap with each other.

as many nucleons as those in the center. The correction is therefore proportional to $A^{2/3}$, which represents the surface of the sphere (because of the dependence of the volume on the radius, Equation 2.1). The third term represents the repulsive Coulomb force between the protons that lowers the binding energy overall, and is proportional to $Z(Z-1)$. The fourth term is the symmetry term, which reflects the fact that the neutrons and protons fill their own separate orbitals. If there are many more neutrons than protons, the final neutrons will be forced into orbitals at higher energies than open proton orbitals, even with the Coulomb force pushing the whole well up. This is the term that explains beta-minus decay, even though it increases the repulsive Coulomb force. Finally, the fifth term is the pairing term. The delta function is positive one for even-even nuclei (all nucleons are paired), zero for even-odd (just one is unpaired) and negative one for odd-odd (two unpaired nucleons). The constants, a_i, have been determined by global fitting.

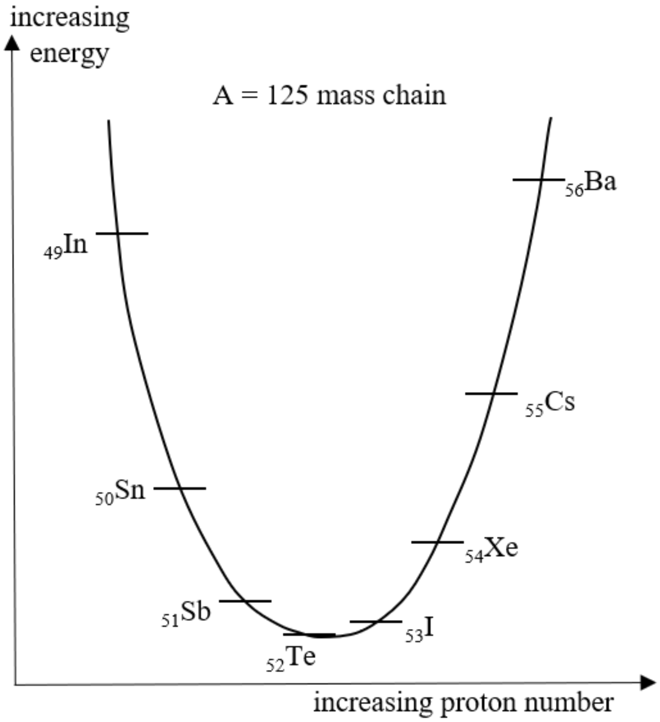

Figure 2.6: Example mass chain for A = 125. The y-axis represents the potential energy of the nucleus, which has a negative relationship with binding energy, so the isotopes lower on the y-axis are more bound. The x-axis represents Z, the number of protons in the nucleus. The minimum of the curve represents the optimization between the Coulomb term, which increases with increasing proton number, and the symmetry term, which increases with increasing neutrons.

The competition between the coulomb term and symmetry term explains the ground state energy of nuclides with the same mass (the mass chains), the “valley of stability” and the neutron and proton drip lines. The mass chain for $A = 125$ is shown in Figure 2.6, with potential energy on the y-axis and proton number on the x-axis. The isotopes in the middle of the mass chain are the most bound. On the left side, with increasing neutron number, the symmetry term in Equation 2.5 increases as the added neutrons fall into orbitals that are higher and higher in energy. On the right side, with increasing proton number, the added protons are in orbitals that are lower in energy than the least bound neutrons, but each one brings a unit of charge and the Coulomb term increases. For each mass number, A, the minimum binding energy occurs at the optimization of these two forces, and for the case of $A = 125$, that occurs at ^{125}Te.

There are, however, many differences between liquid drops and nuclei that prevent this model from being able to capture all of the properties of nuclei. The quantum nature of nucleons, for example, leads to a larger average distance between nucleons than between water molecules, which in turns leads to much less scattering between nucleons. The mean free path of the nucleon in the nucleus is comparable to the size of the nucleus itself, and the nucleons act more like non-interacting gas particles. The quantum nature also leads to "shell effects", which are strong discontinuities or discrepancies from smooth trends around the magic numbers. The liquid drop model enjoys success at fitting the smooth trends, and the shell model can be used to model the quantum effects.

2.1.2.3 Static deformation

As mentioned above, nuclei with a large number of valence particles of both types develop static deformation. The shape of the nucleus is represented by the radius as a function of the angles θ and ϕ, and is in reference to R_0, which is the radius of a sphere of the same volume. The radius is represented by

$$R = R(\theta, \phi) = R_0 \left(1 + \alpha_{00} + \sum_{\lambda=1}^{\infty} \sum_{\mu=-\lambda}^{\lambda} \alpha^*_{\lambda\mu} Y_{\lambda\mu}(\theta, \phi) \right), \tag{2.6}$$

which is an expansion using the spherical harmonics, $Y_{\lambda\mu}$ as basis functions [65]. The constants $\alpha_{\lambda\mu}$ describe the extent of the deformation on each basis function. The first constant, α_{00}, can only describe changes in the total volume, and therefore can be used as a normalization term and is set as

$$\alpha_{00} = -\frac{1}{4\pi} \sum_{\lambda>1} \sum_{\mu} |\alpha_{\lambda,\mu}|^2. \tag{2.7}$$

The next highest order terms, those with $\lambda = 1$, represent movement of the entire system, relative to a laboratory reference frame. The three terms with $\lambda = 1$ are constrained by the requirement that the center of mass be at the origin of the coordinate system.

The expansion terms with $\lambda > 1$ actually represent perturbations to the spherical symmetry of the nucleus itself. Terms with $\mu = 0$ represent axially symmetric deformations, and in the frequent assumption of axial symmetry, all terms with $\mu \neq 0$ are dropped. The constants on the axially symmetric terms, $\alpha_{\lambda,0}$ are also called β_λ.

In the case of quadrupole deformation ($\lambda = 2$) only, there are just five constants that describe the shape of the nucleus, $\alpha_{2,\mu}$, where $-2 \leq \mu \leq 2$. Three of the terms are required to describe the orientation of the nucleus in a laboratory reference frame, and these can be constrained by choosing a coordinate system that is intrinsic to the nucleus. This leaves the problem with two free variables, $\alpha_{2,0}$ and $\alpha_{2,2} = \alpha_{2,-2}$, to describe both the orientation and shape. To describe these in a more intuitive way, the Hill-Wheeler coordinates, β and γ have been introduced as such

$$\alpha_{2,0} = \beta \cos \gamma \tag{2.8}$$

$$\alpha_{2,2} = \alpha_{2,-2} = \frac{1}{\sqrt{2}} \beta \sin \gamma. \tag{2.9}$$

In this representation, the combination of $\beta > 0$ and $0 \leq \gamma \leq 60^\circ$ are enough to describe all shapes seen with quadrupole deformation [65].

2.1.3 Excited Levels

The nucleus is a quantized system, and the eigenvalues of this many-body system correspond to the energy levels. The full solution of the nuclear eigenvalue equation cannot generally be obtained using current computational capabilities, necessitating the use of the phenomenological Shell and Liquid Drop models to describe the spectrum of nuclear excited states. The types of excited levels seen are here split into two groups—single particle levels, which are represented by moving nucleons into new orbitals, and collective levels, which are represented by collective motion of the nucleus.

2.1.3.1 Single Particle Levels

Single particle levels are excitations that can be represented by nucleons occupying specific shell model orbitals. The energy of the excited level is the energy required to move the nucleons from their ground state configuration into different orbital configurations plus a residual interaction, with pairing being the most common. The spin and parity of the level can be described by the orbitals that unpaired nucleons sit in. An example is the first few excited levels of ^{17}O. The ground state and first two excited levels of ^{17}O are shown in Figure 2.7, along with the configuration of the nucleons in those levels. The first few levels in ^{17}O are simple, so the shell model can be used to easily describe them. The ground state is fully described by the one unpaired neutron in the $1d_{5/2}$ orbital, giving it a J^π of $5/2^+$. The lowest energy nucleon transition from the ground state is for the unpaired neutron to move to the $2s_{1/2}$ orbital. This transition requires 0.87 MeV, so the first excited state has an energy of 0.87 MeV and a J^π of $1/2^+$. The next lowest energy configuration is for the pair in the $1p_{1/2}$ to break, and one of the neutrons to move up to the $1d_{5/2}$ orbital and pair with the neutron there. This leaves one unpaired neutron in the $1p_{1/2}$ orbital, which gives the characteristics to the second excited level—energy of 3.06 MeV and J^π $1/2^-$.

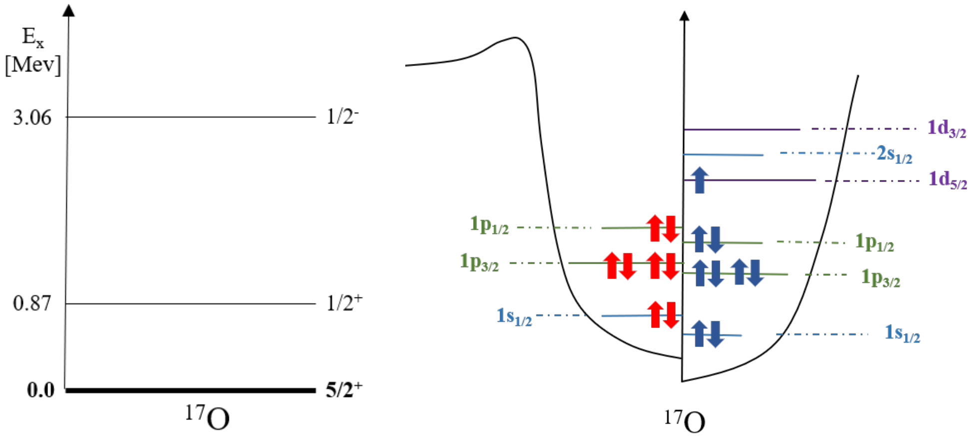

(a) Ground state of ^{17}O (b) Nucleons in ^{17}O in the ground state

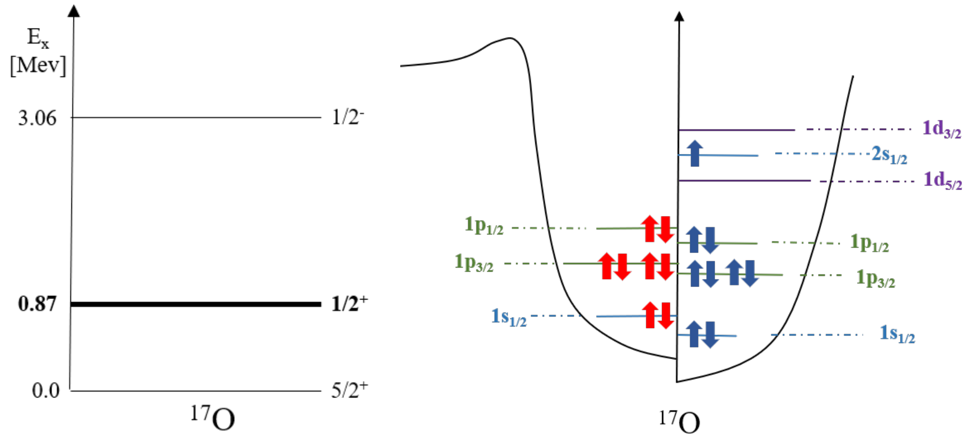

(c) First excited level of ^{17}O (d) Nucleons in ^{17}O in the first excited level

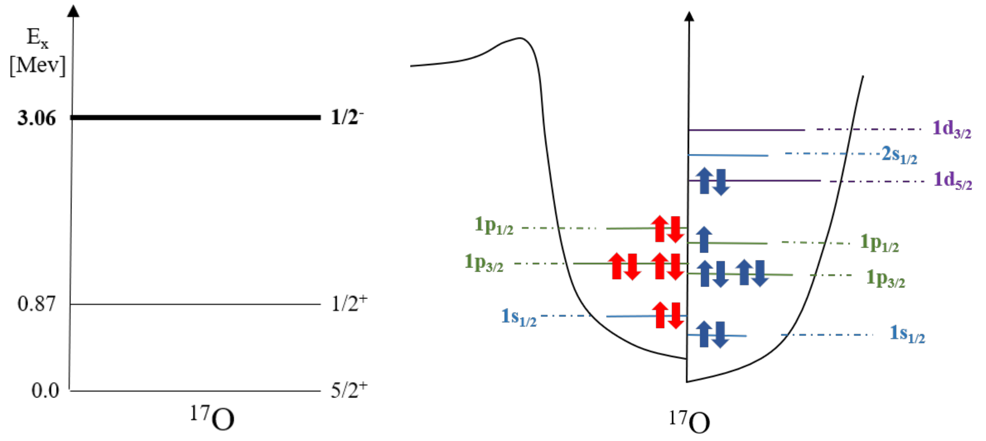

(e) Second excited level of ^{17}O (f) Nucleons in ^{17}O in the second excited level

Figure 2.7: Example of ^{17}O showing how moving nucleons into different shell model orbitals can create excited levels. The level schemes on the left show which level is being demonstrated with the orbital diagrams on the right.

2.1.3.2 Collective Levels

Collective levels are excitations that are comprised of many nucleons, and are often described in terms of the liquid drop model. Nuclei that are statically deformed have the ability to rotate their axis of symmetry, and all nuclei can sustain vibrational excitations which are spherical when time-averaged.

Vibrational excitations can be described as being comprised of phonons, with λ denoting the orbital angular momentum of the excitation. The lowest excitation is a quadrupole vibration, which is described as a single excitation with a $\lambda = 2\hbar$ quantum, reflecting the large energy required to create a dipole excitation with protons and neutrons moving out-of-phase with each other. The next is a octupole vibration, described by a single excitation with a $\lambda = 3\hbar$ quantum [66].

In even-even nuclei that are not statically deformed, vibrational levels are often the lowest excited levels in the level scheme. The first level is the single $\lambda = 2\hbar$ quantum excitation, which combines with the 0^+ ground state to form a 2^+ excited state, generally with excitation energy around 0.5 to 1 MeV. Above this are levels described by a combination of two $\lambda = 2\hbar$ quanta, which can combine with each other and the 0^+ ground state to created three different possible levels, with $\mathrm{J}^\pi = 0^+$, 2^+, and 4^+. These three levels have approximately the same energy, which is twice the energy of the single $\lambda = 2\hbar$ quantum level. The single $\lambda = 3\hbar$ quantum level has $\mathrm{J}^\pi = 3^-$. Higher in energy, the level scheme will likely look more complicated as single particle excitations become energetically possible. The vibrational model no longer provides the simplest description of the spectrum of excited states at this point [66].

The rotational excitations possible in statically deformed nuclei can be modeled as quantum rotations. The energies of the levels in a rotational band starting at level with energy E_i follow a simple equation,

$$E(J) = E_i + \frac{\hbar^2}{2\mathcal{I}} J(J+1), \tag{2.10}$$

where J is the difference between the spin of the level and the spin of the first level in the band, and $\mathcal{I}$ is the moment of inertia. For even-even nuclei, the ground state rotational band starts with with a $\mathrm{J} = 0^+$, $E_i = 0$ level. All rotational bands built on $\mathrm{J} = 0^+$ levels increment by $\Delta\mathrm{J} = 2$, as the parity must be positive for all of the levels in the band [66]. As with vibrational excitations, increasing excitation energy allows for more levels. For example, the level scheme of ^{182}Ta is shown in Figure 2.8, and the distinct low energy rotational levels can be seen transiting into a high density of levels.

Additional degrees of freedom open with increasing excitation energy as the different types of excitations can combine together—a simple example is that in deformed nuclei, rotational bands can be built on vibrational or single particle levels. The Nilsson model is another form of this coupling, as the presence of deformation alters the single particle orbitals and breaks the (2j+1) degeneracy, allowing for many more possible excitations.

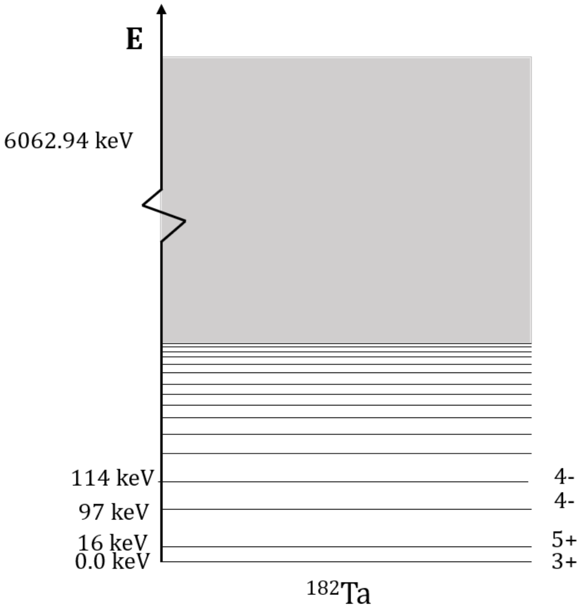

Figure 2.8: Diagram showing the excited levels in ^{182}Ta. The ground state is labeled at zero excitation energy and has a J$^{\pi}$ of 3^{+}. The first excited state, at 16 keV of excitation energy, has a J$^{\pi}$ of 5^{+}. As the excitation energy increases, the levels get more numerous and closer together, which is represented by the grey block.

2.1.3.3 Level Density Models

The simple models described above can be used to approximately predict the lower end of the level scheme for some nuclei, but to know the level scheme with any precision, the levels must be measured experimentally. How many levels are measured is dependent on many things, including the density of levels and whether a researcher has been interested in studying the low-lying structure of the nucleus.

As excitation energy increases, the levels can no longer be measured in their totality and a level density model becomes appropriate. There are two main categories of level density models—phenomenological and microscopic.

The most common phenomenological level density models are the Fermi Gas model [68], the Constant Temperature model [69], and the Generalized Superfluid model [70, 71]. Another common model is known as the Gilbert-Cameron model [72], which combines the Constant Temperature model at lower energies and the Fermi Gas model above.

The Fermi Gas model [68] treats the nucleons as a non-interacting Fermion gas. Only single-particle excitations are treated in this model, and it is assumed that the orbitals are equally spaced. Under the Fermi Gas model, the level density as a function of excitation energy, E, spin, J, is,

$$\rho_F(E,J) = \frac{1}{2}\frac{2J+1}{2\sqrt{2\pi}\sigma^3}\exp\left[-\frac{(J+1/2)^2}{2\sigma^2}\right] \times \frac{\sqrt{\pi}}{12}\frac{2\sqrt{aU}}{a^{1/4}U^{5/4}}. \tag{2.11}$$

In this equation, it is assumed that positive and negative parity levels are equally likely, which gives the leading $\frac{1}{2}$ term. The variable a is an adjustable parameter that represents nucleus-specific information that is not contained in the model. The variable σ is known as the spin-cutoff parameter, and is the standard deviation of the Gaussian distribution used to model the distributions of spins. The energy dependence is in the U variable, which is defined as the effective excitation,

$$U = E - \Delta, \tag{2.12}$$

where E is the excitation energy of the nucleus and Δ is a shift parameter[1] that is proportional to the energy required to break pairs of nucleons before they can be moved in their orbitals. This model comes directly from the single particle excitations, based on shell model orbitals, and does not inherently include collective excitations. A collective enhancement, which is a phenomenological model of the vibrational and rotational excitations, can be applied to model the full level density of the nucleus.

Another commonly used level density model is the Constant Temperature model [69]. It is an empirical model based on the observation that the cumulative number of levels in a nucleus follows an exponential form,

$$N(E) = \exp\left[\frac{E-E_0}{T}\right], \tag{2.13}$$

where E_0 and T are constants that are fit to experimental data[2]. The behavior can be understood as the nucleus undergoing a phase transition, which is often described as being related to shell structure. The level density, ρ_T, is then determined from the cumulative levels,

$$\rho_T(E) = \frac{\mathrm{d}N}{\mathrm{d}E} = \frac{1}{T}\exp\left[\frac{E-E_0}{T}\right]. \tag{2.14}$$

The Constant Temperature model does not distinguish between levels of different spins and parities in its basic form. Typically a Gaussian is applied for the spin distribution, and equal parity is assumed.

The Constant Temperature model can reproduce experimental cumulative level data at lower energies, and the Fermi Gas model has physics that are more applicable to higher energies where collective effects become less important. To this end, Gilbert and Cameron [72]

---

[1] Δ is approximately the pair breaking energy (around 2 MeV), but is often treated as an adjustable parameter.

[2] E_0 represents the energy of the first non-collective level in the nucleus, and T represents a "nuclear temperature".

developed a model that uses the Constant Temperature at lower energies and the Fermi Gas model at higher energies. The two models are normalized to each other by the requirement of a continuous function and first derivative at a specific energy E_M. The variables E_0, T and E_M can be solved for each isotope individually [11].

A more physical model, which includes shell effects and collective excitations, can be found in the Generalized Superfluid model [70, 71]. The overall level density can be described as,

$$\rho_{GS}(E,J) = \rho_{sp}(U,J)K_{vib}(U)K_{rot}(U), \tag{2.15}$$

where ρ_{sp} is the level density for single particle excitations, K_{vib} is the enhancement factor for vibrational excitations and K_{rot} is the enhancement factor for rotational excitations [11]. The single particle excitations are based on superconductivity models and reflect the fact that the strong pairing interaction between nucleons causes the formation of Cooper pairs. There is a phase transition that is analogous to the transition from the Constant Temperature to Fermi Gas descriptions in the Gilbert-Cameron model. The behavior below the transition is similar to that of the Constant Temperature model, and above it is similar to the Fermi Gas description. Shell effects are included in the model, which allows the differences between isotopes to be reproduced. The vibrational enhancement factor, K_{vib}, is based on all of the possible quasi-particle excitations [11],

$$K_{vib}(U) = \prod_i \left[\frac{1-\exp(-\omega_i^0/T)}{1-\exp(-\omega_i/T)}\right]^{g_i}, \tag{2.16}$$

where ω_i is the energy of each vibrational excitation and ω_i^0 is the energy of the quasi-particle excitation that creates it. T represents the temperature of the nucleus and g_i is the degeneracy of each excitation i. The rotational enhancement, K_{rot}, is unity for a spherical nucleus, and

$$K_{rot} = \mathcal{I}_\perp t \tag{2.17}$$

for deformed nuclei, where $\mathcal{I}_\perp$ is the moment of inertia of the nucleus perpendicular to the axis of rotation.

In addition to the phenomenological models described above, many approaches can be used to calculate the level density microscopically. These methods start with the shell model description of the ground state, and use combinatorics and recursive algorithms to count the excited levels that can be created. Some methods can only calculate single particle levels while others include collective enhancements. The details of these methods will not be given here, but a comprehensive description can be found in Reference [11].

2.1.4 De-excitation and Decay

Nuclei will always trend towards lower energy configurations. This includes an excited nucleus emitting gammas to get to its ground state, as well as a nucleus in its ground state

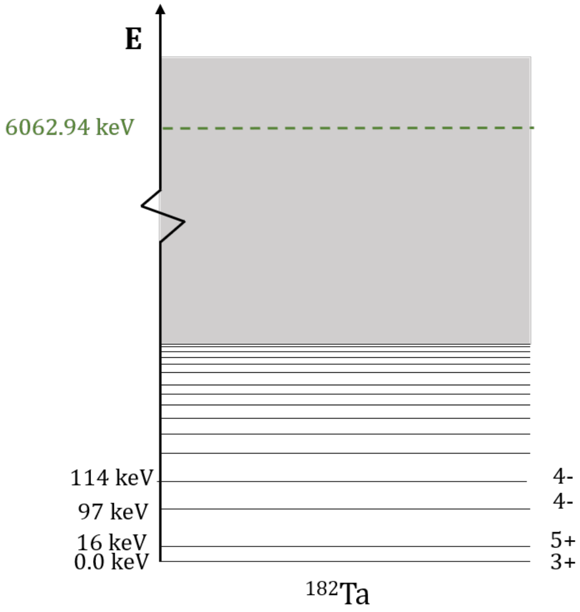

Figure 2.9: Diagram showing the excited levels in ^{182}Ta. The neutron separation energy, $S_n = 6062.94\,\text{keV}$ is indicated by a green dashed line. The neutron separation energy is the binding energy of the least bound neutron in the nucleus. A ^{182}Ta nucleus needs to be excited above S_n in order to emit a neutron. It is equivalently the amount of binding energy released when a ^{181}Ta nucleus absorbs a neutron.

decaying to get to a more stable isotope. There are many different possible decays that nuclei can undergo, only some of which will be energetically possible for any given nucleus. Of the processes that are possible, those with the fastest rates will happen the most often. This competition is seen in many isotopes, such as ^{152}Eu, whose ground state decays by beta decay about 28% of the time, and electron capture about 72% of the time [73]. The first isomeric state in ^{152}Eu, which is a 0^- state at 45.6 keV, decays by beta decay about 73% of the time, and electron capture about 27% of the time. The isomeric state can also decay by gamma emission to the ground state, but the rate is so much slower than the beta and electron capture rates that it does not occur with any significance.

The same kind of competition occurs in the de-excitation of higher energy excited states in a nucleus, where even more processes are possible. For example, a highly-excited nucleus can emit particles, such as neutrons or protons. For particle emission to be energetically possible, the nucleus needs to be excited above the separation energy. The separation energy for a particle is the binding energy of the least bound particle in the nucleus. For example, for ^{182}Ta to emit a neutron, it needs to be excited above the neutron separation energy, S_n, which is 6062.94 keV for this isotope. The neutron separation energy for ^{182}Ta is shown in Figure 2.9.

Protons, alphas and all other particles have similar separation energies. Gammas, which have no mass, do not have binding energy and there is no such threshold on their emission.

The rates of emission can be represented by transmission coefficients, $T_B(E_x, J^\pi)$, which can be used to model the competition [74]. The probability of emission of a specific type of particle, B, at excitation energy E_x, spin J and parity π, is dependent on its own and all other transmission coefficients,

$$\mathbb{P}(B) = \frac{T_B(E_x, J^\pi)}{\sum_C T_C(E_x, J^\pi)}, \tag{2.18}$$

where the sum over C represents all other emissions that are energetically possible (other particles and gammas). The transmission coefficient for each particle/gamma, $T_B(E_x, J^\pi)$, is integrated over the outgoing energy and angular momentum. The models used to calculate transmission coefficients depend on the type of emission, and the models are explained in the following sections. This section covers the emission of particles when the nucleus is excited above the separation energy, the emission of gammas, and internal conversion. The other, typically slower, decay modes (beta decay, alpha decay and spontaneous fission) are not discussed here, as they do not play significant roles in the topics covered in this work.

2.1.4.1 Particle emission

The emission rates for particles are most often calculated using the optical model, which is used to model the potential between the nucleus and particle [75]. The optical model was developed to explain the interaction between an incoming neutron and a target nucleus, and more details about the model are given in Section 2.1.5. The transmission coefficient for the emission of a type of particle, B, is a sum over all possible emission characteristics [74],

$$T_B(E_x, J^\pi) = \sum_{I=|J-j|}^{I=J-j} \int_0^{E_x - S_B} d\epsilon \sum_{\ell j} T_{p,\ell j}(E_x - S_{\mathbf{B}} + \epsilon)\rho(\epsilon, I\pi_I)\delta(\pi\pi_I(-1)^\ell). \tag{2.19}$$

The transmission coefficient is integrated over I, the spin, ϵ, the excitation energy, and ℓ and j, the orbital and total angular momenta of the residual nucleus (after emission). S_B is the separation energy for the particle type B, π_I is the parity of the residual nucleus, and $\rho(\epsilon, I\pi_I)$ is the level density in the residual nucleus. As ϵ decreases, the levels in the residual nucleus are no longer represented by a continuous level density model (ρ), but rather by delta functions, and the integral over $d\epsilon$ becomes a summation over discrete level eneriges.

2.1.4.2 Gamma emission

Below the particle separation energies, the nucleus de-excites through a gamma cascade—the emission of gammas that connect the excited states in the nucleus. The emission of gammas is in most cases on the order of picoseconds or faster, and the slower processes of decay usually cannot compete. There are a few exceptions, which are addressed in the next section. The emission of a gamma is an electromagnetic process, and as such the models that are used are based on quantized electromagnetic radiation. The transmission coefficients for gamma emission can be expressed as,

$$T_{XL}(E_\gamma) = 2\pi f_{XL}(E_\gamma) E_\gamma^{2L+1}, \tag{2.20}$$

where XL represents the multipolarity of the transition, $f_{XL}(E_\gamma)$ is the Gamma Strength Function (γSF) of the transition, and E_γ is the energy of the emitted gamma. The multipolarity of the transition defines the electric or magnetic character ($X = E$ or M) and the angular momentum of the transition (L) [11].

The simplest model for the transmission coefficients is the Weisskopf estimates, which are based on quantized versions of the multiple moments. With several simplifying assumptions, the transition rate for electric transitions of angular momentum L can be approximated by,

$$T_{EL}(E_\gamma) = \frac{8\pi(L+1)}{L[(2L+1)!!]^2} \frac{e^2}{4\pi\epsilon_0 \hbar c} \left(\frac{3}{L+3}\right)^2 cR^{2L} \left(\frac{E_\gamma}{\hbar c}\right)^{2L+1}, \tag{2.21}$$

and for magnetic transitions,

$$T_{ML}(E_\gamma) = \frac{8\pi(L+1)}{L[(2L+1)!!]^2} \frac{e^2}{4\pi\epsilon_0 \hbar c} \left(\frac{\hbar}{m_p c}\right)^2 \left(\mu_p - \frac{1}{L+1}\right) \left(\frac{3}{L+2}\right)^2 cR^{2L-2} \left(\frac{E_\gamma}{\hbar c}\right)^{2L+1} \tag{2.22}$$

the details of which are given in Reference [66]. For the lower order multipoles ($L \leq 4$) simple estimates can be given for the electric transition rates, or transmission coefficients,

$$\begin{aligned} T_{E1}(E_\gamma) &= 10^{14} A^{2/3} E_\gamma^3 \\ T_{E2}(E_\gamma) &= 7.3 \times 10^7 A^{4/3} E_\gamma^5 \\ T_{E3}(E_\gamma) &= 34 A^2 E_\gamma^7 \\ T_{E4}(E_\gamma) &= 1.1 \times 10^{-5} A^{8/3} E_\gamma^9, \end{aligned} \tag{2.23}$$

and for the magnetic transition rates,

$$\begin{aligned} T_{M1}(E_\gamma) &= 5.6 \times 10^{13} E_\gamma^3 \\ T_{M2}(E_\gamma) &= 3.5 \times 10^7 A^{2/3} E_\gamma^5 \\ T_{M3}(E_\gamma) &= 16 A^{4/3} E_\gamma^7 \\ T_{M4}(E_\gamma) &= 4.5 \times 10^{-6} A^2 E_\gamma^9. \end{aligned} \tag{2.24}$$

The Weisskopf estimates are simple, but provide valuable insight into the trends and characteristics of gamma transitions. The estimates in Equations 2.23 and 2.24 show that the rate of electric transitions of a specific multiple (L) are faster than the magnetic transitions. This means that in the case where an excited level can de-excite by either an $E3$

or an $M3$ transition, to different final levels of similar energy, the $E3$ rate will be higher and that transition will have a larger branching ratio. The estimates also show that the rate increases with increasing E_γ, but decreases with increasing L. These factors all compete to determine branching ratios when an excited level has multiple possible transitions. Additionally, the Weisskopf estimates are only valid for transitions between single-particle levels (Section 2.1.3.1). Therefore, large deviations from the estimates can be used to identify when a transition is collective. A typical example is the transitions between levels within a rotational band, which can be thousands of times faster than the Weisskopf estimate.

For the transitions between discrete excited states, these estimates can be calculated for specific, known transitions. In the continuum region, the E_γ and f_{XL} dependences are typically separated, as in Equation 2.20. The γSF model comes from similar physics as the Weisskopf estimates, but must be generalized to account the averaging that occurs in the continuum region. The known discrete transitions of the low-lying levels are replaced with energy "bins", which contain some group of energy levels with some distribution of spins. For this reason, the γSF models usually include a level density model, as the probability of a transition occurring necessarily depends on the existence of states to transition to.

Due to the strong dependence on L, the most studied γSF models are for the lower multipolarities—$E1$, $M1$ and $E2$. The higher multipolarities are typically only seen at the bottom of the level scheme, where there are few levels available for an excited level to decay to. The $E1$ transition is the fastest, and therefore the most probable, transition. There are several different models used for the $E1$ γSF, including a Standard Lorentzian (SLO), the Generalized Lorentzian (GLO), the Modified Lorentzian (MGLO) and the Kadmenskij-Markushev-Furman model (KMF). The details of these models are given in Reference [11]. All of the models are based on the "Giant Dipole Resonance" (GDR), which is a collective excitation mode in the nucleus where the protons and neutrons move relative to each other, creating an electric dipole. This excitation mode acts like an antenna and can rapidly emit gammas, and similarly, the ground state of a nucleus can easily absorb a gamma of the correct energy and enter this excited mode. The GDR is described as a resonance located at an excitation energy that is unique for each isotope, although typically between 8 and 12 MeV. The $E1$ γSF models are typically based heavily on the GDR at higher gamma energies, and its tail at lower gamma energies. The $M1$ γSF models are typically based on other, similar collective excitations, such as the "Pygmy Dipole Resonance" (PDR), which is the valence neutrons moving with respect to the rest of the nucleus. The $E2$ γSF can be modeled after similar quadrupole excitation modes. Similarly to the phenomenological level density models, the phenomenological γSF models are typically simple and require normalization with experimental data. Recently, an enhancement to the γSF was seen at low gamma energies, which has been attributed to $M1$ transitions between excited levels that are very close in energy [76].

The de-excitation of a nucleus by gamma emission can be studied in detail with the use of the γSF and level density models, and experimental information about low-lying discrete levels and their transitions. Codes such as `DICEBOX` [77] and `RAINIER` [78] model the full gamma cascade (all of the gammas emitted as the nucleus de-excites) given information on the initial excitation energy and angular momentum in the de-exciting nucleus. This allows the user to choose a type of reaction (such as low energy capture), or implement specific initial conditions and model the cascade. Both of these codes perform Monte Carlo simulations of the cascade, and so can incorporate fluctuations in quantities such as the level lifetimes. Larger reaction calculation codes such as EMPIRE [74], `CoH`$_3$ [79] and TALYS [80] perform full calculations for an incident particle on a target nucleus. The cross sections and output particles are calculated for all energetically possible reactions, and also perform full deterministic cascade simulations for each residual nucleus as well. This allows the user to see a full cascade calculation that is not based on a single set of initial conditions in the product nucleus. This is important for many reactions, such as inelastic scattering of neutrons, where the initial conditions in the product nucleus depend heavily on the energy and angular momentum of the outgoing neutron.

A gamma cascade calculation has two distinct regimes. One is above E_{cut}, which is the excitation energy at which the modeling of discrete levels gives way to the use of level density models. The excitation energy space is split into “bins” which are each described by a total level density, a spin distribution, and a parity distribution. Deterministic calculations proceed by calculating probabilities of the energy bins de-exciting to lower energy bins, based on the level distributions and the γSF models. These codes also calculate the probability for de-exciting to the discrete levels below E_{cut}. The de-excitations from those discrete levels are based on experimental information on the transitions in the low-lying level scheme. The probabilities of all of the de-excitations are combined to produce predicted cross sections for the low-lying transitions. These low-lying transitions are the discrete gammas that are typically measured and can be connected to the residual nucleus. The Monte Carlo simulation codes create realizations of the level scheme and transitions above E_{cut}, based on the level density and γSF models. The calculation then proceeds by simulating the de-excitation many times.

These codes predict larger scale characteristics of the cascades, such as the multiplicity and gamma energy distributions. They can also predict the intensity of discrete gammas, which is the probability that the gamma is emitted in the cascade. The intensity can be used to determine the cross section for the gamma with the proper accounting for the reaction cross section and the distributions of the outgoing particles. Some reactions are very simple in this regard. For example, thermal and low-energy neutron capture usually provides few possible initial conditions, and the outputs of the code can be easily converted to partial gamma cross sections for this reaction. The use of these codes in certain experimental methods is described in Section 2.2. A new method for estimating uncertainties on reaction cross sections that rely on cascade calculations to combine the experimentally measured discrete gamma cross sections is presented in Chapter 7.

2.1.5 Neutron Induced Reactions

The neutron separation energy of a nucleus defines the energy required to pull the least bound neutron out of a nucleus. For ^{182}Ta, S$_n$ is 6.062 MeV, as shown in Figure 2.9. This is also the amount of excitation energy that is released when ^{181}Ta captures a neutron with zero kinetic energy. The green band around 6.062 MeV in the ^{182}Ta level diagram in Figure 2.10 shows the excited levels accessible by a low-energy (close to thermal) neutron capture on ^{181}Ta. Although the level density is high at S_n relative to the low-lying level scheme, the extremely low kinetic energy of thermal neutrons (eight orders of magnitude smaller than S_n) allows the reaction to precisely pick out levels in the compound nucleus. A low energy neutron does not bring in much orbital angular momentum, so can only access levels that are within $\frac{1}{2}\hbar$ of the ground state of the target nucleus. In this case, the target nucleus, ^{181}Ta, has a ground state with $J^\pi = \frac{7}{2}^+$, so only levels with $J^\pi = 3^+$ or 4^+ can be accessed by a thermal neutron. In Figure 2.10, the zoomed in level scheme has two such levels, a 4^+ level at 6062.944 keV, and a 3^+ level at 6062.95 keV. The levels between have spins which are not accessible to the neutron at this low energy, so they are effectively invisible to the neutron.

This fact is emphasized in the shape of the total neutron cross section for ^{181}Ta, shown in Figure 2.11. At thermal energies, the cross section exhibits a $1/\sqrt{E_n}$ behavior (also known as 1/v). The magnitude of the thermal cross section is dependent on how close S_n is to a level below it in the compound nucleus that is accessible to the neutron. One explanation of the 1/v behavior is the large change in the relative neutron wavelength over those five orders of magnitude, up to the first resonance around $E_n = 10^{-6}$ MeV (10 eV). This entire 1/v energy region, emphasized in cross section plots by the choice of a logarithmic axis, fits within the green dashed line and the first bold black level in the zoomed in level scheme in Figure 2.10. In this region, the cross section is large (increasing to thousands of barns at 10^{-10} MeV) for ^{181}Ta, which is due to the existence of a spin-accessible level close to, but below, S_n in ^{182}Ta. The natural width of the level allows thermal neutrons to access it, but only through the higher energy tail of the resonance.

With sufficient kinetic energy the neutron is able to excite the nucleus to the first accessible level. For reactions on ^{181}Ta, this is about 4 eV, to reach the 4^+ level at 6062.944 keV level, shown in Figure 2.10. The cross section for the reaction dramatically increases at this energy, causing a resonance. This can be seen in Figure 2.12. The first resonance, around 4 eV, corresponds to the first accessible level above S_n, highlighted in purple. The next accessible level, the 3^+ level at 6062.95 keV, creates the next resonance in the neutron cross section, at about $E_n = 10$ eV. Each subsequent resonance in the cross section corresponds to a higher energy excited level in ^{182}Ta that is accessible to the neutron. As the neutron energy increases, it can begin to bring in orbital angular momentum, which opens up more possible excited levels in ^{182}Ta that create resonances. It can be seen in the total cross section evaluation from ENDF/B-VIII.0 [1], shown in Figure 2.11, that as the neutron energy increases, the density of resonances also increases. Although the logarithmic axes can be deceiving in some cases, this trend does exist, and follows from the natural trends of increasing level density, expanded options for angular momentum, and the widths of the levels themselves growing. This region of isolated resonances is known as the Resolved Resonance Region (RRR).

The neutron energy resolution that can be achieved using neutron sources decreases (in

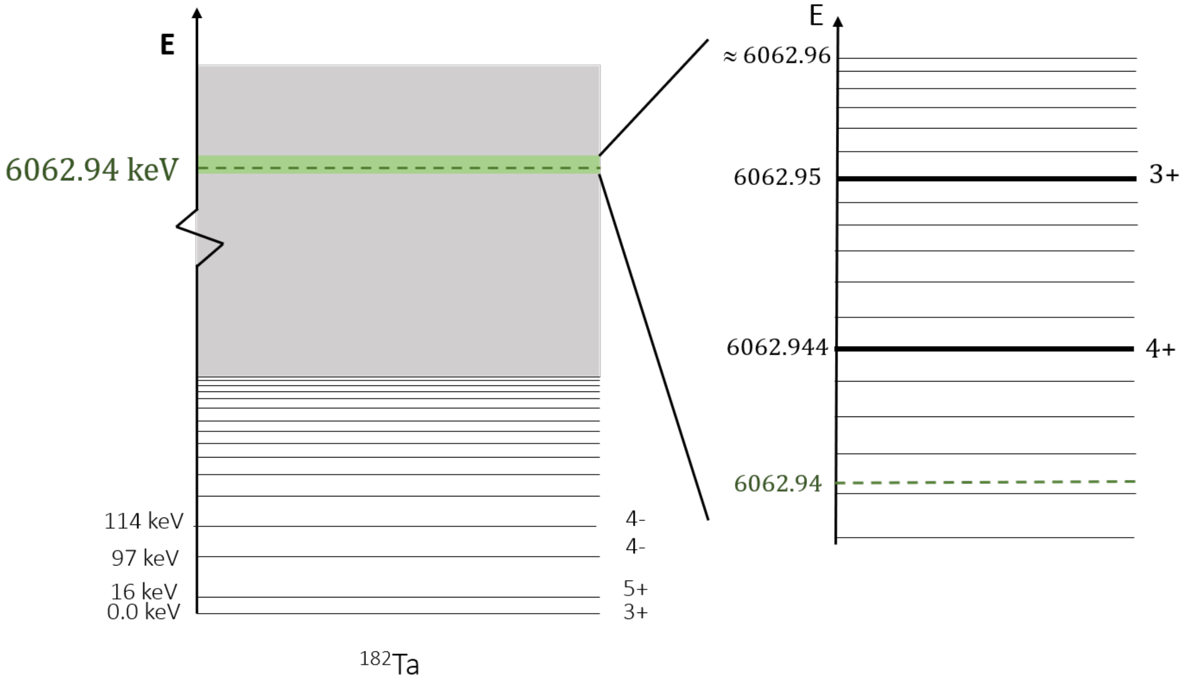

Figure 2.10: The level diagram of excited levels in ^{182}Ta. The neutron separation energy, S_n, for ^{182}Ta is 6062.94 keV. The green band around S_n in the ^{182}Ta level diagram above shows the excited levels accessible by a low-energy (thermal or epithermal) neutron absorption by ^{181}Ta. To the right of the level diagram, the green band is shown on a larger scale. The neutron separation energy is an amount of energy, not an excited level, and so is shown as a dotted green line. The actual levels in ^{182}Ta are shown as black lines. The two levels accessible by a very low energy neutron are shown in a heavier black line and the spins are labeled.

absolute units, not necessarily relative to the neutron energy), and at some point, with the resonance density increasing, the resonances can no longer be resolved experimentally. This energy separates the RRR from the Unresolved Resonance Region (URR). In Figure 2.11, the URR for ^{181}Ta begins around $E_n = 5\times10^{-4}$ MeV, or 0.5 keV. There is no distinction between the RRR and the URR in the structure of ^{182}Ta, it is entirely an artifact of the methods used to measure the cross section. As neutron measurement facilities and methods improve, the energy at which the resonances are no longer resolvable may continue to be pushed higher.

Even higher in energy, the levels themselves begin to overlap and the cross section becomes physically smooth. This is due to the level density and level widths continuing to increase in ^{182}Ta with increasing excitation energy. The large fluctuations in the cross section caused by the neutron exciting the nucleus to a single excited level smooth out naturally

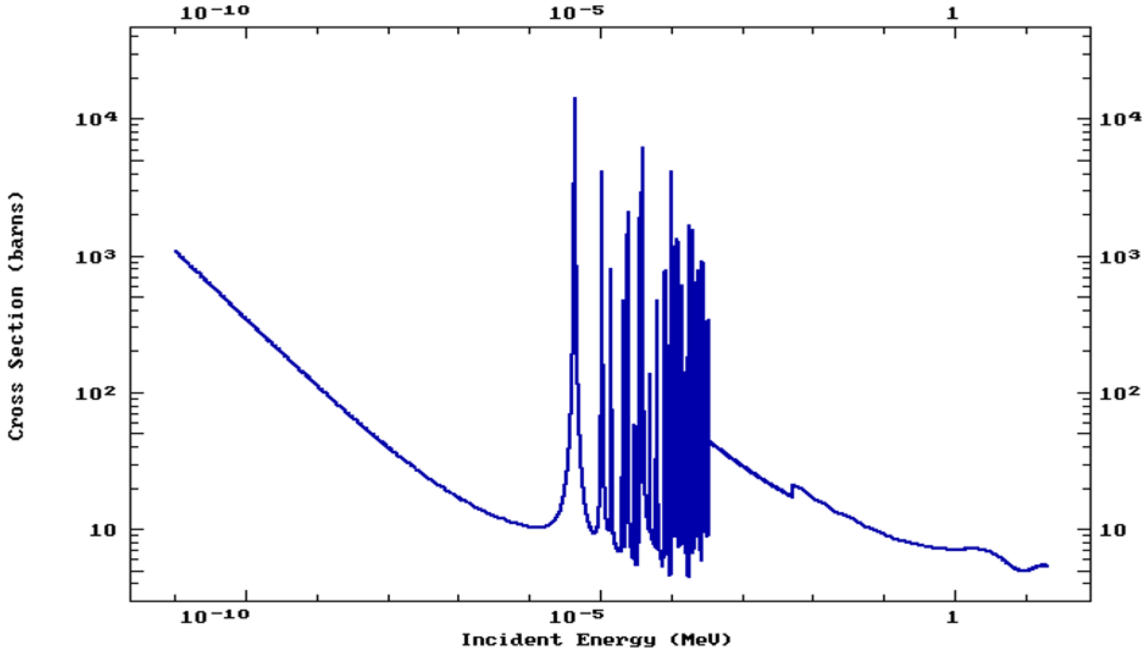

Figure 2.11: Evaluated total neutron cross section for ^{181}Ta from ENDF-B/VIII.0. There are three distinct energy regions, defined by the energy dependence of the cross section. At low energies there are well-defined and separated resonances, which is the Resolved Resonance Region. Above this, the resonances get closer together and when they can no longer be resolved experimentally, the Unresolved Resonance Region begins. Above this, when the resonances become so close and overlap enough that the cross section is physically smooth, the fast region begins. In this plot the fast region is defined by a relatively constant cross section with smooth, large scale oscillations.

due to this overlap. In ^{181}Ta, this Fast Region begins around E_n = 10 keV, as can be seen in Figure 2.11[3]. Although it does represent a real transition, the energy at which the URR ends and the Fast Region begins is not obvious based on our experimental methods and is usually chosen based on the expert judgment of those performing the evaluations.

As the neutron energy continues increasing, the total cross section decreases slowly. Large, slow oscillations are seen, which are caused by interference in the elastic scattering processes [74]. The cross sections for specific reactions have their own characteristics in the fast region. For example, the neutron capture cross section decreases much more rapidly than the total, as it struggles to compete with the other channels that open up. The inelastic scattering cross section opens at a threshold based on the first excited state in the target nu-

---

[3] In most cases, the transition from the URR to the fast region is not as obvious in an evaluated cross section. Physically, the cross section does not grow by five barns instantaneously. The discontinuity seen at 10 keV is a consequence of the two separate evaluation efforts for the resonance regions and the fast region.

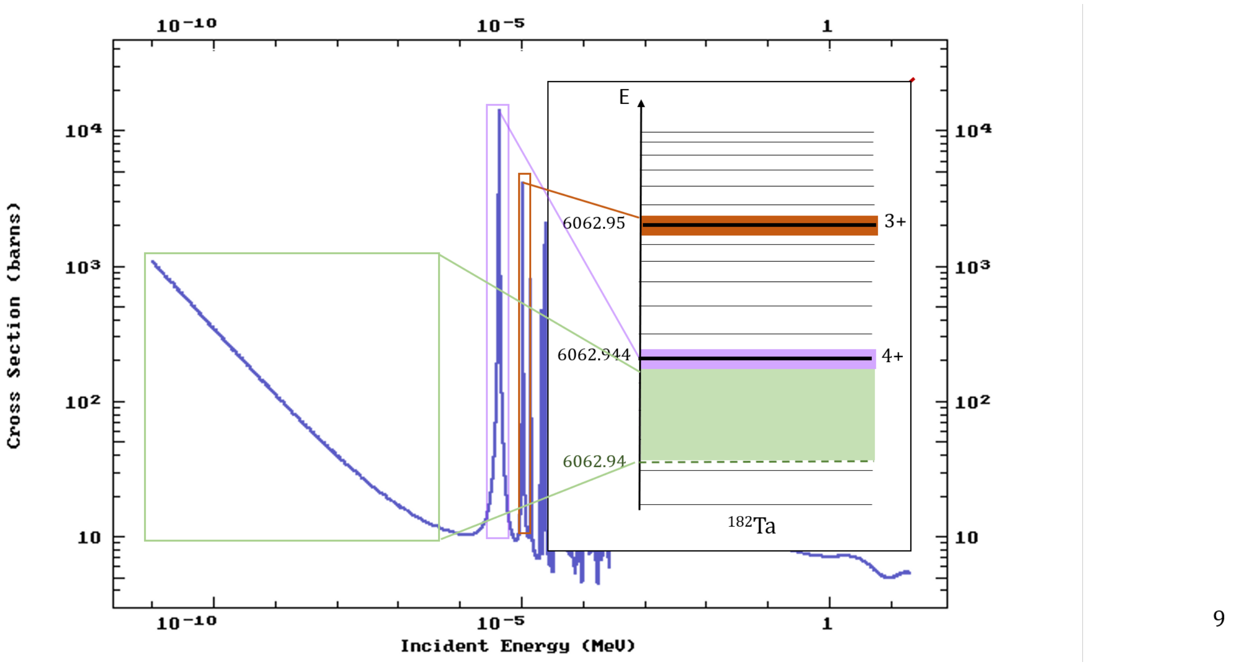

Figure 2.12: The total neutron reaction cross section for ^{181}Ta, is shown in the back, as a function of incident neutron energy from ENDF-B/VIII.0. The zoomed in level scheme of of the compound nucleus, ^{182}Ta, is shown on the right, in front of the cross section plot. The thermal region, highlighted in green, is the low energy portion of the cross section, between S_n and the first accessible level. The first excited state that is accessible to a low energy neutron is at 6062.944 keV, shown in the level scheme highlighed in purple. The cross section has a resonance at this energy, as seen in the cross section plot. The next level accessible to low energy neutrons is at 6062.95 keV, highlighted in brown and creates the second resonance in the cross section.

cleus and then decreases rapidly at the threshold for (n,2n). This pattern repeats for (n,2n) and (n,3n), and so on. For fissionable nuclei, the fission cross sections increase in distinct steps, located at the threshold energy for the “next chance” fission. First chance fission is the fissioning of the compound nucleus. Second chance fission occurs when the compound nucleus emits a neutron, and then that residual nucleus fissions, and so on. Each energy region and each reaction has its own characteristics, and the measurement and evaluation of each much be specialized.

2.2 Experimental Methods

The different characteristics inherent to the energy regions (Thermal Region, Resolved Resonance Region, Unresolved Resonance Region, and Fast Region) lend themselves to different experimental methods. For example, in the RRR where the resonances are experimentally resolvable, any experiment that attempts to measure the true shape of the cross section will need good energy resolution to do so. In the fast region, attaining such high resolution is challenging, but is not necessary due to the smooth cross section.

In addition to differences due to the neutron energy region, different reactions have varied signatures. A capture reaction emits only gammas, but if the product is radioactive it can be measured later, after irradiation. The total cross section includes all reactions, so the product nucleus is not a good way to determine the cross section, and instead in-beam experiments of the transmission of neutrons are used. For many reactions, such as capture, there are many different ways to measure the same cross section, and an evaluator is often left to compare the results of many methods. To properly assess an experiment, the evaluator needs information on the facility, detectors, efficiency, background, sample, normalization, and data analysis method. If proper information is given for all experiments, the evaluator will be able to assess the validity of the presented uncertainties and properly compare the data sets.

For each of the experiment types discussed here, some typical examples and methods are described for each aspect. The list of experiment types is not exhaustive, but rather covers the types of experiments that are analyzed in the later sections of the thesis. Chapter 3 contains an uncertainty template for total cross section measurements, which are almost always performed using the Transmission method. Chapter 4 contains an uncertainty template for capture cross section measurements, which can be performed using any of the other methods discussed in Chapter 4—Total Absorption Spectroscopy (TAS), Total Energy Detection (TED), Partial Gamma Measurements (PG), Activation Analysis (AA) and Accelerator Mass Spectrometry (AMS). The typical energy regions where each of the capture cross section methods are used is shown in Figure 2.13. Finally, Chapter 5 contains a template for AA and PG Measurements, based on distributions of published uncertainty values.

2.2.1 Transmission

The most common method to measure the total cross section is the Transmission method, which is based on the transmission of a collimated neutron beam through the sample. The ratio of the neutrons measured with the sample in the beam and with the sample out of the beam is then used to determine the total cross section. The transmission through the sample, T, is defined as

$$T = \frac{\phi_{in}}{\phi_{out}} = e^{-n\sigma_{tot}}, \tag{2.25}$$

where ϕ_{in} is the flux of neutrons when the sample is in, and ϕ_{out} is the flux when the sample is out (blank measurement). This ratio is equal to the exponential decrease determined by n, the number density of the target (in atoms/barn), and σ_{tot}, the total cross section of the target. A schematic drawing of the sample-in and sample-out measurements is shown in Figure 2.14. Transmission measurements use Time-of-Flight (TOF) techniques to determine

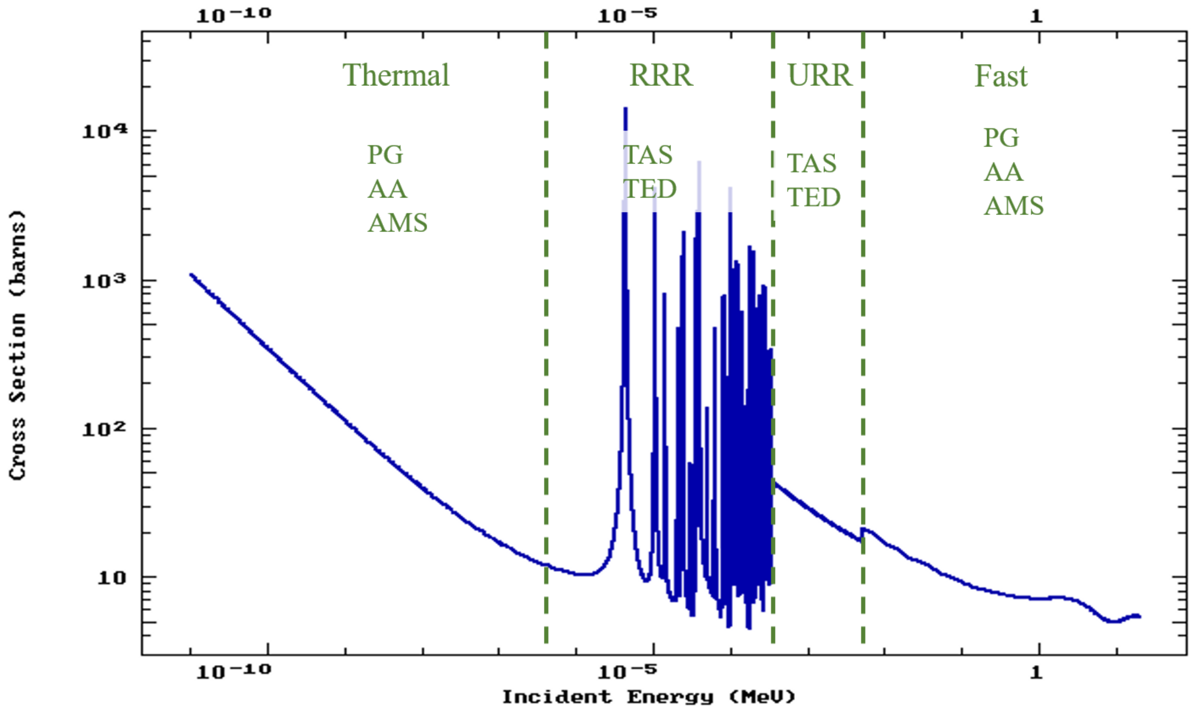

Figure 2.13: The general energy regions of a capture cross section, and the experimental methods that are most commonly used in each. The thermal region, up to the first resonance, does not require high neutron energy resolution and so Partial Gamma (PG), Activation Analysis (AA) and Accelerator Mass Spectrometry (AMS) measurements are common. The fast region is the same. In the resonance region (both RRR and URR), energy resolution is typically of great importance, so the higher resolution Total Absorption Spectroscopy (TAS) and Total Energy Detection (TED) methods are more commonly used. One exception is for Maxwellian-Averaged Cross Sections, which do not require high resolution and can be performed in any of the four regions.

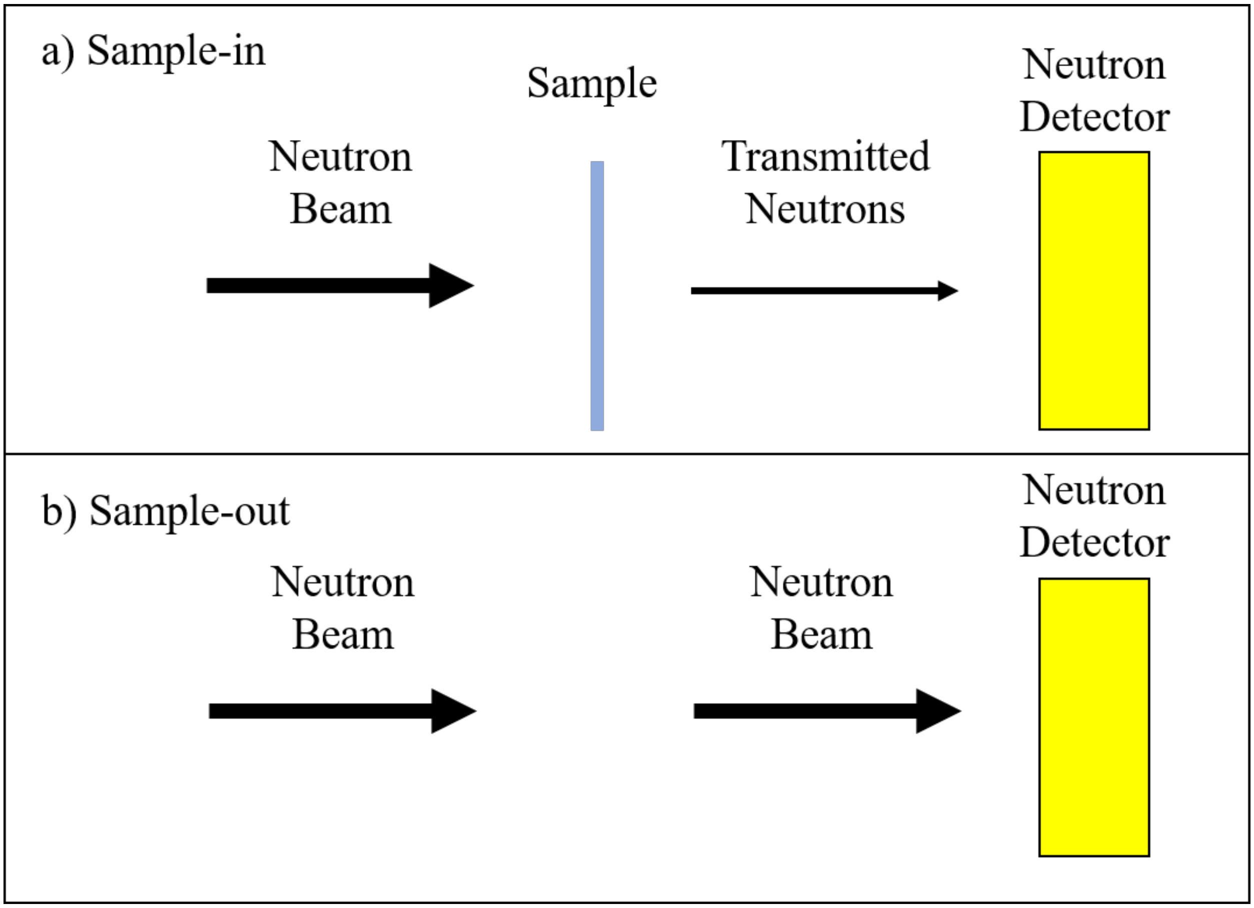

Figure 2.14: Schematic drawing of a transmission cross section measurement showing the sample-out measurement (panel a) and the sample-in measurement (panel b). The experimental observable, the transmission through the sample, is the ratio of the two measurements. For these measurements, the neutron beam must be collimated.

the neutron energy, so they are typically performed at neutron-producing accelerators, such as at RPI [81], GELINA [82], ORNL [83, 84] and LANSCE [85]. Reactors with Chopper setups (a beam line with a rotating shutter that allows for bursts of neutrons with defined starting times), such as at MIT [86, 87], can also be used for these measurements. In addition, tunable neutron sources like as Van de Graaff generators, such as at Karlsruhe [88], are sometimes used.

Transmission measurements are commonly the most precise cross section measurements, with experimental uncertainties around 1% regularly reported in the RRR region between resonances. The whole measurement is a ratio of sample-in to sample-out, so many of the typical systematic uncertainties fall out. The sample composition, counts and correction factors are the main sources of uncertainty.

Neutron detectors, placed in the beam, are used to measure the neutron flux with and without the sample. The neutron detector efficiency, which can be a large source of uncertainty in measurements, is canceled out as the same detectors in the same locations are used for the sample-in and sample-out measurements. Separate beam monitors are used to correct for fluctuations in the beam, in order to correctly relate the sample-in and sample-out measurements. In the Resolved Resonance Region (RRR), counting uncertainties are typically low between resonances but can become a dominant uncertainty source at the peak of the resonance, when fewer neutrons make it out of the sample. In the Unresolved Resonance Region (URR) and the fast region, the cross section, as measured, is smoother and does not have such fluctuations in the counting statistics.

As with most measurements, the background component of the measured neutron counts must be subtracted from the signal. In the case of transmission measurements, this process can be complicated and the background is typically split into several components [89],

$$\dot{B}(t) = \dot{B}_0 + \dot{B}_\gamma(t) + \dot{B}_n(t), \tag{2.26}$$

with a time-independent room background rate, $\dot{B}_0$, and two time-dependent signals. An example background is shown in Figure 2.15. The $\dot{B}_\gamma(t)$ term represents the signal in the neutron detectors from gammas, and $\dot{B}_n(t)$ represents the signal from neutrons that were either scattered in the experimental setup or the surroundings and returned to the detector area. These background components are often fit quantities, not simply background rates, and the time-dependent backgrounds are usually fit to exponential functions. One method for fitting the background is the saturated resonance technique. This method uses a "saturated resonance filter"—a sample that is thick enough that there is effectively no neutron transmission through at least one strong resonance. This allows for the background signal to be determined. It is used to fit the analytical background expression, Equation 2.26, with corrections for the nature of the sample itself [90].

There is no need for a direct flux measurement or determination in transmission measurements, as the only quantity that matters is the ratio of neutrons measured in the sample-in measurement and in the sample-out measurement. There is a normalization that must be done, however, to account for beam instability and differences in the incident flux between the usually many different runs performed in a single experiment. The variable N_T is used to account for this.

The experimental observable, T_{exp}, is determined by the ratio of the background-corrected neutron counts,

$$T_{\text{exp}} = N_T \frac{\dot{C}_{in} - \dot{B}_{in}}{\dot{C}_{out} - \dot{B}_{out}}, \tag{2.27}$$

where $\dot{C}_{in}$ and $\dot{C}_{out}$ are the neutron count rates for the sample-in and sample-out runs, respectively. The variables $\dot{B}_{in}$ and $\dot{B}_{out}$ are the background rates for each.

In the RRR, the experimental transmission is the final result of the measurement that is directly used for the evaluation procedure. For the URR and fast region, the total cross

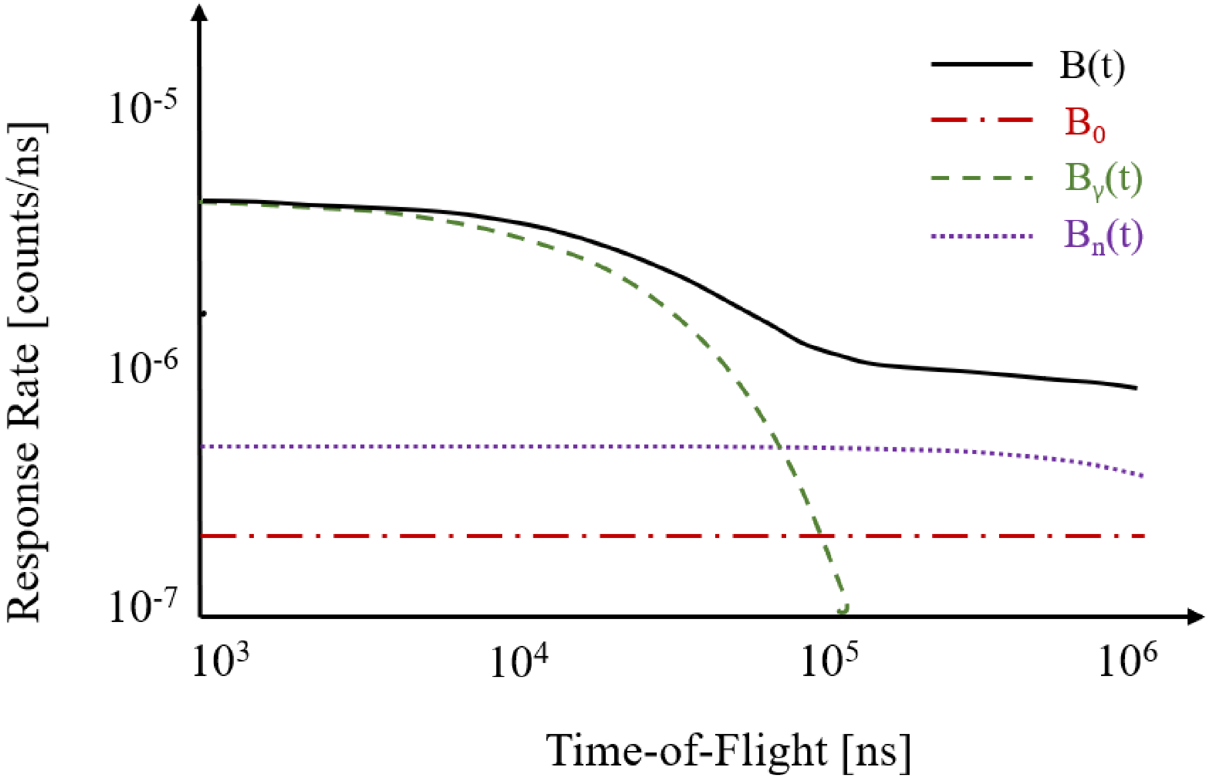

Figure 2.15: Schematic showing the fit background, Equation 2.26, based on Reference [89]. The black line represents the total fitted background rate, $\dot{B}(t)$, which is composed of three different background components. B_0, the red dashed line, is the time-independent background rate. $\dot{B}_\gamma(t)$, the green dashed line, represents the time-dependent gamma background rate in the neutron detectors. $\dot{B}_n(t)$, the purple dashed line, represents the background due to scattered neutrons.

section is directly extracted from the experimental transmission. This is due to the experimental and physical averaging of the resonances that renders the complicated forward modeling with R-Matrix theory unnecessary. In these regions, the averaged transmission is indirectly related to the averaged total cross section,

$$\langle T \rangle = \langle \mathrm{e}^{-n\sigma_{tot}} \rangle, \tag{2.28}$$

and a Taylor expansion approximation can be used to estimate it,

$$\langle T \rangle = \mathrm{e}^{-n\langle \sigma_{tot} \rangle} \left(1 + \frac{n^2}{2} \mathrm{var}(\sigma_{tot}) + ... \right), \tag{2.29}$$

with higher order terms neglected in practice [89]. The second term is the correction for the still present fluctuations in the cross section due to resonances. This correction can be significant for thick samples [91], and can be estimated using simulations. It is represented by F_T, which is defined as the ratio between the averaged transmission and the transmission with the averaged cross section,

$$F_T = \frac{\langle \mathrm{e}^{-n\sigma_{tot}} \rangle}{\mathrm{e}^{-n\langle \sigma_{tot} \rangle}} \approx 1 + \frac{n^2}{2}\mathrm{var}(\sigma_{tot}) \tag{2.30}$$

which is usually simulated using Monte Carlo methods. Resonance parameters are sampled from the distributions that describe widths and spacings, and cross section realizations are created from these doppler-broadened and averaged resonances. Currently these calculations can be done with MCNP [17] and NJOY [92] used together, or with the dedicated code SESH [93]. This correction factor allows for the energy averaged total cross section to be extracted from the experimental transmission,

$$\langle \sigma_{tot} \rangle = -\frac{1}{n} \ln \frac{\langle T_{\mathrm{exp}} \rangle}{F_T}. \tag{2.31}$$

The resulting $\langle \sigma_{tot} \rangle$ is then used in the evaluation process. This correction is very important in the URR, especially for thick samples. It becomes less significant at higher energies where the cross section fluctuations are not as strong [91]. In some measurements in the fast region, the correction is not applied at all [94].

2.2.2 Total Absorption Spectroscopy

For measurements of the capture cross section, there are several different possible experimental methods. The first to be discussed is Total Absorption Spectroscopy (TAS), which utilizes high efficiency scintillator setups to measure as many capture gammas as possible. These measurements can be done in any energy region, and are especially useful in the resonance region, where fast timing ($\leq$1 ns) is needed. Total absorption detectors have been built at CERN [95], RPI [96], KURRI [97], Karlsruhe [98], ANL [99] and LANSCE [100], among others. A schematic diagram of a TAS measurement setup is shown in Figure 2.16. Some of the earlier detectors, such as that at RPI, are made of NaI and used to measure lower energy capture cross sections (typically below 1 keV). Many of the newer detector systems are made of $\mathrm{BaF_2}$ detectors, such as that at CERN and LANSCE. These large detectors are split into multiple sections to allow for multiplicity measurements.

These detectors, by design, have high absolute efficiency in order to detect as much of the cascade as possible. The efficiency, though often close to 100%, is never exactly 100% and must be quantified if an absolute cross section measurement is desired. For TAS measurements, thresholds on multiplicities and minimum energy deposited are both used. The distribution of multiplicities for capture events in a target isotope needs to be understood in order to determine the efficiency of the detector, and often the gamma cascade characteristics are modeled using statistical cascade codes (explained in Section 2.1.4.2). Corrections for the events lost to the thresholds can be made by coupling the gamma cascade codes with

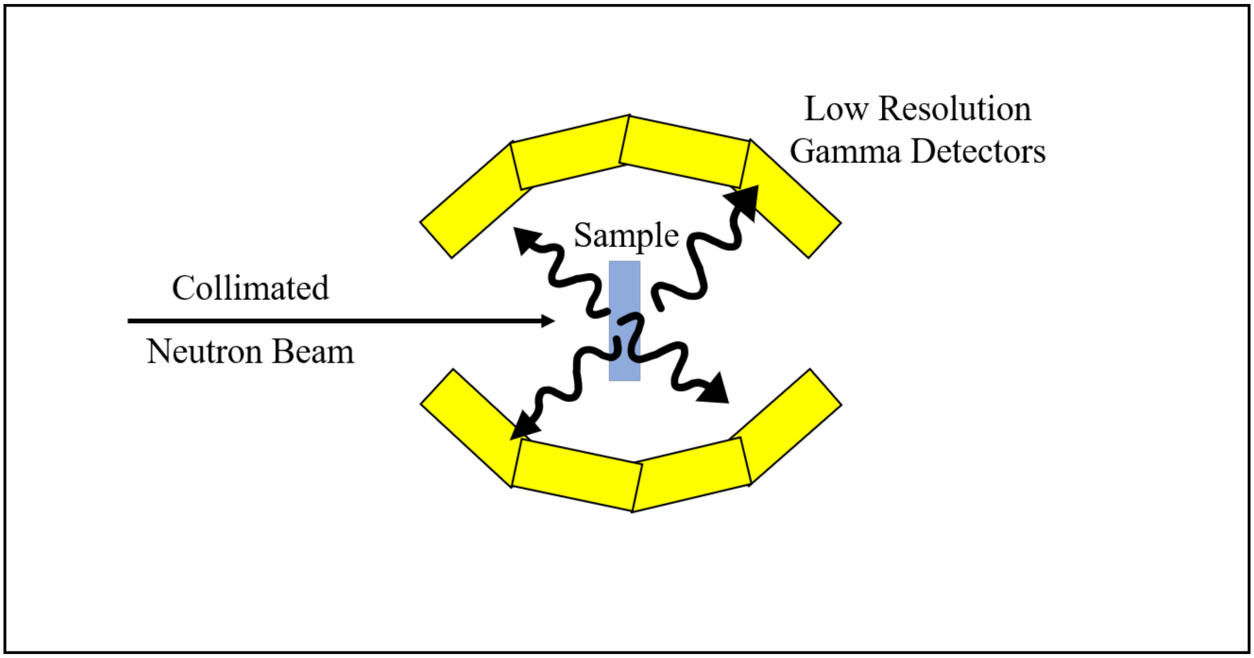

Figure 2.16: Schematic showing the setup of a Total Absorption Spectroscopy measurement. A collimated neutron beam hits a target that is placed inside of the 4π detector. The capture gammas emitted it almost all directions are detected using low energy resolution gamma detectors.

transport codes such as MCNP [17]. These corrections can introduce significant uncertainties, as there are many assumptions and a lot of nuclear data needed for the calculations. The details of a study done using simulations to determine the efficiency of the TAS detector at n_TOF facility is presented in Reference [101].

The background is typically split up into three main sources. An example background function, adapted from Reference [90], is as follows:

$$\dot{B}(t) = \dot{B}_0 + \dot{B}_{OB}(t) + \dot{B}_S(t), \tag{2.32}$$

where $\dot{B}_0$ represents time-independent background rate, $\dot{B}_{OB}$ represents the time-dependent background that is sample-independent, and $\dot{B}_S$ is the background rate that is sample-dependent. The chosen variables may differ between experiments, but in most capture measurements of this type, the background is split up into these three major categories [90, 100, 102]. Time-independent (room) backgrounds can usually be characterized with beam-off measurements. Time-dependent backgrounds that are independent of the sample itself can be similarly characterized with sample-out measurements. The sample-dependent background is more complicated. Neutrons that are scattered in the sample can then be captured in the detector or surrounding materials. These “false captures” are real capture events, but are in isotopes that are not the target, so the Q-value of the reaction is not the same. Detectors with good efficiency, such as BaF_2, are used to increase the probability that the signal is recorded at the full Q-value of the reaction. This can be the basis of data analysis cuts and thresholds that allow for this background to be removed from the data. Background that results from gammas in the environment scattering from the sample into the detector are typically below 3 MeV and can be removed from the data by an overall threshold around that energy. An extensive study of the background for the DANCE detector was done in Reference [100].

Multiplicity thresholds can also be implemented by specifically removing events with low multiplicity where only neighboring detector segments had been triggered [103]. Background events due to the radioactive decay in the BaF_2 detector tend to trigger neighboring detectors, as do captures in the detector itself. These thresholds were used in the 1990 work with the Karlsruhe 4π detector, and were assumed to have removed about 50% of the background from scattered neutrons and only 2% of the signals from true capture events in the sample [103]. These background characterization and suppression techniques should all be validated with measurements, as they can introduce biases in the final results.

Impurities in the sample are an important consideration in these measurements, as capture in different isotopes in the sample will result in different cascades. If all impurity isotopes have Q-values that are significantly different from the isotope of interest, energy discrimination based on the deposited energy can be used as with the false capture background. However, in most cases isotopes of an element have similar Q-values for capture, so the analysis will be complicated if enriched samples are not available.

Using reference cross sections to determine the flux is common with this method. For such a ratio measurement, the difference in efficiency between the target and the reference reaction needs to be determined, because for this experiment type the efficiency is dependent on the cascade characteristics and data analysis. The differences can introduce large biases into the measured cross section if they are not accounted for correctly.

The cross section is based on the events that are left after the various energy and multiplicity thresholds, with a correction for the events that were not detected or were removed due to the thresholds. If a relative cross section is being measured, the ratio of the target events to the reference material events is calculated. For example, the equation used to calculate the capture cross section at neutron energy E_n of isotope “X” based on a gold standard in References [103] and [104], is:

$$\sigma_X(E_n) = \sigma_{Au}(E_n) \times \frac{Z_X(E_n)}{Z_{Au}(E_n)} \times \frac{\sum_{TOF} Z_{Au}}{\sum_{TOF} Z_X} \times \frac{\sum_E Z_X}{\sum_E Z_{Au}} \times \frac{d_{Au}}{d_X} \times F_1 \times F_2. \tag{2.33}$$

In this equation, $Z_X(E_n)$ is the count rate for isotope X in the channel corresponding to neutron energy E_n, $\sum_{TOF} Z_X$ is the count rate integrated over the TOF region used for normalization, $\sum_E Z_X$ is the the count rate integrated over the gamma energy deposited regions chosen for each multiplicity, and d_X is the sample thickness in atoms/b. The subscript Au indicates the respective quantities for the ^{197}Au reference measurement. The term F_1 represents the correction for the capture events that were detected below the energy threshold (a ratio of the corrections for the isotope “X” and ^{197}Au), and F_2 represents the correction for multiple scattering. The calculation of F_1 requires cascade and transport simulations, and in Reference [103], no uncertainties were given on the estimates for the percent of unobserved cascades. The corrections themselves ranged from about 1.5% to above 12%, based on the solid angle assumptions and energy threshold. If an absolute cross section is being measured without a reference, then the neutron flux and the absolute detector efficiency must be known as well.

2.2.3 Total Energy Detection

Another method to measure capture reactions is to detect only one gamma from each cascade. This process allows for detectors with lower gamma and neutron efficiencies, which can lead to lower backgrounds and smaller uncertainties in the final cross section [90]. With manufacturing, cost and multiplicity concerns minimized, the detectors used for total energy detection are optimized for low neutron sensitivity and fast time resolution. For this reason, the Total Energy Detection (TED) method is effective in the resonance region and for isotopes where the scattering cross section is higher than the capture cross section. C_6D_6 scintillation detectors are the preferred detectors, and are used for total energy detection measurements at RPI [105], GELINA [106], CERN [107], KURRI [108], and ORELA [109].

The efficiency of the system to detect capture events is dependent on the absolute efficiency of the detectors, the characteristics of the cascade, and the cuts and thresholds in the data analysis. The absolute efficiency is kept low, as this method only works when a single gamma per cascade is detected. For TED measurements, the dependence on the cascade characteristics is minimized by making the efficiency of detecting a cascade proportional to the Q-value of the cascade. This allows for the probability of detecting a cascade to be the same in different resonances[4]. This was achieved with the Moxon-Rae detector [111] early on, but the pursuit of more accurate and precise measurements has resulted in the use of C_6D_6 detectors with the Pulse Height Weighting Technique (PHWT). The PHWT involves weighting pulses by height to artificially construct a system with efficiency proportional to the gamma energy, and therefore total Q-value [90]. While this does remove some of the dependence on the cascade characteristics, there are extensive data cuts and thresholds that must be applied with this method. Low energy deposition cuts are applied, such as above 2.2 MeV to remove the strong hydrogen capture line. In this case, since only one gamma is detected per cascade, such energy cuts have much larger effects on the efficiency of the system, and a correction must be made for the gammas below that threshold. This correction represents the number of captures where the one gamma detected was below the threshold, and therefore includes both the cascade physics and the gamma transport physics. For the cascade physics, the statistical cascade codes such as `DICEBOX` [77] are used. These codes

---

[4] The Q-value of the reaction is different in each resonance, due to the fact that different neutron energy is required to access each resonance. However, the change is small relative to the magnitude of the Q-value (usually eV compared to MeV). The differences seen in the cascade characteristics between resonances of different spins are in many cases much larger than differences due to the neutron energy [110].

are coupled with transport codes to determine the distributions of gamma energies emitted and detected. These simulations allow for the determination of the efficiency of the detector system based on the cascade characteristics and data cuts and thresholds. Transport simulations are included in the PHWT because the likelihood of a gamma exiting the sample and interacting with the detector is dependent on the gamma energy and the location in the sample where the reaction took place. The gamma energy dependence is straightforward, as we understand the photon interaction physics well. The location in the sample where the reaction took place is much more difficult to simulate, as it depends on the nuclear physics. Strong resonances will create a significant attenuation of the neutron flux between the front and back of the sample, which is known as self-shielding. This will lead to significantly more capture events occurring in the front of the sample. In the transport simulations, therefore, the sample cannot be treated as a uniform source of gammas. The direct dependence on the strength of the resonance will, in effect, create a situation where there should be a specific weighting function for each resonance in the resonance region. This is not feasible for resonance measurements, which regularly measure and report over 100 resonances. Instead, an approximate weighting function is constructed assuming the gammas are created from a homogeneous source throughout the entire sample. Then, a correction is applied to each resonance that is dependent on the total cross section of that resonance. This allows for the weighting function to accurately represent the differences between the resonances without needing a specific simulation for each resonance. The weighting function also accounts for some of the data cuts. In TED measurements, the most common data cut is a low-level discriminator (LLD) which represents the minimum energy deposited in the detector that will be registered. Gamma cascade models can be used to determine the gammas below the LLD and correct down to zero energy deposited, or the weighting function can be set to zero below the LLD and the missing portion corrected for. In both of these cases, gamma cascade models are required for the weighting function simulation [90]. More detail into the method and results are given in References [90, 112, 113].

The backgrounds in total energy detection measurements can be represented by the three terms in Equation 2.32. The time-independent and time-dependent sample-independent backgrounds can be determined and subtracted out with beam-off and sample-out runs. The sample-dependent background is more complicated, and determination of the "false capture" background is necessary. In this case, unlike with TAS, the Q-value of the reaction cannot be used to discriminate between real and "false" captures, so characterization and subtraction is required. To measure the neutron background, a "pure" scattering sample (a material with a low capture cross section) can be placed in the beam. The sample-dependent background can be defined as,

$$\dot{B}_S(t) = R_n(\dot{C}_{scat} - \dot{C}_{OB}), \tag{2.34}$$

where R_n is the ratio of the scattering yields for the scattering sample and the target sample, $\dot{C}_{scat}$ is the count rate for the run with the scattering sample, and $\dot{C}_{OB}$ is the count rate for the open beam run [90]. In this equation, all counts are already normalized by the neutron flux (analogous to the N_T variable in Equation 2.27) [90]. The sample dependent background, however, can also come from background gammas that scatter from the sample into the detectors [100]. For this reason, it is best to choose a scattering sample that has similar material characteristics to the sample. The ratio of the scattering yields of the scattering sample and the target, R_n, is an important correction. The quality of the nuclear data that goes into the calculation of R_n directly impacts the uncertainty on this correction and should be taken into account.

Impurities are important in these measurements, given that only a single gamma is detected in each cascade and Q-values cannot be used to determine which isotope each capture occurred in. Thin samples are preferred, to reduce the multiple scattering and self-shielding corrections. Powder samples and samples with hydrogen impurities typically have larger multiple scattering and shelf-shielding corrections which are more difficult to determine [90]. Power samples can also have voids, which are important in the transport simulations done for the PHWT. In the resonance region the locations of the resonances can help to disentangle reactions in different isotopes, but ideally samples will be highly enriched.

Normalization in the resonance region is usually done with reference to a known cross section using the saturated resonance technique explained in Section 2.2.1. In this case, it is necessary to determine the difference in the system efficiency between the reference and target material. The 4.9 eV resonance in ^{197}Au is one commonly used reference, and it has a cascade that will be similar to that of other heavy, deformed nuclei. However, the spin of the resonance (relative to the spin of the ground state of the product nucleus) can also have a significant impact on the cascade characteristics [110]. Another common method is to use a saturated capture resonance, or at least strong capture resonance, in the isotope itself. This simplifies the normalization procedure and can be done quite accurately with good data. The flux can also be measured directly, but measurements of neutrons in the keV region are difficult, leading to higher uncertainties when the flux is measured directly.

To determine the cross section, the events that are above the LLD are corrected using the weighting function to give the yield. The experimental yield is defined as:

$$Y_{exp} = N_\gamma \frac{\dot{C}_i - \dot{B}_i}{\dot{C}_\phi - \dot{B}_\phi} Y_\phi = N_\gamma \frac{\dot{C}_i - \dot{B}_i}{\phi} \tag{2.35}$$

where N_γ is the normalization for the flux between sample-in and sample-out runs, $\dot{C}_i$ and $\dot{B}_i$ are the sample-in and background rates for the target isotope weighted by the PHWT, $\dot{C}_\phi$ and $\dot{B}_\phi$ are the sample-in and background rates for the reference material weighted by the PHWT, and Y_ϕ is the normalized yield of the reference isotope[90]. In TED measurements, the yield is typically defined as the number of reactions per incident neutron, rather than just the number of reactions. In the case of a direct flux measurement, ϕ is used [90].

In the resonance region, this experimental yield value is directly used in the evaluation. Forward modeling is used to determine the capture cross section, due to effects such as Doppler broadening and multiple scattering. The process and codes used for such modeling are explained in more detail in Section 2.2.1.

In the unresolved resonance region, an indirect relationship exists between the averaged experimental yield and energy averaged cross section,

$$\langle Y_{exp} \rangle = \langle Y_0 + Y_1 + Y_2 + ... \rangle, \tag{2.36}$$

where each Y_i represents the yield from neutrons that scattered i times in the sample before being captured. In the thin-sample approximation, the contribution from the $i > 0$ terms is considered negligible, and what is measured, $\langle Y_{exp} \rangle$, is equal to the yield without multiple scattering or self-shielding, $\langle Y_0 \rangle$. However, with larger samples, the contributions are non-negligible and must be quantified in order to determine the true yield $\langle Y_0 \rangle$. In order to quantify the effect of multiple scattering, a correction factor,

$$F_\gamma = \frac{\langle Y_\gamma(n) \rangle / n}{\langle Y_\gamma(n_{thin}) \rangle / n_{thin}} = \frac{\langle Y_{exp} \rangle}{\langle Y_0 \rangle}, \tag{2.37}$$

is calculated. The calculation involves forward modeling the yield, Y_γ, for an appropriately thin sample with number density, n_{thin}, and then again with number density of the real sample, n. This process is similar to the fluctuation corrections done for transmission experiments, Equation 2.30. With the multiple scattering correction, the experimental yield can be related to the true yield Y_0 and the energy averaged cross section,

$$\langle \sigma_\gamma \rangle = \frac{\langle Y_0 \rangle}{n} = \frac{\langle Y_{exp} \rangle / F_\gamma}{n} = \frac{\langle Y_{exp} \rangle}{F_\gamma n} \tag{2.38}$$

for the URR [90].

2.2.4 Partial Gamma Measurements

Partial gamma (PG) measurements are in-beam measurements, like TAS and TED, where high gamma-energy resolution detectors are used to identify discrete gammas. The discrete gammas that are characteristic of the product nucleus can be used to identify the reaction that occurred. This method requires high resolution detectors such as HPGe or Ge(Li) which are slower than the scintillators utilized in the fast time resolution TAS and TED measurements. For this reason, the neutron energy resolution that can be attained with PG measurements is lower and this type of measurement is used in energy regions where the resolution is not as important, such as in the thermal and fast regions and for Maxwellian-Averaged Cross Sections (MACS)[5]. There are a few facilities that measure partial gamma cross sections, including the Budapest Reactor [114, 115], the GAINS spectrometer at GELINA [116], the accelerator at the University of Kentucky [117], and the new GENESIS setup at LBNL. In addition, numerous partial gamma cross section measurements were performed using the

---

[5] MACS measurements use neutron sources with spectra that are similar to astrophysical neutron spectra. The spectra follow Maxwell-Boltzmann distributions and are defined by the temperature parameter. Thermal cross sections are an example of MACS, with T=273 K, or 25.3 meV. Another common MACS spectrum is at T=25 keV, the solar temperature.

GEANIE spectrometer at WNR at LANSCE [118]. There are more facilities that are set up to perform Prompt Gamma Activation Analysis (PGAA) measurements, including the reactor at the University of Texas [119], NIST [120], the MIT Research Reactor [121], and the Forschungs-Neutronenquelle Heinz Maier-Leibnitz research reactor [122]. However these facilities have not been used for the measurement of cross sections, but instead use known gamma cross sections in other measurements.

The semi-conductor detectors used in PG measurements have low intrinsic efficiencies for gamma interactions, and typically subtend significantly less solid angle than the scintillators used in TAS and TED measurements. The efficiency of the detectors can be determined using calibration sources. For gamma detectors, these calibration sources are common below 2.6 MeV and a fitting process can be used to determine the efficiency[6]. Above 2.6 MeV, calibration sources are less common and often extrapolation must be used. The efficiency can also be simulated over the entire energy region of interest, using particle transport codes like MCNP [17] and GEANT-4 [123], but should be validated with calibration measurements. The experimental quantities measured in this type of experiment are the cross sections for the individual cascade gammas, so the cascade effects on the efficiency are accounted for in the final analysis step.

The efficiency is impacted by the hardware and software cuts used to suppress background. One common method of background suppression utilizes coincident triggers, which can be implemented in the hardware or software. Coincident triggers involve looking at signals that were recorded in coincidence with a known transition in the nucleus of interest. Anti-coincident triggers such as suppressing the Compton background using "Compton Shields" with higher intrinsic efficiencies (such as BGO) placed around the HPGe detectors are used as well. Signals in the Compton shields can be used as a trigger to discard a signal in the HPGe detector, in an attempt to reduce the background from gammas that scattered in the HPGe detector and then interacted in the Compton suppression detector. Beam backgrounds (which are time but not sample-dependent) can be characterized with sample-out runs. Beam-off runs should also be used to characterize the room background and to determine if there are gamma signals from isomeric states or decays.

The backgrounds that are dependent on both the beam and the sample are more difficult to characterize, as with TAS and TED measurements. These can include beam or room gammas scattered off of the sample, but this source of background is typically much less significant than gammas emitted from other reactions occurring in the sample. The high gamma-energy resolution of these detectors offers the ability to distinguish all but the closest of gamma energies. Those that are close enough in energy to be indistinguishable from the gammas being measured, however, present a difficult problem. Neutron energy dependence and consistency with known branching ratios can be used to identify these issues. The initial neutron energy does not have any effect on the relative branching ratios of gammas emitted from the same excited level. If there is a contamination gamma that is produced by a different reaction, the ratio will vary with energy, as the two cross sections do. The 2004 ^{238}U

---

[6] More details of this fitting process and the inherent uncertainties are given in Chapter 6.

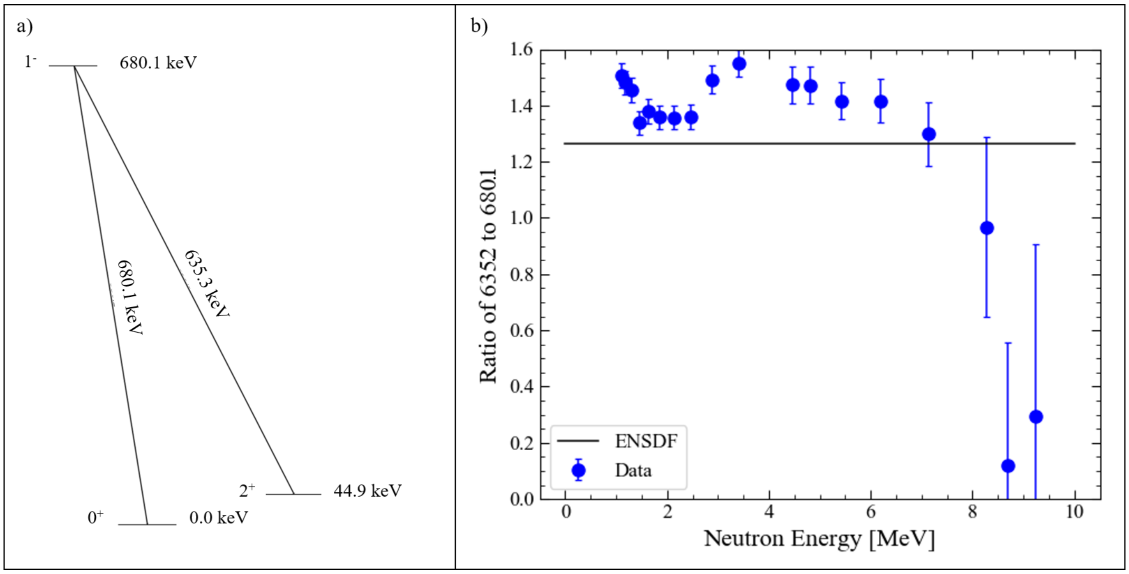

Figure 2.17: Example of peak contamination in the 2004 GEANIE ^{238}U inelastic scattering measurement [47]. The 680.1 keV level in ^{238}U and its two gammas are shown in panel (a). These gammas have a defined and constant branching ratio. In panel (b), the ratio of the measured cross section for the 635.2 keV gamma to the measured cross section for the 680.1 keV gamma is shown. The expected ratio, based on the ENSDF branching ratio is also shown. The prominent energy dependence in the measured ratio is a sign that there was contamination in at least one of the gammas.

inelastic scattering experiment using GEANIE [47] presents an instructive example, shown in Figure 2.17. The 680.1 keV level in ^{238}U emits two gammas, a 680.1 keV gamma to the ground state and a 635.2 keV gamma to the first excited state. These two gammas have a defined and constant branching ratio, which is not dependent on how the nucleus was exited to the 680.1 keV level. Therefore, the experimental cross sections of each of these gammas should be constant with neutron energy. As can be seen in Figure 2.17(b), this was not the case in the 2004 GEANIE measurement. There is an oscillatory neutron dependence, beyond the uncertainties on the ratio. This trend is indicative of contamination in at least one of the gammas. This method is straightforward for excited levels with multiple measured gammas. For all measured gammas, a less precise method to check for contamination is to compare the energy dependence of the gamma signal with that of the reaction itself or the other gammas from the same cascade. While these energy dependencies will not be the same, they should all follow similar physical trends. For example, a gamma cross section that does not decrease as the reaction channel begins to close with increasing neutron energy likely has contamination. The exact implementation of the background checks will vary based on the reaction and the properties of the transitions being measured, but should be attempted in the data analysis to avoid biases caused by the contamination.

Finally, there is a background from neutrons, as this is an in-beam measurement. Semiconductor detectors like HPGe are sensitive to neutrons, and can in fact be damaged by them [124]. The neutron interactions leave a distinct signal in the HPGe spectrum, which can be used to subtract the background [125].

The sample used for PG measurements should be thin enough to minimize multiple scattering, but thick enough to induce sufficient activity for the low efficiency detectors. This optimization must be done individually for each measurement. The size of the sample relative to the beam spot is important. A sample that is smaller than the cross section of the beam will be irradiated in its entirety. Samples that are larger than the beam spot will only be irradiated where the beam hits the sample. With a well-defined beam spot and smooth sample, the beam overlap correction can typically be applied with uncertainties that are much lower than others, such as the number of atoms in the sample (especially for radioactive targets) or the flux. Figure 2.18 shows the difference between an overfilled sample (beam is larger) and an underfilled sample (sample is larger). The composition of the sample should be fully characterized, due to the contamination of gammas from other reactions in the sample, as discussed above.

The normalization of the measured gamma yields to cross sections can be done by measuring the flux directly or in ratio to a reference material. Measuring the flux directly can be done in both the thermal and fast regions with a fission chamber, as was done with the GEANIE [118] and GAINS [116] and at the NIST PGAA setup [120]. Thermal neutrons can be measured with other detectors as well, including ^{3}He [119]. Reference materials in the fast region include ^{56}Fe, for example, used at TUNL [48]. In the thermal region, common reference materials include ^{197}Au [114, 120], and ^{94}Zr [126].

The yield, Y_γ, of each gamma comes from the fit of the photopeak in the HPGe spectrum. Spectrum fitting can be done by defining a region of interest in gamma energy and integrating over all counts in that region, then subtracting a pre-defined background if the peak is isolated and the background seems linear. If the spectrum is more complicated in the region around the gamma of interest, the peaks can be fit using a Gaussian or tailed-Gaussian shape. This fitting can include a Compton background function as well, or a linear Compton background subtraction can be done. This process introduces a fitting uncertainty along with the statistical counting uncertainty, but it is usually just incorporated into the counting uncertainty.

Once the gamma yields have been determined, the cross sections for individual transitions in the cascade are calculated. As an example, the partial cross section equation given in Reference [47] is,

$$\sigma_\gamma(E_n) = \frac{Y_\gamma(E_n)\tau_\gamma(1+\alpha_\gamma)c_\gamma}{\phi(E_n)\tau_\phi\varepsilon_\gamma d}, \tag{2.39}$$

where $Y_\gamma(E_n)$ is the yield of a gamma at neutron energy E_n (here in counts/MeV), and τ_γ and τ_ϕ are the dead time corrections for the gamma detectors and the flux detectors (fission

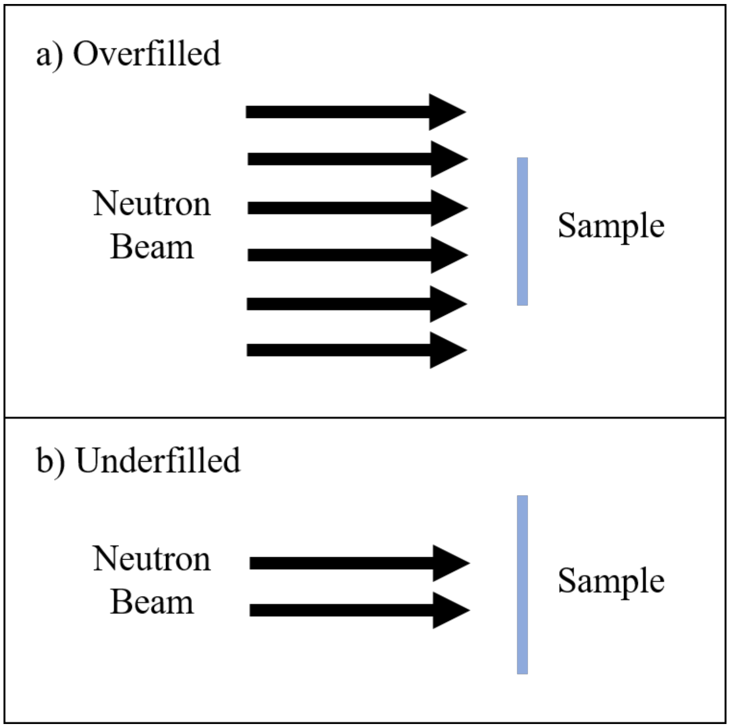

Figure 2.18: Schematic showing the two modes of beam/sample overlap. An overfilled sample, in panel (a), has a smaller areal cross section than the beam. All of the sample is irradiated, and the mass of the sample is the important quantity. An underfilled sample, in panel (b), has a cross section that is larger than the beam profile, and the areal density of the sample is important to characterize.

chambers), respectively. The term $(1+\alpha_\gamma)$ is the correction for internal conversion, c_γ is the angular distribution correction, ε_γ is the gamma detector efficiency for that gamma, and d is the target thickness (here in atoms/mb). The fluence, $\phi(E_n)$, is in neutrons/MeV. This partial cross section, $\sigma_\gamma(E_n)$, is the cross section for the transition, not the emission of the gamma itself, because of the correction for internal conversion.

Finally, the cross section of the reaction is inferred from the partial cross sections, σ_γ, that were measured. This conversion must be simulated and often nuclear reaction codes such as GNASH [127], EMPIRE [74], `CoH3` [79] or TALYS [80] are used. These codes combine Hauser-Feshbach and Optical Model calculations with full gamma-cascade simulations to predict the intensities of these measured transitions for each reaction. More details on the cascade calculations, and a new method for estimating their uncertainties, are presented in Chapter 7.

2.2.5 Activation Analysis

If the product nucleus is radioactive, with a half-life between hours and weeks, then determination of the cross section can also be done through observation of the decay of the product. This method, known as activation analysis (AA), has several advantages over in-beam measurements, such as that the counting can be done in a different location, away from the complicated and time-dependent backgrounds from the beam. The detectors used for AA depend on the decay particles measured in the experiment. If characteristic gammas are measured, which is the most common method, high energy resolution gamma detectors like HPGe are most often used. If charged particles are measured, solid state or liquid scintillator detectors are typically used. For both alpha decay and beta decay, silicon detectors, such as Passivated Implanted Planar Silicon (PIPS) detectors, are often used [128–131]. Liquid scintillation counters (LSC) are also commonly used when the product decays by beta decay. Penning traps [132] and bolometers [133, 134] can also be used for beta decay, but it is rare for these detectors to be used in reaction measurements so this work will not focus on them.

For gamma detectors, the efficiency is determined with calibration sources and/or simulations, as explained in the previous section (Section 2.2.4). If the activation induced in the experiment is low and gammas are being measured, the low intrinsic efficiency of high resolution gamma detectors may lead to unacceptably high statistical uncertainties. However, this should not be remedied by moving the sample closer to the detector to increase the solid angle, as this may introduce coincidence summing. Summing occurs when coincident gammas interact with the detector within the charge collection time (ns-μs), producing a pulse with energy that is not characteristic of either pulse. While some of the summing events can be determined from the spectrum by looking for peaks at the energy that is the sum of the two photopeak energies, the vast majority contribute to a smooth background due to the summing of one or more Compton-scattered interactions in the detector. Summing is dependent on many characteristics of the cascade, such as the multiplicity and gamma energy distributions, and can only be simulated with correct level scheme information and a well modeled detector setup. For decays and reactions with well-understood cascades (including gamma-emission angular correlations), it is possible to apply a correction based on a Monte Carlo simulation of a cascade and detector setup. However, the gamma angular distribution cannot be accurately predicted if the transition multipolarity is not known. If the decay has a more complicated cascade, as is the case with even moderate Q-value beta decays, estimating summing corrections using a simulation may not be possible. In this case, the sample should be moved far enough away from the detector to avoid a significant probability of summing—estimated to be at least 10 cm from the detector. The effects of coincidence summing can be tested by measuring the same sample at two different distances from the detector. The close distance measurement will yield good statistics, and the far distance measurement will have lower (preferably negligible) coincidence summing. The effect of the coincide summing on the efficiency can then be estimated based on the ratios of gamma counts in the two measurements. This method requires that the activity be low enough to not introduce biasing issues such as high dead time, but high enough that the measurement at the far distance yields usable results. If the statistical uncertainty is too large, it is preferable to measure multiple samples or do multiple runs to decrease the statistical uncertainty, rather than move the sample closer to the detector.

For charged particles, the efficiency for the detection of a particle incident on the detector can be close to 100%. The efficiency calibration for a particle detector is based mostly on the solid angle that the detector subtends and on the lower level threshold set on the detector. Particle detector simulations usually include both a solid angle factor and a model for energy loss before the particle reaches the detector [129, 130]. Known alpha and beta sources can be used to validate the simulation, or show that the simulations are biased [130]. Known sources with energy spectra similar to the product nucleus should always be used in the efficiency calibration process. Liquid scintillation counters require that the sample be dissolved into a scintillation cocktail. The charged particles moving through the scintillation material creates light that can then be measured. The intrinsic efficiency can be over 80% in most cases, with the exact value determined by calibration with known samples with similar Q-values.

The backgrounds in activation analysis are typically easier to determine and correct for than in in-beam measurements. After irradiation the sample is transported to a low-background counting room, with a well-characterized background (a recent measurement with high statistics ($\leq$1%)) that can be normalized and subtracted from the measured spectrum. Backgrounds in gamma spectroscopy using high resolution detectors like HPGe include a Compton background below each full-deposition peak and other full-deposition peaks from gammas with energies close to the gamma of interest. For a typical HPGe, an energy difference of a few keV is typically large enough to allow for independent determination of gamma intensity. Contamination of the peak will create a bias in the measured activity that must be corrected for, and should be checked for by looking at the time and energy dependence of the counts. With the neutron-energy dependent data from PG measurements, contamination will lead to an incorrect energy dependence, as discussed in Section 2.2.4. In the case of AA measurements, the time-dependence of the intensity should be verified. These general trends should always be used to validate that there are no unknown backgrounds, even with charged particle detectors, where the backgrounds come from other sources. There will always be background noise, which can be minimized with a well-placed lower level discriminator.

Many of the sample considerations are similar to the PG sample considerations. For measurements where the charged particle from a decay is measured, the sample should be thin enough to allow for most of the particles to be measured.

For AA measurements, the flux is usually determined in ratio to the irradiation of specific reference materials. Reference materials with cross sections that are relatively constant over the energy region can be useful for determining the total neutron flux over the irradiation. Other materials with energy-dependent cross sections can be used to determine the spectrum of the neutron source [135]. The energy spectrum of a neutron source must be well-characterized in activation analysis, since no TOF energy determination is possible. In the case of neutron-producing reactions like DD and DT, where the angle to the beam determines the neutron spectrum, correct geometry is also a factor. Reference reactions with energy-dependent cross sections should be used in most, if not all, locations where samples will be irradiated. Any change in the flux during the irradiation will need to be taken into account via a simultaneous production and decay correction for the reaction and reference products [129]. For one common reference reaction, ^{27}Al(n,α)^{24}Na, another correction is necessary as well—the recoil of the de-exciting ^{24}Na is great enough that a small fraction of the nuclei are emitted from the foil itself [135].

Associated Particle Imaging (API) neutron sources can provide unusually accurate neutron flux values. The associated particle technique involves measuring the charged particle created in the neutron-production reaction, in coincidence with events from a neutron-induced reaction in another detector [136]. This method reduces the effective neutron flux to the subset that cause reactions seen in coincidence with the charged particle. However this method greatly reduces the background in the data and provides a high precision neutron flux value.

The yield, Y, the number of reactions that occurred, is determined by measuring the decay of the sample. The activity of the sample at various times is measured, and with an exponential decay function, the activity at the end of the irradiation, A_0, is calculated. This calculation includes corrections for the decay during the counting time, t_c, the cooling-down or waiting time, t_w, and for simultaneous production and decay during the irradiation time, t_i. For products with half-lives that are comparable to t_i, the simultaneous production and decay correction can be significant. These corrections require the half-life of the product nucleus, which is usually taken from a library such as ENSDF [10]. This decay data information plays a crucial role in the determination of the cross section, and the presence of the half-life in an exponential means that decay uncertainties that are not negligible can drastically increase the overall cross section uncertainty.

The number of reactions that occur can be represented as,

$$Y = \int dt \int dE_n \; \sigma(E_n) \int d\Omega \; \phi(E_n, r, \theta, \varphi, t)\rho(r, \theta, \varphi), \tag{2.40}$$

where ρ is the areal density of the sample, as a function of location, and ϕ is the fluence. The yield is integrated over the energies of the beam, dE_n, the full areal cross section of both the beam and the sample, $d\Omega$, and the irradiation time, dt. The irradiation time can be integrated out, and in the case of highly fluctuating beam, a correction term, $\Delta\phi$, can be used,

$$Y = t\Delta\phi \int dE_n \; \sigma(E_n) \int d\Omega \; \phi(E_n, r, \theta, \varphi)\rho(r, \theta, \varphi). \tag{2.41}$$

For an experiment with an overfilled sample (the beam cross section is larger than the sample cross section) the areal density integral over $d\Omega$ is trivial, and in the end only the mass of the sample, m, is needed,

$$Y_o = t\Delta\phi \; m \int dE_n \; \sigma(E_n) \int d\Omega \; \phi(E_n, r, \theta, \varphi). \tag{2.42}$$

In the case of an underfilled sample (which is larger than the cross section of the beam) the areal density of the sample is important, but the spatial distribution of the flux is less so,

$$Y_u = t\Delta\phi \int dE_n \; I(E_n)\sigma(E_n) \int d\Omega \; \rho(r, \theta, \varphi), \tag{2.43}$$

where I is the current of neutrons (the spatially-averaged flux). From these equations, the energy-averaged cross section can be determined.

2.2.6 Accelerator Mass Spectrometry

Activation analysis can be an accurate method when the product nucleus has a half-life that is amenable to measurement, and when the cross section is large enough to produce high count rates, resulting in acceptable statistical uncertainties. If the half-life is too long or too short, or the cross section is low, an alternative method is using accelerated mass spectrometry (AMS), to determine the number of product nuclei produced in the irradiation. The final result of the AMS measurement is the ratio of the target to the product nuclei in the sample after irradiation, and the method can quantify ratios down to 10^{-15} [137]. AMS facilities such as VERA [138], ATLAS [139, 140] and the Maier- Leibnitz Laboratory [141, 142] have been used in activation-AMS measurements of capture cross sections. The setup of the VERA facility is shown in Figure 2.19[7]. Many of these measurements were done on reactions with low cross sections that are important for astrophysics applications, such as ^{54}Fe(n,γ)^{55}Fe [143], ^{62}Ni(n,γ)^{63}Ni [144] and ^{40}Ca(n,γ)^{41}Ca [145]. The method can produce uncertainties as low as a few percent, in the case where there are good standards for both the flux measurement and the AMS measurement. For example, the thermal ^{54}Fe(n,γ)^{55}Fe cross section was reported with 3% uncertainty [146].

AMS is a destructive measurement method, unlike the previous methods. Atoms are sputtered from the sample, and then the negatively charged ions are injected into an accelerator. After acceleration, the ions are passed through a carbon foil or low pressure gas, which breaks up any molecules and leaves all ions positively charged. The positive ions are then accelerated again, and a magnet is used to select for a specific charge state. In some cases isobars (other isotopes with the same energy at this stage) or molecules can follow the same trajectory as the isotope being measured. If this is an issue, the final acceleration can occur in gas-filled magnets, which separates the ions by Z. At this point, the ions reach detectors and are counted. More details on the method and facilities, along with specific considerations for some important isotopes, can be found in Reference [147].

Several different detectors can be used in AMS measurements. Most often, the more common isotope (the target isotope in cross section measurements) is measured as a current with a Faraday cup. The product nucleus atoms are counted individually. Silicon detectors, which only give information on the energy of the ion, can be used when the separation between the isotopes is large. For isotopes with isobars, more information is needed and

---

[7] Figure, taken from Reference [127], is available with license CC BY 4.0.

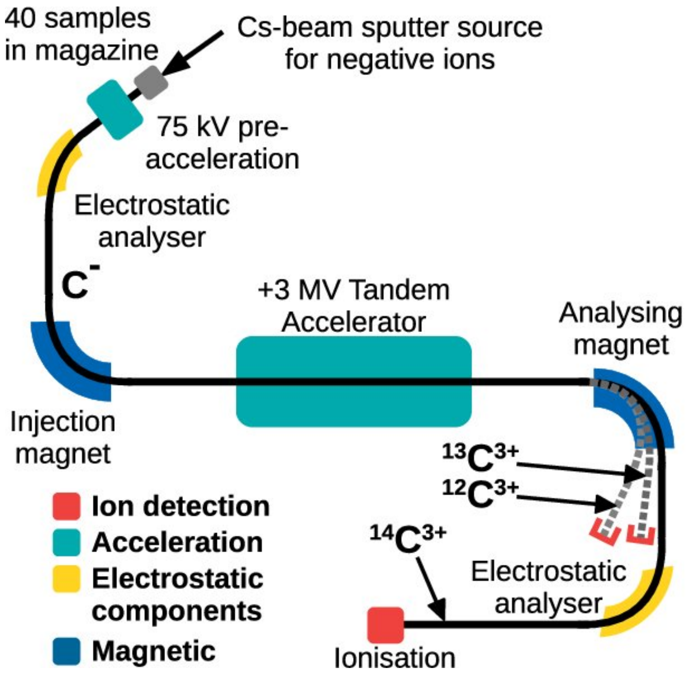

Figure 2.19: Schematic drawing of the VERA facility, taken from Reference [127], in use for a measurement of the ^{13}C(n,γ)^{14}C reaction product. The schematic shows how the isobars, ^{12}C and ^{13}C, are removed from the collimated beam with a magnet.

ionization chambers are utilized to determine both the energy of the ion and the rate of energy loss in the detector. From this, both the energy and Z can be determined, allowing for the separation of the background counts. If higher energy resolution is needed, for example for high mass isotopes, TOF can also be used in the measurement. Short flight paths can be used, as timing resolution of even a few hundred picoseconds is enough to distinguish between isotopes in the A$\sim$120 region [147].

The efficiency of the entire AMS setup varies by isotope, depending on the detectors used and the efficiency of the extraction of negative ions in the initial sputtering step. For specific isotopes of importance, like ^{14}C, AMS setups can be optimized to achieve efficiencies of a few percent. Typical efficiencies are on the order of 10^{-5} to 10^{-3} [137]. The use of the TOF setup will reduce the efficiency, taking the transmission efficiency (typically close to 100%) down to between 50 and 80% [147]. Efficiencies for the sputtering, transmission and detection are usually not reported, because the measurements are in most cases normalized using a known sample of the same isotopes. In one case where no normalization standard was used, the sputtering yield was determined to be $(0.8 \pm 0.2)\%$ [141].

The backgrounds in an AMS measurement are the isobars and molecules that can follow a trajectory similar enough to the isotope of interest that they reach the detector. Isobars can be reduced by the choice of the ion selected after the sputtering stage. For example, in an experiment measuring the capture cross section of ^{78}Se, the isobars of ^{79}Se were reduced by selecting a high charge state, 15^+ [142]. This high charge state had a sputtering yield of 0.64%, contributing to the overall low efficiency of the method. "Blank" samples, which have the target isotope and contaminants but not the product isotope, are also measured and can be used to correct for background counts that cannot be separated out. One source of background that cannot be discriminated against is atoms of the product in the sample before irradiation. The level of this contamination that will affect the measurement depends on the ratio of the product nucleus to the target nucleus after irradiation.

For this reason, the composition of the sample must be precisely quantified before the irradiation, as the number of product nuclei, target nuclei, and contaminants must be known. The composition is much more important than the size or shape of the sample, as AMS measures the ratio. The sample must be in a chemical form that is suitable for creating negative ions in the sputtering process [137]. Even though typical efficiencies are between 10^{-3} and 10^{-5}, the fact that this method counts atoms directly means that only a few milligrams of sample are needed for most measurements [137].

The normalization to determine the efficiency of the AMS measurement is done using a standard sample with a precise composition determination, that contains both the target and product isotope. This replaces the quantification of the efficiency of the AMS setup, which, due to issues such as machine instability and long term drift of the trajectories, typically cannot be quantified with uncertainties less than 5-10% [143]. The creation of precise standards can be quite complicated, given that AMS is specifically used for nuclei that are not easily quantified by decay measurement. The process for creating ^{55}Fe, ^{68}Ge and ^{202g}Pb standards is described in detail in Reference [148]. The ^{55}Fe standard samples had ^{55}Fe/^{56}Fe ratios between 10^{-12} and 10^{-10}, with uncertainties of 1.6%. This precise standard allowed for an unusually precise cross section measurement (3% at thermal) [146]. Standards can also be created by irradiation with thermal neutron sources. In this case the uncertainty on the standard relies on the uncertainty of the thermal cross section, and typical values are around 5% [142]. Standard samples can also be used to quantify any fluctuations in AMS runs beyond statistical fluctuations. This is represented by a systematic uncertainty often called "AMS reproducibility" [146].

If standard samples cannot be created, the relative efficiency of the system for each isotope must be quantified. This is not easy, due to the fact that the common isotope (the target) is measured as a current with a Faraday cup while the product nucleus is counted directly with particle detectors. One method, developed for a measurement of ^{209}Bi(n,γ)^{210m}Bi, is to use beam attentuators to directly quantify both count rates [141]. The authors quote an attenuation factor uncertainty of around 5%, which is similar to some of the standard samples used in other experiments.

AMS is used to measure the product nuclei created after irradiation, so the fluence must be quantified to determine the cross section. As with AA, most often the fluence is determined by the use of monitor reactions. The choice of monitor reaction depends on the neutron spectrum. For example, for the ^{54}Fe(n,γ)^{55}Fe measurement, both ^{196}Au and ^{94}Zn capture were used to determine the thermal flux, and only ^{196}Au capture was used for two different MACS spectra [146]. For measurements with well-defined AMS standards, the uncertainty in the flux is often a large component of the overall uncertainty in the cross section.

To determine the cross section, the traditional reaction rate equation is vastly simplified to

$$\sigma_\gamma(E_n) = \frac{1}{\phi(E_n)} \frac{N_p(E_n)}{N_t(E_n)}, \tag{2.44}$$

where N_p is the number of atoms of the product, and N_t is the number of atoms of the target. In this case, the fluence, $\phi(E_n)$, has units of neutrons per cm^2. The AMS measurement often gives directly the ratio $\frac{N_p}{N_t}$, or sometimes both in ratio to an isotope with a higher number density. For example, in the ^{54}Fe(n,γ)^{55}Fe measurement, both ^{54}Fe and ^{55}Fe were measured in ratio to ^{56}Fe [146].

2.3 Uncertainties and Covariances

The focus of this work is on the uncertainties in experimental data sets, and how to ensure that they are complete and realistic. Some of the theory behind the uncertainty calculations is explained here. Random variables are used to describe any value with an uncertainty in experimental data analysis. Two common methods for uncertainty propagation are described, which can be used to determine the uncertainty on the result of the data analysis procedure. Finally, regression uncertainties are explained, as they are used in the curve fitting processes that are part of many experiments.

2.3.1 Properties of Random Variables

A Random Variable (RV) represents a random event, and the values that the RV can take on represent the possible outcomes of the random event. Random variables can take on discrete values, such as the face that a die can land on, or continuous values, such as the amount of rain that falls in a season. For continuous random variables, which will be the focus here, the probability that the random variable, X, takes on a specific value, x, is given by the probability distribution function,

$$f_X(x) = \mathbb{P}(X = x) \tag{2.45}$$

and the probability that the random variable X takes on a value less than or equal to x is given by the cumulative distribution function,

$$F_X(x) = \mathbb{P}(X \leq x) = \int_{-\infty}^{x} dx' \; f(x'). \tag{2.46}$$

The most commonly used properties of distribution functions of random variables are their mean and variance. The mean is defined as the expectation value, or the probability-weighted average, of the random variable,

$$\mu_X = \mathbb{E}(X) = \int_{-\infty}^{\infty} dx'\ x' f(x'). \tag{2.47}$$

The variance of the random variable, σ^2, is the expectation value of the deviation of the random variable X from its own expectation value, μ_X,

$$\sigma_X^2 = \mathbb{V}(X) = \mathbb{E}\left[(X - \mu_X)^2\right]. \tag{2.48}$$

The shape of the probability distribution function, the mean and the variance of the random variable are usually enough information to describe the random event in this context. The connection between the variance, σ_X^2, of the random variable and confidence intervals is dependent on the distribution.

One of the most common probability distributions utilized in the sciences is a Gaussian or Normal distribution. A random variable that has a normal distribution can be described by,

$$X \sim \mathcal{N}\left(\mu, \sigma^2\right), \tag{2.49}$$

where μ is the mean value of the distribution and σ^2 is the variance. The probability distribution of a normal random variable is

$$f_X(x) = \frac{1}{\sigma\sqrt{2\pi}} \exp\left[-\frac{(x-\mu)^2}{2\sigma^2}\right]. \tag{2.50}$$

2.3.2 Uncertainty Propagation Methods

2.3.2.1 Linear Propagation

The first method that many scientists learn to propagate uncertainties is a simple, linear equation,

$$\delta_u^2 = \sum_x \left(\frac{\partial u}{\partial x}\right)^2 \delta_x^2, \tag{2.51}$$

where $u = f(x_1, x_2, ...)$ is a function of variables x that each have an associated uncertainty, and δ_u is the uncertainty on the quantity u [124]. This equation is only applicable when the x_i variables are independent of each other and normally distributed, which is usually the case in the simple problems encountered by students.

The extension of Equation 2.51 to include several data points that are correlated requires an understanding of the derivation of general error propagation formula. The equation that includes correlations between uncertainty sources and data points is referred to as the "Sandwich Formula", which defines the covariance matrix, $\mathbf{\Sigma}$, as

$$(\mathbf{\Sigma})_{ij} = \sum_x \left.\frac{\partial u}{\partial x}\right|_i \delta x_i \mathrm{corr}(x_i, x_j) \delta x_j \left.\frac{\partial u}{\partial x}\right|_j, \tag{2.52}$$

where x represents sources of uncertainty and i and j are indices representing data points [149]. The next extension, to include uncertainty sources that are correlated, gives

$$(\mathbf{\Sigma})_{ij} = \sum_x \sum_y \left.\frac{\partial u}{\partial x}\right|_i \delta x_i \mathrm{corr}(x_i, y_j) \delta y_j \left.\frac{\partial u}{\partial y}\right|_j. \tag{2.53}$$

In this case, x and y each loop over the sources of uncertainty, and i and j each loop over the data point indices. Correlated uncertainty sources come up in many applications, such as experiments that measure multiple gammas at each incident particle energy. The detector efficiency is usually a fitted curve, so there is a correlation between the efficiency values.

There are strong assumptions in the derivation of Equations 2.51 through 2.53 which limit the circumstances under which they are applicable. These equations are derived using a Taylor expansion, and so are only valid when the function u is linear in all of the variables x, and when the uncertainties are "small". This excludes any calculations where the non-linear terms have non-negligible uncertainty. One solution for significant non-linear uncertainty components is to include another term in the Taylor expansion, up to third order [149]. This derivation also assumes that all uncertainties are described by Gaussian PDF's and cannot easily be generalized to other distribution functions.

2.3.2.2 Monte Carlo Propagation

A more time consuming method for error propagation, with fewer assumptions, is Monte Carlo propagation. This method involves simulating the entire space of possible final values by varying each of the variables according to their uncertainties. In each iteration, each of the values are sampled, and the efficiency is calculated. This process is repeated until the statistical fluctuations inherent to such a stochastic process are minimized, and the resulting distribution of values is used to determine the uncertainty. Correlations between the data points can also easily be extracted from this calculation, if the values from each iteration are stored. A Cholesky decomposition can be applied to the matrix of iteration results to determine the data covariance matrix, $\mathbf{\Sigma}$. The Cholesky decomposition method is frequently used to generate correlated random variables when given a correlation matrix [149] and can also be used to determine a correlation matrix given correlated random variables.

This method is general enough to correctly account for non-linear terms, large uncertainties, non-parametric uncertainty distributions and correlations. For example, in measurements where the half-life of the source is a non-negligible uncertainty source, or the time elapsed is not known well enough, the Monte Carlo method makes uncertainty propagation simple. With Monte Carlo propagation, non-linear terms and non-parametric distributions create no extra complexity.

Correlations between the variables at different data points is easily taken into account. For variables that can be described by Gaussian distributions, the correlated variables are represented by multivariate normal distributions. The joint distribution of variables $\mathbf{X} = \{X_1, X_2, ..., X_p\}$ is represented as

$$\boldsymbol{X} \sim \mathcal{N}\left(\boldsymbol{\mu}, \boldsymbol{\Sigma}_p\right), \tag{2.54}$$

where $\boldsymbol{\mu}$ is the vector of means for each random variable X_i, $\boldsymbol{\Sigma}_p$ is the covariance matrix between the variables [150]. In the case of two variables, the bivariate normal distribution can be written as

$$X_2|X_1 = x_1 \sim \mathcal{N}\left(\mu_2 + \frac{\sigma_2}{\sigma_1}\rho(x_1 - \mu_1), (1-\rho)^2\sigma_2^2\right), \tag{2.55}$$

where ρ is the correlation coefficient between X_1 and X_2. This representation is instructive, as it shows that when the correlation between the two variables is unity, the variance of the distribution of X_2 goes to zero—once X_1 is known, X_2 is known. If the variables are not fully correlated, the mean and variance of the distribution of X_2 are changed based on the value of X_1. The most straightforward method for sampling many variables that are correlated is to draw independent values for each and then modify them based on the correlations. The details of this method can be found in Reference [151], and are implemented in the `random.multivariate.normal` function in the Python package `NumPy` [152]. The Python package `NumPy` also has functions to apply the Cholesky decomposition to extract the covariance (`numpy.cov`) and correlation (`numpy.corrcoef`) matrices from the simulation results [152].

A detailed explanation of the two uncertainty propagation methods, along with summaries of the advantages and disadvantages of each, is given in Reference [153]. One of the main disadvantages of the Monte Carlo approach, the time required to do the calculation, is possibly exaggerated in importance in this reference—quick, order of magnitude calculations can always be done with the linear approximation if necessary. For the final uncertainty analysis, which is likely performed once, it is worth taking the time for the full Monte Carlo calculation to avoid biased results. The exception is in the case where all of the relevant uncertainties are linear and Gaussian, in which case the two methods give the same result.

2.3.3 Fitting Uncertainty

2.3.3.1 Ordinary Least Squares

The least squares method can be used to estimate parameters for a set of equations. Curve fitting for interpolation is a common example in the physical sciences. For linear equations, the set of equations is written in matrix form as such,

$$\boldsymbol{Y} = \boldsymbol{X}\boldsymbol{\beta} + \boldsymbol{e}, \tag{2.56}$$

where $\boldsymbol{Y}$ is the $(n \times 1)$ vector of responses, $\boldsymbol{X}$ is the $(n \times p)$ matrix of independent variables and $\boldsymbol{\beta}$ is the $(p \times 1)$ vector of the parameters relating the independent variables to the responses. The $(n \times 1)$ vector $\boldsymbol{e}$ contains the scatter of the responses around this defined relationship. In the derivations of regression, $\boldsymbol{e}$ typically represents the unknowable variance of the distribution of $\boldsymbol{Y}$, which is centered at $\boldsymbol{X}\boldsymbol{\beta}$.

The least squares method for solving for $\boldsymbol{\beta}$ minimizes the squares of the residuals. The residuals are calculated with estimated parameters $\hat{\boldsymbol{\beta}}$, as the difference between the predicted and observed responses. The calculated residuals, $\hat{\boldsymbol{e}}$, are used to estimate the scatter vector, $\boldsymbol{e}$, and are defined as

$$\hat{\boldsymbol{e}} \equiv \boldsymbol{Y} - \boldsymbol{X}\hat{\boldsymbol{\beta}}. \tag{2.57}$$

The squares of the residuals, $\hat{\boldsymbol{e}}$ is then,

$$\begin{aligned} \hat{\boldsymbol{e}}^T\hat{\boldsymbol{e}} &= \left(\boldsymbol{Y} - \boldsymbol{X}\hat{\boldsymbol{\beta}}\right)^T \left(\boldsymbol{Y} - \boldsymbol{X}\hat{\boldsymbol{\beta}}\right) \\ &= \left(\boldsymbol{Y}^T - \hat{\boldsymbol{\beta}}^T\boldsymbol{X}^T\right) \left(\boldsymbol{Y} - \boldsymbol{X}\hat{\boldsymbol{\beta}}\right) \\ &= \boldsymbol{Y}^T\boldsymbol{Y} - \hat{\boldsymbol{\beta}}^T\boldsymbol{X}^T\boldsymbol{Y} - \boldsymbol{Y}^T\boldsymbol{X}\hat{\boldsymbol{\beta}} + \hat{\boldsymbol{\beta}}^T\boldsymbol{X}^T\boldsymbol{X}\hat{\boldsymbol{\beta}} \\ &= \boldsymbol{Y}^T\boldsymbol{Y} - 2\hat{\boldsymbol{\beta}}^T\boldsymbol{X}^T\boldsymbol{Y} + \hat{\boldsymbol{\beta}}^T\boldsymbol{X}^T\boldsymbol{X}\hat{\boldsymbol{\beta}}. \end{aligned} \tag{2.58}$$

The minimization of $\hat{\boldsymbol{e}}^T\hat{\boldsymbol{e}}$ with respect to the estimated parameters $\hat{\boldsymbol{\beta}}$,

$$\begin{aligned} 0 &= \frac{\partial \hat{\boldsymbol{e}}^T\hat{\boldsymbol{e}}}{\partial \hat{\boldsymbol{\beta}}} \\ &= 0 - 2\boldsymbol{X}^T\boldsymbol{Y} + 2\hat{\boldsymbol{\beta}}\boldsymbol{X}^T\boldsymbol{X} \\ &= \hat{\boldsymbol{\beta}}\boldsymbol{X}^T\boldsymbol{X} - 2\boldsymbol{X}^T\boldsymbol{Y} \end{aligned} \tag{2.59}$$

leads to the normal equations,

$$(\boldsymbol{X}^T\boldsymbol{X})\hat{\boldsymbol{\beta}} = \boldsymbol{X}^T\boldsymbol{Y}. \tag{2.60}$$

The normal equations can be solved for $\hat{\boldsymbol{\beta}}$, giving the ordinary least squares equation for the parameters,

$$\hat{\boldsymbol{\beta}} = (\boldsymbol{X}^T\boldsymbol{X})^{-1}\boldsymbol{X}^T\boldsymbol{Y}. \tag{2.61}$$

For $\hat{\boldsymbol{e}}$ that are independent and Gaussian distributed, $\hat{\boldsymbol{\beta}}$ calculated with this equation is the BLUE (Best[8] Linear Unbiased Estimator) for the linear equation [154].

---

[8] "Best" here means the lowest variance in the estimated parameter values.

The derivation of the ordinary least squares normal equations is based on the assumption that there is scatter in the data, but that all of the data points come from the same distribution. This means that the $\boldsymbol{e}$ values can all be represented as a single Gaussian distribution centered at zero, with a variance, σ^2. The covariance of $\boldsymbol{Y}$ is therefore,

$$\mathbb{C}(\boldsymbol{Y}) = \sigma^2\mathbb{I}, \tag{2.62}$$

where $\mathbb{I}$ is the identity matrix.

The uncertainties on the parameters $\hat{\boldsymbol{\beta}}$ can be calculated using the normal equations, Equation 2.60,

$$\begin{aligned}\mathbb{C}(\hat{\boldsymbol{\beta}}) &= \mathbb{C}\left[(\boldsymbol{X}^T\boldsymbol{X})^{-1}\boldsymbol{X}^T\boldsymbol{Y}\right] \\ &= (\boldsymbol{X}^T\boldsymbol{X})^{-1}\boldsymbol{X}^T\mathbb{C}(\boldsymbol{Y})\left[(\boldsymbol{X}^T\boldsymbol{X})^{-1}\boldsymbol{X}^T\right]^T \\ &= (\boldsymbol{X}^T\boldsymbol{X})^{-1}\boldsymbol{X}^T(\sigma^2\mathbb{I})\boldsymbol{X}(\boldsymbol{X}^T\boldsymbol{X})^{-1} \\ &= \sigma^2(\boldsymbol{X}^T\boldsymbol{X})^{-1}(\boldsymbol{X}^T\boldsymbol{X})(\boldsymbol{X}^T\boldsymbol{X})^{-1} \\ &= \sigma^2(\boldsymbol{X}^T\boldsymbol{X})^{-1},\end{aligned} \tag{2.63}$$

due to the fact that the matrix $(\boldsymbol{X}^T\boldsymbol{X})^{-1}\boldsymbol{X}^T$ is a constant and that $(\boldsymbol{X}^T\boldsymbol{X})^{-1}$ is its own transpose.

The value of σ^2, which is not known due to the assumptions in this derivation, is estimated based on the residuals, $\boldsymbol{e}$. The residual sum of squares (RSS), $\hat{\boldsymbol{e}}^T\hat{\boldsymbol{e}}$, has expectation value,

$$RSS = \mathbb{E}(\hat{\boldsymbol{e}}^T\hat{\boldsymbol{e}}) = \sigma^2(n-p), \tag{2.64}$$

and so can be used to estimate the value of σ. The estimate, represented by $\hat{\sigma}^2$, is,

$$\hat{\sigma}^2 = \frac{\hat{\boldsymbol{e}}^T\hat{\boldsymbol{e}}}{n-p}. \tag{2.65}$$

This follows from the idea the the distribution of $\boldsymbol{Y}$ cannot be known, and the use of $\hat{\sigma}^2$ to estimate σ^2 implies that the model is correct [154].

2.3.3.2 Weighted Least Squares

If relative weights can be assigned to the data points, then the minimization should reflect this. In the usual statistics derivations, the weights are applied when there are some observations that are considered less reliable than others [154]. It is still assumed that the $\boldsymbol{Y}$ values all come from the same distribution, centered around $\boldsymbol{X\beta}$, with variance σ^2.

The covariance matrix of $\boldsymbol{Y}$ is no longer an identity matrix, but is instead,

$$\mathbb{C}(\boldsymbol{Y}) = \sigma^2\boldsymbol{W}^{-1}, \tag{2.66}$$

where $\boldsymbol{W}$ is the matrix of weights,

$$\boldsymbol{W}^{-1} = \begin{bmatrix} 1/w_1 & 0 & ... & 0 \\ 0 & 1/w_2 & ... & 0 \\ \vdots & \vdots & & \vdots \\ 0 & 0 & ... & 1/w_n \end{bmatrix} \tag{2.67}$$

with w_i representing the weight put on the i^{th} data point. The ordinary least squares normal equations, Equation 2.60, will give a biased estimate of $\boldsymbol{\beta}$ for weighted points, and the weighted least squares normal equations,

$$(\boldsymbol{X}^T\boldsymbol{W}\boldsymbol{X})\hat{\boldsymbol{\beta}}_{WLS} = \boldsymbol{X}^T\boldsymbol{W}\boldsymbol{Y}, \tag{2.68}$$

are used instead to give an unbiased estimate for $\boldsymbol{\beta}$ [154],

$$\hat{\boldsymbol{\beta}}_{WLS} = (\boldsymbol{X}^T\boldsymbol{W}\boldsymbol{X})^{-1}\boldsymbol{X}^T\boldsymbol{W}\boldsymbol{Y}. \tag{2.69}$$

The uncertainty on the WLS parameters can be determined from the covariance matrix,

$$\begin{aligned} \mathbb{C}(\hat{\boldsymbol{\beta}}_{WLS}) &= \mathbb{C}\left[(\boldsymbol{X}^T\boldsymbol{W}\boldsymbol{X})^{-1}\boldsymbol{X}^T\boldsymbol{W}\boldsymbol{Y}\right] \\ &= \sigma^2(\boldsymbol{X}^T\boldsymbol{W}\boldsymbol{X})^{-1}, \end{aligned} \tag{2.70}$$

which represents how the weights on the data points is incorporated into the final uncertainties on the parameters. If data point uncertainties are known, only the relative[9] values are used in WLS to determine the weights. The magnitude of the uncertainty on the data points is therefore lost, so the value of σ^2 is again estimated using the residual sum of squares, Equation 2.65.

2.3.3.3 Generalized Least Squares

In order to account for the magnitude of the uncertainties on the data points, rather than just relative weights, Generalized Least Squares (GLS) can be used instead. The derivation GLS and WLS is the same, except that the covariance matrix for $\boldsymbol{Y}$ is,

$$\mathbb{C}(Y) = \boldsymbol{\Sigma} = \sigma^2\boldsymbol{W}, \tag{2.71}$$

where in this case $\boldsymbol{W}$ does not have to be a diagonal matrix, and can instead include correlations between the data points [154]. In the derivations of these equations, it is still assumed that the real uncertainty magnitudes are not known, and are usually estimated from the residual sum of squares. However the equations include the $\boldsymbol{\Sigma}$ matrix, so it can

---

[9] In this case, relative uncertainties do not refer to the uncertainty as a percent of the value of the data point, but rather the magnitude of the uncertainty relative to the other uncertainty values.

be used in the physical sciences where the distributions of the $\boldsymbol{Y}$ are known. The normal equations for GLS are,

$$(\boldsymbol{X}^T\boldsymbol{\Sigma}^{-1}\boldsymbol{X})\hat{\boldsymbol{\beta}}_{GLS} = \boldsymbol{X}^T\boldsymbol{\Sigma}^{-1}\boldsymbol{Y}, \tag{2.72}$$

which gives the GLS estimate for $\boldsymbol{\beta}$,

$$\hat{\boldsymbol{\beta}}_{GLS} = (\boldsymbol{X}^T\boldsymbol{\Sigma}^{-1}\boldsymbol{X})^{-1}\boldsymbol{X}^T\boldsymbol{\Sigma}^{-1}\boldsymbol{Y}. \tag{2.73}$$

The covariance on the parameters,

$$\mathbb{C}(\hat{\boldsymbol{\beta}}_{GLS}) = (\boldsymbol{X}^T\boldsymbol{\Sigma}^{-1}\boldsymbol{X})^{-1}, \tag{2.74}$$

in this case does not require an estimate for σ^2, as the magnitudes of the uncertainties are included [154].The uncertainty on the fit parameters, therefore, reflects the uncertainty on the data points that are used in the fit, and does not require the assumption of a correct model.

2.3.3.4 Non-Linear Least Squares

For equations that are non-linear in the parameters $\boldsymbol{\beta}$, the minimization cannot be done analytically. The problem is set up similarly, but the notation and variables used are different. In non-linear regression, the independent variables ($\boldsymbol{X}$) are denoted as $\boldsymbol{\xi}$, and the parameters ($\boldsymbol{\beta}$) are denoted as $\boldsymbol{\theta}$ [154]. The model can be represented as,

$$\boldsymbol{Y} = f(\boldsymbol{\xi}, \boldsymbol{\theta}) + \boldsymbol{e}, \tag{2.75}$$

and the residual sum of squares is given by

$$S(\boldsymbol{\theta}) = \sum_{i=1}^{n} \left[Y_i - f(\xi_i, \boldsymbol{\theta})\right]^2, \tag{2.76}$$

which is also known as the χ^2 of a fit.

The least-squares estimate of $\boldsymbol{\theta}$, denoted by $\hat{\boldsymbol{\theta}}$, minimizes Equation 2.76 [154]. The minimization is performed numerically, and many algorithms exist for this problem. For problems without bounds on the parameters, one of the most commonly used methods is the Levenberg-Marquardt method [155, 156]. For method with bounds, the Trust Region Reflective method [157] can be used. Iterative methods can be extremely sensitive to the initial values, and these should be considered carefully [154]. The model with the initial parameters should at resemble the data, which can be checked visually with a single independent variable (such as energy, for cross section or efficiency fits).

The uncertainty on the parameters $\hat{\boldsymbol{\theta}}$ similarly cannot be analytically determined. Instead, uncertainty contours (lines where the uncertainty is the same) are estimated using the sensitivity of the model to the parameters and the uncertainty on the data points. The covariance matrix, based on the 1-sigma contour, can be estimated by,

$$\mathbb{C}(\hat{\boldsymbol{\theta}}) = \boldsymbol{J}^T(\hat{\boldsymbol{\theta}})\mathbb{C}(\boldsymbol{Y})\boldsymbol{J}(\hat{\boldsymbol{\theta}}) \tag{2.77}$$

such as is used in the `optimize.curve_fit` function in the Python package `SciPy` [158]. $\boldsymbol{J}(\hat{\boldsymbol{\theta}})$, the Jacobian of the function, is defined as,

$$\boldsymbol{J} = \begin{bmatrix} \frac{\partial f_1}{\partial \theta_1} & \cdots & \frac{\partial f_1}{\partial \theta_p} \\ \vdots & \ddots & \vdots \\ \frac{\partial f_m}{\partial \theta_1} & \cdots & \frac{\partial f_m}{\partial \theta_p} \end{bmatrix}, \tag{2.78}$$

where there are p total parameters and m total equations. In the curve fitting encountered in this work, there are always only one equation, so the Jacobian is a $(1 \times p)$ matrix.

The magnitude of the uncertainty is directly dependent on the covariance matrix of $\boldsymbol{Y}$, which can again be split into $\boldsymbol{\Sigma} = \sigma^2 W^{-1}$. It is therefore possible with the non-linear least squares to either use the magnitude of the uncertainties, as is done with GLS, Equation 2.74, or to estimate σ^2 using the residuals, as is done with WLS, Equation 2.70. In this case, the reduced χ^2 metric is used to estimate σ^2,

$$\hat{\sigma^2} = \frac{\chi^2}{n-p} = \chi^2_{n-p}, \tag{2.79}$$

where the χ^2 metric is equivalent the residual sum of squares of the fit. These two options are given in the `SciPy`function `optimize.curve_fit`, with the default option being the WLS estimate of $\hat{\sigma}^2$ [158].

Chapter 3

Experimental Uncertainties in Total Cross Section Measurements

The process of evaluating physical quantities such as reaction cross sections often involves consideration of multiple data sets. The trust put into each should reflect the uncertainties, and each data set is weighted relative to the others accordingly. For this reason, it is important that the uncertainty analysis for all data sets is performed in a consistent manner and that there are no missing uncertainties that will falsely increase the weight of one data set over the others. An example of an evaluator carefully working through the uncertainty sources that were presented and that were unjustifiably neglected can be found in Section 3.1 of Reference [159]. Systematic uncertainties were added when neglected, and at times increased from their original values, for each of seven data sets that were used in the evaluation of the thermal cross section of the ^{59}Ni(n,α) reaction. This is a process that must be done for any evaluation, and can be quite time-consuming and subjective—two issues that a template of experimental uncertainties will help to alleviate. A template of uncertainties allows for the evaluator to quickly check that a minimum number of uncertainty sources have been accounted for, and that there are no values that are unreasonably high or low. It also allows the evaluator to use consistent correlation shapes for the uncertainty sources, as they usually must be estimated. A template has already been created for fission cross section measurements [160, 161], and this work extends the idea to a broader set of experiments. The template is mostly for use by evaluators who are incorporating data sets into their evaluations, but can also be helpful to experimentalists who want to ensure that they are accounting for all important uncertainty sources. A template has also been created for reporting experimental results and uncertainties in the resonance region, which includes all information from the experiment that is necessary to evaluate the resulting data[162].

In this thesis, templates are presented for total cross section measurements and capture cross section measurements. Each consists of a description of the evaluation methods, the information needed by the evaluator in order to properly apply the template, and then the template itself. Typical uncertainty sources and values are presented along with recommended correlations. For uncertainty sources that are not easily summarized by a single value, some description is given for how the evaluator should check or estimate the value for a data set. For total cross section measurements the most common experimental method is transmission, so the template focuses solely on transmission. A detailed description of the method is given in Section 2.2.1.

3.1 Evaluation Methods

The evaluation methods for total cross sections vary between the energy regions. For the RRR, the individual resonance parameters (the energy of the resonance, E_R, and width of the resonance, Γ_n) are evaluated by forward fitting. The process to unfold the experimental transmission to obtain the needed resonance parameters is not feasible for several reasons. One reason for this is due to how R-Matrix theory [163, 164] accounts for interference between resonances with the same spin and parity. The second is due to the nature of physical corrections, like that of Doppler broadening, which can be extremely difficult to account for without forward modeling [164]. Instead, initial resonance parameter guesses (often previous evaluations) are input into the R-Matrix equations to give resonances at zero degrees, and corrections are applied for Doppler broadening. This gives the physical cross section, at the temperature of the experiment, based on the initial guesses. The physical cross section is then convolved with the resolution function, $R(t_t, E_n)$, in order to compare it to the experimental quantity, transmission. The resolution function accounts for the neutron source, the sample thickness and composition and the detector setup. It is, in effect, the distribution of neutron energies at t_t, which represents the time between the creation of the neutron and when it leaves the moderator in the collimated beam. The transmission based on the initial guesses is then compared to the experimental transmission, and the resonance parameters are updated based on the differences. SAMMY [165], REFIT [166], CONRAD [167] and EDA [168] are codes that perform this forward fitting.

In the URR, the individual resonances can no longer be distinguished and parameter distributions are fit instead. The spacing between resonances of the same spin and parity can be described by a Wigner distribution [169], and resonance widths are described by a Porter-Thomas distribution [91, 170]. The averaged cross section is used to fit averaged parameters, including the scattering radius, R', the neutron strength function, S_ℓ, for each relevant value of orbital angular momentum $\ell = 0, 1, 2...$, and R_∞.

In the fast region, the cross section becomes smooth and can be predicted by phyiscal models like the optical model. There are many parameters that can affect the total cross section calculation, so the evaluation process is not a straightforward fitting procedure but rather a parameter tuning process. The optical model is not as comprehensive as R-Matrix theory, and even with its many parameters cannot always reproduce experimental cross sections. One example of this, shown in Figure 3.1, is the current ENDF/B-VIII.0 [1] evaluation of ^{181}Ta. ^{181}Ta is deformed, which allows for coupling with the low-lying states that reduces the total cross section [171]. This theory was not included in the code used for the evaluation that is in ENDF/B-VIII.0, so the calculation is not able to reproduce the experimental cross

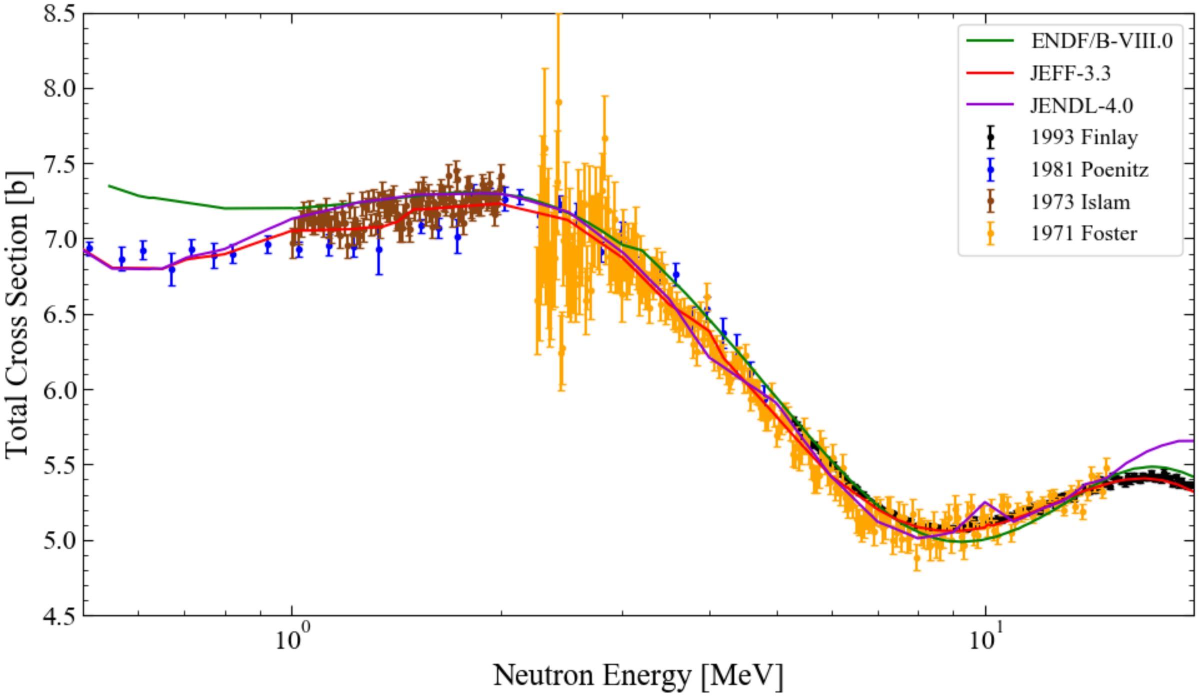

Figure 3.1: The total cross section for neutrons on ^{181}Ta, with some experimental data from EXFOR. The cross section is smooth, with slow oscillations. Three different evaluations are plotted along with experimental data, and it can be seen that the evaluations do not correctly follow the shape of the data. The ENDF/B-VIII.0 evaluation has an especially large bias at low energies, which is likely due to effects of the deformation of the nucleus not being included in the optical model used in the calculation.

section. The final outcome of an evaluation in the fast region is the point-wise cross section.

3.2 Information Needed for Evaluations

There has been previous work [162] documenting the information that should be included in the compilation of resonance region data into the EXFOR database [13]. Templates on what information should be provided were created for this purpose, and they include the information that the evaluators need to understand and reproduce the experimental conditions. The work here is not intended to overlap with or remove the need for those templates, which are important to ensure that all necessary meta-data is communicated to the evaluators and will help to further the goal of reproducible work. The template created here is instead narrowly focused on the important uncertainties, with the intent to provide evaluators with a path forward when presented with old data sets with no uncertainty information and with the ability to check that given uncertainty values are reasonable.

There has also been a recommendation made on how to report uncertainties, based on the Analysis of Geel Spectra (AGS) data analysis framework [172]. This is a format for the columns that will end up in the EXFOR compilation. It allows for clear, consistent reporting of the uncertainties of several variables. For RRR measurements, the AGS code outputs T_{exp} and the uncertainty on T_{exp} for each neutron energy point. The partial uncertainty due to the uncorrelated errors (counting statistics), the background and the flux normalization, N_T, are also recorded for each data point. For URR measurements, the AGS code outputs $\langle\sigma_{tot}\rangle$, the uncertainty on $\langle\sigma_{tot}\rangle$ and the value for F_T for each neutron energy point. Partial uncertainties (as the uncertainty multiplied by the sensitivity) are given for the uncorrelated uncertainties, the background, the flux normalization and the number density of the sample, n.

The values of the measured quantity and the neutron energy and their respective uncertainties are the minimum information that is needed for an evaluator to perform an evaluation. However, more information about the experiment, and values for variables and their uncertainties can go a long way to allow an evaluator to fully understand an experiment and determine if the uncertainties are realistic. Additionally, correlation analysis, which is typically not reported in an experimental paper, can only be undertaken if the magnitudes of the different uncertainty sources are known. The following paragraphs detail for experimentalists what information is useful for the evaluator, and the following section explains what the evaluator can do to estimate missing information if need be.

The resolution function, $R(t_t, E_n)$, is needed for RRR measurements so that the forward modeling process done in the evaluation is accurate. For example, in the experiment information template report [162], an example resolution function was described by the distribution of the initial pulse (normal distribution with FWHM of 2 ns), the distribution from the neutron scattering target/moderator assembly (from simulations, given with two references and the link to an included file) and the distribution from the dectector (an analytic distribution in the REFIT manual, given with a reference and the link to an included file).

The method used to characterize and subtract the background is important for an evaluator to understand the data. The values for the specific variables in the equation and their uncertainty help with correlation analysis, but are typically not given. The background can be separated into two components, $\dot{B} = K\dot{b}$, where $\dot{b}$ has only statistical uncertainties and K has the systematic background uncertainties. This changes the way that the uncertainties are reported, but does not fundamentally change the method or result. The overall background uncertainty, either as one value or split into uncertainties on K and $\dot{b}$, should be given for each neutron energy data point.

The thickness, number density, composition and physical form of the sample can help the evaluator determine if there are contamination or self-shielding effects that should be included in the forward fit. For the RRR, the full set of sample characteristics, including the effective sample temperature, are necessary in order for the experimental quantity, transmission, to be used in the forward modeling evaluation process.

The partial uncertainty on N_T, the normalization of the flux between the sample-in and sample-out runs, should be provided. If cycling was utilized (repeated sample-in and sample-out measurement pairs) this should be indicated, as it can significantly reduce the uncertainty on N_T. This is one of the few fully correlated variables, so it is helpful to understand how large the uncertainty is compared to the other sources.

Finally, for URR measurements, the method for calculating F_T should be described, including which code was used and what evaluated averaged values were input. If any attempt was made to assess the uncertainties on the calculated F_T value, this should also be included. Typically, however, no uncertainty is given and so information about simulation can help the evaluator estimate the uncertainty.

3.3 Template

If information and partial uncertainty values are not given as detailed in the previous section, the following template of uncertainties and correlations can be used to estimate their values. This estimation should be done if there is no way to determine specific information for the experiment under study. Estimation of missing uncertainties ensures that different experimental measurements each have realistic influence over the final evaluation. Some uncertainty values can be estimated, and those values are given in Table 3.1.

Recommended correlations are also provided for each uncertainty source, as these are often not included in the published results. Table 3.2 contains the recommended correlations between data points in an experiment. In the first section, a description of the uncertainty and the recommended correlations between different data points in the same experiment are given. In the second section, recommendations for correlations between different experiments is given. Correlations are described by a shape and a magnitude. The “shape” of a correlation describes the dependence of the correlation on the neutron energy. When the correlation is constant, it is described by the magnitude—fully, strongly, weakly or uncorrelated. Fully correlated means that the correlation between every data point is unity. Uncorrelated means that the correlation between every data point is zero. An example of an uncorrelated uncertainty source is counting statistics, and an example of a fully correlated uncertainty source is the mass of the sample (when the same sample is used for all data points). For correlations that are not constant in neutron energy, the Gaussian shape is used. This represents that data points that are closer in energy are more highly correlated than those further apart, and is an approximation used when the real source of the correlations cannot be fully accounted for. An example of a Gaussian-shaped correlation is the uncertainty on the neutron flux. The methods of determining the neutron flux are often complex, or include nuclear data. If a full accounting of the correlations in the determination are not provided, the Gaussian shape is recommended. This is the due to the fact that it is likely that the flux at two neutron energies that are close together will be influenced by the same uncertainties, whether they are nuclear data or due to a neutron detector response. Two data points that are far apart will be influenced by different uncertainties, leading to a weaker correlation. In the case of

Table 3.1: Uncertainty template for transmission measurements of the total cross section. The values are relative uncertainties on the parameter, and given in percents. The important uncertainties that cannot be estimated as easily are counting statistics, uncertainty on neutron energy resolution, the resolution function and on F_T.

Uncertainty Source	Value
Background (K)	> 3
Target isotope number density (metal)	0.1-1
Target isotope number density (powder)	2-5
Target isotope number density (liquid)	2-5
Flux normalization (N_T) with cycling	< 1
Flux normalization (N_T) without cycling	3

Gaussian correlations, no magnitude is recommended in the tables, but some guidance is given in the descriptions. The uncertainties with Gaussian correlations are specific to the experiment, and whether the correlation is strong or weak should be determined for each measurement individually.

3.3.1 Uncertainties and Correlations Within an Experiment

3.3.1.1 Counting Statistics

Counting statistics should be given for each neutron energy data point. The sample-in and sample-out counting statistics can be combined, and in many papers are combined into one variable, called “uncorrelated errors”. It is not recommended to try and estimate counting statistics, as they are dependent on too many factors that are not usually detailed in transmission experiments—the irradiation time, the neutron detector efficiency, the neutron source strength, the collimation, and more. If uncorrelated or counting uncertainties are not given for an experiment, it is recommended to be careful about trusting the results. Counting statistics are uncorrelated between data points.

3.3.1.2 Neutron Energy

The uncertainty on the neutron energy values or bins is also hard to estimate, as it dependents strongly on the flight path length and timing resolution of the experiment. It is not recommended to estimate this uncertainty, and experiments that do not give this uncertainty should also be used with extreme caution. The correlation between the neutron

Table 3.2: Correlation template for transmission total cross section measurements. These are the correlations between different neutron energy data points within the same experiment.

Uncertainty Source	Correlation Shape
Counting Statistics	Uncorrelated
Neutron Energy Resolution	Gaussian
Resolution Function	Gaussian
Background (K)	Fully Correlated
Target isotope number density	Fully Correlated
Flux normalization (N_T)	Fully Correlated
Fluctuation Correction (F_T)	Gaussian

energy uncertainties can be estimated with strong, Gaussian correlations, unless otherwise determined.

3.3.1.3 Resolution Function

The resolution function does not contribute to the uncertainty on the experimental transmission, but is needed in order to determine resonance parameters for RRR measurements. Therefore, uncertainties on $R(t_t, E_n)$ are important for the evaluation process. Uncertainties are usually not given with resolution functions, so this needs to be addressed before typical values or bounds can be suggested. These values will be correlated between neutron energy points. The correlation can likely be represented with a Gaussian shape.

3.3.1.4 Background

The uncertainty on the background spectrum depends on the fitting method. In most cases the uncorrelated uncertainties have been combined with the other counting statistics, leaving the uncertainty on K. With a fixed saturated resonance filter, it is reasonable to have uncertainties down to 3%. If no information is given about the use of a saturated resonance, an uncertainty around 5% may be warranted. The uncertainty on K is fully correlated between different neutron energy data points.

3.3.1.5 Sample Characteristics

The uncertainty on the number density of the sample can be estimated based on the physical form of the sample. For example, metal samples tend to have lower uncertainties on number density than powder or liquid. Additional caution must be taken with powder samples, which can have an unknown amount of moisture and hard to model voids. The hydrogen in the absorbed water can have a large impact on the transmission and a correction must be made for this with power samples. This uncertainty is fully correlated between neutron energy data points.

The effective sample temperature, which is needed for Doppler broadening, is in many cases a negligible uncertainty. However, with liquid samples, it is not obvious how to calculate the effective temperature and the uncertainty on this quantity should not be neglected. No recommended value is given here because it may be negligible in many experiments.

3.3.1.6 Flux Normalization

The uncertainty in N_T is typically one of the smaller uncertainties in the transmission experiment. If cycling was used, it is reasonable to have uncertainties around 0.25%, as this uncertainty can be reduced with multiple runs. If cycling was not performed or there is no mention of it, the uncertainty should be much larger, around 3%. The uncertainty is fully correlated between neutron energy data points.

3.3.1.7 Fluctuation Correction

The uncertainty on F_T, the correction for cross section fluctuations in the URR, is not often given. These values are entirely simulated and rely on averaged resonance parameters, usually from evaluations. The nuclear data uncertainty should be included, as it is expected to dominate compared to the Monte Carlo statistics uncertainties. The uncertainties here will be highly dependent on the nucleus, and reasonable uncertainties should be estimated by the evaluator based on the state of the nuclear data at the time of the experiment. The uncertainties will be correlated in neutron energy, and can likely be represented by a strong Gaussian shaped correlation function as well.

3.3.2 Correlations Between Experiments

3.3.2.1 Counting Statistics

Counting statistics are uncorrelated between experiments.

3.3.2.2 Neutron Energy

The uncertainty of the neutron energy values or bins is likely to be highly correlated between experiments at the same facility, and weakly correlated between experiments the same type of facility. For experiments performed at different types of experiments or where characterization methods are different, the uncertainties can be assumed to be uncorrelated.

3.3.2.3 Resolution Function

The resolution function uncertainty will be highly correlated for experiments at the same facility, due to the fact that the resolution will either be the same (and then fully correlated) or will be mostly the same and have the same methods of determination. Some correlation will also be introduced by the use of the same simulation code. Further study on the uncertainties in the resolution function need to be undertaken before recommendations can be made for experiments at different facilities.

3.3.2.4 Background

K, the systematic uncertainty in the background, will be correlated between experiments using the same method and functional forms. Since most experiments use the same functional form, Equation 2.26, it is likely that this uncertainty is at least weakly correlated between most experiments. Stronger correlations can be assumed for experiments using the same saturated resonances.

3.3.2.5 Sample Characteristics

The number density of the sample, n, will be fully correlated between experiments using the same sample, and have a medium to high correlation for experiments using the same method/equipment for determining n. For experiments with different types of samples and different methods of measuring n, this correlation should be zero.

3.3.2.6 Flux Normalization

N_T values should be independent of each other for different experiments, even those at the same facility, as it is related to random fluctuations in the neutron beam.

3.3.2.7 Fluctuation Correction

F_T uncertainties will be highly correlated for experiments on the same isotope, with the exact strength based on the nuclear data used in each simulation. For different isotopes, one could assume a small correlation due to the method to determine the averaged parameters being the same.

Chapter 4

Experimental Uncertainties in Capture Cross Section Measurements

For neutron capture reactions, there are several experimental methods that are commonly used. In the resolved and unresolved resonance regions, Total Absorption Spectroscopy (TAS) and Total Energy Detection (TED) are the typical methods. For the thermal and fast energy regions, and for energy-averaged measurements in the resonance region, the methods of Activation Analysis (AA), Partial Gamma (PG) and Accelerator Mass Spectrometry (AMS) are used. These methods are explained in detail in Sections 2.2.2 through 2.2.6.

4.1 Evaluation Methods

Evaluation methods for neutron capture cross sections vary with incident neutron energy. In the Resolved Resonance Region (RRR) the parameters of each individual resonance are evaluated using R-Matrix theory [163][1]. The evaluation methods in the RRR and the Unresolved Resonance Region (URR) are similar for the total and capture reactions. As they are described in detail in Section 3.1, only a brief description will be given here. For neutron capture, the cross section is proportional to the product of Γ_n, representing neutron absorption, and Γ_γ, representing gamma emission,

$$\sigma_\gamma \propto \Gamma_n \Gamma_\gamma, \tag{4.1}$$

for each resonance. The full R-Matrix equations account for the effects of all resonances on the cross section at a particular neutron energy and the complicated interference between different resonances of the same spin group.

In a commonly used approximation, known as the Reich-Moore Approximation [173], it is assumed that the gamma widths for all resonances in a nucleus follow a chi-square

---

[1] New and recent evaluations use R-Matrix Theory, but many old evaluations were performed using the Multi-Level Breit-Wigner model.

distribution with enough degrees of freedom to allow for all widths to be represented by one averaged value, $\overline{\Gamma_\gamma}$,

$$\Gamma_\gamma(E_n) \approx \overline{\Gamma_\gamma}. \tag{4.2}$$

This assumption is valid for heavy nuclei with high level densities around S_n, but should be used with caution for lighter nuclei or those around shell closures. The experimental quantity, yield, is used to forward fit the resonance parameters. Initial guesses (usually an earlier evaluation, if it is available) are used to calculate a physical, zero-temperature cross section using R-Matrix theory. From there, Doppler-broadening is applied and the cross section is convoluted with the resolution function of the measurement, and an updating procedure is used to optimize the resonance parameters. The resolution function describes the neutron energy spectrum, the detector setup and the sample properties. For the URR, the experimental quantity is an energy-averaged cross section, and the evaluation procedure optimizes parameters such as $\overline{\Gamma_\gamma}$ and the average spacing between resonances. In most cases the total and capture cross sections are evaluated at the same time, given that they are dependent on almost the same quantities. From these two, the scattering cross section can be determined.

In the fast energy region, where the cross section is smooth due to overlapping resonances, predictive theory can be used. Hauser-Feshbach (HF) theory, which represents the energy-averaging of the cross section over multiple resonances in an energy window, describes cross sections as the competition between transmission coefficients. As explained in Section 3.1, the optical model can be used to calculate the cross section of neutron absorption or scattering of neutrons. The total cross section acts like a constraint on all of the reaction cross sections—scattering, capture, charged particle emission, etc. The relative transmission coefficients determine the cross section for each reaction.

Simple HF capture calculations only account for compound capture, and a separate calculation should be performed for the direct and semi-direct (DSD) capture mechanisms. The DSD capture cross section is typically negligible compared to compound capture up to neutron energies around 10 MeV, depending on the mass of the nucleus. Figure 4.1 shows an example CoH [79] calculation of the capture cross section for ^{181}Ta, with the contributions from compound, direct and semi-direct shown individually. It can be seen that the DSD component is needed to match the measured cross section at 14 MeV, based on the two data points [174, 175]. In the fast region, capture is usually a small component of the total cross section, so parameters in the scattering or fission cross section calculations can have significant effects on the capture cross section as well. For this reason, all of the reactions are usually evaluated together with the total cross section, in one calculation. The evaluations focus on reproducing the reactions that have experimental data. For reactions without any data points, the evaluation is physical and consistent with the other reactions, but not necessarily accurate.

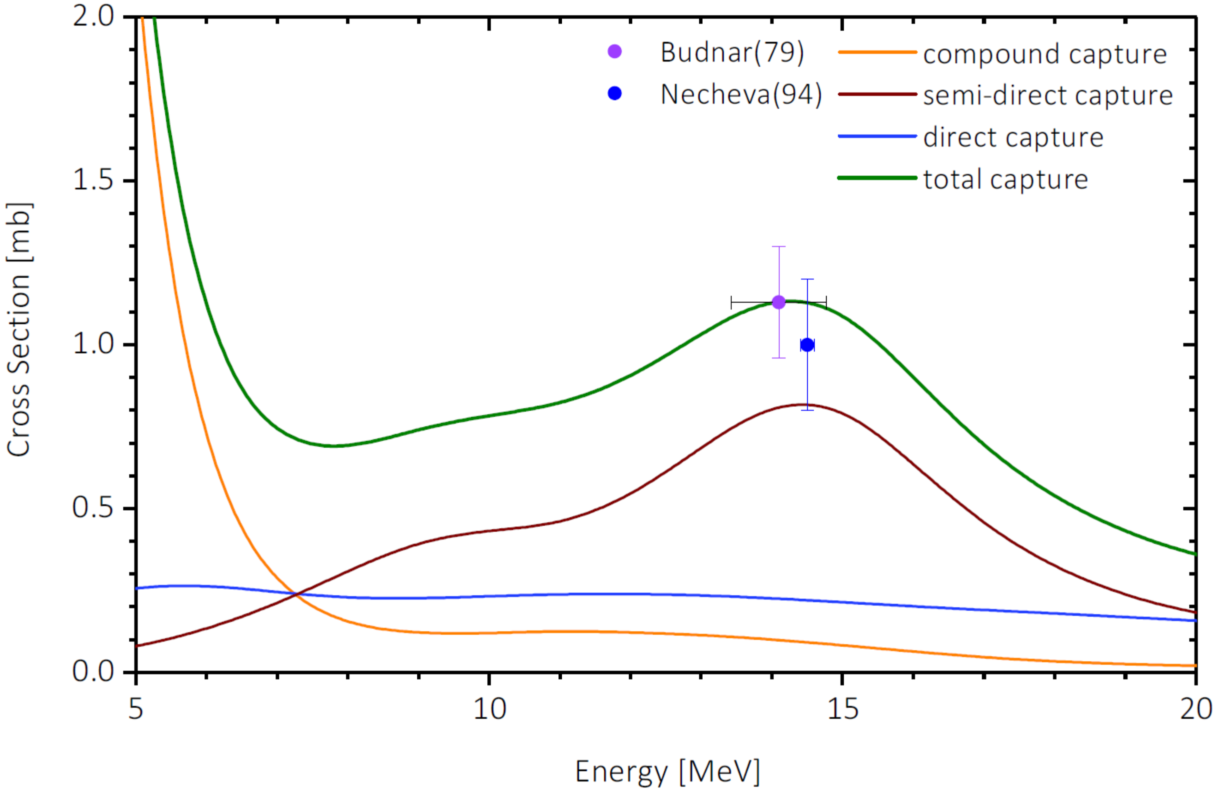

Figure 4.1: Capture cross section for ^{181}Ta above 5 MeV. The compound capture cross section is in orange. The two measured data points around 14 MeV can only be matched with the direct and semi-direct contributions included.

4.2 Information Needed for Evaluations

The values and uncertainties for the measured quantity, as well as the neutron energy values and their uncertainty and/or resolution values (δE_n or ΔE_n) are all that is necessary in most evaluations. In order to properly assess an experiment for missing uncertainties and apply the template, however, evaluators need some information about the experiment and how the analysis was performed.

The evaluator needs to know the measurement method that was used. The five methods that are focused on for this template are Total Absorption Spectroscopy (TAS), Total Energy Detection (TED), Partial Gamma Measurements (PG), Activation Analysis (AA), and Accelerator Mass Spectroscopy (AMS), which are explained in Section 2.2.

The method used to determine the flux should be provided. If the flux was determined using a reference cross section, the reaction(s) used and the source of the cross section data are valuable in the event that the evaluation is updated. If simulations were used to determine the flux, the simulation tools and nuclear data libraries used should be recorded. Additional information about the simulation is welcome, but are usually not provided. Fission chambers are dependent on evaluated fission cross sections, which are periodically updated. Neutron detectors are difficult to fully characterize, and it is important that the evaluator understand if the efficiency uncertainties are properly estimated. If the flux is measured directly (with neutron detectors), the type of detector and relevant partial uncertainties are important to record.

It should be indicated if additional normalizations, standards, or nuclear data are used. The source of the nuclear data (such as the library version, or a mass chain evaluation) should be provided, if the nuclear data values and uncertainties themselves are not. For TED measurements, the sample and the method for determining R_n (Equation 2.34) are needed if a scattering sample was used for the sample-dependent background. For AMS measurements, the isotopic standard used should be described, and the uncertainty on its composition recorded.

Information should be provided about the detectors used, including the type of detector and the calibration. The method used to calibrate the detector for energy and efficiency should be described. If calibration sources were used, the isotopes should be provided. Information on the activity uncertainty is welcome, as this can vary drastically and is not always easy to estimate. If the efficiency was based on interpolation from a fitted function, the function should be indicated for proper correlation analysis. If simulations were used to determine the efficiency, the simulation tool should be indicated. In addition, the method used to estimate the uncertainties on the simulation should be described. For measurements with lower resolution detectors, such as TAS and TED measurements, the efficiency is complicated and simulations often include characteristics of the gamma cascade, transport of the gammas, and the detector (or detector setup) absolute efficiency. The simulation tools and the efforts at uncertainty quantification are especially important in this case, as there are so many factors that enter these simulations. If discrete gammas were measured, the efficiency values and uncertainties at each gamma energy are helpful, but at least the efficiency uncertainties should be provided as relevant to each data point. If corrections were made for coincidence summing, the method for calculating the correction (and simplifying assumptions) can help the evaluator to determine if biases or larger uncertainties may exist.

The methods used to characterize, suppress, or subtract the background should be described. If possible, background uncertainties should be given for each data point, but in some cases an estimate of the overall background uncertainty can be provided for the whole experiment. The methods used will allow an evaluator to assess if all relevant backgrounds have been accounted for. Backgrounds can include room background (all methods), beam backgrounds (TAS, TED, PG), Compton backgrounds (PG, AA), peak contamination (PG, AA), and backgrounds attributable to room return neutrons[2] (all methods).

---

[2] Room return neutrons are neutrons that are scattered out of the experimental setup and then are scattered back into the detector. They can interact with the walls, floor, ceiling, or anything else in the room. In TOF measurements, room return neutrons have energies that are not correlated with the time of

Characteristics of the sample that are relevant to its uncertainties should be described. The sample mass, thickness, or areal density and its uncertainty are important as this is a fully correlated and usually significant uncertainty. The isotopic composition and its uncertainty should be provided as well, as this can affect some types of background. For Resonance Region measurements, more information is necessary to simulate the sample, including the phase (liquid, metal, powder, etc).

Multiple scattering and self-shielding corrections (or the neglect of such corrections) should be explained. These corrections are often determined by simulations that use evaluated nuclear data, and the source of the data is important for updating the results. The relative uncertainties on the multiple scattering correction values should be given, for each data point if possible. In addition, if the actual correction values are not provided, the approximate magnitude of the correction will allow the evaluator to assess if updating the correction with new evaluations is important.

The basic equations used for the analysis are useful for determining sensitives. If forward modeling was used for the majority of the analysis, some description of that process and the efforts at uncertainty propagation should be provided. This is often provided through a citation to earlier work, but in these cases a review of the equations is invaluable to the evaluation process. Small changes in the analysis process occurring gradually over time can lead to significant differences from an earlier reference.

For measurements involving decay (AA, and any experiment using AA for a flux standard), the various times (irradiation time, t_i, cooling or waiting time, t_w, and the counting time, t_c) and their uncertainties should be recorded. If the uncertainties are negligible and have been neglected in the uncertainty analysis, this fact should be indicated. Even with negligible uncertainties, the values for the times should still be provided for proper correlation analysis due to half-lives.

For Resolved Resonance Region measurements, all information needed for proper forward modeling should be provided. In practice this usually means the experimental yield and neutron energy values, the TOF length, the resolution function, the normalization and the sample characteristics, including the effective temperature of the sample. In addition, if there are transmission data available from the experiment, these should be included. The uncertainties on these quantities should be included as well, as they can be utilized in the generation of covariance for the evaluation [20]. Any additional information that can improve the simulation is welcome, and the methods to quantify the uncertainty on the resolution function should be described.

For the Unresolved Resonance Region measurements, the value of F_γ (Equation 2.37), and the method of calculation should be explained. If the correction has not been made and the quantity provided is the experimental yield, this should be made clear so that the evaluator (and compiler) are aware that the values are not cross sections.

---

their detection. In other measurements, their energies are not correlated with the source spectrum. These are especially impactful for fast region measurements on nuclei with large thermal cross sections. Even a relatively small flux of room return neutrons can create a significant background signal in this case.

Finally, if any other corrections were made to the data, they should be listed and their uncertainties provided. Relative uncertainties should be provided for: counting statistics, gamma absorption corrections, counting geometry corrections and irradiation geometry/beam overlap corrections, where applicable. For AMS specifically, the current and "reproducibility" uncertainties should be provided.

4.3 Template

This template can be used to determine if the uncertainties relevant to a capture measurement are realistic, and how to proceed if any are missing. For some uncertainties, the values can be estimated from Tables 4.1 and 4.2, but for many the evaluator will need to make an educated estimate based on the specific information. The descriptions in the template are provided to help guide the evaluator to quantify the missing uncertainties. There are some uncertainties that will be negligible in comparison to others and need not be included in the uncertainty analysis. These uncertainties, and the reason they are considered negligible, should be stated in the experimental write up to make it clear to the evaluator that they have not been forgotten. Recommended correlations are given as well, and summarized in Tables 4.3 and 4.4.

4.3.1 Uncertainties and Correlations Within an Experiment

4.3.1.1 Counting Statistics

Counting statistics should be given for each data point. The sample-in and background counting statistics can be combined. No values for counting statistics are given in the template, as they cannot be estimated for any given measurement. The use of a data set that does not provide counting statistics in some form is not recommended. Counting statistics are generally considered to be uncorrelated between data points.

4.3.1.2 Neutron Energy

The neutron energy uncertainty, δE_n and/or resolution, ΔE_n, is difficult to estimate from this type of table in a TOF measurement. The values depend on the neutron source, the flight path length and uncertainty, the timing resolution of the detectors, and the incident neutron energy. It is not recommended to estimate this uncertainty.

In the thermal region and MACS measurements, the neutron spectrum is designed around the neutron energy (sometimes represented as the temperature of a Maxwell-Boltzmann distribution). The uncertainty is therefore typically not applied to the neutron energy, but to the "thermal equivalent" flux, which is the flux within the specified energy region.

In the fast region, with defined energy points, the uncertainty and resolution depend on the neutron source and setup. Most of the reactions that are used to produce neutrons are

Table 4.1: Uncertainty template for resonance region measurements by the Total Absorption Spectroscopy (TAS) and Total Energy Detection (TED) methods. The values given are relative uncertainties on the parameter, and are all percents. The template uncertainties that cannot be estimated this way are: counting statistics, uncertainty on neutron energy and resolution, the multiple scattering correction in the URR and the normalization standard cross section uncertainty.

Uncertainty Source	TAS	TED
Flux normalization (N_γ) by internal resonance	1 - 2	1 - 2
Flux normalization (N_γ) by external resonance	2 - 6	2 - 6
Efficiency (same isotope or validated)	$\leq$2	$\leq$2
Efficiency (other)	$\geq$3	$\geq$3
Fit Background (k_γ or B)	$\leq$3	$\leq$3
Target isotope number/density (metal)	0.1 - 1	0.1 - 1
Target isotope number/density (powder)	2-5	2-5
Target isotope number/density (liquid)	2-5	2-5
Sample composition (stable, common isotope)	0.1 - 0.3	0.1 - 0.3
Sample composition (radioactive, common isotope)	1-2	1-2

well known, but the incident particle energy will usually alter the neutron spectrum, bringing a reasonable uncertainty up to around 1%.

The correlations between different neutron energy points should be Gaussian shaped, and strong, for most measurements.

4.3.1.3 Flux Values

The neutron flux uncertainty, $\delta\phi$, should be provided for each neutron energy and/or data point. In the fast and thermal regions, where well-known reference cross sections are often used to determine the flux, typical uncertainties are 2-5%. In the resonance region, the flux is also typically based on reference cross sections, but the uncertainty is usually accounted for by the uncertainty on the normalization factor, N_γ. Using a saturated resonance in the target isotope, the uncertainty on N_γ can in some cases be below 1%, but around 2% is more typical. If a saturated resonance in another isotope is used, the uncertainty on N_γ should be larger and dependent on the similarity between the gamma cascade characteristics

Table 4.2: Uncertainty template for thermal and fast region capture cross sections measured by Partial Gamma (PG), Activation Analysis (AA) and Accelerated Mass Spectrometry (AMS). The values are relative uncertainties, given in percent, on the parameter. The template uncertainties that cannot be estimated this way are: counting statistics and nuclear data. Uncertainties that are typically negligible (but should be noted) are geometry corrections, background fitting and decay data. Uncertainties that are not applicable to the measurement method are denoted with "—".

Uncertainty Source	PG	AA	AMS
Neutron energy	1	1	1
Neutron flux (reference reaction)	2-5	2-5	2-5
Neutron flux (API)	1	1	1
Neutron flux (direct)	≥ 3	≥ 3	≥ 3
Gamma detector efficiency (<0.2 MeV)	4	4	4
Gamma detector efficiency (0.2 - 2.6 MeV)	2	2	2
Gamma detector efficiency (>2.6 MeV)	5	5	5
Charged particle detector efficiency	—	2	—
Multiple scattering correction (thick, well-known)	2-5	2-5	2-5
Multiple scattering correction (thick, not well-known)	5-20	5-20	5-20
Target isotope number/density (metal)	0.1 - 1	0.1 - 1	—
Target isotope number/density (powder)	2-5	2-5	—
Target isotope number/density (liquid)	2-5	2-5	—
Sample composition (stable, common isotope)	0.1 - 0.3	0.1 - 0.3	0.1 - 0.3
Sample composition (radioactive, common isotope)	1-2	1-2	1-2
Sample composition (rare isotope)	—	—	3-5
AMS current	—	—	1
AMS "reproducibility"	—	—	1-3

Table 4.3: Recommended correlation shapes for the uncertainties in TAS and TED measurements. These correlations are between data points within a single experiment. Nuclear data correlations should be taken from, or based on, the reference.

Uncertainty Source	TAS	TED
Counting statistics	Uncorrelated	Uncorrelated
Neutron energy	Gaussian	Gaussian
Neutron flux	Gaussian	Gaussian
Efficiency	Gaussian	Gaussian
Multiple scattering in URR (F_γ)	Gaussian	Gaussian
Background	Gaussian	Gaussian
Target isotope number/density	Fully	Fully
Sample composition	Fully	Fully

of the two isotopes. If the reference isotope is very similar to the target, an uncertainty of 2-3% may be realistic. If the reference isotope has gamma characteristics that are different from the target isotope (for example, using ^{197}Au as a reference for a much lighter target) then the uncertainty on this normalization should be larger, even up to 5-6%. If the flux is measured directly using neutron detectors, the template values should be used with caution, as neutron detector efficiencies are typically several percent themselves. If an API generator is used, the flux is measured directly by the charged particle emitted from the reaction, and the flux uncertainty can reasonably be as low as 1%. However, incorrect characterization of the geometry of the charged particle detection setup can lead to biases in the measured flux. For thermal measurements, there should be some correction for epithermal neutrons, or the use of a “thermal equivalent” flux. This correction increases the otherwise low flux uncertainty that can be obtained at high flux, static neutron sources like reactors, and 2-5% is appropriate. A lower uncertainty can be estimated if it is clearly stated that the epithermal correction (and therefore uncertainty) was negligible. The correlation between flux values is recommended to be treated as Gaussian in neutron energy. If the information is available, the relative statistical uncertainties on the flux can help to determine the strength of the correlation.

Table 4.4: Recommended correlation shapes between data points of a single experiment for the uncertainties in PG, AA and AMS measurements. Nuclear data correlations should be taken from, or based on, the reference. Uncertainties that are not applicable to the measurement method are denoted with "—"

Uncertainty Source	PG	AA	AMS
Counting Statistics	Uncorrelated	Uncorrelated	Uncorrelated
Neutron energy	Gaussian	Gaussian	Gaussian
Neutron flux	Gaussian	Gaussian	Gaussian
Detector efficiency	Fully	Fully	—
Multiple scattering	Gaussian	Gaussian	Gaussian
Target isotope number/density	Fully	Fully (strongly if different)	Fully
Sample composition	Fully	Fully (strongly if different)	Fully
AMS current	—	—	Uncorrelated
AMS "reproducibility"	—	—	Fully

4.3.1.4 Efficiency

The detector efficiency depends on the type of detector and the energy of the measured particles or gammas. For gamma detectors, the absolute efficiency can be measured with calibration sources and solid angle calculations. For measurements of gammas between 200 keV and 2.6 MeV, typical uncertainty values are between 1 and 3%, and 2% is given in the template. Above 2.6 MeV, few commonly available calibration sources exist, and the calibration is either done with standards created in-house, simulations, or by extrapolating from the lower energy standards. Uncertainty values that are below 5% should be justified, and the uncertainty analysis described. If no uncertainty value is given, or the gamma energy regions are not distinguished, a 5% uncertainty is recommended in this region. Below 200 keV, the intrinsic efficiency of a typical HPGe detector reaches a maximum and begins to decrease with increasing gamma energy. If the experiment includes calibration sources that can constrain the peak of the efficiency curve and the lower energy portion, then 2% may be reasonable. However, if not enough information is given to confirm that the efficiency below 200 keV was sufficiently constrained, a 4% uncertainty is recommended. If coincidence summing corrections are mentioned or information about the setup indicates that corrections should have been performed, a larger uncertainty should be used for the efficiency. Coincidence summing can have a large effect, or can be negligible, so the evaluator is encouraged to use their knowledge of the reaction being measured to estimate an uncertainty. For charged particle detectors, the absolute efficiency uncertainty is based on how well the solid angle is known, and the magnitude of the correction for the lower level discriminator (LLD). Unless there are specific issues with the LLD, an efficiency uncertainty of 1 - 2% is reasonable. If no information is given, 2% is recommended. The correlations between different detector absolute efficiency values is based on the functional form used. If the form is not presented, or simulations were used, a Gaussian distribution is recommended.

For TAS and TED measurements, the efficiency uncertainty cannot be estimated as easily. This is due to the simulations of the cascade and gamma transport are included in the efficiency. For TAS measurements, this includes the correction factor for the cascades below the energy or multiplicity thresholds, and for TED, this includes the PHWT correction for the cascade properties. In both cases, the efficiency uncertainty can be quite small if the reference material is similar in cascade characteristics. The use of a saturated resonance in the target isotope can therefore bring the efficiency uncertainty down to below 2%. This is also the case when the simulated weighting functions or cascade simulations are validated by experiment. If a saturated resonance in another isotope is used, or no information is given, an uncertainty of at least 3% is recommended.

This uncertainty should be strongly correlated between different neutron energy data points. If it is indicated that different simulations or calculations were performed for different neutron energies/resonances, then a Gaussian shape is recommended.

4.3.1.5 Multiple Scattering Corrections

In the thermal region and in MACS measurements, multiple scattering does not usually present a problem, as the neutron energy resolution is broad.

In the Resolved Resonance Region (RRR), multiple scattering is not corrected for in the experimental analysis. The experimental quantity, yield (Equation 2.36), includes the effects of multiple scattering. During the forward fit of the evaluation, multiple scattering is modeled based on the resonance strength and the sample thickness.

In the Unresolved Resonance Region (URR), multiple scattering is corrected for in the calculation of the neutron-energy averaged cross section. This correction is done using Monte Carlo simulations of resonances based on the averaged parameters, explained in Section 2.2.3. The correction factor, F_γ, is usually not presented with an uncertainty, and the AGS framework does not include this uncertainty. More work should be done to establish estimates of this uncertainty, and the evaluator is advised to base their estimate on how well the resonance parameters of the target nucleus were known at the time of the experiment.

In the fast region, multiple scattering corrections are typically performed with simulations. The magnitude of the correction depends on the thickness of the sample, the energy of the neutrons and the scattering cross section of the target isotopes. These corrections should be done iteratively, as the measured cross section plays a role in the simulated correction factor. For thin samples, the correction is likely to be small and the uncertainty on the correction can be neglected. For thicker samples, the correction and its uncertainty is larger. The nuclear data involved in the simulation is likely the major source of uncertainty. If no uncertainty is given for a multiple scattering correction, the evaluator should estimate the uncertainty based on the state of the nuclear data at the time of the experiment. For a thick sample made of isotopes with well known scattering cross sections (for example, natural Fe) the uncertainty on the correction may be as low as a few percent. For a sample with isotopes that have (or had) less well-known scattering cross sections, an uncertainty of up to 20% on the correction may be warranted. If simple methods were used, a larger uncertainty should be assumed.

The multiple scattering correction uncertainty is likely to be strongly correlated between different neutron energy data points. A Gaussian shape is recommended, due to the nature of the simulations and use of nuclear data.

4.3.1.6 Background Corrections

For TAS and TED measurements, the background is represented by a function, Equation 2.32, that accounts for the time-independent background, the time-dependent beam background, and the sample-dependent background. The background is typically measured with a saturated resonance and a scattering sample, and together the uncertainties can be below 3%. A value of 3% is recommended if no information is given for an experiment. The correlations between different neutron energies should be supplied with the experimental data, as the background is based on a fit to a functional form. If no correlations are given, a strong Gaussian correlation is recommended.

For PG and AA measurements, the background is the counts below the gamma ray photopeak in the HPGe spectrum. The characterization of the time-independent backgrounds for each is straightforward. The in-beam measurements PG also have time-dependent backgrounds. The characterization of the beam and Compton backgrounds can be more complicated, and background due to contamination gamma rays (explained in Section 2.2.4) can lead to large bias if not corrected, with large uncertainties on the correction. Similarly for AA measurements, contamination in the spectrum peak can create large biases that cannot be predicted generally. In both PG and AA measurements, there is often no background uncertainty presented, as it is determined in the peak fitting process and is included in the count uncertainty. This should be avoided, as it will often induce correlations between the counting uncertainty, due to the consistent background subtraction method and the possibility of the degradation of the detector affecting the peak shape. No specific background uncertainties are recommended for these measurements, due to the strong variations between experiments and the inclusion in counting uncertainties.

For AMS measurements, the background consists of isobars that follow the same trajectory as the isotope being measured. The background is suppressed by the use of filters and magnets along the trajectory. Blank samples can be used to measure and subtract out any background that is not suppressed. Uncertainties on the background are typically not provided for AMS measurements, which is likely due to the uncertainty being negligible relative to the other uncertainties.

4.3.1.7 Sample Mass or Areal Density

The uncertainty in the number of target atoms can be presented as a combination of the target mass, density, number density or thickness, depending on the relative size of the sample and the neutron beam. This value will depend on the physical form of the sample (metal, liquid, or powder). For metal samples, uncertainties between 0.1 and 1% are common. For liquid and power samples, a larger uncertainty of 2 - 5% is expected. In the case where one sample is used for all data points, this uncertainty is fully correlated between data points. For certain fast region measurements, different samples are used for different neutron energies and the correlations then depend on the creation and characterization of the samples. If no information is given, it should be assumed that the characterization was done with the same equipment and a strong, constant correlation is recommended.

4.3.1.8 Sample Isotopic Composition

The uncertainty on the composition of the sample is dependent on whether the isotope of interest is stable or radioactive and whether it is a common isotope or a rare isotope. If a sample is natural abundance, the literature values and uncertainties should be used. If the sample is enriched, but the isotope is relatively common and stable, the isotopic composition uncertainty can be between 0.1 and 0.3%. If the sample is enriched in a common but radioactive isotope, the uncertainty is usually around 1 - 2%. For samples that are enriched in rare isotopes (for AMS measurements), the composition uncertainty is around 3 - 5%. If one sample is used for all data points, this uncertainty is fully correlated. As with the mass uncertainty, if no information is given, a strong, constant correlation is recommended.

4.3.1.9 Nuclear Data

The uncertainty on the nuclear data used in the measurement (both reaction and structure data) should not be estimated generally. If a reference is given for the data, any uncertainties given in that library should be adopted, or modified/estimated with hindsight. If no reference is given, the year of publication should be used to guess the library used. The correlations should be taken from, or estimated based on, the source of the data.

4.3.1.10 AMS Current and “Reproducibility Factor”

The current in AMS measurements represents the number of the “common” isotope. The uncertainties are low, due to the high statistics that can easily be obtained with the common isotope, and can be less than 1% at times. If no information is given, an uncertainty of 1% is recommended. Often a single uncertainty is given for the measurement, which is fully correlated between data points.

The AMS "reproducibility" value is an uncertainty representing non-statistical fluctuations in the AMS system, and is typically 1-3%. This uncertainty is fully correlated between neutron energy data points.

4.3.1.11 Uncertainties That are Often Negligible

If low energy gammas are being measured, a correction for gamma attenuation in the sample may be necessary. In some cases, such as TAS and TED measurements, this is included the simulations of gamma cascades and transport. For PG and AA measurements, the correction can be calculated with gamma attenuation coefficients. The attenuation coefficients are typically well known, and though the correction may become large, the uncertainty on the correction is typically better than 1%. However, a complicated or poorly modeled geometry can introduce larger uncertainties in the attenuation correction. This uncertainty is fully correlated between different neutron energy data points, if the same gammas are used. A strong Gaussian correlation is recommended between different gamma energies.

A counting geometry correction may be necessary in PG and AA measurements if the size and shape of the sample are different than the calibration standards. This correction may be included in the efficiency uncertainty. There is no recommended value for this uncertainty, as it is highly dependent on the counting setup and is in many cases negligible. If there is a counting geometry uncertainty, it is fully correlated between neutron energy data points.

A sample-beam overlap correction may be necessary if the sample is not fully overfilled or underfilled. No recommendation is given for this uncertainty, as it will be negligible in most experiments. If it is not negligible, it is fully correlated between neutron energy data points.

The beam fluctuation correction, applied in AA measurements where the half-life of the product is comparable to the irradiation time, is another uncertainty that is usually negligible. No recommendation is given for this uncertainty, but if it is given, it is likely to be full correlated between neutron energy data points.

The uncertainties on the recorded times in the experiment (such as the irradiation time, and the counting time in AA) are usually negligible compared to other uncertainties. No recommendations are given for timing uncertainties. If they are given, they are independent of each other, but likely fully correlated between neutron energy data points.

Gamma angular distribution corrections are sometimes necessary in PG and AA measurements. The correction is made based on the multipolarity of the transition, so the correction will be biased if this is not well established. If no correction was performed and the distribution was assumed to be isotropic, an appropriate uncertainty should be determined based on the multipolarity. This uncertainty is dependent on the transition that is being measured, so no general recommendation is given here. Between neutron energy data points, this uncertainty is fully correlated, due to the fact that the same gammas are measured at each neutron energy.

4.3.2 Correlations Between Experiments

4.3.2.1 Counting Statistics

Counting statistics are uncorrelated between experiments.

4.3.2.2 Neutron Energy

The neutron energy uncertainty and resolution are strongly correlated between experiments using the same neutron source. They are not typically fully correlated, unless the experiments were run at the same time, or otherwise used the exact same neutron energy values and uncertainties. The uncertainties are likely to have a moderate correlation between experiments run with the same type of neutron source, as the methods of characterizing the energy are limited. Two experiments that used the same reference cross section for the energy spectrum determination are moderately correlated. The uncertainties are likely to be uncorrelated between experiments that used different neutron source types and different characterization methods. A weak correlation is possible for different neutron sources characterized in the same way.

4.3.2.3 Flux Values

The flux uncertainties are strongly correlated between experiments at the same facility, unless it is clear that different methods of flux characterization were used for the two measurements. If reference materials were used to determine the flux in both cases, the similar method and equipment will impart a moderate correlation. For experiments performed at different facilities, similar methods will lead to weak correlations. The flux values can be assumed to be uncorrelated for facilities with different neutron sources and different methods of characterization.

4.3.2.4 Efficiency

If the experiments were performed at the same facility using the same detectors, the efficiency uncertainty values will be strongly correlated. Efficiencies determined by the same method and same simulation codes will be correlated, even if they are at different facilities, based on the nuclear data used in the simulations. Efficiencies that are measured with calibration sources will have a weak correlation with other experiments that used the same functional form or method.

4.3.2.5 Multiple Scattering Corrections

Multiple scattering corrections are usually determined by simulations, so the recommendation for the correlations between experiments is similar to the simulated detector efficiency. If the same codes and/or nuclear data are used to calculate the correction, then a strong correlation should be used. If the experiments were performed at the same facility, strong correlations should be assumed unless information from the authors indicates that different methods were used.

In the URR, the uncertainty on F_γ is highly correlated between experiments measuring the same reaction, due to the method used to determine the correction.

4.3.2.6 Background Corrections

In TAS and TED measurements, background corrections are likely moderately correlated between experiments at the same type of facility, unless it is clear that different methods and/or different functional forms are used.

For PG, AA and AMS experiments, there is no recommended correlation as the background uncertainty is typically not split out for these measurements.

4.3.2.7 Sample Mass or Areal Density

Correlations between experiments for the sample mass/number of nuclei uncertainties depend on the method of characterization of the sample. Experiments done at the same facility are likely to have used the same methods and equipment for this purpose, and so can be assumed to have a moderate correlation if no information is given. Weak correlations can be assumed between experiments at different facilities if the same methods were used.

4.3.2.8 Sample Isotopic Composition

The sample composition correlations are much the same as though for the sample mass/number of nuclei. If the methods are similar, correlations exist and may be moderate if the experiments were at the same facility.

4.3.2.9 Nuclear Data

The correlations for uncertainties on any nuclear data used should be taken from, or estimated based on, the sources of the nuclear data.

4.3.2.10 AMS Current and “Reproducibility Factor”

Uncertainty in the current measurement is uncorrelated between different experiments. The “reproducibility” value is fully correlated between experiments that used the same value, which is likely to be most experiments at the same facility. At different facilities, the value is likely to be weakly correlated due to the methods of determination.

4.3.2.11 Uncertainties That are Often Negligible

For the gamma absorption correction, moderate correlations should be assumed between different experiments. If it is clear that different gamma attenuation coefficient data or different correction methods were used, then the correlations may be weaker.

Counting geometry correction correlations may be strong if the experiments were at the same facility and the same method was used. Experiments at different facilities can be assumed to have weak or zero correlations for this uncertainty.

The uncertainty in the sample-beam overlap correction should be strongly correlated between experiments at the same facility. If the experiments were performed at different facilities, a weak correlation or no correlation can be assumed.

Beam fluctuation correction uncertainties are likely to be weakly correlated between experiments at the same facility, as the same methods were used. Weak or no correlations can be assumed at different facilities.

Uncertainties on times are generally uncorrelated to each other, and so can be considered uncorrelated between different experiments, even at the same facility.

The uncertainty in the gamma angular corrections for a specific transition are likely to be strongly correlated if the same assumptions were made (such as isotropic). If two experiments used different transitions in their analysis, the correlations will be weak (if they use the same methods to correct the different transitions) or zero (if they used different methods).

Chapter 5

Experimental Uncertainties in EXFOR

There is a push within the field of nuclear data towards more reproducible, transparent and regulated methods in evaluations [176–178], and the templates of expected uncertainties (previously published [160, 161], and presented in Chapters 3 and 4) are beneficial to this goal. The templates allow for fair comparison of data sets with different degrees of uncertainty analysis. Newer data sets tend to have uncertainties that are based on more stringent analysis methods. Many older data sets have more neglected, forgotten, or simply not reported sources of uncertainty.

However, even within the templates, there are still remnants of older, less transparent methods. The templates are created based on "expert judgment"—an oft-used but undefinable reference for knowledge in the field of nuclear data. One solution to make the template creation more transparent is to do a large-scale literature search of the uncertainties presented in reaction experiments, and base the template values on those.

The use of published literature values for partial uncertainties, rather than "expert judgment" by the evaluator, helps to minimize the bias of the evaluator. It also improves the ability of the templates to put experiments on the same level—one of the main uses of the template is to fill in missing uncertainties in a realistic way so that the weighting of experiments is realistic. Uncertainties that are systematically underestimated in the literature will be underestimated in the template as well. While this limits the usefulness of the templates for studying true uncertainties, it ensures that the relative weights on different experiments will be more accurate. A full study of whether the uncertainty values given in EXFOR are representative of true uncertainties is well beyond the scope of this work, and should be undertaken by a group with expertise both in running experiments and in evaluating data sets.

However, an uncertainty template created entirely by distributions of literature values has drawbacks as well. The minimization of the bias of the evaluator is offset by the magnification of the bias of the experimentalist, which can be just as strong. After all, another purpose of the templates is to check that the given uncertainty values are realistic [160, 161]. Certain assumptions or methods used by a single group can end up being overly influential, due to the fact that uncertainties defined for an experiment have a tendency to be used again for later experiments at the same facility or by the same group. Groups that are prolific and include detailed uncertainty analysis in their papers will end up contributing more uncertainty values to the distributions than others, and may have undue influence on the template values. This could be remedied by removing "repeat" uncertainties, but determining which to remove is not a straightforward process. There also might be similar correlations between uncertainties from experiments at different facilities, as well. A detailed uncertainty analysis written in a paper will surely influence the thought process and data analysis of other groups. It is important to keep in mind that evaluators will also be highly influenced by these prolific groups and detailed papers. Finally, there is an issue that the full uncertainty analysis and partial uncertainty values are often not reported. While recent experimental papers usually include some information, many older papers included no uncertainty analysis beyond the statistical uncertainties, such as Reference [179]. For some papers, information is given about sources were included in the total uncertainty, but not always an exhaustive list, and without the relative contributions, such as in Reference [180]. Total uncertainties that are reported without the partial uncertainties quantified cannot be used in the templates, so this information has been lost. The literature values that can be used are limited to those that are detailed.

5.1 EXFOR Uncertainty Documentation

The EXFOR database [13] is a large compilation of reaction measurements. A lot of information about the experimental measurements is included in the EXFOR compilation, including the uncertainties. In this work, the EXFOR database was used for the large-scale literature search of uncertainty values.

The EXFOR format, which is described in detail in Reference [181], attempts to capture the metadata on the experiment. This includes the facility, the experimental methods, the detectors used, and much more. There is a dedicated keyword for uncertainties as well—`ERR-ANALYS`. The error analysis section for EXFOR entry 13176 is shown in Figure 5.1 as an example of an entry that provides information that is valuable for the templates. The uncertainties are each given a number, which is used to identify the uncertainties if they are listed later in a table. There are some uncertainties that are given with a single uncertainty value, like the ^{47}Ti isotopic abundance uncertainty of 1.4%. It can be assumed from this that all data points share this uncertainty. Others, like the fission deposit thickness, have ranges of uncertainty values. The compilation of the uncertainty as a range results in the loss of information. It cannot be determined from this entry if the uncertainty could not be quantified to any better precision, if there were several fission foils with quantified uncertainties that all fell between 0.2 and 0.9%, for example. In addition, it is not clear from this recording how to apply this uncertainty to the different data points, as it is not specified if this uncertainty changes with neutron energy. Others, like "Calibration procedure", are

```
ERR-ANALYS (ERR-T) Total uncertainty                   (5.2-12.7%)
            includes the following sources:
           (ERR-1,2.1,10.7) All random components       (2.1-10.7%)
           (ERR-2,1.1,2.0)  Fission deposit mass         (1.1-2.0%)
             Deposit Rel.Std.Dev.  Correlation matrix
              U-235     1.1%         1.00
              U-238     2.0%         0.55    1.00
           (ERR-3,0.2,0.4)  Sample Ti content            (0.2-0.4%)
           (ERR-4,0.2,0.9)  Fission deposit thickness
                            correction                  (0.2-0.9%)
           (ERR-5,0.0,0.4)  Low energy neutron fission  (0.0-0.4%)
           (ERR-6,1.7,4.7)  Calibration procedure       (1.7-4.7%)
           (ERR-7)          47Ti isotopic abundance         (1.4%)
           (ERR-8)          47Sc decay scheme               (1.0%)
           (ERR-9)          Neutron source effects          (2.0%)
           (ERR-10,1.0,1.5) Neutron absorption and scattering
                                                        (1.0-1.5%)
           (ERR-11)         Sample and uranium deposit solid angle
                                                            (1.5%)
           (ERR-12,0.4,5.7) Neutron energy scale definition
                                                        (0.4-5.7%)
           (MONIT-ERR)      Monitor cross section uncertainty
```

Figure 5.1: Example of the `ERR-ANALYS` section of EXFOR entry 13176. Many uncertainty sources are listed, and each is given an identifying number. For some uncertainties, a single value is given, such as the 1.4% uncertainty on the ^{47}Ti isotopic abundance. For others, a range of values is given, such as the 0.2-0.9% uncertainty for the fission deposit thickness.

not specific and could apply to a calibration of the neutron source energy or flux, or the detector energy or efficiency.

There are other examples of EXFOR entries that do not include all of the information given in the journal article, such as EXFOR entry 30484, based on Reference [182], and EXFOR entry 10513, based on Reference [183]. The use of EXFOR to conduct this large-scale literature review therefore limits the completeness of a final template, but at the same time, makes the process feasible. EXFOR contains data from over 20,000 experiments, and the only alternative for the literature search of the same scale would be to collect and read all of the journal articles, conference proceedings and internal reports that the information came from.

The template presented in this chapter is based on two specific experiment types, Partial Gamma Measurements (described in Section 2.2.4) and Activation Analysis (described in Section 2.2.5), so the initial EXFOR search focused on compilations of those experiments. In the future, distributions of the uncertainties presented in the whole of the EXFOR database

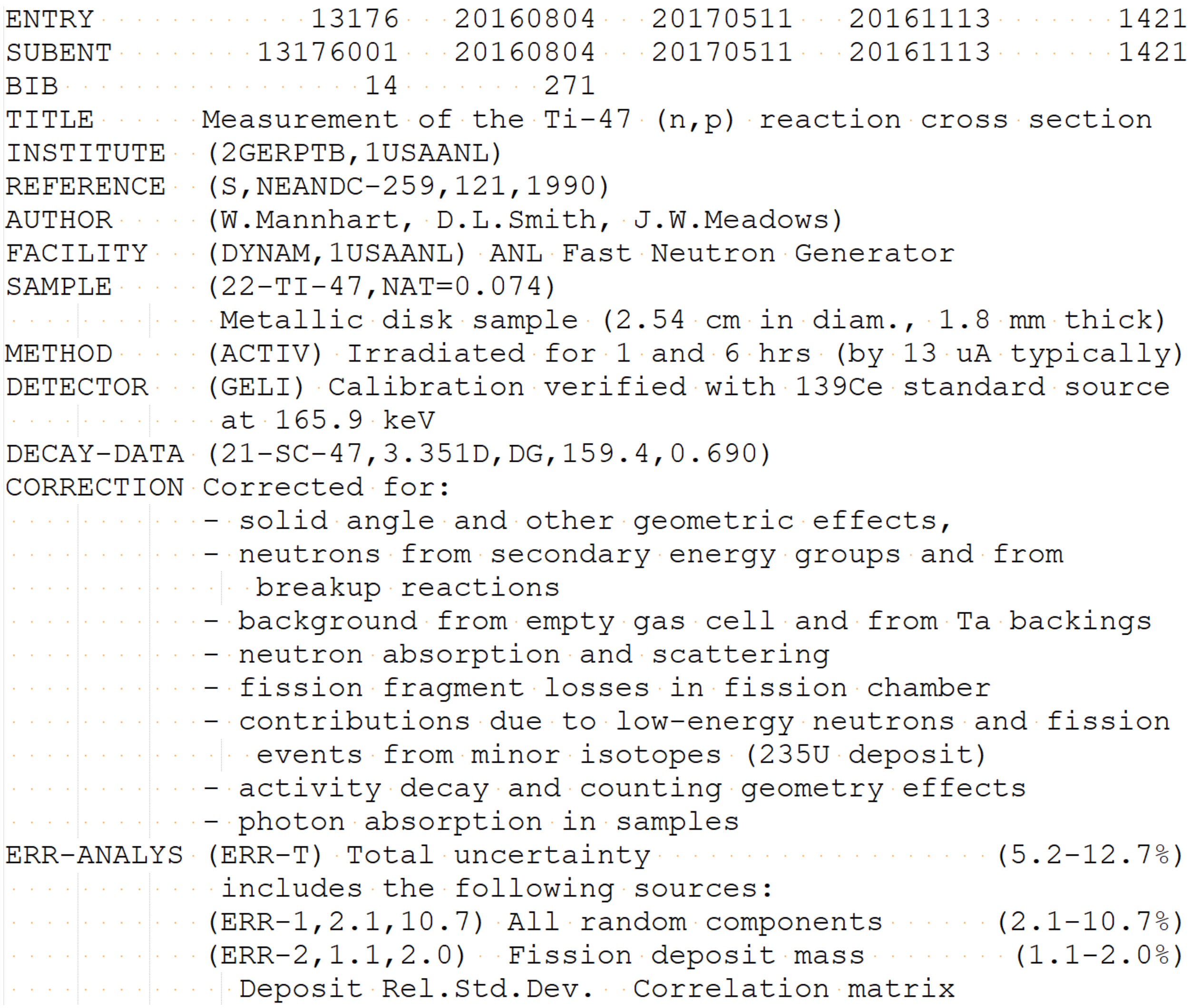

```
ENTRY            13176   20160804   20170511   20161113       1421
SUBENT        13176001   20160804   20170511   20161113       1421
BIB                 14        271
TITLE      Measurement of the Ti-47 (n,p) reaction cross section
INSTITUTE  (2GERPTB,1USAANL)
REFERENCE  (S,NEANDC-259,121,1990)
AUTHOR     (W.Mannhart, D.L.Smith, J.W.Meadows)
FACILITY   (DYNAM,1USAANL) ANL Fast Neutron Generator
SAMPLE     (22-TI-47,NAT=0.074)
            Metallic disk sample (2.54 cm in diam., 1.8 mm thick)
METHOD     (ACTIV) Irradiated for 1 and 6 hrs (by 13 uA typically)
DETECTOR   (GELI) Calibration verified with 139Ce standard source
            at 165.9 keV
DECAY-DATA (21-SC-47,3.351D,DG,159.4,0.690)
CORRECTION Corrected for:
           - solid angle and other geometric effects,
           - neutrons from secondary energy groups and from
              breakup reactions
           - background from empty gas cell and from Ta backings
           - neutron absorption and scattering
           - fission fragment losses in fission chamber
           - contributions due to low-energy neutrons and fission
              events from minor isotopes (235U deposit)
           - activity decay and counting geometry effects
           - photon absorption in samples
ERR-ANALYS (ERR-T) Total uncertainty                   (5.2-12.7%)
            includes the following sources:
           (ERR-1,2.1,10.7) All random components      (2.1-10.7%)
           (ERR-2,1.1,2.0)  Fission deposit mass        (1.1-2.0%)
             Deposit Rel.Std.Dev.  Correlation matrix
```

Figure 5.2: The beginning of EXFOR entry 13176. Some of the information is machine-readable, such as the institute, facility, method type, and detector type. Other information is free-form, and must be interpreted as natural language, including the sample information, the corrections and the details on the method and detector.

will be compiled, but that monumental task has not yet been completed.

The collected EXFOR entries were parsed with a highly interactive script, which read in the machine-readable sections of the entries. The beginning of EXFOR entry 13176 is shown in Figure 5.2. There is machine-readable information in the entry, such as the type of method and type of detector, and both the facility type and location. Other information that is important for understanding the experiment, however, is stored in free-form sections. This includes the corrections that were made, the sample information, the information about the method and detector, and as can be seen in Figure 5.1, all of the uncertainty information.

The interactive script, after parsing the fixed-format sections, prints the error analysis section in its entirety to the screen. The user can then choose to input uncertainty values, or move on to the next entry if there is no information on systematic uncertainties. If the user chooses to enter uncertainty values, the interactive script then prints other free-form sections and prompts the user to enter information on the type of uncertainty and the metadata that is relevant. For example, for the ^{47}Ti isotopic abundance uncertainty, the relevant information is the type of sample (metallic disk), the target mass (47) and whether or not the target is radioactive. The interactive script that was used to extract uncertainty values is given in Appendix A.

There is still some judgment required in this process. In this example, the uncertainty source "calibration procedure" would have to be interpreted. It most likely relates to the detector, which is a Ge(Li) gamma detector, and the fact that the uncertainty is a few percent points to it being the efficiency calibration, not the energy calibration. This process requires some understanding of the experiments and the expected uncertainties, and does include human bias just like the previous templates.

5.2 EXFOR Uncertainty Distributions

Two experiment types were chosen for this template—Partial Gamma (PG) measurements and Activation Analysis (AA) measurements. The details of PG measurements are given in Section 2.2.4, and of AA measurements in Section 2.2.5. A template for all capture cross section measurement types, created by "expert judgment", is presented in Chapter 4. These two measurement types were chosen for the first example of using literature values to construct uncertainty template due to their similarity with each other, and their concise set of experimental uncertainties. The most common corrections that are based on models, for example multiple scattering and gamma cascade characteristics, are usually not big factors in these experiments[1], so the template is focused on experimental uncertainties that are more likely to be recorded in EXFOR.

The EXFOR entries used to create the distributions are listed in Appendix B. The `R` function `ecdf` was used (through the `Python` package `rpy2` [184]) to create empirical cumulative distribution functions from the given uncertainty values. The median value of the distribution for each source is given in the tables below, with the number of values found in parentheses. The median values were chosen over the mean values, as the median is a better estimate for a skewed distribution. These distributions are bounded by zero, so any large uncertainty values have an overly large effect on the mean. In the case where an evaluator is analyzing an experiment of this type, the distributions can be used to check if each uncertainty value given is unusually high or low compared to other experiments, and the template can be used to fill in values that are neglected by the author. These distributions, of course, can only be used to check if the uncertainties given for an experiment are in line

---

[1] Gamma cascade calculations are used to convert PG measurements into cross sections, but are not necessary to determine the actual experimental quantity, which is the cross section of the discrete gammas.

with other experiments, not whether or not the uncertainty value itself is actually realistic. Some uncertainties will be neutron-energy dependent, based on the experiment setup. If it is clear to the evaluator that an uncertainty that is not given should be energy dependent, the simple median value in this template should not be used. Rather, the evaluator should use any information available (from the experimental paper, conversations with the author, other papers that discuss the same facility, etc) to better estimate the uncertainties.

The median values are presented in Tables 5.1 through 5.3 and the distributions are presented in the following sections. Short descriptions of the uncertainties are given as well, and more details can be found in Sections 2.2.4 and 2.2.5, and Chapter 4. All uncertainties are given relative to the uncertainty source, as a percent of the quantity.

5.2.1 Sample Uncertainties

Table 5.1: Median values for relative uncertainty (in percent) for sample uncertainty sources. The numbers given in parentheses are the number of EXFOR uncertainty values found.

Sample type	Mass (m)	Isotopic Abundance (w)	Self-Absorption (ξ)
Stable Metal	0.3 (21)	0.2 (10)	0.7 (17)

The uncertainties related to the samples are on the sample mass, δm, isotopic composition, δw, and the correction for the self-absorption of gammas, $\delta \xi$. The distributions are presented in Figures 5.3 through 5.5. The methods of measuring the mass and isotopic composition of metal samples are the same for foil and disk samples so the uncertainties associated are also the same. If the abundance uncertainty is not given but the sample is known to be natural, the uncertainty can be found in isotopic composition compilations such as Reference [185]. The correction for gamma absorption is a function of the sample dimensions, gamma energy and the attenuation data, and is usually calculated or simulated. For low energy gammas, this correction can be quite large and highly dependent on the sample geometry, so it is important to understand. While the magnitude of the correction itself will vary for different types of samples, the method of calculation, and therefore the associated uncertainties, should be comparable. For this reason, all metal samples made of stable, abundant materials have been grouped into a single category called "Stable Metal". This distribution does not apply to samples that are radioactive or are not metal, as these sample types usually have different measurement methods.

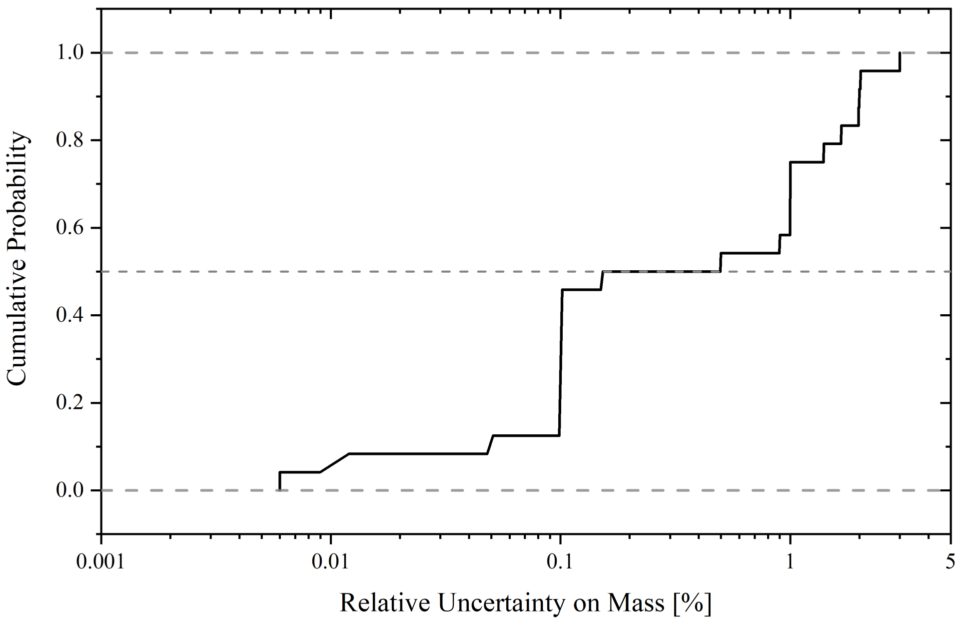

Figure 5.3: Cumulative distribution function of the 21 uncertainty values on the mass of a stable metal sample.

5.2.2 Detector Uncertainties

Table 5.2: Median values for relative uncertainty (in percent) for detectors

Detector type	Efficiency (ε)
HPGe	2.0 (23)
Ge(Li)	2.0 (28)
NaI	3.0 (7)

The only gamma detector uncertainty studied here is the detector photo-peak efficiency, $\delta\varepsilon$. Two other uncertainties, the deadtime correction factor, $\delta\tau$, and the counts, δC, cannot be estimated based on the experimental setup. The efficiency of a gamma detector is experimentally determined by measuring well-characterized calibration sources. The inherent uncertainties come from the activity of the calibration sources, the fractional feeding intensity of the gammas in the decays, the half-lives of the calibration sources, and the counts recorded. The efficiency is measured at several different gamma energies, and then fit to a

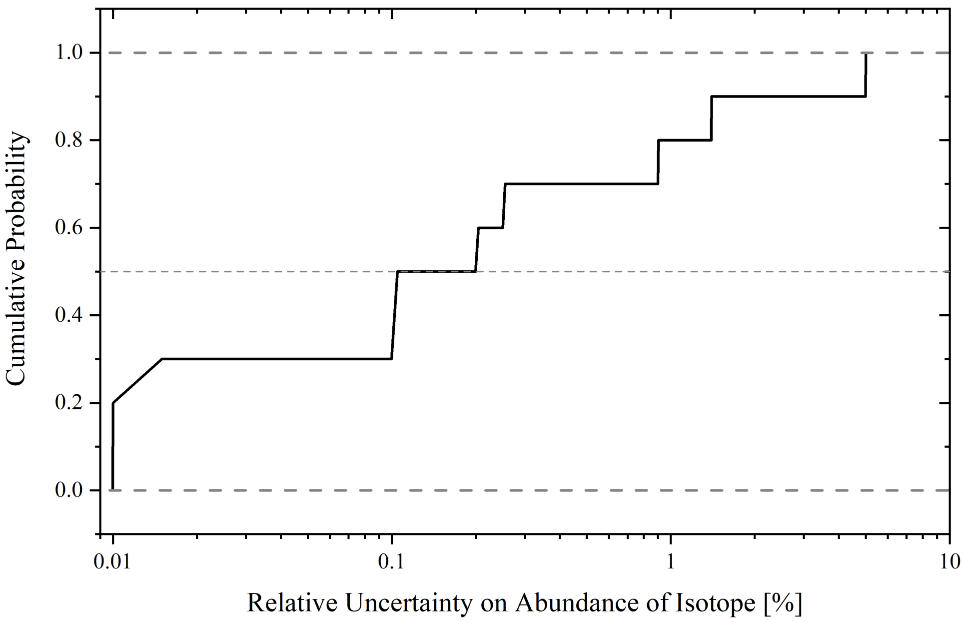

Figure 5.4: Cumulative distribution function of the 10 uncertainty values on abundance of the target isotope in a metal sample.

curve that is used for interpolation. If the detector is Compton-suppressed, which means that other detectors close by are used for coincidence rejection of scattered photons, then there will be additional uncertainty. The detector efficiency should be measured with the detector in the setup that it will be used in for the experiment. The method used is the same for all three types of detectors, HPGe, Ge(Li) and NaI crystals, and so the distributions of the uncertainty values are similar, as can be seen in Figure 5.6.

5.2.3 Neutron Source Uncertainties

The neutron sources were categorized by the method of neutron production and measurement. The categories are Associated Particle measurements, Gas Target generators (D-D, D-T and p-^{7}Li are all included), Solid Target generators (D-D, D-T and p-^{7}Li are all included) and White Sources. The neutron sources were categorized this way to reflect physically meaningful differences in the production and measurement of the neutron flux. For example, in Associated Particle measurements, the charged particle created by the neutron production reaction is measured in order to determine the flux. The solid and gas targets are separated out because the state of the target can influence the energy spectrum of the outgoing neutrons. The white source measurements require measurement of the flux, and

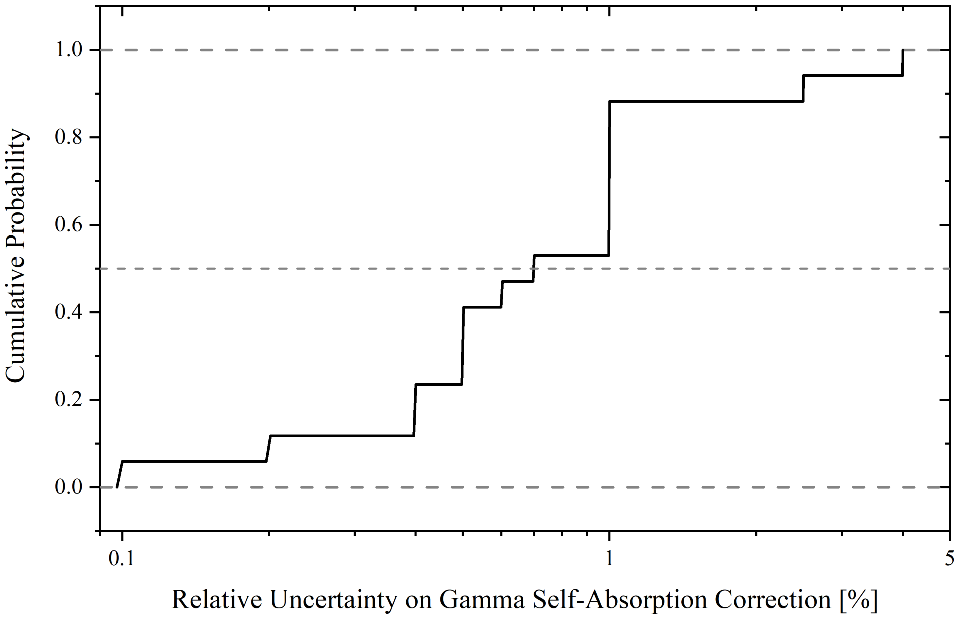

Figure 5.5: Cumulative distribution function of the 17 uncertainty values on the correction for the absorption of gammas by a thin metal sample.

Table 5.3: Median values for uncertainty (in percent) for neutron sources

Source type	Flux (ϕ)	Energy (E_n)	Resolution
Associated Particle	1.0 (8)	1.3 (87)	0.7 (10)
Gas Target Generator	3.0 (9)	1.0 (9)	2.3 (6)
Solid Target Generator	2.6 (18)	0.7 (26)	1.7 (11)
White Source	2.0 (28)	2.9 (22)	5.7 (20)

a combination of measurement and modeling to determine the neutron energy. The uncertainties related to the source of neutrons are on the flux, $\delta\phi$, the neutron energy, δE_n and the neutron energy resolution, ΔE_n.

The uncertainty on the flux, $\delta\phi$, is dependent on the method used to determine the flux, which may be done by directly measuring it with neutron detectors, modeling it with transport codes or calculating it using monitor reactions. All three sources have their own inherent uncertainties. In the case of the monitor reaction, it is possible to deconstruct the flux calculation and use the same uncertainty sources as for the reaction itself. In the

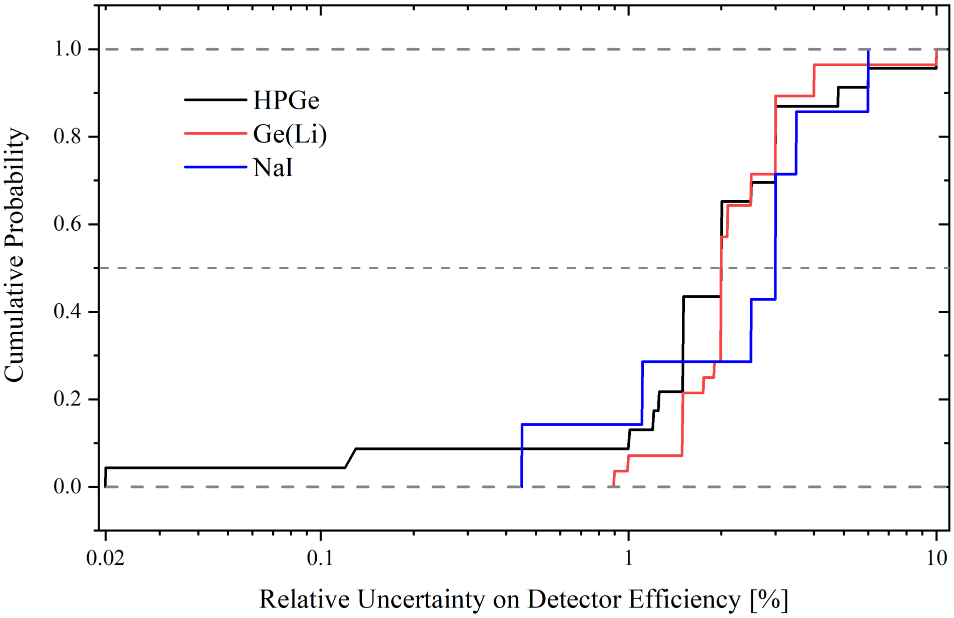

Figure 5.6: Cumulative distribution function of the uncertainty values on the correction for the efficiency of the gamma detector. There are 23 values for HPGe, 28 values for Ge(Li) and 7 values for NaI.

case of direct measurement or modeling, the flux uncertainty is more complex and when the uncertainty is not provided the distribution of values found in EXFOR, shown in Figure 5.7, can be used.

The uncertainty on the energy of the neutrons, δE_n, is important when comparing how well a reaction calculation matches experimental data. It can be converted into an uncertainty on the cross section when the experimental values are being averaged together or an optimization algorithm is used to find the best fit to the data. The uncertainty on the energy of the neutron is given here for all neutron source types, but this distribution should be used with caution for the White Sources. The uncertainty is highly dependent on the flight path length and the neutron energy, and can in most cases be estimated from information about the facility and flight path used for that measurement, rather than from this distribution.

The resolution of the neutron source, ΔE_n, is not directly used in the calculation of the uncertainty on the cross section, but is important to understand. A source with a broad resolution will have neutrons of many energies grouped into one cross section value at one central neutron energy. In a region with a fluctuating cross section or near channel thresholds, this is important to keep in mind. The distributions for the sources are shown in Figure 5.9. The White Source distribution should again be used with caution, given the

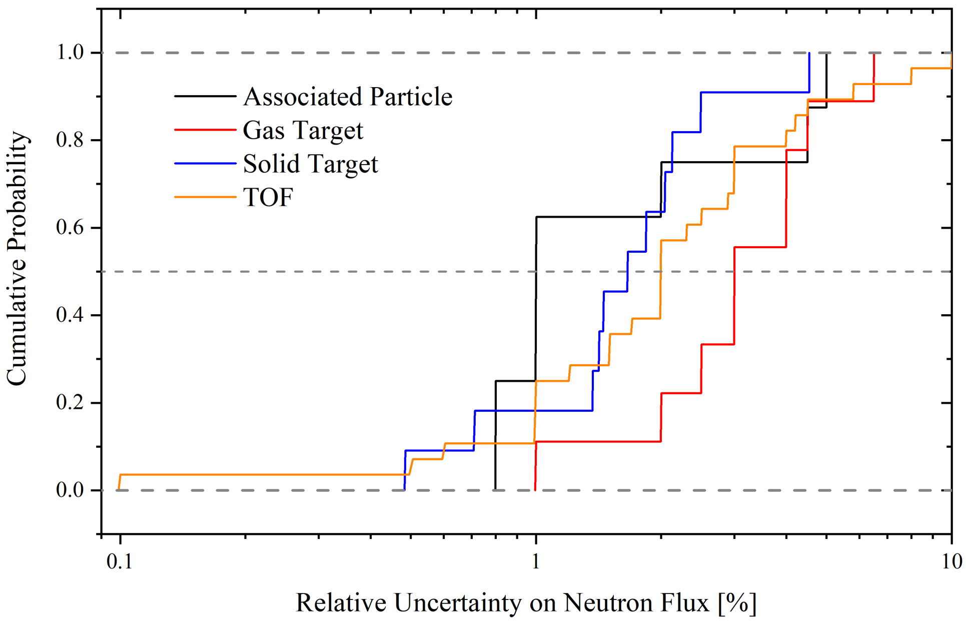

Figure 5.7: Cumulative distribution function of the uncertainty values on the neutron flux. There are 8 values for Associated Particle, 18 values for Solid Target, 9 values for Gas Target and 28 values for White Source.

dependence on the facility setup.

5.3 Interpretation of Uncertainty Distributions

These compiled uncertainty distributions need to be interpreted before they can be turned into an experimental uncertainty template, and for some sources of uncertainty, the distribution of literature values will not be a good estimate.

For example, the distributions are not meaningful for uncertainty sources that vary widely and are dependent on the exact experimental parameters. One example of this is the neutron energy resolution at white source facilities. The energy resolution is based on the flight path length, the method of neutron production, the timing resolution, and how the data was binned in the analysis. For this reason, it is not recommended to estimate the neutron energy resolution of a white source experiment with this distribution, which, as can be seen in Figure 5.9, spans four orders of magnitude. Another case are uncertainties that are often neglected, such as dead time correction or timing uncertainties. In most experiments, these are much smaller than other uncertainty sources, and so are not quantified or reported. The instances of dead time and timing uncertainties that come up in the EXFOR, therefore,

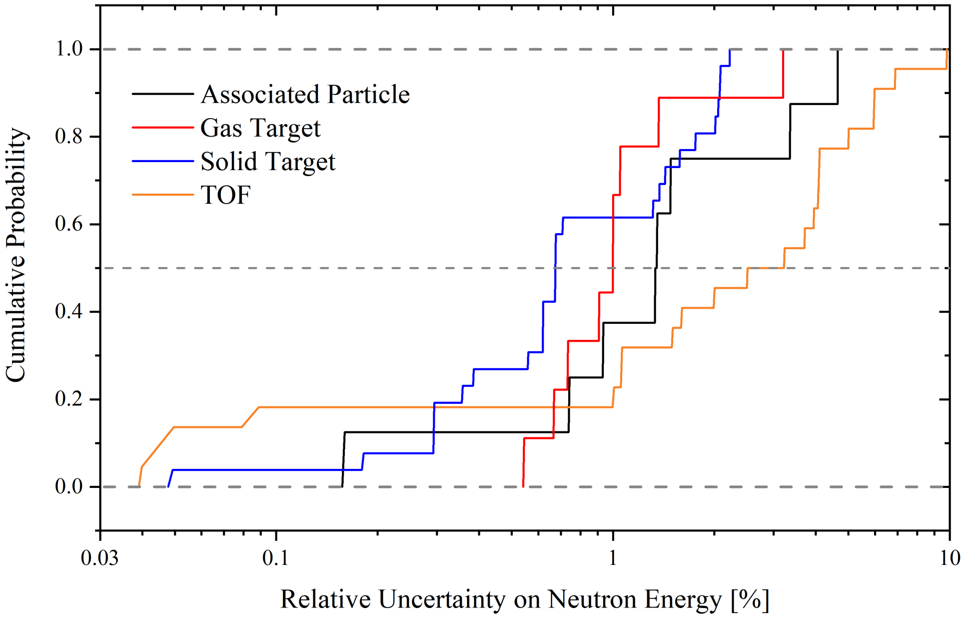

Figure 5.8: Cumulative distribution function of the uncertainty values of the neutron energy. There are 8 values for Associated Particle, 26 values for Solid Target, 9 values for Gas Target and 22 values for White Source.

are the unusual cases where the uncertainty is very large, for a specific reason. It is not appropriate to apply the median of this biased distribution to other data sets.

In other cases, the uncertainty values are given, but there is not enough detail. For example, the efficiency of a gamma detector has three distinct regimes when it comes to calibration. For low gamma energies, the efficiency has a direct relationship with gamma energy—as the gamma energy increases, so does the efficiency. Somewhere below 200 keV for most detectors, the efficiency peaks begins to decrease as the gamma energy increases. Constraining the low energy function and the energy where it peaks is important if low energy gammas will be measured, and requires multiple data points in the region. The uncertainty below 200 keV should, in most cases, be higher than above 200 keV, unless a lot of effort was put into fitting that region. In the region between 200 keV and 2 MeV, the efficiency smoothly decreases and there are many standard calibration sources that can be used to constrain the fit[2]. Above 2 MeV, extrapolation, simulation or in-house calibration standards tend to be used, which leads to larger uncertainties. In the capture cross section template, Section 4.3, the uncertainty on gamma detector efficiency is split up in this way. However, in the vast majority of the EXFOR entries used in this process, the gamma detector efficiency

---

[2] More detail on the proper uncertainty propagation for fitted efficiency values is given in Chapter 6.

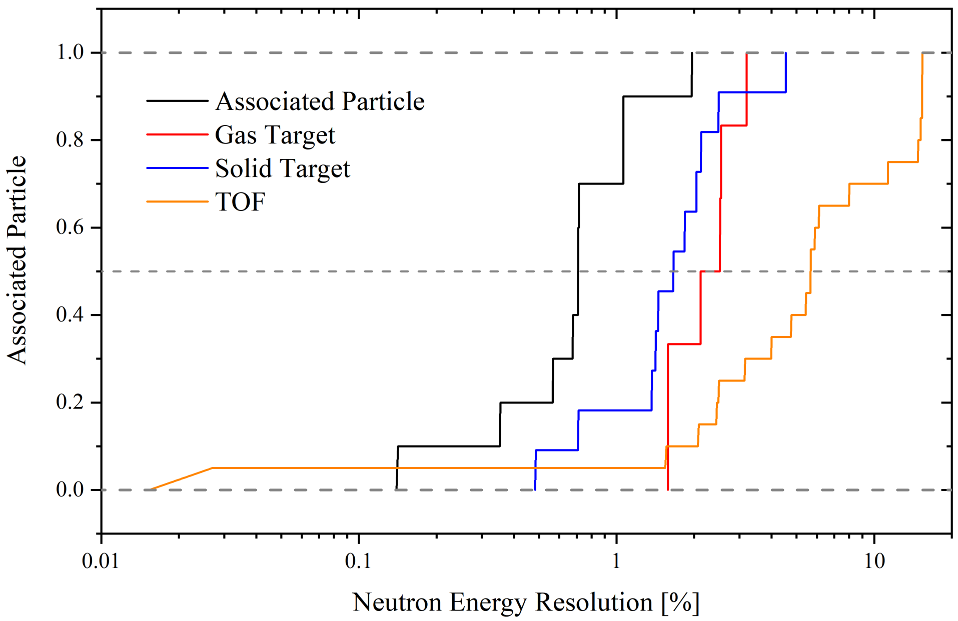

Figure 5.9: Cumulative distribution function of the values of resolution the neutron energy. There are 10 values for Associated Particle, 11 values for Solid Target, 6 values for Gas Target and 20 values for White Source.

was given with a single uncertainty, and with no indication of what gamma energy it applied to. For this reason, the distribution presented in Figure 5.6 was put together without any gamma energy dependence. In this case, not enough detail is provided in the literature to fully characterize this uncertainty.

Finally, there are cases where the optimism of the experimentalist may lead to biased distributions. Multiple scattering corrections are one example, as are corrections and calculations that include gamma cascade simulations. In-depth study of multiple scattering corrections show that they are highly dependent on the geometry, the isotopic composition of the sample, and nuclear data used. The correction should be calculated iteratively in cross section measurements, as the measured cross sections affect the multiple scattering. There are a few cases where extensive and detailed studies of multiple scattering have been performed [186, 187] but in many cases, simple calculations are used, without iteration. In those cases, the uncertainties on these corrections should be large, but are typically underestimated or not reported. In this case, the EXFOR entries used here did not contain enough values for multiple scattering correction uncertainties to create a distribution.

Experiments that include calculations of gamma cascades as part of the data analysis also seem to underestimate the uncertainties inherent in the cascade physics. For example, RRR capture measurements, explained in Sections 2.2.2 and 2.2.3, use gamma cascade simulations to determine the efficiency of detecting capture events. However, the influence of these simulations tend to be downplayed in the final experiment paper, and the uncertainties are almost never mentioned. Simply using the literature uncertainties to construct uncertainty templates for these RRR capture measurements would result in the neglect of a potentially large source of uncertainty. More details on the use of gamma cascades in cross section determinations and a new method for estimating that uncertainty is presented in Chapter 7.

With these limitations in mind, the literature distributions of uncertainties can be useful in the construction of a template, along with the "expert judgment" of the evaluator. For example, the distributions shown here informed the sample and flux uncertainties in the capture template presented in Chapter 4. In addition, the ability to construct entire distributions, not just expected values, can help the evaluator determine if a given uncertainty is out of the ordinary. Many of the distributions compiled here span more than one order of magnitude, so the median value alone may not be a good indication of whether a given uncertainty value is unusually low. The quantile in the distribution is a better measure of how the uncertainty compares with other experiments. The use of EXFOR distributions in the creation of the templates will provide a way to make the templates more consistent with the experimental literature. The missing values filled in with the templates will, therefore, provide more accurate relative weights between experiments.

Chapter 6

Uncertainty in HPGe Efficiency Calibration

One of the significant sources of uncertainty in Activation Analysis (AA) and Partial Gamma (PG) measurements is the uncertainty on the efficiency of the gamma detector. In the vast majority of measurements, the energies of the measured gammas are different than the calibration standard gammas, thus requiring interpolation to determine the needed efficiencies. In some cases, the efficiency over the entire energy region of interest is simulated with transport codes such as MCNP [17] or GEANT-4 [123]. This method should always be validated with calibration standards, but does not require a fitted function. Fitting a function for interpolation is the more common method, and the uncertainties on the interpolated efficiency values is important to understand. The process of calibration starts by measuring calibrated sources and calculating the efficiency at those known gamma energies, thus providing the data set to use for fitting. The uncertainties on the measured efficiency for calibration sources, and the correlations between the data points (together, the data covariance matrix) must be properly calculated. The uncertainty on the fit of the chosen functional form to the data points should then include both the data covariance matrix and a measure of the ability of the function to fit and interpolate the data points. This chapter details the correct way to construct the data covariance matrix, and then presents both the typical regression uncertainties and a new method that is more appropriate.

6.1 Data Covariance Matrix

The first step in proper fitting is to define and create the data covariance matrix, $\mathbf{\Sigma}$. $\mathbf{\Sigma}$ is an $n \times n$ symmetric matrix, where n is the number of data points. In the case of fully independent data points, this matrix is diagonal and filled with the variances of data points. In most real cases, there are correlations between the different data points that lead to non-zero off-diagonal elements. All sources of uncertainty in the data points should be considered when creating the data covariance matrix, and the most common sources are described in

Table 6.1: Uncertainty sources in the efficiency calculation using Equation 6.1. The recommended distribution is provided in the second column. The correlations recommended between data points from the same calibration source are labeled as "same source" and the correlations between data points from different samples are labeled as "different source".

Uncertainty	Distribution	Correlation (same source)	Correlation (different source)
$C(E_\gamma)$	Gaussian	Uncorrelated	Uncorrelated
A_0	Gaussian	Fully	Weak or Uncorrelated
t_c	Uniform	Fully	Fully or Uncorrelated
λ	Gaussian	Fully	Uncorrelated
$B_\gamma(E_\gamma)$	Gaussian	See Appendix D	Uncorrelated
$\xi(E_\gamma)$	Gaussian	Strong	Strong
$S(E_\gamma)$	Gaussian	Strong	Weak

the following sections. Two methods to create the matrix from the set of uncertainty sources are then explained.

The typical equation used to calculate the efficiency at each gamma energy with a data point is

$$\varepsilon(E_\gamma) = \frac{C(E_\gamma)\ \xi(E_\gamma)\ S(E_\gamma)}{A_0 e^{-\lambda t} B_\gamma(E_\gamma)}, \tag{6.1}$$

where C is the count rate, A_0 is the initial activity of the source, λ is the decay constant of the source, t is the time between the source creation and the start of the measurement, and B_γ is the branching ratio of of that gamma (not transition) in the decay. The other terms are corrections—ξ is the correction for gamma attenuation in the sample, and S is the correction for coincidence summing. Each variable contributes some uncertainty to the efficiency, and each will be addressed in the following section. More details about the data set and the uncertainty values chosen are given in Appendix C. The distributions and correlations are summarized in Table 6.1.

6.1.1 Sources of Uncertainty

6.1.1.1 Counts

For photopeak efficiency calibration, the count rate is determined by integrating over the photopeak in the gamma spectrum. There are two common methods for performing this integration. If the peak is well-isolated and the Compton background seems linear, the integration can be done simply by choosing the region of interest around the peak, summing all of the bins in that region, then subtracting out the linear background. In this case, the uncertainties on the counts are usually considered to be entirely statistical, as both the counts in the region of interest and the background are statistical. This is likely true in the case where the background is correctly estimated under the peak. However, if the background is not correct, the consistent use of this incorrect model will introduce correlations between the different peaks.

Alternatively, the integration can be performed by first fitting the peak to a functional form and then integrating the fitted form. A tailed Gaussian is a good choice for the photopeak, and a background function can be included that is physically reasonable for the spectrum. If the background is known (or suspected) to not be linear, it is better to use this fitting method to account for it properly. The uncertainty in the counts in this case includes fitting uncertainties, and so cannot be considered statistical. In most cases, however, the uncertainties are still presented as statistical, Poisson uncertainties. More work needs to be done on the best way to put uncertainties and correlations on counts determined by fitting, and for the current work the statistical Poisson uncertainties are used.

6.1.1.2 Source Activity

Calibration sources are calibrated in activity when they are created, and labeled with the source strength and date. The uncertainties on these strengths are sometimes given in the documentation, but are sometimes assumed by users to be represented by the last digit. These significant figure-based uncertainties can be quite small—less than 1% at times—which are not realistic. It is recommended to not assume an uncertainty smaller than 1%. The maximum between the stated uncertainty and 1% should be used, unless there is strong evidence that a calibration source is known better than 1%. The source activities are likely to be weakly correlated if the sources came from the same place, such as NIST, as the same or similar measurement systems were used to calibrate them. Strong correlations could be assumed if it is known that the same detector was used, as counting statistics are likely to be low in these measurements. In most cases that information is not available and a weak correlation (around 0.2 or 0.3) should be assumed. If the sources came from different manufacturers or were created years apart, they can be assumed to be uncorrelated. In this data set, the ^{137}Cs and ^{60}Co sources were reported to have been created on the same day, so they were given a weak correlation (0.3), and the other sources were assumed to be independent of each other.

6.1.1.3 Decay Constant and Elapsed Time

To convert the source strength at the time it was created, A_0, into the source strength at the time of the efficiency calibration measurement, the decay constant, λ, and elapsed times, t and t_c, are necessary. The time elapsed between the creation of the sample and the efficiency measurement, t, can be determined by the date on the label of the source. Often this cannot be known better than to the day, which is significant if the half-life is on the order of weeks or months. Even knowing to a day might be an underestimate—for the calibration sources used in this work, all of the dates were either on the first or fifteenth of the month, and several were reportedly created on weekends. For this reason, it was assumed for these sources that the time elapsed could not be known better than two weeks. The uncertainty put on the elapsed time should be represented by a uniform distribution, as it is not any more likely to have been created at a certain point during time window (with the probable exception of nights and weekends). The continuous uniform distribution, represented by a simple PDF,

$$\mathbb{P}(t) = \frac{1}{t_{max} - t_{min}}, \tag{6.2}$$

is constant between the minimum and maximum values and zero elsewhere [188]. The assumption of normality in the linear propagation methods require that the uniform time uncertainty distribution be approximated by a Gaussian distribution. By setting the mean and variance of the two distributions equal, the parameters of the Gaussian can be determined as

$$\begin{aligned} \mu &= \frac{t_{min} + t_{max}}{2} \\ \sigma^2 &= \frac{(t_{max} - t_{min})^2}{12}. \end{aligned} \tag{6.3}$$

These are both symmetric distributions, so the third moment of the Gaussian, skewness, can be neglected. The main difference between these distributions is the likelihood of values far from the mean. The time elapsed is fully correlated between gammas from the same source, and due to the random nature of the creation time, is uncorrelated with other calibration sources.

The decay constant of the parent nucleus (including all decay modes) and its uncertainty can be obtained from the ENSDF evaluation [10]. The decay constant, λ, is related to the half-life, $t_{1/2}$, by the simple relation

$$\lambda = \frac{\ln 2}{t_{1/2}}. \tag{6.4}$$

The decay constants are evaluated values, and their uncertainties represent all of the information available at the time of the evaluation. There may be correlations between decay constants of different isotopes, but these correlations are not feasible to estimate and can be assumed to be zero. Decay constants for typical calibration sources are well-known and often have negligible uncertainties. If the decay constant does not have negligible uncertainty, its propagation must be performed carefully, due to the non-linearity of the term. In the case where $t << t_{1/2}$, the whole term $e^{-\lambda t}$ can be treated as linear. However if this is not the case, the exponential term can contribute a significant uncertainty to the efficiency measurement, and this must be accounted for.

6.1.1.4 Gamma Intensities

The intensity of the measured gamma is the probability that the gamma is emitted per parent decay (including all decay modes). This is not the intensity of the transition, but of the gamma itself (this distinction is only necessary where internal conversion is non-negligible). Gamma intensities should be taken from the same ENSDF evaluations [10] as the decay constant. Uncertainties on the gamma intensities can be taken from the evaluation as well. Although previous work has assumed that these intensities are independent due to the statistical nature of the counts [189], there are many constraints used in the both the experiments and evaluations that create correlations between the intensity values. The intensity evaluations make use of experiments that measure gamma counts in calibrated detectors, and often have trigger conditions or coincidence methods. Therefore the intensities in the experiments are highly correlated to each other. In addition to this, the evaluation takes into account external constraints, such as that gamma intensities must sum together in a way consistent with the physical cascades, and that the sum of the transitions out of a level must be greater than that of a level that feeds it. These add even more correlations between the intensity values, but they are not provided in the ENSDF evaluations.

These correlations can be estimated using simulations of the decays and subsequent gamma cascades, and this has been done for the commonly used calibration sources ^{152}Eu, ^{133}Ba and ^{60}Co. These simulations can be used to represent "physical" correlations between the gamma transitions—not based on the measurement uncertainty, but based on the physical constraints that were used in the evaluation. The simulations were performed by varying the intensity of the decay to feed each level and the branching ratios from the excited levels based on their stated uncertainties in the ENSDF evaluations. The resulting correlation matrices for each of the three common sources are given in Appendix D. The correlation matrix for ^{133}Ba is also shown in Figure 6.1. Correlations between directly competing transitions, such as the 80.9 keV gamma and the 383.8 keV gamma, which both feed the ground state of ^{133}Cs, are strongly negatively correlated. Correlations between transitions within a cascade path, such as the 356.0 keV gamma, which feeds the first excited state, and the 80.9 keV gamma, which de-excites the first excited state, are strongly positively correlated. These correlations, some of which are very strong, are important to take into account when fitting the efficiency curve, as the under-prediction of correlations between data points can inflate the trust in a fit. These correlation matrices are applicable to all measurements using these standards, until the evaluations change, and are provided in Appendix D for use in future work.

6.1.1.5 Gamma Attenuation Correction

For low energy gammas, the correction for attenuation in the sample can be significant. The correction is usually made using a simple gamma attenuation equation,

$$\frac{I}{I_0} = e^{-\mu(E_\gamma)d}, \tag{6.5}$$

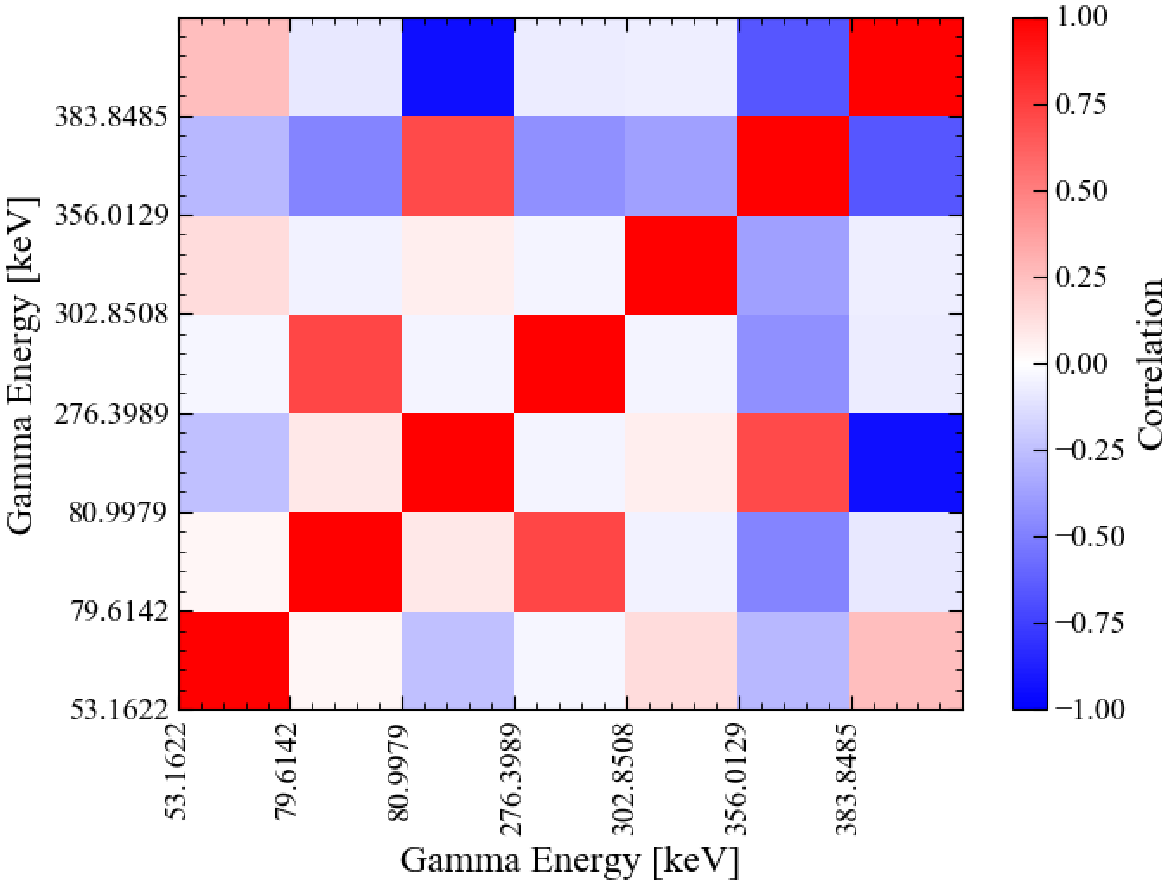

Figure 6.1: Correlation matrix for the intensity values of the decay gammas from a ^{133}Ba source that are commonly used for calibration. The correlations are based on a Monte Carlo simulation of the decay of ^{133}Ba.

where I_0 is the intensity of the gammas incident on a sample, I is the intensity of the gammas emitted from the sample, μ is the gamma attenuation coefficient in the sample material and d is the thickness of sample that the gammas travel through [124]. This is the "good geometry" equation, which should only be used for thin samples. The exact definition of d in this case should depend on the type of calibration source (spot source, deposit, etc) and the casing or backing. The gamma attenuation correction factor, ξ, in Equation 6.1, is based on this model of attenuation,

$$\xi(E_\gamma) = \frac{I_0 - I}{I_0} = 1 - e^{-\mu(E_\gamma)d}, \tag{6.6}$$

and should have an uncertainty that is based on the uncertainties in the attenuation coefficient and the thickness chosen.

This correction can also be determined with transport simulation codes such as MCNP [17] or GEANT [123]. Simulations may help to reduce the uncertainty in d (if the calibration source is modeled correctly) but do not improve on the uncertainty in μ, and an uncertainty should be added to the statistical Monte Carlo uncertainty to account for this.

For most thin, disk-shaped calibration sources, this correction should be negligible, even down to 10's of keV. The sources are usually designed to minimize the gamma interactions. For other source geometries or x-rays, this may not be the case and the effect should be studied.

Similar methods for calculating the correct d will induce correlations between all of the corrections. The uncertainty in the attenuation coefficients are strongly correlated between different gammas as well. The characteristics of the sources are also likely to be similar, especially the casing, and the density estimate is likely to be the same. Strong correlations are recommended, unless the experimentalist has reason to believe that the calibration sources they used are different enough in geometry, casing and density to reduce the correlations.

6.1.1.6 Coincidence Correction

Coincidence summing occurs when two gammas from a single cascade interact with the detector within a small enough time window to be considered a single event (for more details, see Section 2.2.5). The energy of the event is the sum of the energy deposited by each gamma, and can warp the efficiency shape. The most common interaction in HPGe detectors for gammas above 200 keV is Compton scattering, so many summed events will not appear at the "sum peak", which is the sum of the energies of the two gammas. That peak will be populated strictly by events where both gammas deposited their full energy. Coincidence summing has the effect of artificially decreasing the measured full-deposition efficiency at the calibration gamma energies. The magnitude of the effect is dependent on the cascade characteristics (such as multiplicity and gamma angular distributions), the gamma energies and the distance from the detector.

This correction can usually be avoided by placing the samples at least 10 cm from the detector face, and for measurements with calibration sources, this should always be done. Close distance counting, which increases the geometric efficiency and reduces the necessary counting time, should not be necessary with calibration sources.

If the sources have been counted closer than 10 cm, the correction $S(E_\gamma)$ in Equation 6.1 must be determined and applied. For calibration sources, the decay and subsequent cascade is usually known well enough to allow for direct correction of coincidence summing. The detector geometry, sample geometry, distance between the sample and detector, and the intrinsic photopeak and total efficiencies are needed for this correction. The angular distributions of the emitted gammas are important to the calculation, but are often unknown and assumed to be isotropic. This can introduce a bias into the correction factor which cannot be quantified without angular distribution information. The multiplicity of the cascade can offer some insight into the significance of the summing correction without a lengthy simulation process. The multiplicity distributions for both ^{133}Ba and ^{152}Eu decays are shown in Figure 6.2, based on the simulations done for the gamma intensity correlation matrices. For ^{133}Ba, the average cascade produces two gammas, and few produce greater than three. This indicates that the coincidence summing correction will likely not be significant until the source is extremely close to the detector. For ^{152}Eu, the average cascade produces 2.5 gammas, so the probability of a significant summing correction is higher for ^{152}Eu.

Coincidence summing uncertainties can be assumed to have Gaussian distribution, due to lack of information. If a full simulation is performed to determine the correction, the distribution from the simulation can be used instead. Strong correlations are recommended between gammas from the same source, due to the same simulation or calculation producing both corrections. For gammas from different sources, weak correlations are recommended to reflect the similar methodology and potential biases in the calculations.

6.1.2 Linear Uncertainty Propagation

The uncertainty in the efficiency values were first calculated using linear uncertainty propagation. The “Sandwich Formula”, Equation 2.52, was used to create the data covariance matrix. The uncertainties in the time and decay constants were neglected, as they are much smaller than the count and activity uncertainties. The uncertainties calculated for each efficiency value are presented in Table 6.2, and the correlation matrix is shown in Figure 6.3(a). The A_0 uncertainties create correlations between gammas of the same source. For some of the data points, the largest uncertainty source was the counts, which are independent, as seen in Table C.2. The non-linear uncertainties in this data set are small enough to justify neglecting, as proven by the similarity between the linear uncertainties and the Monte Carlo uncertainties.

6.1.3 Monte Carlo Uncertainty Propagation

The Monte Carlo uncertainty propagation method was also used to determine the uncertainty on the efficiency values. In this method, non-linear uncertainties and non-Gaussian distributions are easily accounted for. The uncertainties in the decay constants and elapsed time were included, and the uniform distribution was used for the time. The data covariance matrix was constructed by varying the values of Equation 6.1 and calculating the efficiency at each gamma energy, 10^5 times. In each iteration, new values for A_0, λ and t are chosen for each calibration source, based on the uncertainty distributions. Then, the branching ratios for all of the gammas within the source are chosen together, using the `random.multivariate.normal` function in the Python package `NumPy` [152]. Finally, values for counts are chosen for each data point, independently. More details about how the values are chosen are given in Section 2.3.2.2. With all the temporary values chosen, the efficiency was calculated at each gamma energy. This process was repeated 10^5 times and then a Choleskly decomposition was used to determine the efficiency at each gamma energy and the data covariance matrix, as described in Section 2.3.2.2.

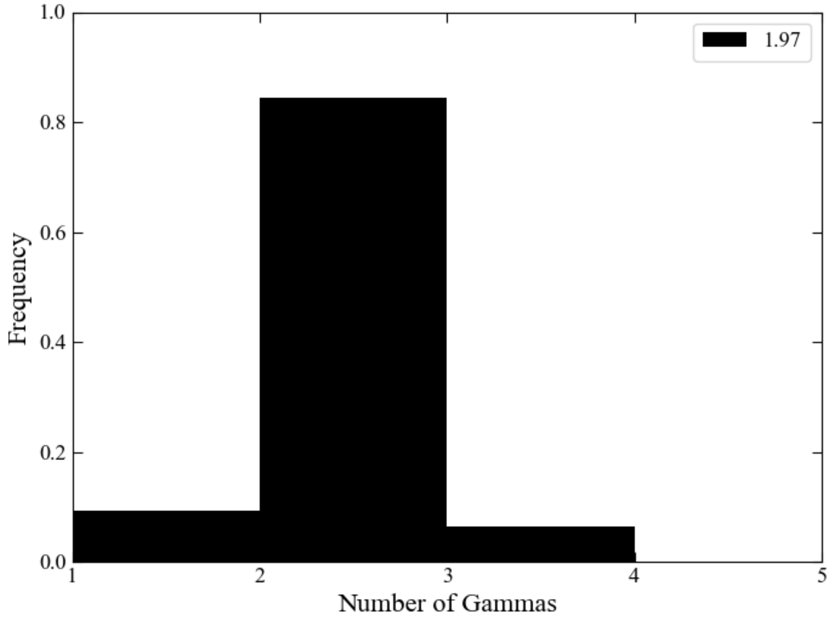

(a) ^{133}Ba

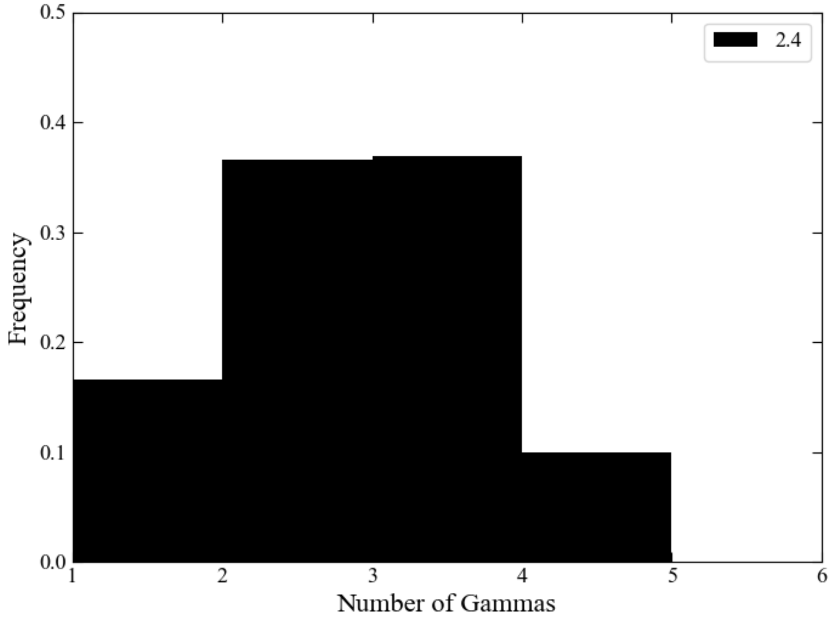

(b) ^{152}Eu

Figure 6.2: Gamma multiplicity distributions for the decays of ^{133}Ba and ^{152}Eu, based on 10^6 decay simulations. The average multiplicity for each is labeled on the plot. For ^{133}Ba, the average multiplicity is 1.97 gammas per cascade, with only a small percentage of cascades producing more than three gammas. For ^{152}Eu, the average multiplicity is 2.4 gammas, with few cascades producing more than four gammas. These distributions help to determine the significance of coincidence summing.

In the case of this data set, the non-linear sources of uncertainty were almost negligible so the Monte Carlo uncertainty method gave the same uncertainties values as the linear method, as seen in Table 6.2, as expected. The correlation matrix, shown in Figure 6.3(b), is also very similar to the correlation matrix from the linear error propagation method.

Table 6.2: Calculated uncertainties on the efficiency data points, based on both linear and MC propagation. Monte Carlo uncertainties are based on 10^5 iterations. In this case, where the linear uncertainties are dominant, linear propagation and MC propagation give the same uncertainties, as expected.

E_γ [keV]	Source	Abs ε	$\delta\varepsilon$ [%] (lin)	$\delta\varepsilon$ [%] (MC)
59.5409	^{241}Am	0.00124	3.2	3.2
121.7817	^{152}Eu	0.00372	1.2	1.2
244.6974	^{152}Eu	0.00206	1.2	1.2
302.0129	^{133}Ba	0.00168	1.3	1.3
344.2785	^{152}Eu	0.00138	1.3	1.3
356.0192	^{133}Ba	0.00128	1.1	1.1
383.8485	^{133}Ba	0.00121	1.3	1.3
411.1165	^{152}Eu	0.0001	1.5	1.5
443.9606	^{152}Eu	0.0011	1.4	1.3
661.657	^{137}Cs	0.00061	1	1
778.9045	^{152}Eu	0.00049	1.3	1.3
867.38	^{152}Eu	0.0004	1.6	1.6
964.057	^{152}Eu	0.00037	1.3	1.3
1085.837	^{152}Eu	0.00034	1.3	1.3
1112.076	^{152}Eu	0.00032	1.3	1.3
1173.228	^{60}Co	0.00031	1.2	1
1212.948	^{152}Eu	0.00031	2.3	2.3
1299.142	^{152}Eu	0.00033	2.2	2.2
1332.492	^{60}Co	0.00027	1.2	1.1
1408.013	^{152}Eu	0.00025	1.2	1.2
1528.1	^{152}Eu	0.0002	5.7	5.7

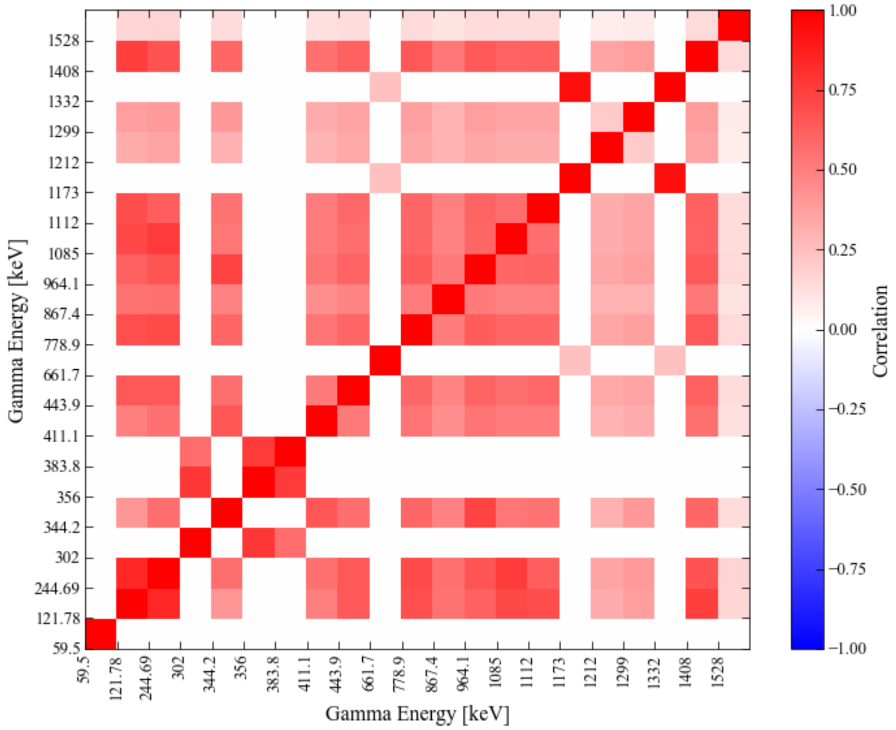

(a) linear

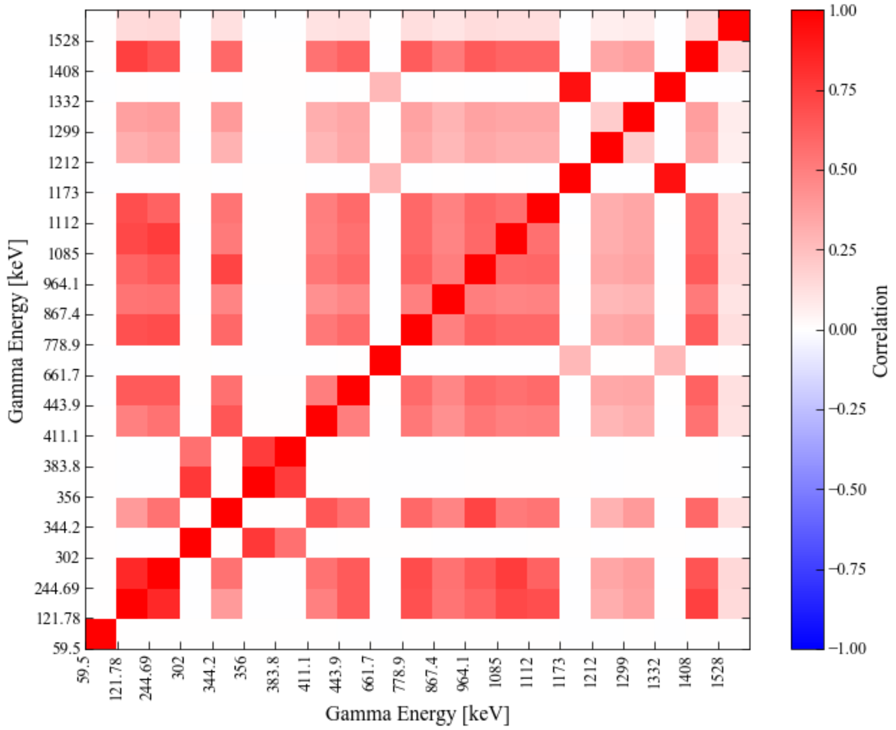

(b) Monte Carlo

Figure 6.3: Calculated efficiency values with uncertainties from the linear propagation and Monte Carlo propagation.

6.2 Fitting the Efficiency Function

The data set was used to fit an efficiency function that is physically meaningful over the energy region between 200 keV and 3 MeV [190],

$$\varepsilon(E_\gamma) = B_0\, e^{-B_1 E_\gamma^{B_2}} \left(1 - e^{-B_3 E_\gamma^{B4}}\right), \tag{6.7}$$

where B_0 represents normalization term to put the efficiency in real units, $(1 - e^{-B_3 E_\gamma^{B4}})$ represents the probability of a gamma getting through the dead layer, and $e^{-B_1 E_\gamma^{B_2}}$ represents the probability of a gamma depositing its full energy in the active volume of the detector. The function was fit using the `optimize.curve_fit` function from the Python package `Scipy` [158], using the Trust Region Reflective method [157] with good initial guesses. The function has five parameters, two of which are not sensitive to data points above 250 keV (B_3 and B_4). The overall degrees of freedom in the fit is $(n - p) = 22 - 5 = 17$. However, there are only three data points below 250 keV, so the fit of B_3 and B_4 only has one degree of freedom. More data points below 250 keV would constrain that fit more, which would lead to a smaller uncertainty on these two parameters.

This function is based on a physical model and is more rigid than the polynomial function that is commonly used. This means that it may not be flexible enough to fit every data point, but the underlying physics will likely improve the accuracy of the interpolation [190]. The goal of an efficiency calibration is to determine a function that accurately represents the efficiency of the detector and can be used for interpolation. Traditional regression methods, such as Weighted Least Squares (WLS) and Generalized Least Squares (GLS) are typically used to fit the efficiency function and determine the uncertainties on the fit parameters. However, these methods have many drawbacks, and in some cases can be completely inadequate. The limitations of WLS and GLS are reviewed below, and a new Hybrid Method, which is more appropriate for fitting the efficiency function, is presented.

6.2.1 Traditional Regression Uncertainties

Descriptions of WLS and GLS are given in Section 2.3.3, and the assumptions and limitations are summarized here. The basic assumptions behind regression include that,

1. the responses, $\boldsymbol{Y}$, follow a single distribution centered about $\boldsymbol{X\beta}$ with variance σ^2
2. the variance σ^2 is not known, but can be estimated based on the residuals, assuming the model is correct, and
3. the main purpose of the fit is to determine the relationship between the explanatory and response variables, and the uncertainties on the fit parameters should reflect this [191].

In the case of fitting efficiency values, however, these three assumptions are not met. The response values all follow their own distributions, which are known. The model is not assumed to be correct, so the residuals are not an estimate of the data uncertainties. The main purpose of the fit is to interpolate, and the residuals do not necessarily represent how well the model can interpolate.

Weighted Least Squares (WLS) uses the weight matrix $\boldsymbol{W}$ (Equation 2.67) to account for some data points being more "trustworthy" than others. As explained in Section 2.3.3, in WLS the relative uncertainties are used to create a weight matrix, but the residuals are used to estimate the magnitude of σ^2. In linear least squares, σ^2 is estimated by the residual sum of squares, Equation 2.65, and in non-linear least squares, by the reduced χ^2, Equation 2.79. WLS, therefore, uses only the relative uncertainties and correlations between the data points, and neglects the actual uncertainty magnitudes. In this case, $\hat{\sigma}^2$ does not represent a data uncertainty, but rather the ability of the model to fit the data points. Large residuals can indicate a model that is either not at all physically correct (for example, fitting the efficiency with a straight line) or one that is too rigid to match the given data set. If the data is trusted, then this indicates that the model has a deficiency. If the model is trusted (for example, fitting radioactive decay with an exponential) then this indicates that the data set has a deficiency. Deficiencies in the data set can be caused by inappropriately small uncertainties or a hidden bias. The residuals represent a source of uncertainty (model fit) that is important to include when interpolating, but WLS leaves out the magnitude of the data uncertainty. A plot of the fit with WLS uncertainties is shown in Figure 6.4. The WLS uncertainties are a good approximation of the true parameter uncertainties in the case that $\hat{\sigma}^2$ estimated from the residuals is significantly larger than the uncertainties on the data points. The `scipy.optimize.curve_fit` function returns non-linear WLS uncertainties by default. The fit, and the WLS uncertainties, are shown in red in Figure 6.4.

Generalized Least Squares (GLS) allows for the inclusion of the magnitude of the data uncertainties, using the data covariance matrix, $\boldsymbol{\Sigma}$. The covariance matrix for the parameters, Equation 2.74, is dependent on $\boldsymbol{\Sigma}$ and does not depend on any measure of the residuals. For this reason, the uncertainties on the parameters do not include how well the model matches the data set. The GLS uncertainties are a good approximation of the fit uncertainty if the uncertainties on the data points are significantly larger than the estimate of σ^2 from the residuals. The `scipy.optimize.curve_fit` function can return the non-linear GLS uncertainties on the fitted parameters with the argument `absolute_sigma` set to `True`. The fit to the data set used here with the GLS uncertainties is shown in blue in Figure 6.4. For this data set and function, the WLS uncertainties are larger than the GLS uncertainties, indicating that the function is too rigid to fit all of the data points. This might be due to underestimated uncertainties in the data points which might have hidden biases, or that this model is not appropriate for this data set.

6.2.2 Hybrid Method

In a case where the WLS uncertainties are comparable with the GLS uncertainties for a data set, then neither can fully represent the fit uncertainties. The total fit uncertainty can be calculated by combining the data point and residual uncertainty. If the two sources

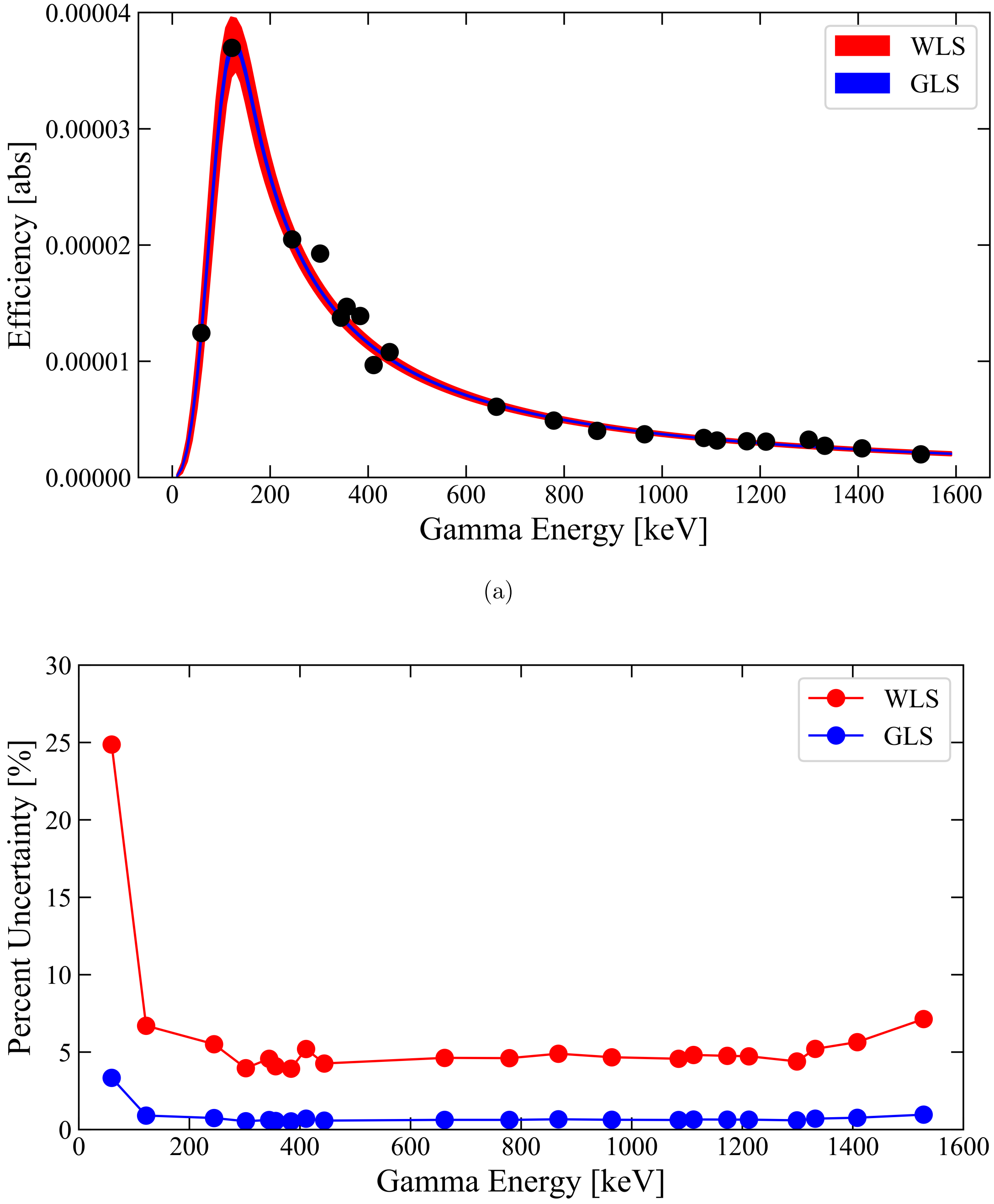

(a)

(b)

Figure 6.4: Fitted efficiency function (Equation 6.7) for the data set used here, with uncertainties based on the Weighted Least Squares (WLS) method and the Generalized Least Squares (GLS) method. The uncertainties on the fitted functions for each are shown in (a) with the data points, and in (b) as percent uncertainties. For this data set, the WLS uncertainties were larger than the GLS uncertainties.

of uncertainty are independent and normally distributed, then the covariance matrices can simply be added together. The non-linear least squares covariance matrix for $\hat{\boldsymbol{\theta}}$[1] is,

$$\mathbb{C}(\hat{\boldsymbol{\theta}}) = \boldsymbol{J}^{\dagger}(\hat{\boldsymbol{\theta}})\mathbb{C}(\boldsymbol{Y})\boldsymbol{J}(\hat{\boldsymbol{\theta}}), \tag{6.8}$$

where $\boldsymbol{J}(\hat{\boldsymbol{\theta}})$ is the Jacobian (Equation 2.78) of the efficiency function, Equation 6.7, at $\hat{\boldsymbol{\theta}}$, the estimate of $\boldsymbol{\theta}$. The covariance matrix of $\boldsymbol{Y}$ is split into the two sources of uncertainty,

$$\mathbb{C}(\boldsymbol{Y}) = \hat{\sigma}^2\boldsymbol{W}^{-1} + \sigma_y^2\boldsymbol{W}^{-1}, \tag{6.9}$$

where σ_y^2 is the scalar value needed such that $\boldsymbol{\Sigma} = \sigma_y^2\boldsymbol{W}^{-1}$. Then the covariance matrix of the fit parameters can be written as

$$\begin{aligned}\mathbb{C}(\hat{\boldsymbol{\theta}}) &= \boldsymbol{J}^{\dagger}(\hat{\boldsymbol{\theta}})\mathbb{C}(\boldsymbol{Y})\boldsymbol{J}(\hat{\boldsymbol{\theta}}) \\ &= \boldsymbol{J}^{\dagger}(\hat{\boldsymbol{\theta}})\left(\hat{\sigma}^2\boldsymbol{W}^{-1} + \sigma_y^2\boldsymbol{W}^{-1}\right)\boldsymbol{J}(\hat{\boldsymbol{\theta}}) \\ &= \left(\hat{\sigma}^2 + \sigma_y^2\right)\boldsymbol{J}^{\dagger}(\hat{\boldsymbol{\theta}})\boldsymbol{W}^{-1}\boldsymbol{J}(\hat{\boldsymbol{\theta}}).\end{aligned} \tag{6.10}$$

This is equivalent to adding the covariance matrix obtained from the fit with WLS uncertainties to the covariance matrix obtained from the fit with GLS uncertainties. This method has been applied to the efficiency data set, and the uncertainty obtained is shown in Figure 6.5.

This method relies on the assumption that the two sources of uncertainty (σ_y^2 and $\hat{\sigma}^2$) are independent, thus allowing the covariance matrices to be simply added. If there exists any correlation between them, this would need to be accounted for in the $\mathbb{C}(\boldsymbol{Y})$ calculation, Equation 6.9. A full proof of the independence is beyond the scope of this work, but it can be shown that the correlation between these two uncertainties is zero for this data set.

First, the uncertainty on each of the data points was multiplied by ten, uniformly. This left the correlation matrix unchanged, and thus did not change the weight matrix $\boldsymbol{W}$. The fit was then performed again, and the results can be seen in Figure 6.6. The uncertainties on the GLS fit increased by a factor of 10, which is expected, as a scalar multiplication of $\boldsymbol{\Sigma}$ will be transferred directly onto σ_y^2. The uncertainties on the WLS fit did not change at all, showing that the magnitude of the parameter uncertainties in WLS is based exclusively on the residuals.

A second test was performed, where the data covariance matrix, $\boldsymbol{\Sigma}$, was left unchanged but the values for four of the data points were changed. The 344.2 keV efficiency value was decreased by 10%, the 383.8 keV efficiency value was increased by 10%, the 964.1 keV efficiency value was decreased by 20%, and the 1112.0 keV efficiency value was increased by 20%. These changes were done in pairs to minimize the changes to the fitted parameter values. The data covariance matrix was not changed, so the percent uncertainty of each of these data points was changed in the fitting. The results of the fit are shown in Figure 6.7. It can be seen that the GLS uncertainties are the same as for the original fit (Figure 6.4), which is expected as $\boldsymbol{\Sigma}$ was left unchanged. The WLS uncertainties, however, increased universally

---

[1] As explained in Section 2.3.3.4, $\boldsymbol{\theta}$ is the non-linear equivalent to $\boldsymbol{\beta}$, the fit parameters.

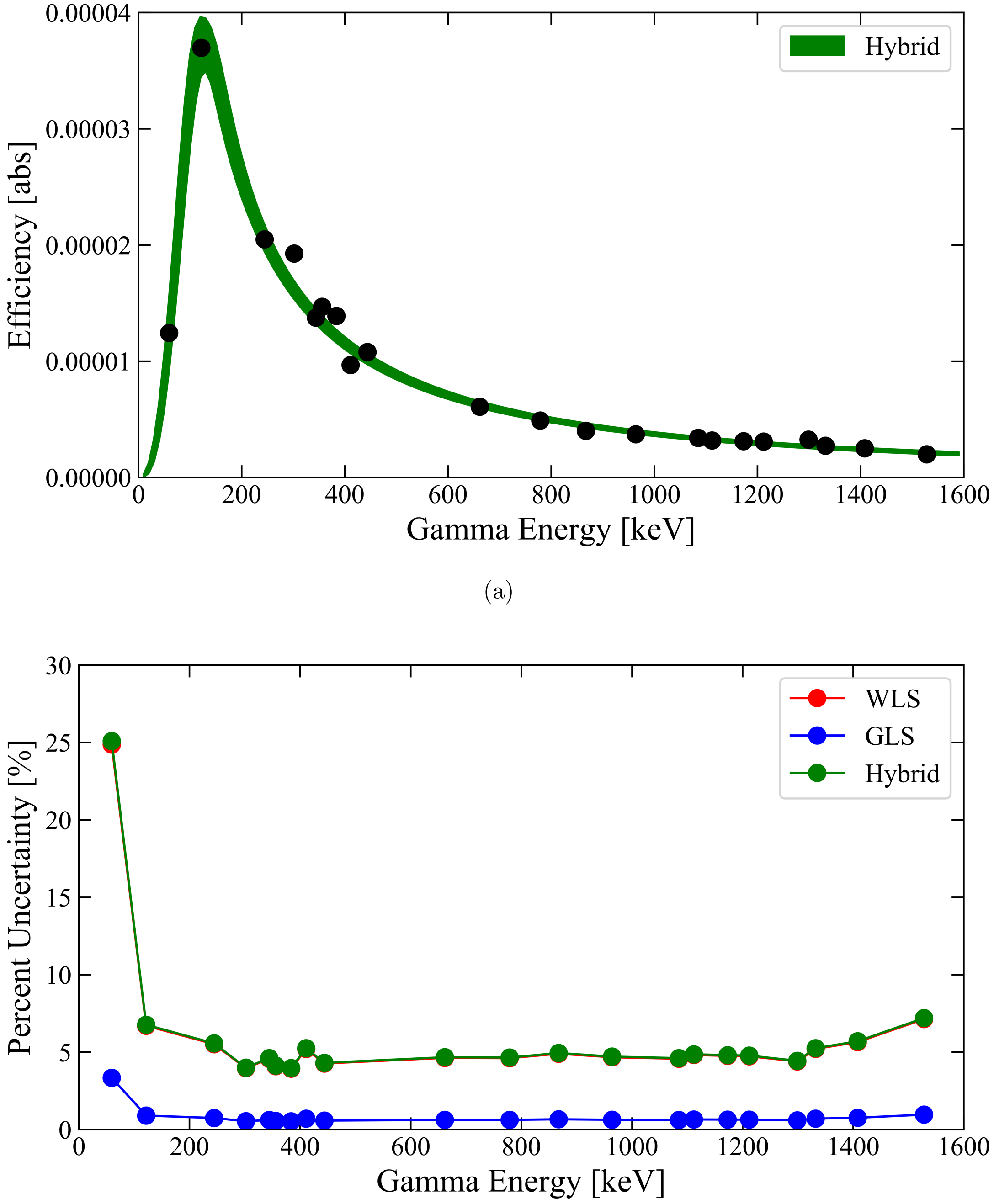

(a)

(b)

Figure 6.5: Fitted efficiency function (Equation 6.7) for the data set used here, with uncertainties based on the Hybrid Method, presented here. The uncertainties on the fitted functions for each are shown in (a) with the data points, and in (b) as percent uncertainties. The Hybrid Method accounts for both the data point uncertainties (GLS) and the discrepancy between the model and the data points (WLS).

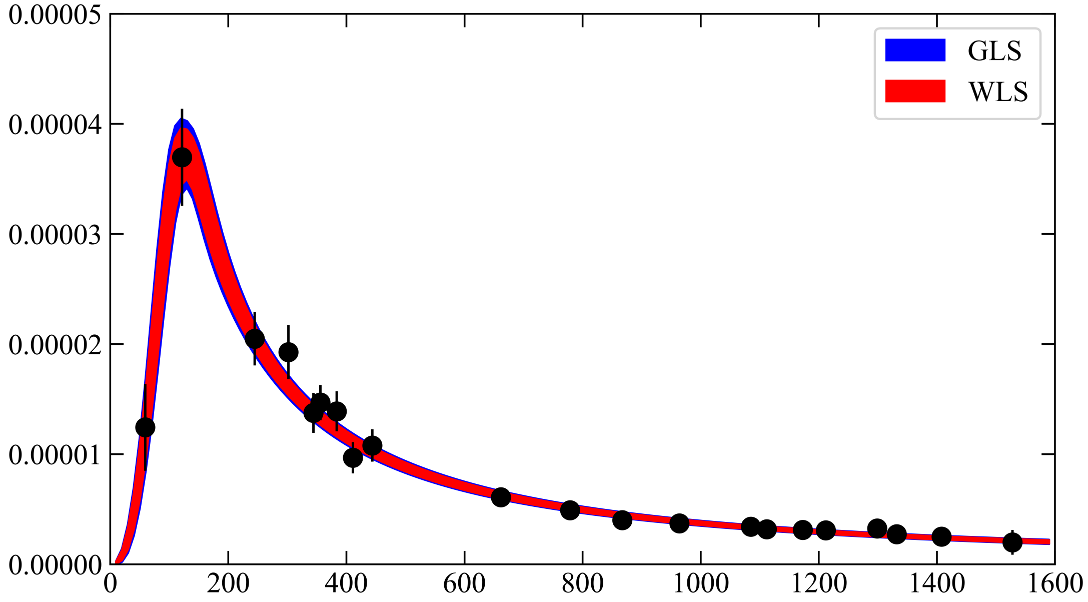

(a)

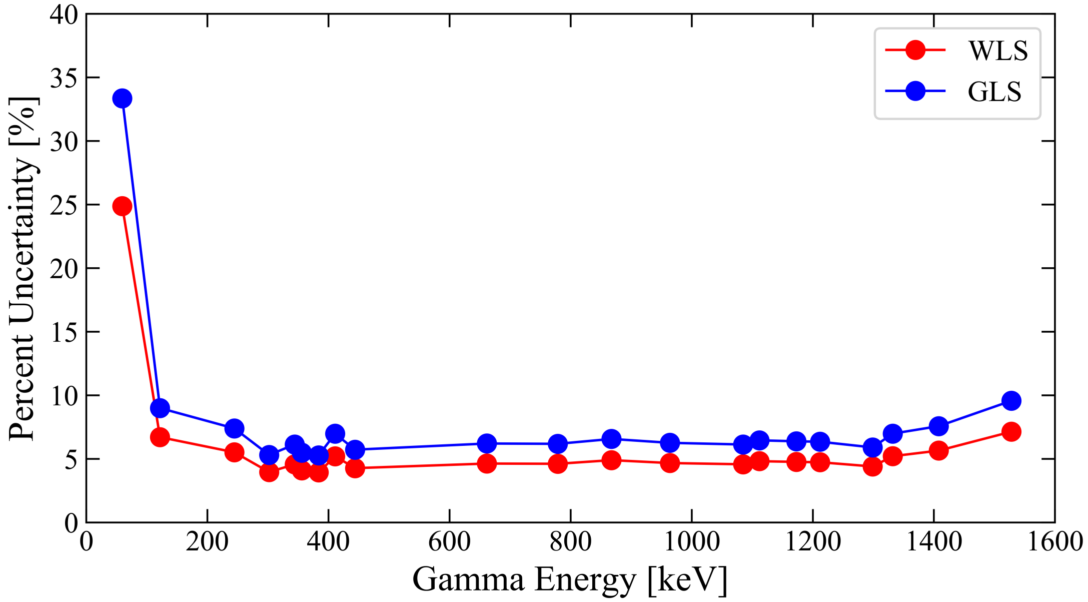

(b)

Figure 6.6: The fit uncertainties for both WLS and GLS when the data uncertainties are uniformly multiplied by ten. The fit and uncertainties are shown in (a) with the data points, and as the percent uncertainty on the fit at each data point in (b). When the data point uncertainties are changed, but the data point values are not, the GLS uncertainties increase by a factor of ten, and the WLS uncertainties remain unchanged.

over the energy region, due to the larger residuals in the four changed efficiency values. This demonstration does not constitute a general proof of independence, but rather shows that the Hybrid Method represents a full accounting of two separate sources of uncertainty in this case. A full proof and further applications of this method will be explored in future work.

The Hybrid Method uncertainty is a better representation of the uncertainty on the fitting parameters, as it accounts for both data uncertainty and model/data deficiency. However, it is not applicable in all situations and still has several drawbacks. One is shown in Figure 6.7, where only four of the efficiency values were changed, but the WLS uncertainties increased uniformly over the entire energy region. This is the result of the use of the RSS (Equation 2.64) or χ^2 metric, which applies an "averaged" residual to all of the parameters uniformly. Another drawback is that the Hybrid Method still does not address the ability of the fitted function to interpolate. The RSS metric only measures how well the function is able to fit the given points. For this reason, the Hybrid Method is a physically appropriate method to put uncertainties on the fit parameters when interpolation is not the goal. For example, when fitting a curve in a HPGe spectrum, with the intent to integrate over the curve to get the number of counts, this method is applicable. For cases such as the efficiency function, used here, which is fit with the express intent to interpolate, the Hybrid Method still does not provide a full accounting of the uncertainties.

A new method to determine fitting parameter uncertainties for use in interpolation would expand on the Hybrid Method, but replace the RSS metric with one that measures the interpolation accuracy. One possible metric is the Predicted REsidual Sum of Squares (PRESS) statistic [192]. This is based on the predicted residuals [193], rather than the residuals. Predicted residuals are the residuals for each data point when the model is fit without that data point,

$$\text{PRESS} = \sum_{i=1}^{n} \frac{(y_i - \hat{y}_{[i]})^2}{(1 - h_{ii})^2}, \tag{6.11}$$

where y_i is the value of the i^{th} data point and $\hat{y}_{[i]}$ is the prediction of the i^{th} data point when the model is fit without it. The variable h_{ii} is the leverage of the i^{th} data point, which is a measure of how sensitive the fit is to that point. This measures the ability of the model to predict each data point, based on the others. The PRESS statistic, unlike RSS, will be increased by a model that is too rigid to match the data points, and also by a model that is too flexible to interpolate accurately.

The uniform increase in the WLS uncertainties due to just a few value changes could be addressed by retaining the x-dependence of the predicted residuals. The PRESS statistic, just like the RSS statistic, loses this dependence by summing over all of the data points. If, instead, a diagonal matrix were created, such that each term were the predicted residual at that x-value,

$$(\boldsymbol{P})_{ii} = \frac{(y_i - \hat{y}_{[i]})^2}{(1 - h_{ii})^2}, \tag{6.12}$$

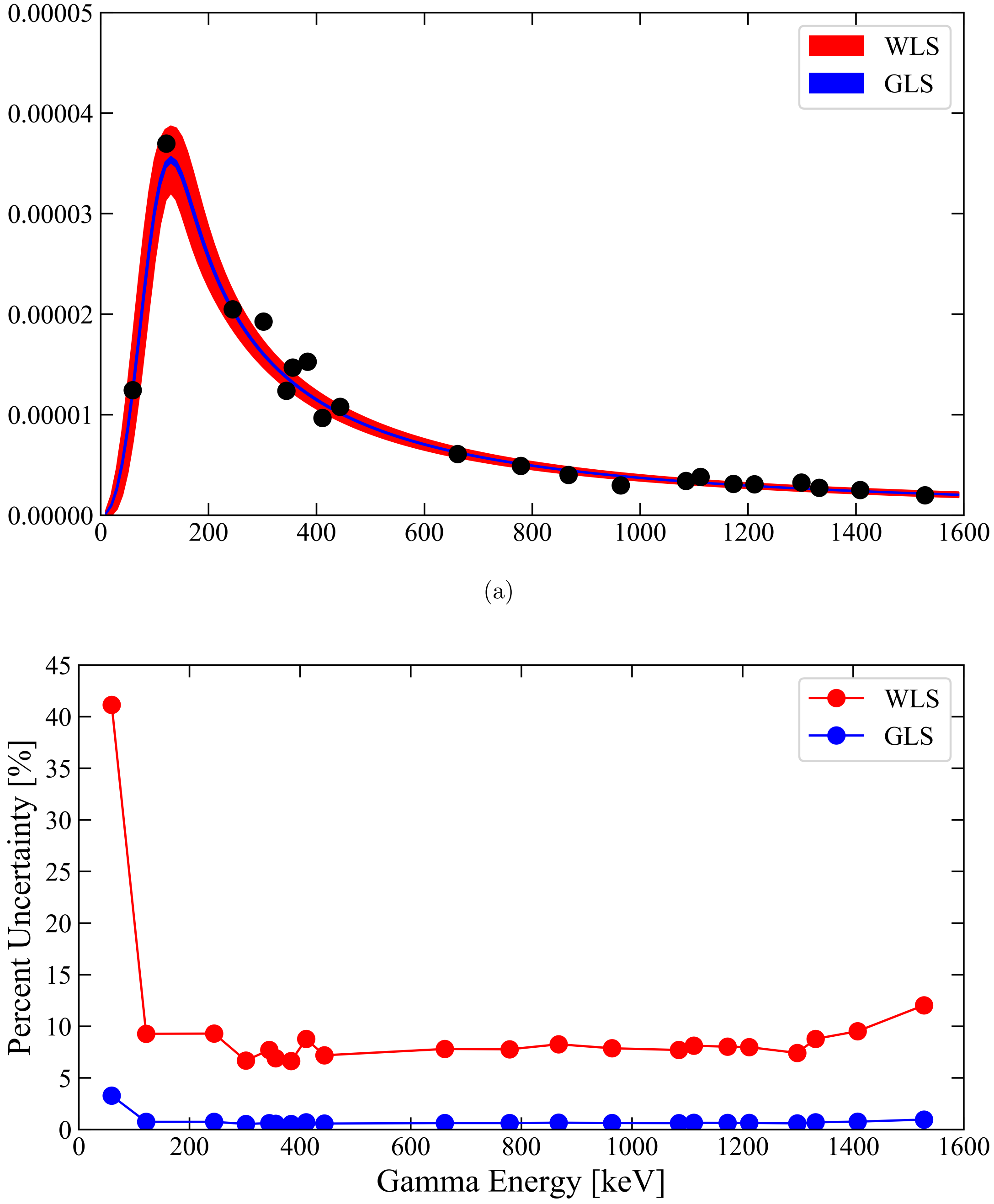

(a)

(b)

Figure 6.7: The fit uncertainties for both WLS and GLS when the values of four of the data points are varied. The data covariance matrix, $\boldsymbol{\Sigma}$, was left unchanged. The fit and uncertainties are shown in (a) with the data points, and as percent uncertainty on the fit at each data point in (b). The change in the four values increased the residual sum of the squares, and so uniformly increased the WLS uncertainties. The GLS uncertainties, based on the data covariance matrix, did not change.

then the predicted residual matrix, $\boldsymbol{P}$, could be used in the fit uncertainty term. In the Hybrid Method, the fit uncertainty term $\hat{\sigma}^2\boldsymbol{W}^{-1}$ transfers the relative uncertainties of the data points onto the parameters. In this case, the predicted residual matrix $\boldsymbol{P}$ could transfer the interpolation accuracy onto the parameters, as it contains information about the magnitude and relative magnitudes of the predicted residuals. This would allow for the parameters that are most sensitive to regions that are accurately interpolated to have lower uncertainties than those sensitive to regions with worse interpolation. The exact formulation of this fit covariance term will be determined in future work. This is not trivial, as a covariance matrix needs to be positive semi-definite, and the independence of the two uncertainty sources needs to be ensured.

Proper quantification of regression uncertainties is important to many different types of experiments. For example, for experiments using high resolution gamma detectors like HPGe, curve fitting is employed for the efficiency, and sometimes for the determination of the counts in the photopeaks in the HPGe spectrum. In AA measurements, the activation at the end of the irradiation is determined based on an exponential fit to the measured activity over time. The determination of half-lives of isotopes is also done with fitted exponential functions. Monitor cross sections, like those available from the IAEA [6], often use fitting procedures to determine point-wise cross sections on energy grids that differ from the available experimental data. Finally, in many different experiments, the determination of the flux at specific neutron energies can be done using interpolation between data points measured with monitor reactions. For curves that are not fit for interpolation purposes, the Hybrid Method presented here would be appropriate. For example, the determination of counts under the peak and the half-life of an isotope require the uncertainty on the parameter values only. For the rest of the examples, the interpolation uncertainty is important and the extension of the Hybrid Method would be needed.

Chapter 7

Ratio Method for Estimating Uncertainty in Calculated Gamma Cascades

All of the uncertainty sources studied so far have been experimental, and necessary for understanding the precision of measured quantities. The evaluation process, however, often requires combining reaction modeling with the measured quantities. For example, partial gamma measurements, detailed in Section 2.2.4, produce cross sections for individual transitions that de-excite the product nucleus. The cross section for the reaction itself must be deduced from this information.

One simple method for deducing the cross section, which can be used in handful of situations, is to take the cross section of the lowest-lying level as an estimate of the channel cross section. This assumption may be valid with collective, even-even nuclei, where most of the gamma cascade intensity goes through the lowest 2^+ state. This method was used in a 2013 measurement of the inelastic cross section of ^{86}Kr done with the GEANIE spectrometer at LANSCE [194]. In this work, it was assumed that the probability of a cascade by-passing the first excited state was smaller than the considerable uncertainty on its cross section, which was about 10%. The large uncertainty on the transition from the first excited state to the ground state was due to contamination by another gamma from higher up in the level scheme, which was assumed to have about a 10% effect. The two uncertainties (the contaminating gamma and the missing transitions) are both asymmetrical in the same direction. The cross section of the transition between the first excited state and the ground state was therefore taken as the reaction cross section, with a 10% uncertainty.

The situation becomes more complicated when the lowest transition is not seen in experiments. This occurs for isotopes with a very low energy first excited state, such as ^{57}Fe, at 14.4 keV [195], and ^{238}U, at 44.9 keV [196]. Measurements of partial gamma cross sections typically do not include these transitions, and the conversion to the channel cross section must be done without them. There have been many attempts to do so, and a brief overview is given here, using examples with ^{57}Fe and ^{238}U.

The simplest situation is for an isotope with a well-known level scheme. This has been achieved up to the neutron separation energy, with considerable effort, for ^{57}Fe. This nearly complete level scheme is described in Reference [197], which also explains how it was then used to deduce the thermal capture cross section for ^{56}Fe. Thermal neutron capture on isotopes with spin-zero ground states (^{56}Fe, for example) excites a single level in the compound nucleus, here a $1/2^+$ level at 7646.2 keV. With a single capture state and a nearly-complete level scheme between that level and the ground state of ^{57}Fe, the reaction is almost entirely understood.The 14.4 keV gamma de-exciting the first excited state was not measured, so the known transitions directly feeding both the ground state and the first excited state were used to account for the overall feeding of the ground state. The first check of the internal consistency of the measured partial cross sections was a comparison of the intensity of the primary transitions (those de-exciting the capture state) with the intensity of the transitions directly feeding the ground and first excited states. They found that the intensity of the primary transitions was (98.5±1.3)% of the intensity of the ground and first excited states. This difference indicates that at least (1.5±1.3)% of the transition intensity de-exciting the capture state was not measured. However, there may be more missing intensity if not all of the transitions feeding the ground and first excited states were identified. The second check was to use the intensity balance,

$$\frac{\sum_{\gamma} \mathbb{P}(\gamma) \times E_{\gamma}}{100} \approx S_n, \tag{7.1}$$

which compares the overall total energy released in the reaction (S_n), with the probability-weighted energies, E_{γ}, of each individual gamma in the cascade (subscript γ). They found that the probability-weighted gamma energies added up to (98.9±0.01)% of the total energy released in the reaction. Finally, the measured gammas were put in order by intensity, and then an exponential was fit to the intensity vs. sequence number. The highest and lowest intensity gammas were not included in the fit, due to large deviations from the exponential curve. Separate curves were fit for the primary transitions, those feeding the ground state, those feeding the first excited state, and all of the transitions. The fitted curve for all transitions was then integrated out to an arbitrary maximum number of transitions (chosen to be 1000), and the difference was used to estimate the missing transitions. This result, about 1%, was close to the probability-weighted gamma energy comparison. This missing intensity was used as a correction, which does not appear to have any uncertainty. The final thermal cross section was presented with a 0.8% uncertainty, and it is noted that this result has a lower uncertainty than the previous measurements, which are both about 10% higher in magnitude. The probability-weighted gamma energy comparison is only approximate, but there is no discussion about the uncertainties induced by using that or the method of fitting with an exponential. In addition, this method is only valid when the level scheme and reaction are both well understood.

When that is not the case, the method to deduce the reaction cross section is considerably more complicated. For most nuclei, the level scheme is not known up to S_n, and for reactions with fast neutrons, various levels in the compound nucleus can be excited. For example, the inelastic scattering cross section for ^{57}Fe was measured at GELINA, using the GAINS spectrometer, in 2017 [198]. The 14.4 keV transition between the first excited state and the ground state was again not measured. The reaction cross section was calculated by summing the cross sections of the first two levels with the cross sections of transitions known to de-excite directly to the ground state, by-passing the first excited state. In total, the measured cross sections of four gammas were used, and the cross section of the first excited state was modeled using reactions codes EMPIRE [74] and TALYS [80]. An overall uncertainty of 10% was applied to the calculated 14.4 keV cross section, based on the overlap between the EMPIRE and experimental inelastic reaction results. There was limited description of the process used to quantify the overlap and determine the 10% uncertainty.

In the case of gamma cascades in deformed, fissionable nuclei, the modeling accuracy is often not sufficient to directly use calculated cross sections. This was discovered in the 2002 measurement of the ^{239}Pu(n,2n)^{238}Pu cross section with the GEANIE spectrometer at LANSCE [199]. The de-excitations of the first two excited states in ^{238}Pu were not seen in the experiment, leading to an even stronger dependence on the modeled gamma cascades. However, the model could not reproduce many of the measured gammas. A significant issue was seen with the ratios between the yrast[1] and off-yrast transitions. The "parallel paths" method was developed for this measurement, to combine the modeling and measurement in the most accurate way. All of the parallel transitions (non-coincident transitions) were summed together, which integrated over the incorrect intensity branching between those levels. The modeling code GNASH [127] was then used to calculate what percent of the intensity was missing from this sum. The calculated missing intensity was about 50% at the peak of the cross section ($E_n \approx 11$ MeV). There was no discussion of the uncertainties in this method, but two conditions under which this method would not work were stated. The first is if there was contamination in one of the stronger gammas, as these summation methods are all heavily based on the largest intensity transition. The second was if there were numerous decay paths that by-passed all of the levels used in the summation.

This same method was then applied for the measurement of the inelastic scattering cross section of ^{238}U with the GEANIE spectrometer in 2004 [47]. In this measurement, only the gamma from the first excited state was not seen, so the parallel gammas chosen were 16 measured gammas that fed the ground state and first excited state. Large discrepancies were again seen between the measured and modeled gamma cross sections. The GNASH calculation indicated that that sum represented about 70% of the total intensity, but the neutron energy dependence of the deduced reaction cross section did not seem consistent with an inelastic scattering cross section. More detail about the potential issues with this data set are given in the following work, which was published in 2019 [200]. This work provides a method for determining which measured gammas are the best for determining the reaction cross section, which is not always the highest intensity transition that was measured.

A recent publication [201] provides context and details about the partial gamma mea-

---

[1] "Yrast" levels refer to the lowest energy level of a particular J^π in a nucleus. For an even-even, deformed nucleus like ^{238}Pu, the even yrast levels are the rotational band built on 0^+ ground state.

surements and how modeling can be used to fill in the missing intensity when the level scheme is not well known, as in these cases. The focus is mainly on how the improvement of the modeling can improve the final cross section calculation, and the lack of methods for estimating these uncertainties is noted. The recent publication included in this chapter [200] provides a detailed, reproducible method that uses the aspects of the calculation that are the most consistent with the measured cross sections, as well as a new method to estimate the uncertainty on that cross section, based on the consistency between the measured and modeled cascades.

Relevant Publications:

Amanda M. Lewis, Lee A. Bernstein, Toshihiko Kawano, Denise Neudecker, "Ratio method for estimating uncertainty in calculated gamma cascades," The European Physical Journal A, vol. 55, pp. 141, 2019, `https://doi.org/10.1140/epja/i2019-12826-y`.

The text and figures of this paper (copyright Springer Nature 2019)[200], of which I was the primary author, are included in this chapter with the permission of all authors and with kind permission of The European Physical Journal (EPJ). The only changes made to the published article are alterations to some figures to better fit the page formatting, and renumbering of the references, equations, tables and figures.

7.1 Abstract

The assessment of uncertainty on deduced quantities obtained through both measurement and modeling must include contributions from both components. There are several methods to estimate the uncertainty due to modeling, such as the parametric uncertainty and that stemming from model bias. However, in the case where experimental data exists for partial cross sections, such as discrete gammas emitted in the de-excitation of the product nucleus following the reaction, the discrepancy between the measured and modeled gamma cascades provides more information and allows for uncertainty estimation that can account for all types of model and data uncertainty. This work presents a method for estimating that uncertainty, using ratios of gammas to get a measure of the accuracy of different parts of the modeled gamma cascade. The gamma with the lowest intensity uncertainty is shown to be the best for determining the channel cross section with realistic uncertainties, indicating that it should be used rather than the most intense gamma or a sum of gammas. This method provides both a simple procedure for calculating realistic uncertainties and identifies the best gamma for use in converting a set of measured partial gamma cross sections to the deduced total channel cross section.

7.2 Introduction

A realistic and complete uncertainty quantification is an essential part of the analysis of experimental data and requires careful consideration of all sources of statistical and systematic uncertainty [153]. Experimental results with total uncertainty values that do not account for all sources will tend to be weighted more heavily than they should be in comparison to other data sets with more complete uncertainty analysis, and can introduce biases into evaluations of nuclear reaction observables. This is especially true in cases such as cross sections where the experimental data are indirectly quantified and the conversion is not known. An example of this is inelastic scattering on ^{238}U, where the measurement of the de-excitation gammas is used to deduce the cross section, but it is not known what portion of the cross section is not seen. The inelastic scattering cross section is important for nuclear energy, criticality and neutronics applications, and it is important to understand what realistic uncertainties are [202].

Efforts have been made to begin to standardize the assessment of uncertainty in experimental measurements, such as templates for fission cross section measurements [160] and prompt fission neutron spectra measurements [203], among others [20, 204, 205]. These templates allow evaluators to account for all experimental uncertainty sources that are present in every measurement, and estimate missing sources if necessary.

However, some experiments also require modeled quantities in their analysis. In this case, it is important to propagate the uncertainty in the modeled quantity through to the final deduced quantity. Determining the uncertainty in a modeled quantity is difficult, owing to the various sources of possible uncertainty in the calculation—uncertainty in the parameter values, any data sets used for tuning or comparison, and even the physics of the model and its implementation in a code. In this paper, a method is presented to estimate the uncertainty on the deduced channel cross section which can account for all these sources of uncertainty but does not require that they be separated out and determined individually.

The method can be used with any gamma cascade model and any experiment that measured multiple gamma cross sections. The uncertainty values obtained will reflect the consistency between those measured and modeled gammas, and, thus, depends on the specifics of the measurement and selected model. For this reason, while the method is applicable for any combination of data and calculation, the uncertainty values presented here are tied to this particular data set and this particular calculation. The sensitivity of this uncertainty to the reaction code calculation will benefit evaluators searching for the best calculation to put into an evaluation as well as anyone trying to compare models and parameters that influence modeled gamma cascades.

7.2.1 Cross section measurements with discrete gammas

The experiments considered in this work are those that measure characteristic discrete gammas that de-excite the low lying excited states of the product nucleus. These characteristic gammas are used to determine the number of product nuclei produced by the reaction, which can then be used to deduce the cross section. These experiments are similar to activation measurements, which measure decay gammas in the de-excitation of the daughter of the product nucleus. In activation measurements, however, the intensities of the decay gammas are independent of the reaction that produced the product nucleus, making them well-suited for determination of the number of nuclei formed. Discrete gammas from non-elastic reactions are less straightforward to convert to reaction cross sections because the intensity of the gammas are dependent on the reaction type and incident particle energy. For these measurements, the partial cross section for each gamma is calculated using a nuclear reaction code and the calculated ratio to the total channel cross section is used to determine the reaction cross section for the channel producing that residual nucleus

One example is the 2004 Fotiades, *et al.*, measurement of neutron-induced inelastic scattering on ^{238}U between 1 and 100 MeV [47]. The partial cross sections for 24 discrete gammas in the low-lying level scheme of ^{238}U were measured and the reaction code GNASH [127] was used to model the gamma cascade in ^{238}U following the scattering reaction. The measured partial gamma cross sections were then converted to the inelastic channel cross section using the GNASH calculated intensities. In this experiment, significant discrepancies were seen between the measured and modeled partial gamma cross sections, so sixteen of the gammas that represented non-coincident "parallel paths" in the gamma cascade were summed together to integrate over the inaccuracies in the gamma cascade paths. The idea of "parallel paths" down the cascade is to find transitions that go directly to the ground state and do not feed each other, to avoid double-counting any transition strength. In this case, since the first excited state transition could not be measured, gammas de-exciting directly to the ground state and the first excited state were used.

7.2.2 Uncertainty propagation

The uncertainty on the final cross section value can be calculated by propagation of all sources through the equations used to calculate the cross section. In the case where the uncertainties on the non-linear terms (such as half-lives and irradiation time) are negligible, and all uncertainties are "small", a Taylor expansion can be used and the uncertainties propagated through to the cross section through the "Sandwich" formula [203]. The covariance between the channel cross section, σ, at two different incident neutron energy points i and j due to the uncertainty source x is

$$\mathrm{cov}_x(\sigma_i, \sigma_j) = \left.\frac{\partial \sigma}{\partial x}\right|_i \delta x_i \ \mathrm{corr}(x_i, x_j) \delta x_j \left.\frac{\partial \sigma}{\partial x}\right|_j , \tag{7.2}$$

where δx_i is the 1-sigma uncertainty on x at energy i and $\mathrm{corr}(x_i,x_j)$ is the correlation between the values of the uncertainty on x at energy i and energy j. In the case of uncertainty sources that are independent of each other, the full covariance matrix, V, is calculated by summing over all uncertainty sources for each energy point,

$$(V)_{i,j} = \sum_x \left.\frac{\partial \sigma}{\partial x}\right|_i \delta x_i \ \mathrm{corr}(x_i, x_j) \delta x_j \left.\frac{\partial \sigma}{\partial x}\right|_j . \tag{7.3}$$

The i,j-th element of the covariance matrix V represents the covariance between the cross section at energies i and j, and the diagonal element i,i represents the variance (the square of the uncertainty) of the cross section at the i-th energy point.

If there are correlations between uncertainty sources, such as between the measured detector efficiency at different gamma energies, then the covariance matrix is also summed over each combination of uncertainty sources,

$$(V)_{i,j} = \sum_x \sum_y \left.\frac{\partial \sigma}{\partial x}\right|_i \delta x_i \ \mathrm{corr}(x_i, y_j) \delta y_j \left.\frac{\partial \sigma}{\partial y}\right|_j , \tag{7.4}$$

where i and j represent neutron energy points and x and y represent uncertainty sources.

For a simple example, consider a cross section experiment that only has a systematic uncertainty in the mass, m, and statistical uncertainty in the counts, C. The i,j-th element of the covariance matrix would then be

$$\begin{aligned}(V)_{i,j} = {} & \left.\frac{\partial \sigma}{\partial m}\right|_i \delta m_i \ \mathrm{corr}(m_i, m_j) \delta m_j \left.\frac{\partial \sigma}{\partial m}\right|_j \\ & + \left.\frac{\partial \sigma}{\partial m}\right|_i \delta m_i \ \mathrm{corr}(m_i, C_j) \delta C_j \left.\frac{\partial \sigma}{\partial C}\right|_j \\ & + \left.\frac{\partial \sigma}{\partial C}\right|_i \delta C_i \ \mathrm{corr}(C_i, m_j) \delta m_j \left.\frac{\partial \sigma}{\partial m}\right|_j \\ & + \left.\frac{\partial \sigma}{\partial C}\right|_i \delta C_i \ \mathrm{corr}(C_i, C_j) \delta C_j \left.\frac{\partial \sigma}{\partial C}\right|_j . \end{aligned} \tag{7.5}$$

Statistical uncertainties, which are based on Poisson statistics, are usually independent of each other and all other sources of uncertainties. The mass uncertainty is sample-dependent, and so as long as the same sample and same uncertainty value was used for each energy data point, the uncertainty will be fully correlated between all points. The diagonal elements, $i = j$, are therefore

$$(V)_{i,i} = \left(\frac{\partial \sigma}{\partial m} \delta m\right)^2 + \left(\frac{\partial \sigma}{\partial C} \delta C_i\right)^2 , \tag{7.6}$$

and the off-diagonal elements, $i \neq j$ are

$$(V)_{i,j} = \left(\frac{\partial \sigma}{\partial m} \delta m\right)^2 . \tag{7.7}$$

This process should include all uncertainty sources that are not negligible. In the case of the ^{238}U inelastic scattering measurement, as in most cases of this type of measurement, the uncertainty on the reaction code calculated intensity was not included. This is not a negligible uncertainty, since the accuracy of modeled gamma cascades varies widely between isotopes and tuning is usually required to reproduce measured partial gamma cross sections. How to determine the true uncertainty on a modeled quantity such as this is not obvious. Therefore, the method presented in this paper focuses on estimating the inconsistency between the data and calculation and propagating that through to the channel cross section.

The Unified Monte Carlo methods (UMC-B/G) [22, 206], are another way to propagate modeling uncertainty onto a deduced quantity. These methods require that there are both calculated and measured values and uncertainties for the same observable. However, in this case there is no measurement of the observable of interest—the inelastic channel cross section. For this reason, it is necessary to first calculate that uncertainty on the link between the experimental data and the observable of interest, which is the intensity of the measured gamma or gammas. Other methods, such as Marginal Likelihood Optimization [207], require the Bayesian version of this discrepancy, $\mathbb{P}(D|M)$, the probability of the data given the model. While this result could be used to determine the likelihood of the modeled inelastic channel cross section based on the measured and modeled partial gamma cross sections, there still remains the open question of how to calculate $\mathbb{P}(D|M)$, as there are no analytical distributions. In this work, it is argued that the measure of probability, and eventually the uncertainty on the deduced quantity, should be based on the discrepancy between the measured and modeled cascades, and a method is presented to allow for systematic calculation of that discrepancy.

7.2.3 Modeling Uncertainties

Uncertainties in modeled quantities can arise from many sources. The uncertainty from the parameter values is in some ways the simplest to account for, as they can be propagated through the calculation using Monte Carlo methods. An example of this type of parametric uncertainty calculation is the Total Monte Carlo method (TMC) [208], in which correlations between parameters are introduced by the rejection of calculations that do not match available experimental data. The parametric uncertainty method is limited, however, in that it does not account for deficiencies in the physics or implementation of the model itself, and can only constrain parameters that are sensitive to the data that is available. Certain quantities that have not been measured or for which the portion of the observable not measured is not known will not be improved by this type of calculation. In addition, the basis of the parametric uncertainty method is the uncertainties in the parameters themselves. In some cases this can be quite simple—if a parameter value is measured directly or has been determined by a fitting procedure based on experimental data, then there is a clearly defined mean and uncertainty, and a Gaussian or log-normal distribution can be used based on the magnitude of the uncertainty [22]. However, there are many cases where there are no obvious distributions for the parameters, and the choice can have huge impacts on the final uncertainty.

The uncertainty in the model itself, based on incomplete understanding of the physics, necessary approximations or the implementation of the model into a code, is referred to as model deficiency or model defect. As explained in detail in Reference [209], it is very difficult to determine the extent of a model deficiency, as it requires determining a systematic deviation from trusted data sets and makes the assumption that the deviation from these trusted data sets is consistent with the deviation for the reaction of interest. This means that it is not easy to find data sets to use—they have to be determined to not have significant issues themselves, and the reaction needs to have characteristics similar enough that it can be trusted to reflect the modeling of the isotope of interest. In this case, that would require trusted data sets for actinide inelastic scattering, which are not numerous, or possibly trusted data sets for equally deformed rare earths. While these data sets are more plentiful, it would require the assumption that the fission channel does not affect the modeling of the inelastic scattering. Another method for model defect is Bayesian Monte Carlo (BMC) [210]. This method makes a trade-off between data trustworthiness and availability, since it is part of large calculation and it is not feasible to put in the same amount of time understanding the reliability of data sets discussed in Reference [209]. In these cases, as with the parametric uncertainty, the uncertainty calculation cannot be sensitive to quantities that are not well measured, such as inelastic scattering on fissionable nuclei.

In this specific case with measured partial gamma cross sections, there exists in these data more information about the modeling of this particular isotope than can be gained from either parametric or model deficiency uncertainty analysis. The discrepancies between the measured partial gamma cross sections and modeled partial gamma cross sections are immediately relevant to the reaction of interest, and are an integral measure of all of the sources of uncertainty—the model, the parameters, and issues with the data itself.

7.3 Uncertainty in gamma cascade calculations

Nuclear reaction codes such as GNASH, `CoH`$_3$ [79], EMPIRE [74] and TALYS [80] calculate the cross section of each discrete gamma by first determining the energy and spin distribution of the excited residual nucleus and then modeling the cascade of gammas down to the ground state. These calculations require optical model parameters and level densities to determine the spin distributions of the compound and residual nuclei, level density and gamma strength parameters to calculate the de-excitation process in the continuum, and discrete levels and branching ratios to calculate the gamma cascade at lower excitation energies. These inputs are mostly from phenomenological models and are often fit to experimental data, but do not have uncertainties that are propagated through to the calculated cross sections. The discrete level spin and parity assignments and branching ratios are one exception to this—they are taken from experimental measurements [11] but are used in the calculation without any uncertainties.

Parametric and model defect uncertainties, discussed in Section 7.2.3, are powerful tools when there is not enough information about a particular quantity, but are less efficient when there is directly relevant information such as measured partial gamma cross sections. The ratio method presented here makes use of this information to give a more informative result, and is general enough to account for parameter uncertainty, model defect uncertainty, and problems with the data that are not reflected in the experimental uncertainties. The uncertainty estimated for the calculated intensity value instead reflects the inconsistency between the gamma cascade calculation and the data set being used. The inconsistency between the data and calculation will be measured by ratios between gammas. Most experiments of this type measure numerous gammas from the nucleus of interest, and usually obtain enough to determine several ratios. Ratios between different gammas are a strong measure of the consistency between the modeled gamma cascade and measured gammas, as they are not highly affected by the competition between different reaction channels in the model. They are sensitive instead to the initial angular momentum distribution, the level density (both magnitude and spin distribution) and gamma strength of the product nucleus, and the branching ratios.

7.3.1 Choosing ratios

The measure of how well the modeled cascade matches the data is based on the comparison between ratios of the gamma of interest to several other gammas that are relevant. The set of gammas chosen for this purpose should be all measured gammas that de-excite to the same final level as the gamma of interest. This choice has two characteristics that make it a good measure: they are all parallel gammas, meaning that they necessarily probe different paths down the cascade, and this method pulls out separate “slices” of the cascade that can then be studied. The gamma that will be used for the conversion of the partial gamma cross section to the channel cross section is the “main” gamma of the slice, and the other gammas are the “comparison” gammas.

The calculation of direct inelastic components populating specific levels and transitions from the continuum that go directly to the ground state (and in this case, the first excited state as well) is much harder to constrain with experiments that only measure low-lying discrete transitions, and total inelastic channel measurements are needed to fully understand this component. This ratio method does not attempt to quantify the magnitude of this component, but rather finds the slices of the cascade that are the least affected by this miscalculation.

In the case where there are several gammas with cross sections large enough to be considered for the intensity calculation, this method allows for several slices of the cascade to be compared against each other, and the one that is the best modeled can be used.

7.3.2 Calculation of intensity uncertainty

For the main gamma of each slice, a reactions code is run to determine the intensity, I, of the gamma at each neutron energy (this can be done by calculating a partial gamma cross section and dividing it by the calculated channel cross section). Then, for the uncertainty on the intensity, the ratio of each comparison gamma to the main gamma is calculated at each neutron energy point. The same ratios are obtained from the measured data. Each ratio is one measure or observation of the inconsistency between the measured cascade and the calculated cascade, and they are averaged together to get the inconsistency value, $\bar{\Delta}$. The main gamma should be in the same position in the ratios, to allow for simple correlation calculation.

$\bar{\Delta}$ is a weighted average of the relative difference between the calculated ratios and the measured ratios, and the weights are the relative uncertainties on the experimental ratios. An example is shown here for a single slice, with n ratios, with index i representing the ratio of the main gamma to the i^{th} comparison gamma.

The ratio of the main gamma to the i^{th} comparison gamma for the calculated cascade is

$$R_i^{calc}(E_n) = \frac{\sigma_m^{calc}(E_n)}{\sigma_i^{calc}(E_n)}, \tag{7.8}$$

where $\sigma_m^{calc}(E_n)$ is the calculated partial cross section of the main gamma at neutron energy E_n, and $\sigma_i^{calc}(E_n)$ is the calculated partial cross section of the i^{th} comparison gamma at neutron energy E_n. The calculation for the experimental ratios are the same.

The difference between the measured and modeled ratio is calculated for each comparison gamma, i,

$$\Delta_i(E_n) = R_i^{exp}(E_n) - R_i^{calc}(E_n). \tag{7.9}$$

The relative differences are averaged together to determine the inconsistency value, $\bar{\Delta}$,

$$\bar{\Delta}(E_n) = \sum_{i=1}^{n} \frac{|\Delta_i(E_n)|}{R_i^{exp}(E_n)} w_i(E_n). \tag{7.10}$$

The weights, $w_i(E_n)$, are based on the relative uncertainty of the measured ratios

$$w_i(E_n) = \frac{R_i^{exp}(E_n)/\delta_i(E_n)}{\sum_{j=1}^{n} R_j^{exp}(E_n)/\delta_j(E_n)}, \tag{7.11}$$

where δ_i is the 1-sigma uncertainty of the experimental ratio with the i^{th} comparison gamma, which should account for the experimental correlations between the two gammas. The ratios with lower experimental uncertainty will be weighted more highly in the final inconsistency value, as they should be more reliable.

Combining Equations 7.10 and 7.11,

$$\bar{\Delta}(E_n) = \sum_{i=1}^{n} \frac{|\Delta_i(E_n)|}{R_i^{exp}(E_n)} \times \frac{R_i^{exp}(E_n) / \delta_i(E_n)}{\sum_{j=1}^{n} R_j^{exp}(E_n) / \delta_j(E_n)}, \tag{7.12}$$

and simplifying gives the final equation for the measure of the inconsistency between the calculated gamma cascade and the measured gamma cascade,

$$\bar{\Delta}(E_n) = \frac{\sum_{i=1}^{n} |\Delta_i(E_n)| / \delta_i(E_n)}{\sum_{j=1}^{n} R_j^{exp}(E_n) / \delta_j(E_n)}. \tag{7.13}$$

The inconsistency is then converted into a 1-sigma uncertainty by treating it like a measured bias that is not corrected for, as discussed in Appendix 1 of Reference [211]. The calculated inconsistency is truly a bias and is not symmetric, but it is treated here in the most conservative way and turned into a symmetric uncertainty that can be used in the many applications that cannot easily handle bias, but are equipped to deal with uncertainty. This treatment is both conservative in that it produces an uncertainty bar that is large enough to fully cover biases in both directions, and also in that it does not restrict this method to only be used when the measurement is fully trusted and the model is expected to be the source of the discrepancy. Therefore, the 1-sigma relative uncertainty of the calculated intensity of the main gamma, I, is calculated by dividing the discrepancy by the coverage factor of the "extent" of a Gaussian (the FWHM), 2.35, giving,

$$\delta_I(E_n) = \frac{\bar{\Delta}(E_n)}{2.35}, \tag{7.14}$$

which is determined for each neutron energy data point.

Three potential cascade slices have been studied from the Fotiades *et al.* data set using this method—those with the largest two measured gammas and a third that de-excites directly to the ground state. The gamma with the largest cross section (although likely not the lowest statistical uncertainty due to internal conversion) that was measured in the experiment is the 103.5 keV gamma connecting the yrast 4^+ state to the yrast 2^+, which is shown in Figure 7.1 along with the six comparison gammas that make up that slice of the cascade. The gamma with the next largest cross section is the 159.0 keV gamma, which connects the yrast 6^+ to the yrast 4^+. This gamma and the four others that make up this slice are shown in Figure 7.2. Finally, a third gamma was chosen that de-excites to the ground state, to capture the lowest spin slice. The largest measured transition to the ground state is the 680.1 keV gamma, coming from the first 1^- state, and is shown in Figure 7.3 along with the two other transitions to the ground state. The low number of comparison gammas to use for the uncertainty calculation, and the fact this slice only includes two initial spin states, indicates that this is likely not a good choice for the conversion to the channel cross section, but the calculations have been done as an example. It is also likely to produce an uncertainty that may not be accurate—this method is more accurate with at least three parallel gammas and more than two initial state spins.

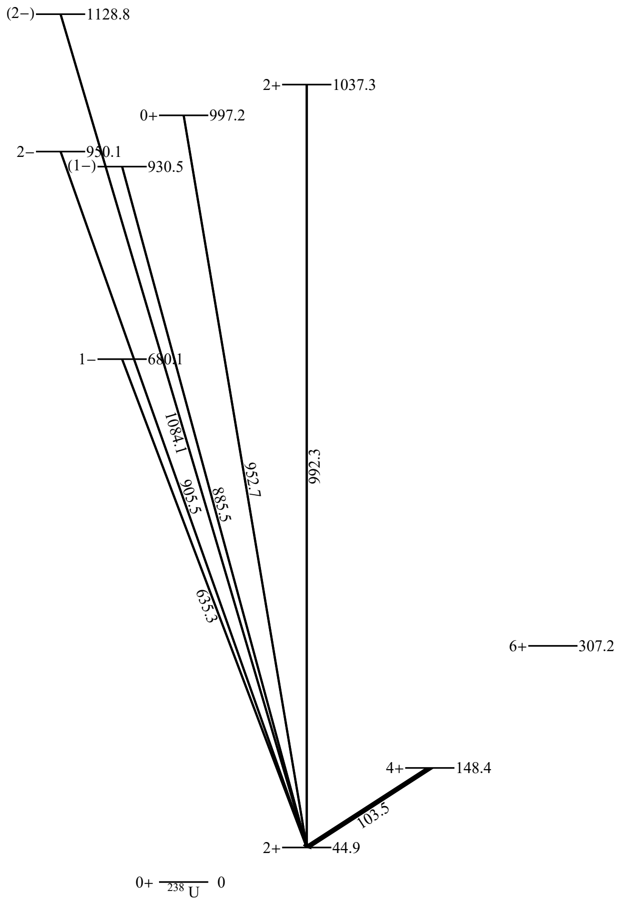

Figure 7.1: Partial level scheme showing the gamma transitions used to determine the uncertainty on the intensity of the main gamma in this slice, the 103.5 keV gamma. The 103.5 keV gamma is shown in bold, connecting the yrast 4^+ level to the yrast 2^+ level. The other comparison gammas all come from higher energy, lower spin states.

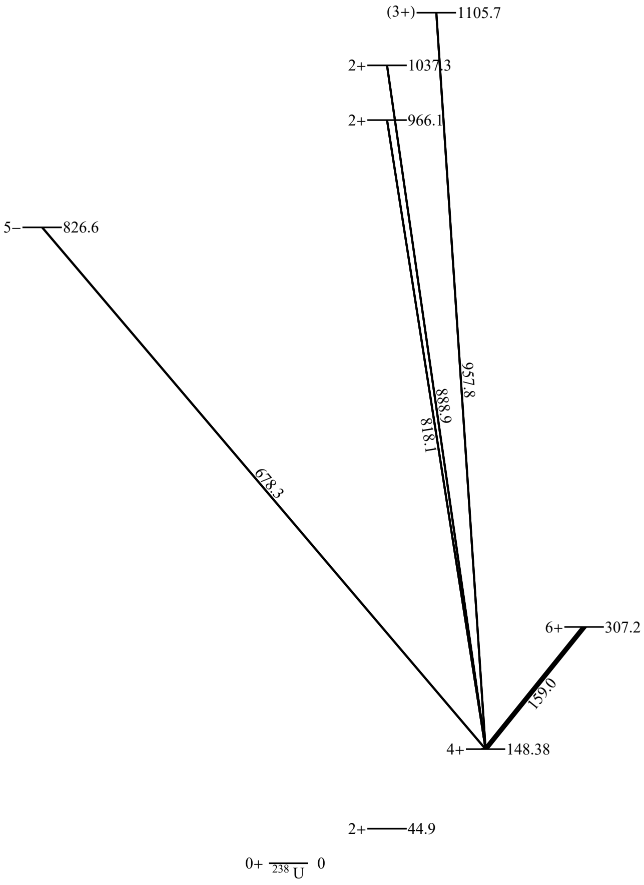

Figure 7.2: Partial level scheme showing the gamma transitions used to determine the uncertainty on the intensity of the main gamma of this slice, the 159.0 keV gamma. The 159.0 keV gamma is shown in bold, connecting the yrast 6^+ level to the yrast 4^+ level. There are four other gammas, three of which come from lower spin states and one from a high spin negative parity state.

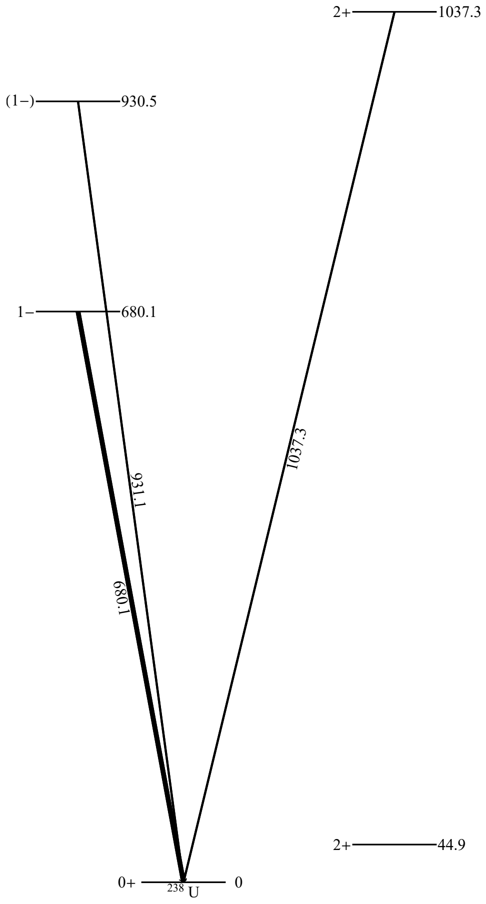

Figure 7.3: Partial level scheme showing the gamma transitions used to determine the uncertainty on the intensity of the main gamma of this slice, the 680.1 keV gamma. The 680.1 keV gamma is shown in bold, connecting the first 1^- level to the ground state. There were only two other measured gammas that go to the ground state, and two of the three gammas come from 1^- states, so this may not be a representative slice.

The reaction code `CoH`$_3$ was used for the calculations of the inelastic and partial gamma cross sections, using a tuned calculation as described in Reference [212]. The tuning of this calculation was an attempt to improve the modeling of the measured cross sections in all channels and may have improved the gamma cascade modeling. If the tuning has produced gamma cross sections that are closer to the data, the uncertainty values calculated for this example will be lower than they would be with a default calculation, but the method can be used with either model. For each main gamma, the intensity was calculated by dividing the partial gamma cross section by the channel cross section. The uncertainty on the intensity for each of the three main gammas was then calculated using the procedure explained above, with the final relative uncertainty coming from Equation 7.14. For the 103.5 keV gamma, the uncertainty on the intensity, shown in Figure 7.4a, was over 50% for all data points. This massive uncertainty is due to the code calculating a partial cross section for the 103.5 keV line that is much larger than the measurement. As this calculated uncertainty is dependent on the reaction code calculation, this large uncertainty could be decreased by changing the calculation in such a way as to improve the match with the measured 103.5 keV gamma cross section. This method both encourages the user to improve their modeling and search out possible issues with the experimental data, and also provides insights into where the largest discrepancies are.

For the purposes of decreasing the uncertainty, an alternative to changing the calculation is to look for parts of the cascade that are more accurately modeled with the current calculation. For the 159.0 keV gamma, the uncertainty on the intensity was much lower, below 30% for all data points, as shown in Figure 7.4b. The calculated gamma cascade was more well-balanced between the four gammas in that slice, leading to a smaller uncertainty overall. Finally, for the 680.1 keV gamma, in Figure 7.4c, the intensity was very small and the uncertainty very large. The calculated gamma cascade seemed to be in line with the measured partial cross sections below 3 MeV, but at higher energies the 680.1 keV cross section was over-predicted and the two comparison gammas were under-predicted. The differences between the calculated and measured ratios were larger than the experimental uncertainties on the ratios, leading to a very large intensity uncertainty.

7.3.3 Correlations between energy points

The use of multiple ratios allows for a simple calculation of correlations between the intensity values at different neutron energies. Each term of the sum in Equation 7.13, without the application of the absolute value function, represents one observation of the inconsistency between the modeled and measured cascade, and can be used to calculate a correlation matrix. An example of the the array is shown in Table 7.1.

This method allows for the calculation of the correlation between the magnitude and sign of the difference between the modeled and measured cascades. The correlations were calculated for all three of the main gammas considered from the Fotiades *et al.* measurement, and the correlation matrix for the 159.0 keV gamma is shown in Figure 7.5. The intensity values above and below 3 MeV appear to be in groups, with positive correlations amongst

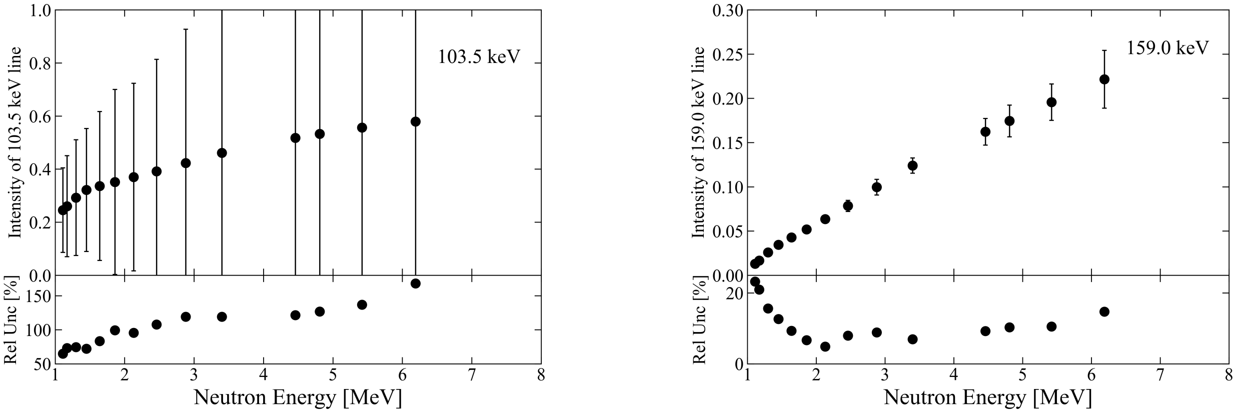

(a) The intensity for the 103.5 keV gamma

(b) The intensity for the 159.0 keV gamma

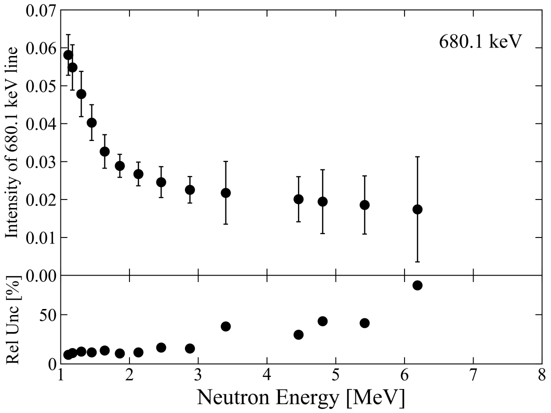

(c) The intensity for the 680.1 keV gamma

Figure 7.4: Comparison of the calculated intensities for each of the three main gammas studied, along with their uncertainties based on the ratio method. Below the main plots are the relative uncertainties, as percents. (a) The intensity for the 103.5 keV gamma. (b) The intensity for the 159.0 keV gamma. (c) The intensity for the 680.1 keV gamma.

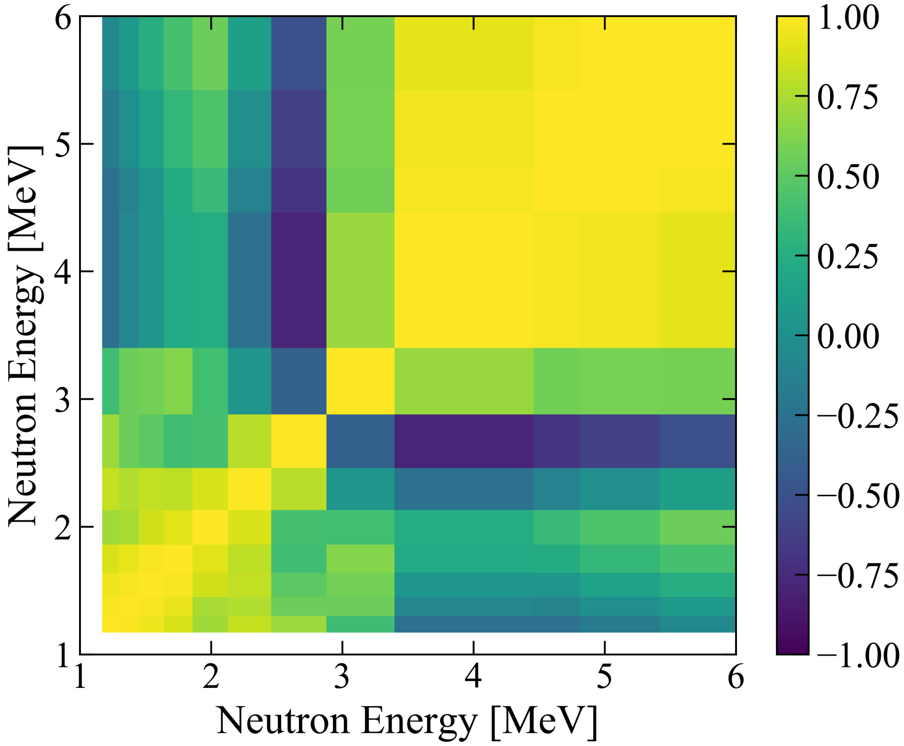

Figure 7.5: Correlation matrix for the intensity values calculated for the 159.0 keV gamma. The correlations between the data points above 3 MeV are positively correlated, as are the data points below 3 MeV, but between the groups are negative correlations. This represents the fact that the accuracy of the calculated gamma cascade above and below 3 MeV are not entirely related for the four comparison gammas used for the uncertainty calculation.

themselves, and negative correlations with the intensity values in the other group. This shape comes from the interesting trend among all of the gammas in that slice, where the over- or under-prediction of the cross section by the code was not consistent between the two energy regions.

7.4 Conversion to channel cross section

The purpose behind all of this work, and behind the use of modeled quantities in this type of experiment, is to convert the measured quantity, the partial gamma cross sections, into a deduced quantity, the channel cross section, for a particular experiment. This can be done by dividing the measured partial cross section by the modeled intensity, but the choice of which,

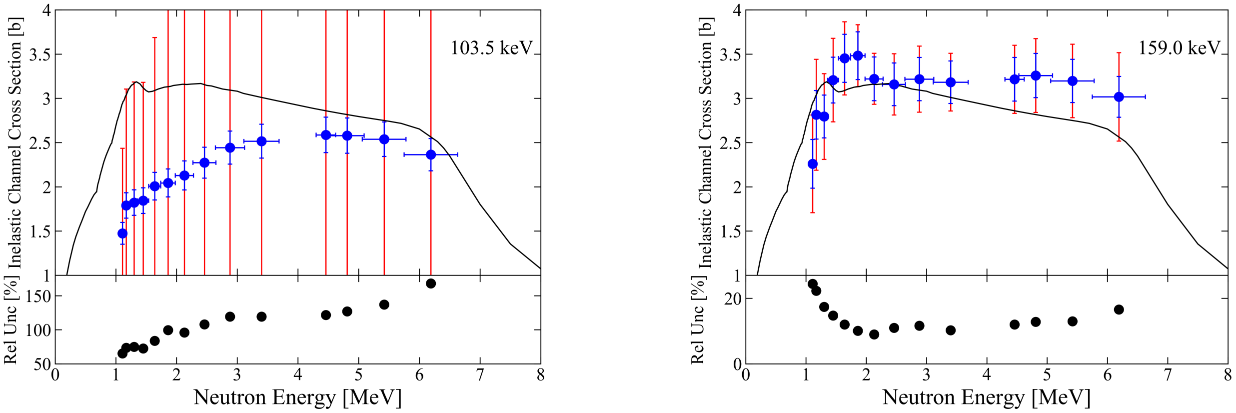

(a) from the 103.5 keV gamma (b) from the 159.0 keV gamma

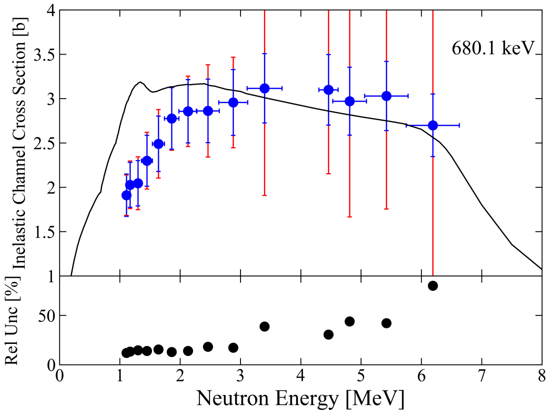

(c) from the 680.1 keV gamma

Figure 7.6: Comparison of the inelastic channel cross section calculated with the three different main gammas to the ENDF/B-VIII.0 evaluation. The black solid lines are the evaluation and the blue data points are the calculated channel cross section based on the measured partial gamma cross section and the calculated intensity of that gamma. The blue error bars represent the propagation of the experimental uncertainty alone, while the red (larger) error bars represent the total uncertainty with both the experimental and modeling components. Below each main plot is the relative uncertainty of the red error bars. The channel cross section (a) calculated from the measured 103.5 keV gamma partial cross section, (b) calculated from the measured 159.0 keV gamma partial cross section, and (c) calculated from the measured 680.1 keV gamma partial cross section.

Table 7.1: Array of observations used to calculate correlations between the neutron energy points for the fractional feeding intensity uncertainty. Here, $d(E_n) = \left(\sum_{j=1}^{3} {}^{R_j^{exp}(E_n)}/_{\delta_j(E_n)}\right)^{-1}$ is the denominator of Equation 7.13.

	ratio 1	ratio 2	ratio 3	…
E_1	$\frac{\Delta_1(E_1)}{\delta_1(E_1)}d(E_1)$	$\frac{\Delta_2(E_1)}{\delta_2(E_1)}d(E_1)$	$\frac{\Delta_3(E_1)}{\delta_3(E_1)}d(E_1)$	…
E_2	$\frac{\Delta_1(E_2)}{\delta_1(E_2)}d(E_2)$	$\frac{\Delta_2(E_2)}{\delta_2(E_2)}d(E_2)$	$\frac{\Delta_3(E_2)}{\delta_3(E_2)}d(E_2)$	…
⋮	⋮	⋮	⋮	⋱

or how many, gammas to use must be made. Often the measured gamma with the largest cross section is chosen, as it is thought to best represent the cascade. Another method, and the one used in the original work by Fotiades *et al.*, is to sum together as many parallel gammas as possible, as this sum should contain the total amount of information about the cascade that is known from the experiment. Using this ratio method to calculate intensity uncertainties, it can be shown that the best method, with this data set and calculation, is to use a single gamma, and not necessarily the largest one, to determine the channel cross section.

7.4.1 Choosing the best gamma

The best gamma to use for the conversion to channel cross section should be the main gamma with the smallest intensity uncertainty. The gamma with the smallest uncertainty would be the first choice for anyone looking to produce a channel cross section with reasonable uncertainties, but the choice also has deeper reasoning. The gamma with the smallest intensity uncertainty comes from the slice of the gamma cascade that is the most consistent with the data, and therefore is likely the least affected by the issues described in Section 7.3.1 with direct and continuum feeding. This is the part of the cascade that should be trusted the most, and so should be the part used for this calculation.

To show this, the channel cross section was calculated for each of the three main gammas from the Fotiades *et al.* measurement, and each are compared to the ENDF/B-VIII.0 [1] evaluation, which is a physically reasonable evaluation of the cross section that is based on physical models, direct measurements below the fission threshold, and experimental constraints from other channels. The partial gamma cross sections that are studied here were not used in the evaluation [213]. The 103.5 keV transition, which is the single gamma that would most likely be chosen since it has the largest cross section of all of the measured gammas, produces a channel cross section that does not follow the shape of the evaluated cross section, as seen in Figure 7.6a. The evaluated cross section rises to its maximum around 1.5 MeV and then slowly decreases until the channel begins to close around 6 MeV. The calculated channel cross section instead increases for most of the energy region, which is not a physical shape for this cross section. The very large uncertainty, which is even larger than the discrepancy, would successfully dissuade the use of this gamma even without the comparison.

As expected, the uncertainties on the channel calculated from the 680.1 keV gamma do not adequately represent the large discrepancy with the evaluation, seen in Figure 7.6c. This slice only had two gammas for comparison, and both came from the same spin—they were not representative enough of the cascade to allow for the calculation of a realistic uncertainty.

The 159.0 keV transition, Figure 7.6b, which has the smallest intensity uncertainty, produces a channel cross section that is the most similar to the evaluated cross section. The energy dependence of the channel cross section is correct, and in the regions where the data points are furthest from the evaluation (the highest and lowest energy points) the uncertainty is largest and is representative of the discrepancy. This gamma, which is in the most accurately modeled part of the gamma cascade with this particular calculation, also gives the most accurate and realistic channel cross section when combining this measurement and model.

7.4.2 Summing multiple gammas

In the original experimental work, instead of using a single gamma, sixteen gammas that represented parallel paths through the cascade were chosen and summed together to try and integrate over incorrect modeling of the paths down the cascade. The sum of the measured partial gamma cross sections was then divided by the GNASH calculation of the intensity of all of those paths to obtain the channel cross section. This "parallel path" method was repeated using `CoH`$_3$ to calculate the intensity of the sum of the measured partial gammas, and compared with the channel cross section from the 159.0 keV gamma based on the ratio method. The gammas chosen in that work were: 103.5, 635.2, 680.1, 687.0, 885.5, 905.2, 922, 931.1, 952.7, 992.3, 1015.3, 1037.4, 1060.3, 1084.1, 1437.4 and 1485.3 keV. In the comparison done in this work, all of the same gammas have been used with the exception of the 687.0, 922 and 1015.3 keV gammas, as the experimental data for these lines was not included in the EXFOR [13] compilation, and the 1437.4 keV and 1485.3 keV gammas, as they were above the energy limit in the `CoH`$_3$ calculation for discrete gamma cascade calculation. The comparison between the channel from the summation, the channel from the single 159.0 keV gamma, and the ENDF/B-VIII.0 cross section are shown in Figure 7.7. While the summed cross section does a better job representing the channel cross section than the 103.5 keV gamma alone did, it is not as physical as the channel from the 159.0 keV line. The uncertainties on the summed cross section are only experimental as there is no way to calculate ratios to parallel gammas.

The idea that the sum of all of the gammas integrates over incorrect cascade modeling is true for some of the cascade problems, but not for the issue of the direct and continuum transition cross section components discussed in Section 7.3.1. In addition, these sums are dominated by the largest partial cross sections—in this case, the 103.5 keV gamma has a maximum cross section of about 1500 mb, the 159.0 keV gamma peaks at around 700 mb, and all other gammas are less than 200 mb. Large issues with the largest cross sections therefore cannot be compensated for by the other gammas, and so the sum has similar problems to the single largest gamma. The gamma that has the smallest intensity uncertainty, which represents the slice of the cascade that is the most accurately modeled, is the best method to get a realistic channel cross section from a single data set of measured partial gamma cross sections. In many cases, if the lowest-lying transition is well-modeled and not highly internally converted, it will likely be the gamma with the smallest total uncertainties due to small experimental uncertainties and the collection of the cascade into this low-lying transition. In that case, the summation method would give a similar channel cross section, due to the lowest-lying transition dominating the sum. However, the ratio method with a single gamma should still be used, to allow for the estimation of the intensity uncertainty. There should not be many cases where the summed cross section is better than any possible cascade slice, with the exception of experiments with few gammas measured. In most cases, the dominant low-lying yrast band transitions, like the 103.5 keV and 159.0 keV gammas here, will either be modeled well, and then the slice including the low-lying transitions is at least as accurate as the sum, or are modeled poorly and adding the much smaller parallel transitions will not substantially improve the result.

7.5 Conclusions

Realistic and complete uncertainty analysis requires the assessment of all sources of uncertainty, including uncertainty on modeled quantities. In this work, a method is presented to estimate the uncertainty in one particular modeled quantity—the intensity of a de-excitation gamma in the product nucleus after a reaction. The uncertainty is estimated by the inconsistency between the measured and modeled gamma cascades, which is based on ratios of gammas. This method also allows for the identification of the parts of the gamma cascade that are well modeled and should be used in the calculation of the total channel cross section. The ^{238}U inelastic scattering partial gamma measurement by Fotiades *et al.* is used as an example, and the uncertainty on the intensity is calculated for three largest measured transitions, the 103.5 keV gamma, the 159.0 keV gamma and the 680.1 keV gamma. The 159.0 keV transition, which had the smallest intensity uncertainty of the three, also reproduced the ENDF/B-VIII.0 evaluation the best, indicating that it should be used instead of the 103.5 keV gamma, which had the largest cross section. The 159.0 keV gamma, with incorporated intensity uncertainty, also reproduced the evaluated cross section better than the sum of all parallel gammas, a method employed in the original work to minimize modeling issues. This method provides a way to estimate a very important uncertainty, that of the

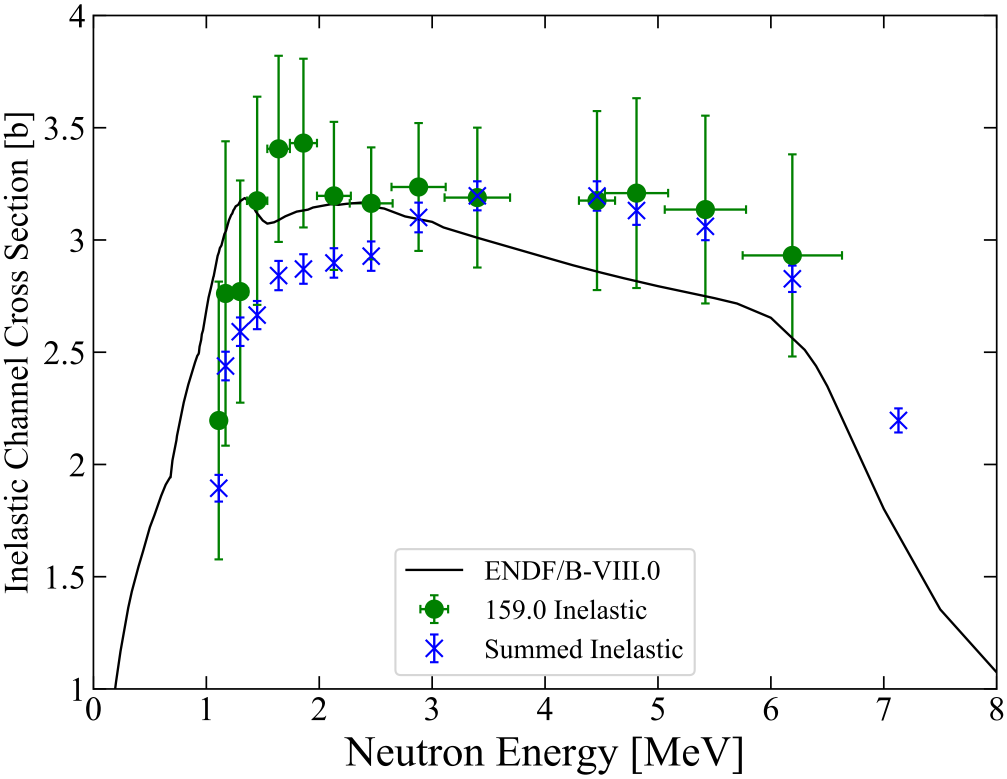

Figure 7.7: Plot of the inelastic channel cross section calculated by summing of the parallel gammas as done in the Fotiades *et al.* measurement, and calculated from the 159.0 keV gamma as done in Section 7.3.2. Both are compared to the ENDF/B-VIII.0 evaluation. At the lower neutron energies the summing method produces a cross section that is much lower than the evaluated cross section and has unrealistically small uncertainties. The ratio method produces a channel cross section that is closer, and has uncertainties that are much more representative of the difference. For neutron energies above 3 MeV, both methods produce channel cross sections that are very similar in magnitude but the ratio method again produces uncertainties that are more realistic.

modeled gamma intensity, and also identifies which gamma should be used in the conversion from partial gamma cross sections to channel cross section, which will allow for more accurate channel cross section results with more realistic uncertainties from such discrete gamma measurements.

7.6 Additional Discussion

The focus of the published paper was on the determination of the ^{238}U inelastic scattering cross section based on one experimental data set, but this method is applicable to any partial gamma measurement, as long as enough gamma transitions were measured. In the case of well-known level schemes, such as the thermal neutron capture cross section of ^{56}Fe, the methods used in Reference [197] are likely more accurate, as they use all of the available information. However, in some cases the use of all of the available information actually leads to a less accurate cross section. This method can be used to determine if this is the case, and then calculate the cross section with a subset of the cascade.

One large issue with the 2004 ^{238}U reaction cross section calculation was a strange energy dependence in the measured 103.5 keV gamma, which is the transition between the yrast 4^+ level and the yrast 2^+ level. This was the largest intensity measured gamma, so its energy dependence effectively determined the energy dependence of the sum of parallel gammas. It was discovered after the publication of this work that there was potential contamination in the 103.5 keV gamma. This is based on the energy dependence of the measured cross section, which increases relatively slowly and then peaks around 5 MeV. This is inconsistent with the expected behavior of this reaction, which peaks around 2 MeV and then levels off. The population of this level is not expected to track the reaction cross section perfectly, but it should peak at a lower energy than 5 MeV. It is also too consistent with the behavior seen in the yrast 6^+ to yrast 4^+ transition, which also peaks around 5 MeV. The peak of the population of the higher-spin 6^+ level should be at a higher neutron energy than the 4^+ level. The non-physical energy dependence of the reaction cross section determined by the parallel paths method in Reference [47] is shown in Figure 7.7. The inelastic channel based on the parallel paths method (blue x's) is lower than expected below its peak at 5 MeV, and is higher than expected beyond the peak. The inelastic scattering reaction cross section determined by the 159.0 keV gamma has the expected energy dependence over the entire region. The ratio method, therefore, provides a way to avoid the worst modeled and the worst experimentally measured gammas, and accounts for the remaining discrepancies with a straightforward uncertainty calculation.

Using this method, the 2004 data set is still able to provide a reaction cross section that is physical, with the expected energy dependence. This is due to the use of only a subset of the cascade, specifically the slice of the 150.0 keV gamma. The probable measurement contamination in the data set is avoided, and the best parts of the experiment and model are combined into a physical cross section with realistic uncertainties.

Chapter 8

Conclusions

Experimental uncertainties have significant impacts on evaluated nuclear data uncertainties, so it is important that they are consistent, complete, and realistic. In this thesis, all three aspects have been addressed, and several new methods for uncertainty quantification are presented.

The experimental uncertainty templates are useful for evaluators when comparing data sets, as they can help to ensure that the analysis is complete. Two templates are presented here, for total cross section and capture cross section measurements. Total cross sections are almost always measured using the transmission method, so the template focuses on that one experiment type. The information that is needed by the evaluator to properly apply the template is discussed first, followed by the template recommendations for uncertainty values and correlations. For transmission measurements, the background is often the dominant source of uncertainty, and is based on the method used. The template recommends an uncertainty below 3% only if the saturated resonance technique is used, and higher otherwise. This shows the value of both the information needed and the template of uncertainties in the handling of experimental data sets.

A second template for capture cross section measurements is presented, which covers five different experiment types. The measurement types and the template are split up by energy region. The flux and detector efficiency uncertainties are significant in these measurements, and the template allows evaluators to ensure that these two important sources are properly accounted for. The uncertainty on the detector efficiency in the resonance region should be studied further, as it relies on simulations of gamma cascades, whose accuracy varies between isotopes.

The use of a literature review of uncertainties in the creation of the templates is introduced. In this case, the EXFOR database was used to perform the literature search, and a new parsing script was written for the purpose of extracting the free-form uncertainty information in the database. Distributions of uncertainties were compiled for the important uncertainties in activation analysis and partial gamma measurements. Some of the sources of uncertainty do not lend themselves well to a literature distribution, such as counting statistics or nuclear data uncertainties. However, the distributions that were compiled will be valuable to evaluators. One purpose of the templates is to determine whether the uncertainties quoted in publications are realistic, and the full distribution allows for proper checking of uncertainties that can span orders of magnitude. A literature review such as this should be included as part of the template creation process, but does not replace the "expert judgment" that goes into the process. An example of the importance of expert judgment is for the uncertainty on the efficiency of a HPGe or Ge(Li) detector, which should be split into three distinct gamma energy regions but rarely is in the literature.

The uncertainty on the efficiency of a HPGe or Ge(Li) detector is explored in detail, as it is a significant uncertainty in many experiments. Two methods to calculate a data covariance matrix are discussed, and recommendations are made for some uncertainty magnitudes and their correlations. A new method to estimate correlations between gamma intensities in calibration sources is presented, and the calculated matrices are included for three of the most common calibration sources, ^{152}Eu, ^{133}Ba and ^{60}Co. The regression uncertainties calculated with typical curve fitting routines are explained, and a new method for regression uncertainty quantification is developed that is more appropriate for curve fitting in the physical sciences. Future developments to the method are discussed, to calculate more accurate interpolation uncertainties.

Finally, an uncertainty specific to partial gamma measurements is discussed. For these experiments, the cross sections of individual de-excitation gammas are measured and combined with a gamma cascade model calculation to deduce the reaction cross section. This method is relevant to Gen IV reactors, as it is one of the best ways to measure critical cross sections such as inelastic scattering on actinides. A new method to select which experimental information is used and how to estimate the uncertainties is presented. In previous work, it was considered important to include as much of the experimental information as possible. It is shown here that a more accurate cross section results from only using the subsets of the cascade where the calculation reproduces the experimental data. Large discrepancies can be caused by inaccurate cascade modeling or by problems with the experimental data, and this method avoids these problem areas. The uncertainty on the deduced cross section is based on a simple calculation of the discrepancy between the calculation and experimental data in the region chosen, and represents how well the cross section is known. An example is shown where a data set that has significant unexplained problems in the strongest gamma transition is still able to provide an accurate channel cross section with realistic uncertainties.

All of the presented methods will help to ensure that the experimental data used in evaluations have realistic uncertainties. Improving the uncertainties on evaluations that are based on experimental data is the first step to improving entire library. More work still needs to be done on the model uncertainty front for evaluations based on theory, such as ^{35}Cl(n,p) and many charged particle reactions in TENDL. Realistic evaluation uncertainties will benefit all of the fields that are using nuclear data. In the nuclear energy field, sophisticated uncertainty analysis methods have been developed, but are only as accurate as the nuclear data uncertainties that they propagate. Accurate experimental uncertainties will allow for realistic evaluation uncertainties that can be propagated to the measures of reactor performance which impact the reactor design. This will allow for designs that behave as expected, and will enable nuclear power to be an integral part of the solution to climate change.

Bibliography

[1] D. A. Brown, M. B. Chadwick, R. Capote, et al., ENDF/B-VIII.0: The 8th Major Release of the Nuclear Reaction Data Library with CIELO-project Cross Sections, New Standards and Thermal Scattering Data, Nuclear Data Sheets 148 (2018) 1–142. `doi:10.1016/J.NDS.2018.02.001`.

[2] K. Shibata, O. Iwamoto, T. Nakagawa, et al., JENDL-4.0: A new library for nuclear science and engineering, Journal of Nuclear Science and Technology 48 (1) (2011) 1–30. `doi:10.1080/18811248.2011.9711675`.

[3] A. Koning, R. Forrest, M. Kellett, et al., The JEFF-3.1 Nuclear Data Library - JEFF Report 21, Tech. rep. (2006). `doi:ISBN92-64-02314-3`.

[4] S. F. Mughabghab, Atlas of Neutron Resonances, 6th Edition, Elsevier, Amsterdam, 2018. `doi:10.1016/C2015-0-00522-6`.

[5] R. A. Forrest, C. Kalbach Walker, M. Avrigeanu, et al., FENDL-3 Library / INDC(NDS)-0645, Tech. rep., IAEA (2013).
URL `https://www-nds.iaea.org/fendl/`

[6] A. Hermanne, A. V. Ignatyuk, R. Capote, et al., Reference Cross Sections for Charged-particle Monitor Reactions, Nuclear Data Sheets 148 (2018) 338–382. `doi:10.1016/j.nds.2018.02.009`.

[7] H. D. Choi, R. B. Firestone, R. M. Lindstrom, et al., Database of Prompt Gamma Rays from Slow Neutron Capture for Elemental Analysis, IAEA, Vienna, 2007.
URL `http://www-pub.iaea.org/MTCD/publications/PDF/Pub1263_web.pdf`

[8] International Reactor Dosimetry File 2002 (IRDF-2002), no. 452 in Technical Reports Series, IAEA, Vienna, 2006.

[9] A. Trkov, P. Griffin, S. Simakov, et al., IRDFF-II: A New Neutron Metrology Library, Nuclear Data Sheets 163 (2020) 1–108. `doi:10.1016/j.nds.2019.12.001`.

[10] M. R. Bhat, Evaluated Nuclear Structure Data File (ENSDF), in: S. M. Qaim (Ed.), Nuclear Data for Science and Technology, Springer, Berlin, Heidelberg, 1992, pp. 817–821. `doi:https://doi.org/10.1007/978-3-642-58113-7_227`.

[11] R. Capote, M. Herman, P. Obložinský, et al., RIPL – Reference Input Parameter Library for Calculation of Nuclear Reactions and Nuclear Data Evaluations, Nuclear Data Sheets 110 (12) (2009) 3107–3214. `doi:10.1016/j.nds.2009.10.004`.

[12] J. B. Briggs, et al., International Handbook of Evaluated Criticality Safety Benchmark Experiments, Tech. rep., NEA/NSC/DOC(95)04/I, Paris, France (2004).

[13] V. Zerkin, B. Pritychenko, The experimental nuclear reaction data (EXFOR): Extended computer database and Web retrieval system, Nuclear Instruments and Methods in Physics Research Section A: Accelerators, Spectrometers, Detectors and Associated Equipment 888 (2018) 31–43. `doi:10.1016/J.NIMA.2018.01.045`.

[14] NNDC, XUNDL: Experimental Unevaluated Nuclear Data List Search and Retrieval, Tech. rep., Brookhaven National Laboratory, Upton, NY.
URL `https://www.nndc.bnl.gov/ensdf/ensdf/xundl.jsp`

[15] A. Koning, D. Rochman, J.-C. Sublet, et al., TENDL: Complete Nuclear Data Library for Innovative Nuclear Science and Technology, Nuclear Data Sheets 155 (2019) 1–55. `doi:10.1016/j.nds.2019.01.002`.

[16] L. A. Bernstein, D. A. Brown, A. J. Koning, et al., Our Future Nuclear Data Needs, Annual Review of Nuclear and Particle Science 69 (1) (2019). `doi:10.1146/annurev-nucl-101918-023708`.

[17] C. D. Werner, et al., MCNP Users Manual - Code Version 6.2 Los Alamos National Laboratory Report LA-UR-17-29981, Tech. rep. (2017).

[18] CSEWG Covariance Committee, Guidance on Generating Neutron Reaction Data Covariances for the ENDF/B Library, Tech. rep., Brookhaven National Laboratory (2013).
URL `http://www.nndc.bnl.gov/csewg/covdocs.jsp`

[19] P. Obložinský, M. Herman, S. F. Mughabghab, Evaluated Nuclear Data, in: Handbook of Nuclear Engineering, Springer US, Boston, MA, 2010, Ch. 2, pp. 83–187. `doi:10.1007/978-0-387-98149-9_2`.

[20] L. C. Leal, K. H. Guber, D. Wiarda, et al., ORNL Resolved Resonance Covariance Generation for ENDF/B-VII.1, Nuclear Data Sheets 113 (12) (2012) 3101–3119. `doi:10.1016/J.NDS.2012.11.006`.

[21] M. Herman, M. Pigni, P. Obložinský, et al., Development of Covariance Capabilities in EMPIRE Code, Nuclear Data Sheets 109 (12) (2008) 2752–2761. `doi:10.1016/j.nds.2008.11.005`.

[22] D. Smith, Argonne National Laboratory Report ANL/NDM-166, Tech. rep. (2008).
URL `https://www.ne.anl.gov/capabilities/nd/reports/ANLNDM-166.pdf`

[23] IPCC, Climate Change 2014: Synthesis Report. Contribution of Working Groups I, II and III to the Fifth Assessment Report of the Intergovernmental Panel on Climate Change, Tech. rep., IPCC, Geneva, Switzerland (2014).
URL `https://www.ipcc.ch/site/assets/uploads/2018/05/SYR_AR5_FINAL_full_wcover.pdf`

[24] V. Knapp, D. Pevec, Promises and limitations of nuclear fission energy in combating climate change, Energy Policy 120 (May) (2018) 94–99. `doi:10.1016/j.enpol.2018.05.027`.

[25] B. W. Brook, A. Alonso, D. A. Meneley, et al., Why nuclear energy is sustainable and has to be part of the energy mix, Sustainable Materials and Technologies 1 (2014) 8–16. `doi:10.1016/j.susmat.2014.11.001`.

[26] B. W. Brook, J. B. van Erp, D. A. Meneley, T. A. Blees, The case for a near-term commercial demonstration of the Integral Fast Reactor, Sustainable Materials and Technologies 3 (2015) 2–6. `doi:10.1016/j.susmat.2014.11.004`.

[27] F. D'Auria, Best Estimate Plus Uncertainty (BEPU): Status and perspectives, Nuclear Engineering and Design 352 (2019) 110190. `doi:10.1016/J.NUCENGDES.2019.110190`.

[28] M. Salvatores, G. Aliberti, G. Palmiotti, The Role of Uncertainty Quantification for Reactor Physics, Nuclear Data Sheets 123 (2015) 68–73. `doi:10.1016/J.NDS.2014.12.012`.

[29] M. I. Radaideh, W. A. Wieselquist, T. Kozlowski, A new framework for sampling-based uncertainty quantification of the six-group reactor kinetic parameters, Annals of Nuclear Energy 127 (2019) 1–11. `doi:10.1016/J.ANUCENE.2018.11.043`.

[30] M. Coste-Delclaux, C. M. Diop, S. Lahaye, Use of probability tables for propagating uncertainties in neutronics, Annals of Nuclear Energy 102 (2017) 376–385. `doi:10.1016/j.anucene.2016.11.044`.

[31] W. Wieselquist, T. Zhu, A. Vasiliev, H. Ferroukhi, PSI Methodologies for Nuclear Data Uncertainty Propagation with CASMO-5M and MCNPX: Results for OECD/NEA UAM Benchmark Phase I, Science and Technology of Nuclear Installations 2013 (2013) 1–15. `doi:10.1155/2013/549793`.

[32] A. Aures, F. Bostelmann, M. Hursin, O. Leray, Benchmarking and application of the state-of-the-art uncertainty analysis methods XSUSA and SHARK-X, Annals of Nuclear Energy 101 (2017) 262–269. `doi:10.1016/j.anucene.2016.11.025`.

[33] A. Labarile, C. Mesado, R. Miró, G. Verdú, Cross-Section Generation Using TXT2NTAB Code for Uncertainty Propagation with Burnup Dependence, Nuclear Technology 205 (12) (2019) 1675–1684. `doi:10.1080/00295450.2019.1631051`.

[34] A. Hoefer, O. Buss, M. Hennebach, et al., MOCABA: A general Monte Carlo–Bayes procedure for improved predictions of integral functions of nuclear data, Annals of Nuclear Energy 77 (2015) 514–521. `doi:10.1016/J.ANUCENE.2014.11.038`.

[35] A. Vasiliev, D. Rochman, M. Pecchia, H. Ferroukhi, On the options for incorporating nuclear data uncertainties in criticality safety assessments for LWR fuel, Annals of Nuclear Energy 116 (2018) 57–68. `doi:10.1016/J.ANUCENE.2018.01.046`.

[36] C. M. Perfetti, B. T. Rearden, Development of a Generalized Perturbation Theory Method for Sensitivity Analysis Using Continuous-Energy Monte Carlo Methods, Nuclear Science and Engineering 182 (3) (2016) 354–368. `doi:10.13182/NSE15-13`.

[37] Q. Wu, X. Peng, F. Xu, et al., Generalized sensitivity analysis of responses to nuclear data in 2-D/1-D transport code KYADJ, Progress in Nuclear Energy 113 (2019) 128–134. `doi:10.1016/J.PNUCENE.2019.01.018`.

[38] N. W. Touran, J. Yang, Sensitivities and Uncertainties Due To Nuclear Data in a Traveling Wave Reactor, in: PHYSOR 2016: Unifying Theory and Experiments in the 21st Century, Sun Valley, ID, 2016.

[39] P. Hejzlar, R. Petroski, J. Cheatham, et al., Terrapower, LLC traveling wave reactor development program overview, Nuclear Engineering and Technology 45 (6) (2013) 731–744. `doi:10.5516/NET.02.2013.520`.

[40] H. Harada, K. Shibata, K. Nishio, et al., Meeting Nuclear Data Needs for Advanced Reactor Systems - NEA/WPEC-31, Tech. rep., NEA/WPEC (2014).
URL `https://www.oecd-nea.org/science/wpec/sg31/`

[41] T. Miura, M. Baba, M. a. Ibaraki, Measurements of double-differential neutron emission cross-sections of ^{238}U and ^{232}Th for 2.6, 3.6 and 11.8 MeV neutrons, Annals of Nuclear Energy 28 (10) (2001) 937–951. `doi:10.1016/S0306-4549(00)00102-X`.

[42] A. J. M. Plompen, C. Goddio, V. M. Maslov, Y. V. Porodzinskij, Excitation of octupole, beta and gamma bands of ^{238}U by inelastic neutron scattering, in: Int. Sem. on Interactions of Neutrons with Nuclei, No.8, Russia, 2000, p. 153.

[43] J. Q. Shao, G. P. Couchell, J. J. Egan, et al., Fast Neutron Inelastic Scattering Cross Sections of ^{238}U for States Between 680 and 1530 kev, Nuclear Science and Engineering 92 (3) (1986) 350–371. `doi:10.13182/NSE86-A17525`.

[44] N. V. Kornilov, A. B. Kagalenko, Inelastic Neutron Scattering on the First Level of U-238, in: Int. Sem. on Interactions of Neutrons with Nuclei, No.4, Russia, 1996, p. 4.

[45] L. L. Litvinsky, V. P. Vertebnyi, V. A. Libman, A. V. Murzin, Neutron Cross Sections and Average Resonance Parameters of ^{238}U for 55- and 144-keV Neutrons, Atomnaya Energiya 62 (3) (1987) 192.

[46] D. K. Olsen, G. L. Morgan, J. W. McConnell, Measurement of ^{238}U(n,n′γ)^{238}U Cross Sections, in: Int. Conf. on Nuclear Cross Sections for Technology, Knoxville, 1979, pp. 677–679.

[47] N. Fotiades, G. D. Johns, R. O. Nelson, et al., Measurements and calculations of ^{238}U(n,xnγ) partial γ-ray cross sections, Phys. Rev. C 21 (10) (2004). `doi:10.1103/PhysRevC.69.024601`.

[48] A. L. Hutcheson, C. Angell, J. A. Becker, et al., Cross sections for ^{238}U(n,n'γ) and ^{238}U(n,2nγ) reactions at incident neutron energies between 5 and 14 MeV, Physical Review C 080 (01) (2009). `doi:10.1103/PhysRevC.80.014603`.

[49] A. Bacquias, P. Dessagne, M. Kerveno, et al., Neutron Inelastic Scattering Measurements for Na, Ge, Zr, Mo and U, Nuclear Data Sheets 119 (2014) 186–189. `doi:10.1016/J.NDS.2014.08.052`.

[50] R. Capote, A. Trkov, M. Sin, et al., IAEA CIELO Evaluation of Neutron-induced Reactions on ^{235}U and ^{238}U Targets, Nuclear Data Sheets 148 (2018) 254–292. `doi:10.1016/j.nds.2018.02.005`.

[51] J. Serp, M. Allibert, O. Beneš, et al., The molten salt reactor (MSR) in generation IV: Overview and perspectives, Progress in Nuclear Energy 77 (2014) 308–319. `doi:10.1016/j.pnucene.2014.02.014`.

[52] D. Broder, A. Gamalij, A. Lashuk, et al., Cross Sections for Gamma-Quanta Production in (n,nγ) Reactions on Light Nuclei of Fluorine, Cobalt, Antimony and Tantalum – Obninsk Reports, No.155, Tech. rep., Fiz.-Energ Institut (1969).

[53] R. Romatoski, L. Hu, Fluoride salt coolant properties for nuclear reactor applications: A review, Annals of Nuclear Energy 109 (2017) 635–647. `doi:10.1016/J.ANUCENE.2017.05.036`.

[54] R. R. Romatoski, L. W. Hu, Fluoride-Salt-Cooled High-Temperature Test Reactor Thermal-Hydraulic Licensing and Uncertainty Propagation Analysis, Nuclear Technology 205 (11) (2019) 1495–1512. `doi:10.1080/00295450.2019.1610686`.

[55] S. Delpech, C. Cabet, C. Slim, G. S. Picard, Molten fluorides for nuclear applications, Materials Today 13 (12) (2010) 34–41. `doi:10.1016/S1369-7021(10)70222-4`.

[56] R. Serrano-López, J. Fradera, S. Cuesta-López, Molten salts database for energy applications, Chemical Engineering and Processing: Process Intensification 73 (2013) 87–102. `doi:10.1016/j.cep.2013.07.008`.

[57] S. Guo, J. Zhang, W. Wu, W. Zhou, Corrosion in the molten fluoride and chloride salts and materials development for nuclear applications, Progress in Materials Science 97 (2018) 448–487. `doi:10.1016/j.pmatsci.2018.05.003`.

[58] J. Powers, N. Brown, D. Mueller, et al., Sensitivity/uncertainty analyses comparing LR-0 reactor experiments containing FLiBe salt with models for molten-salt-cooled and molten-salt-fueled reactors, Annals of Nuclear Energy 120 (2018) 319–332. `doi:10.1016/j.anucene.2018.05.052`.

[59] D. Neudecker, Validating Nuclear Data by Means of Machine Learning Methods, in: CSEWG, Upton, NY, 2019.
URL `https://indico.bnl.gov/event/6642/contributions/32057/`

[60] E. Losa, M. Košťál, V. Rypar, et al., Effect of inserted fluoride salts on criticality in the LR-0 reactor, Annals of Nuclear Energy 81 (2015) 18–25. `doi:10.1016/j.anucene.2015.03.009`.

[61] J. C. Batchelder, S. A. Chong, J. Morrell, et al., Possible evidence of nonstatistical properties in the ^{35}Cl(n,p)^{35}S cross section, Physical Review C 99 (4) (2019) 1–12. `doi:10.1103/PhysRevC.99.044612`.

[62] W. Nagel, Some Nuclear Reactions Induced by D+T Neutrons, Ph.D. thesis, University of Amsterdam (1966).

[63] W. Schantl, Measurement of (n,p) cross section for light nuclei., Ph.D. thesis, University of Vienna (1970).

[64] N. Takigawa, K. Washiyama, Fundamentals of Nuclear Physics, Springer Japan, Tokyo, 2017. `doi:10.1007/978-4-431-55378-6`.

[65] P. Ring, P. Schuck, Nuclear Many-Body Problem, Springer-Verlag, New York, 1980.

[66] K. S. Krane, Introductory Nuclear Physics, John Wiley and Sons, 1988.

[67] R. F. Casten, D. S. Brenner, P. E. Haustein, Valence p - n interactions and the development of collectivity in heavy nuclei, Physical Review Letters 58 (7) (1987) 658–661. `doi:10.1103/PhysRevLett.58.658`.

[68] H. A. Bethe, Nuclear Physics: B. Nuclear Dynamics, Theoretical, Reviews of Modern Physics 9 (2) (1937) 69–244. `doi:10.1103/RevModPhys.9.69`.

[69] T. Ericson, The statistical model and nuclear level densities, Advances in Physics 9 (36) (1960) 425–511. `doi:10.1080/00018736000101239`.

[70] A. V. Ignatyuk, K. K. Istenkov, G. N. Smirenkin, Role of the collective effects in a systematics of nuclear level density. [150 <= A <= 210; A >= 230], Soviet Journal of Nuclear Physics 29 (4) (1979).

[71] A. V. Ignatyuk, J. L. Weil, S. Raman, S. Kahane, Density of discrete levels in ^{116}Sn, Physical Review C 47 (4) (1993) 1504–1513. `doi:10.1103/PhysRevC.47.1504`.

[72] A. Gilbert, A. G. W. Cameron, A Composite Nuclear-Level Density Formula With Shell Corrections, Canadian Journal of Physics 43 (1965). `doi:https://doi.org/10.1139/p65-139`.

[73] M. J. Martin, Nuclear Data Sheets for A = 152, Nuclear Data Sheets 114 (11) (2013) 1497–1847. `doi:10.1016/J.NDS.2013.11.001`.

[74] M. Herman, et al., Empire: Nuclear reaction model code system for data evaluation, NDS 108 (12) (2007) 2655–2715. `doi:10.1016/j.nds.2007.11.003`.

[75] A. Koning, J. Delaroche, Local and global nucleon optical models from 1 keV to 200 MeV, Nuclear Physics A 713 (3-4) (2003) 231–310. `doi:10.1016/S0375-9474(02)01321-0`.

[76] J. E. Midtbø, A. C. Larsen, T. Renstrøm, et al., Systematic low-energy enhancement of the gamma-ray strength function, in: Nuclei in the Cosmos XV, Springer International Publishing, Cham, 2019, pp. 405–407.

[77] F. Bečvář, Simulation of γ cascades in complex nuclei with emphasis on assessment of uncertainties of cascade-related quantities, Nuclear Instruments and Methods in Physics Research Section A: Accelerators, Spectrometers, Detectors and Associated Equipment 417 (2-3) (1998) 434–449. `doi:10.1016/S0168-9002(98)00787-6`.

[78] L. E. Kirsch, L. A. Bernstein, RAINIER: A simulation tool for distributions of excited nuclear states and cascade fluctuations, Nuclear Instruments and Methods in Physics Research Section A: Accelerators, Spectrometers, Detectors and Associated Equipment 892 (2018) 30–40. `doi:10.1016/J.NIMA.2018.02.096`.

[79] T. Kawano, P. Talou, M. B. Chadwick, T. Watanabe, Monte Carlo Simulation for Particle and γ-Ray Emissions in Statistical Hauser-Feshbach Model, Journal of Nuclear Science and Technology 47 (5) (2010) 462–469. `doi:10.1080/18811248.2010.9711637`.

[80] A. Koning, D. Rochman, Modern Nuclear Data Evaluation with the TALYS Code System, Nuclear Data Sheets 113 (12) (2012) 2841–2934. `doi:10.1016/J.NDS.2012.11.002`.

[81] R. Slovacek, R. Block, Y. Danon, et al., Neutron cross-section measurements at the Rensselaer LINAC, in: Proc. Topl. Mtg. Advances in Reactor Physics, Vol. 2, American Nuclear Society Knoxville, Tennessee, 1994, p. 193.

[82] W. Mondelaers, P. Schillebeeckx, GELINA, a neutron time-of-flight facility for high-resolution neutron data measurements, Notiziario Neutroni e Luce di Sincrotrone 11 (July) (2006) 19–25.

[83] K. H. Guber, et al., in: G. Reffo, A. Ventura, C. Grandi (Eds.), Proceedings of the International Conference on Nuclear Data for Science and Technology, Trieste, Italy, 1997, p. 559.

[84] H. Beer, R. L. Macklin, ^{178,179,180}Hf and ^{180}Ta(n,γ) cross sections and their contribution to stellar nucleosynthesis, Physical Review C 26 (4) (1982) 1404–1416. `doi:10.1103/PhysRevC.26.1404`.

[85] P. W. Lisowski, C. D. Bowman, G. J. Russell, S. A. Wender, Los Alamos National Laboratory spallation neutron sources, Nuclear Science and Engineering 106 (2) (1990) 208–218. `doi:10.13182/NSE90-A27471`.

[86] V. Sobes, K. H. Guber, L. C. Leal, Finalizing the ^{63}Cu and ^{65}Cu Resonance Evaluations for the ENDF/B-VIII Release, in: Trans. Am. Nucl. Soc., Vol. 115, 2016, pp. 719–721. URL `http://epubs.ans.org/?a=39271`

[87] Neutron Physics, Tech. rep., MIT Department of Physics (2014).
URL `http://web.mit.edu/8.13/www/JLExperiments/JLExp38.pdf`

[88] K. Wisshak, F. Voss, F. Käppeler, L. Kazakov, Neutron capture cross sections for stellar Cd production, Physical Review C 66 (2) (2002) 258011–2580111. `doi:10.1103/PhysRevC.66.025801`.

[89] P. Schillebeeckx, Transmission TOF Measurements Uncertainty Components and Reporting of Data, in: Mini-CSEWG, Los Alamos, NM, 2019.

[90] P. Schillebeeckx, B. Becker, Y. Danon, et al., Determination of Resonance Parameters and their Covariances from Neutron Induced Reaction Cross Section Data, Nuclear Data Sheets 113 (12) (2012) 3054–3100. `doi:10.1016/J.NDS.2012.11.005`.

[91] F. H. Froehner, Evaluation and Analysis of Nuclear Resonance Data – JEFF Report 18, Tech. rep., OECD (2000).
URL `https://www.oecd-nea.org/dbdata/nds_jefreports/jefreport-18/jeff18.pdf`

[92] R. MacFarlane, A. Kahler, Methods for Processing ENDF/B-VII with NJOY, Nuclear Data Sheets 111 (12) (2010) 2739–2890. `doi:10.1016/J.NDS.2010.11.001`.

[93] F. H. Froehner, Technical report GA-8380, Tech. rep., Gulf General Atomics (1968).

[94] M. J. Rapp, D. P. Barry, G. Leinweber, et al., Tantalum, Titanium, and Zirconium Neutron Total Cross-Section Measurements from 0.4 to 25 MeV, Nuclear Science and Engineering 193 (8) (2019) 903–915. `doi:https://doi.org/10.1080/00295639.2019.1570750`.

[95] C. Guerrero, U. Abbondanno, G. Aerts, et al., The n_TOF Total Absorption Calorimeter for neutron capture measurements at CERN, Nuclear Instruments and Methods in Physics Research, Section A: Accelerators, Spectrometers, Detectors and Associated Equipment 608 (3) (2009) 424–433. `doi:10.1016/j.nima.2009.07.025`.

[96] R. C. Block, P. J. Marano, N. J. Drindak, et al., A Multiplicity Detector for Accurate Low-Energy Capture Measurement, in: Nuclear Data for Science and Technology, JEARI, Mito, 1988.
URL `https://wwwndc.jaea.go.jp/nd1988/index.html`

[97] K. Kobayashi, S. Lee, S. Yamamoto, T. Kawano, Neutron capture cross-section measurement of ^{99}Tc by LINAC time-of-flight method and the resonance analysis, Nuclear Science and Engineering 146 (2) (2004) 209–220. `doi:10.13182/NSE04-A2404`.

[98] K. Wisshak, K. Guber, F. Voss, et al., Neutron capture in ^{148,150}Sm: A sensitive probe of the s-process neutron density, Physical Review C 48 (3) (1993) 1401–1419. `doi:https://doi.org/10.1103/PhysRevC.48.1401`.

[99] B. C. Diven, J. Terrell, A. Hemmendinger, Radiative Capture Cross Sections for Fast Neutrons, Physical Review 120 (2) (1960) 556–569. `doi:10.1103/PhysRev.120.556`.

[100] R. Reifarth, T. Bredeweg, A. Alpizar-Vicente, et al., Background identification and suppression for the measurement of (n,γ) reactions with the DANCE array at LANSCE, Nuclear Instruments and Methods in Physics Research Section A: Accelerators, Spectrometers, Detectors and Associated Equipment 531 (3) (2004) 530–543. `doi:10.1016/J.NIMA.2004.05.096`.

[101] C. Guerrero, D. Cano-Ott, E. Mendoza, et al., Monte Carlo simulation of the n-TOF Total Absorption Calorimeter, Nuclear Instruments and Methods in Physics Research, Section A: Accelerators, Spectrometers, Detectors and Associated Equipment 671 (2012) 108–117. `doi:10.1016/j.nima.2011.12.046`.

[102] K. Wisshak, K. Guber, F. Käppeler, F. Voss, The Karlsruhe 4π barium fluoride detector, Nuclear Instruments and Methods in Physics Research, Section A: Accelerators, Spectrometers, Detectors and Associated Equipmen 299 (1-3) (1990) 60–65. `doi:10.1016/0168-9002(90)90748-U`.

[103] K. Wisshak, F. Voss, F. Kaeppler, G. Reffo, Measurements of keV neutron capture cross sections with a 4pi barium fluoride detector: Examples of ^{93}Nb, ^{103}Rh, and ^{181}Ta, Physical Review C 42 (4) (1990).

[104] K. Wisshak, F. Voss, F. Käppeler, et al., Fast neutron capture on the Hf isotopes: Cross sections, isomer production, and stellar aspects, Physical Review C 73 (4) (2006) 1–18. `doi:10.1103/PhysRevC.73.045807`.

[105] B. J. McDermott, Resonance Region Capture Cross Section Measurements in Iron and Tantalum Using a New C6D6 Detector Array, Ph.D. thesis, Rensselaer Polytechinc Institute (2016).

[106] A. Borella, K. Volev, A. Brusegan, et al., Determination of the ^{232}Th(n,γ) cross section from 4 to 140 keV at GELINA, Nuclear Science and Engineering 152 (1) (2006) 1–14. `doi:10.13182/NSE06-A2557`.

[107] G. Aerts, U. Abbondanno, H. Álvarez, et al., Neutron capture cross section of Th232 measured at the n_TOF facility at CERN in the unresolved resonance region up to 1 MeV, Physical Review C 73 (5) (2006) 1–10. `doi:10.1103/PhysRevC.73.054610`.

[108] K. Kobayashi, S. Lee, S. Yamamoto, et al., Measurement of neutron capture cross section of ^{237}Np by linac time-of-flight method and with linac-driven lead slowing-down spectrometer, Journal of Nuclear Science and Technology 39 (2) (2002) 111–119. `doi:10.1080/18811248.2002.9715164`.

[109] P. E. Koehler, R. R. Winters, K. H. Guber, et al., High-resolution neutron capture and transmission measurements, and the stellar neutron-capture cross section of ^{88}Sr, Physical Review C 62 (5) (2000) 15. `doi:10.1103/PhysRevC.62.055803`.

[110] S. Wang, M. Lubert, Y. Danon, et al., The RPI multiplicity detector response to γ -ray cascades following neutron capture in ^{149}Sm and ^{150}Sm, Nuclear Instruments and Methods in Physics Research, Section A: Accelerators, Spectrometers, Detectors and Associated Equipment 513 (3) (2003) 585–595. `doi:10.1016/S0168-9002(03)01941-7`.

[111] M. Moxon, E. Rae, A gamma-ray detector for neutron capture cross-section measurements, Nuclear Instruments and Methods 24 (1963) 445–455. `doi:10.1016/0029-554X(63)90364-1`.

[112] A. Borella, G. Aerts, F. Gunsing, et al., The use of C6D6 detectors for neutron induced capture cross-section measurements in the resonance region, Nuclear Instruments and Methods in Physics Research Section A: Accelerators, Spectrometers, Detectors and Associated Equipment 577 (3) (2007) 626–640. `doi:10.1016/J.NIMA.2007.03.034`.

[113] R. L. MacKlin, J. H. Gibbons, Capture-cross-section studies for 30-220-keV neutrons using a new technique, Physical Review 159 (4) (1967) 1007–1012. `doi:10.1103/PhysRev.159.1007`.

[114] Z. Révay, T. Belgya, Z. Kasztovszky, et al., Cold neutron PGAA facility at Budapest, Nuclear Instruments and Methods in Physics Research Section B: Beam Interactions with Materials and Atoms 213 (2004) 385–388. `doi:10.1016/S0168-583X(03)01653-7`.

[115] T. Belgya, Prompt Gamma Activation Analysis at the Budapest Research Reactor, Physics Procedia 31 (2012) 99–109. `doi:10.1016/j.phpro.2012.04.014`.

[116] A. Olacel, F. Belloni, C. Borcea, et al., High precision neutron inelastic cross section measurements, in: AIP Conference Proceedings, Vol. 1852, 2017. `doi:10.1063/1.4984880`.

[117] A. P. Ramirez, J. R. Vanhoy, S. F. Hicks, et al., Neutron scattering cross section measurements for ^{56}Fe, Physical Review C 95 (6) (2017) 1–9. `doi:10.1103/PhysRevC.95.064605`.

[118] J. A. Becker, R. O. Nelson, New physics opportunities with GEANIE at LANSCE/WNR, International Journal of Phytoremediation 7 (2) (1997) 11–14. `doi:10.1080/10506899709410550`.

[119] B. Wehring, K. Ünlü, C. Ríos-Martínez, Application of cold-neutron prompt gamma activation analysis at the University of Texas reactor, Applied Radiation and Isotopes 48 (10-12) (1997) 1343–1348. `doi:10.1016/S0969-8043(97)00129-2`.

[120] E. A. Mackey, D. L. Anderson, P. J. Liposky, et al., New thermal neutron prompt γ-ray activation analysis instrument at the National Institute of Standards and Technology Center for Neutron Research, Nuclear Instruments and Methods in Physics Research, Section B: Beam Interactions with Materials and Atoms 226 (3) (2004) 426–440. `doi:10.1016/j.nimb.2004.05.038`.

[121] O. K. Harling, J. M. Chabeuf, F. Lambert, G. Yasuda, A prompt gamma neutron activation analysis facility using a diffracted beam, Nuclear Instruments and Methods in Physics Research, Section B: Beam Interactions with Materials and Atoms 83 (4) (1993) 557–562. `doi:10.1016/0168-583X(93)95887-B`.

[122] L. Canella, P. Kudějová, R. Schulze, et al., Characterisation and optimisation of the new Prompt Gamma-ray Activation Analysis (PGAA) facility at FRM II, Nuclear Instruments and Methods in Physics Research, Section A: Accelerators, Spectrometers, Detectors and Associated Equipment 636 (1) (2011) 108–113. `doi:10.1016/j.nima.2011.01.126`.

[123] S. Agostinelli, J. Allison, K. Amako, et al., Geant4—a simulation toolkit, Nuclear Instruments and Methods in Physics Research Section A: Accelerators, Spectrometers, Detectors and Associated Equipment 506 (3) (2003) 250–303. `doi:10.1016/S0168-9002(03)01368-8`.

[124] G. Knoll, Radiation Detection and Measurement, 3rd Edition, John Wiley and Sons Inc, 2000.

[125] E. Gete, D. Measday, B. Moftah, et al., Neutron-induced peaks in Ge detectors from evaporation neutrons, Nuclear Instruments and Methods in Physics Research Section A: Accelerators, Spectrometers, Detectors and Associated Equipment 388 (1-2) (1997) 212–219. `doi:10.1016/S0168-9002(96)01163-1`.

[126] A. Wallner, M. Bichler, L. Coquard, et al., Stellar and thermal neutron capture cross section of ^{9}Be, Physical Review C 99 (1) (2019) 1–11. `doi:10.1103/PhysRevC.99.015804`.

[127] P. G. Young, E. D. Arthur, M. B. Chadwick, Los Alamos National Laboratory Report LA-12343-MS, Tech. rep. (1992).

[128] F. Marie, A. Letourneau, G. Fioni, et al., Thermal neutron capture cross-section measurements of ^{243}Am and ^{242}Pu using the new mini-INCA α- And γ-spectroscopy station, Nuclear Instruments and Methods in Physics Research, Section A: Accelerators, Spectrometers, Detectors and Associated Equipment 556 (2) (2006) 547–555. `doi:10.1016/j.nima.2005.10.125`.

[129] S. Bisterzo, F. Käppeler, R. Gallino, et al., Measurement of the ^{209}Bi(n,γ)^{210}Bi g cross section and updated s-process analysis of the Pb/Bi region (2007) 2–5`doi:10.1051/ndata:07488`.

[130] L. Weissman, M. Tessler, A. Arenshtam, et al., Measurement of ^{208}Pb(n,γ)^{209}Pb Maxwellian averaged neutron capture cross section, Physical Review C 96 (1) (2017) 1–8. `doi:10.1103/PhysRevC.96.015802`.

[131] C. Goessling, M. Junker, H. Kiel, et al., Experimental study of ^{113}Cd β decay using CdZnTe detectors, Physical Review C 72 (6) (2005) 4–7. `doi:10.1103/PhysRevC.72.064328`.

[132] L. S. Brown, G. Gabrielse, Geonium theory: Physics of a single electron or ion in a Penning trap, Reviews of Modern Physics 58 (1) (1986) 233–311. `doi:10.1103/RevModPhys.58.233`.

[133] F. Alessandria, R. Ardito, D. R. Artusa, et al., The low energy spectrum of TeO$_2$ bolometers: Results and dark matter perspectives for the CUORE-0 and CUORE experiments, Journal of Cosmology and Astroparticle Physics 2013 (1) (2013). `doi:10.1088/1475-7516/2013/01/038`.

[134] C. Arnaboldi, D. R. Artusa, F. T. Avignone, et al., Results from a search for the 0 $\nu\beta\beta$-decay of ^{130}Te, Physical Review C 78 (3) (2008) 1–17. `doi:10.1103/PhysRevC.78.035502`.

[135] R. W. Lougheed, W. Webster, M. N. Namboodiri, et al., Pu and ^{241}Am(n,2n) cross-section measurements near E$_n$ = 14 MeV, Radiochimica Acta 90 (12_2002) (2002) 833–843. `doi:10.1524/ract.2002.90.12_2002.833`.

[136] D. G. Schuster, Production of collimated monoenergetic beams of neutrons from 2 MeV to 14 MeV by the associated particle method, Nuclear Instruments and Methods in Physics Research, Section A: Accelerators, Spectrometers, Detectors and Associated Equipment 76 (1969) 35–42. `doi:https://doi.org/10.1016/0029-554X(69)90285-7`.

[137] A. Wallner, R. Golser, W. Kutschera, et al., AMS –A powerful tool for probing nucleosynthesis via long-lived radionuclides, The European Physical Journal A 27 (S1) (2006) 337–342. `doi:10.1140/epja/i2006-08-052-3`.

[138] P. Steier, R. Golser, W. Kutschera, et al., VERA, an AMS facility for "all" isotopes, Nuclear Instruments and Methods in Physics Research, Section B: Beam Interactions with Materials and Atoms 223-224 (SPEC. ISS.) (2004) 67–71. `doi:10.1016/j.nimb.2004.04.017`.

[139] M. Paul, B. G. Glagola, W. Henning, et al., Heavy ion separation with a gas-filled magnetic spectrograph, Nuclear Instruments and Methods in Physics Research Section A: Accelerators, Spectrometers, Detectors and Associated Equipment 277 (2-3) (1989) 418–430. `doi:10.1016/0168-9002(89)90771-7`.

[140] M. Schlapp, R. C. Pardo, R. C. Vondrasek, et al., A new 14 GHz electron-cyclotron-resonance ion source for the heavy ion accelerator facility ATLAS, Review of Scientific Instruments 69 (2) (1998) 631–633. `doi:10.1063/1.1148725`.

[141] C. Stan-Sion, A. Letourneau, H. Reithmeier, et al., AMS measurement of the neutron capture cross-section ^{209}Bi(n, γ)^{210m}Bi, Nuclear Instruments and Methods in Physics Research, Section B: Beam Interactions with Materials and Atoms 259 (1) (2007) 739–744. `doi:10.1016/j.nimb.2007.01.211`.

[142] G. Rugel, I. Dillmann, T. Faestermann, et al., Measurement of (n,γ) reaction cross sections at stellar energies for ^{58}Ni and ^{78}Se, Nuclear Instruments and Methods in Physics Research, Section B: Beam Interactions with Materials and Atoms 259 (1) (2007) 683–687. `doi:10.1016/j.nimb.2007.01.206`.

[143] A. Wallner, M. Bichler, I. Dillmann, et al., AMS measurements of ^{41}Ca and ^{55}Fe at VERA - two radionuclides of astrophysical interest, Nuclear Instruments and Methods in Physics Research, Section B: Beam Interactions with Materials and Atoms 259 (1) (2007) 677–682. `doi:10.1016/j.nimb.2007.01.207`.

[144] H. Nassar, M. Paul, I. Ahmad, et al., Stellar (n,γ) cross section of ^{62}Ni, Physical Review Letters 94 (9) (2005) 7–10. `doi:10.1103/PhysRevLett.94.092504`.

[145] I. Dillmann, C. Domingo-Pardo, M. Heil, et al., Determination of the stellar (n,γ) cross section of ^{40}Ca with accelerator mass spectrometry, Physical Review C 79 (6) (2009) 1–8. `doi:10.1103/PhysRevC.79.065805`.

[146] A. Wallner, K. Buczak, T. Belgya, et al., Precise measurement of the thermal and stellar ^{54}Fe(n,γ)^{55}Fe cross sections via accelerator mass spectrometry, Physical Review C 96 (2) (2017) 1–13. `doi:10.1103/PhysRevC.96.025808`.

[147] L. K. Fifield, Accelerator mass spectrometry and its applications, Reports on Progress in Physics 62 (8) (1999) 1223–1274. `doi:10.1088/0034-4885/62/8/202`.

[148] A. Wallner, M. Bichler, K. Buczak, et al., High-sensitivity isobar-free AMS measurements and reference materials for ^{55}Fe, ^{68}Ge and ^{202g}Pb, Nuclear Instruments and Methods in Physics Research, Section B: Beam Interactions with Materials and Atoms 294 (2013) 374–381. `doi:10.1016/j.nimb.2012.03.029`.

[149] Joint Commitee for Guides in Metrology, Evaluation of measurement data — Guide to the expression of uncertainty in measurement, Tech. rep., International Organization for Standardization Geneva ISBN (2008).
URL `http://www.bipm.org/en/publications/guides/gum.html`

[150] N. H. Timm, Applied Multivariate Analysis, Springer-Verlag, New York, 2002.

[151] R. O. Duda, P. E. Hart, D. G. Stork, Pattern Classification, 2nd Edition, Wiley, 2000.

[152] S. van der Walt, S. C. Colbert, G. Varoquaux, The NumPy Array: A Structure for Efficient Numerical Computation, Computing in Science & Engineering 13 (2) (2011) 22–30. `doi:10.1109/MCSE.2011.37`.

[153] D. Smith, N. Otuka, Experimental nuclear reaction data uncertainties: Basic concepts and documentation, Nuclear Data Sheets 113 (12) (2012) 3006–3053. `doi:10.1016/J.NDS.2012.11.004`.

[154] N. R. Draper, H. Smith, Applied Regression Analysis., 3rd Edition, John Wiley & Sons, Inc, New York, 1998.

[155] K. Levenberg, A method for the solution of certain non-linear problems in least squares, Quarterly of Applied Mathematics 2 (2) (1944) 164–168. `doi:10.1090/qam/10666`.

[156] D. W. Marquardt, An Algorithm for Least-Squares Estimation of Nonlinear Parameters, Journal of the Society for Industrial and Applied Mathematics 11 (2) (1963) 431–441. `doi:10.1137/0111030`.

[157] M. A. Branch, T. F. Coleman, Y. Li, A Subspace, Interior, and Conjugate Gradient Method for Large-Scale Bound-Constrained Minimization Problems, SIAM Journal on Scientific Computing 21 (1) (1999) 1–23. `doi:10.1137/S1064827595289108`.

[158] P. Virtanen, R. Gommers, T. E. Oliphant, et al., SciPy 1.0–Fundamental Algorithms for Scientific Computing in Python, arXiv e-prints (2019) arXiv:1907.10121`arXiv:1907.10121`.

[159] P. Helgesson, Experimental data and Total Monte Carlo - Towards justified, transparent and complete nuclear data uncertainties, Ph.D. thesis, Uppsala University (2015).

[160] D. Neudecker, B. Hejnal, F. Tovesson, et al., Template for estimating uncertainties of measured neutron-induced fission cross-sections, EPJ Nuclear Sci. Technol 4 (21) (2018). `doi:https://doi.org/10.1051/epjn/2018026`.

[161] D. Neudecker, D. L. Smith, F. Tovesson, et al., Applying a Template of Expected Uncertainties to Updating ^{239}Pu(n,f) Cross-section Covariances in the Neutron Data Standards Database, Nuclear Data Sheets 163 (2020) 228–248. `doi:10.1016/j.nds.2019.12.005`.

[162] F. C. S. Gunsing, P. Schillebeeckx, V. Semkova, EXFOR Data in Resonance Region and Spectrometer Response Function, Tech. Rep. March 2012, IAEA (2012).
URL `http://www.osti.gov/scitech/biblio/1056460`

[163] A. M. Lane, R. G. Thomas, R-matrix theory of nuclear reactions, Reviews of Modern Physics 30 (2) (1958) 257–353. `doi:10.1103/RevModPhys.30.257`.

[164] V. Sobes, L. Heilbronn, NE 697: Nuclear Data, Spring 2018, University of Tennessee, Knoxville .
URL `https://www.youtube.com/playlist?list=PLA-IQaSyWKTD9mMu89i3a55RrWD-8hDGQ`

[165] N. M. Larson, Updated users' guide for SAMMY: Multilevel R-matrix fits to neutron data using Bayes' equations, Technical Report ORNL/TM-9179/R6, Oak Ridge National Lab, TN (2003).

[166] M. C. Moxon, J. B. Brisland, GEEL REFIT, A least squares fitting program for resonance analysis of neutron transmission and capture data computer code, Technical Report AEA-InTec-0630, AEA Technology (October 1991).

[167] P. Archier, C. De Saint Jean, O. Litaize, et al., CONRAD Evaluation Code: Development Status and Perspectives, Nuclear Data Sheets 118 (2014) 488–490. `doi:10.1016/j.nds.2014.04.114`.

[168] G. M. Hale, Use of R-matrix Methods for Light Element Evaluations – LA-UR-93-102 , in: B. Magurno, S. Pearlstein (Eds.), Proc. of the Conference on Nuclear Data Evaluation Methods and Procedures, Brookhaven National Lab, Upton, NY, BNL-NCS-51363, 1981, pp. 509–531.

[169] E. P. Wigner, Random Matrices in Physics, SIAM Review 9 (1) (1967) 1–23. `doi:10.1137/1009001`.

[170] C. E. Porter, R. G. Thomas, Fluctuations of nuclear reaction widths, Physical Review 104 (2) (1956) 483–491. `doi:10.1103/PhysRev.104.483`.

[171] G. P. Nobre, F. S. Dietrich, M. Herman, et al., Towards an optical potential for rare-earths through coupled channels, AIP Conference Proceedings 1625 (2014) 45–51. `arXiv:arXiv:1311.1735v1`, `doi:10.1063/1.4901763`.

[172] B. Becker, C. Bastian, J. Heyse, et al., Analysis of Geel Spectra - AGS, Technical Report NEA/DB/DOC(2014)4, Nuclear Energy Agency (2014).

[173] C. W. Reich, M. S. Moore, Multilevel formula for the fission process, Physical Review 111 (3) (1958) 929–933. `doi:10.1103/PhysRev.111.929`.

[174] M. Budnar, F. Cvelbar, E. Hodgson, et al., Prompt γ-ray spectra and integrated cross sections for the radiative capture of 14 MeV neutrons for 28 natural targets in the mass region from 12 to 208 — INDC(YUG)-6/L, Tech. rep., IAEA (1979).

[175] C. Necheva, D. Kolev, M. Vlasarev, 14.5 MeV neutron capture cross-section measurements in ^{181}Ta with activation technique, Journal of Physics G: Nuclear and Particle Physics 20 (2) (1994) L33–L36. `doi:10.1088/0954-3899/20/2/002`.

[176] A. Koning, D. Rochman, Modern Nuclear Data Evaluation with the TALYS Code System, Nuclear Data Sheets 113 (12) (2012) 2841–2934. `doi:10.1016/j.nds.2012.11.002`.

[177] D. Rochman, M. Herman, WPEC sub-group proposal - WPEC-49 (2019).
URL `https://www.oecd-nea.org/science/wpec/sg49/`

[178] M. Herman, New paradigm for nuclear data evaluation, in: CSEWG, Upton, NY, 2019.
URL `https://indico.bnl.gov/event/6642/contributions/32432/`

[179] U. N. Singh, J. Rainwater, H. I. Liou, et al., Neutron resonance spectroscopy: Aluminum, Physical Review C 11 (4) (1975) 1117–1121. `doi:10.1103/PhysRevC.11.1117`.

[180] S. Ghorai, J. Gaiser, W. Alford, The (n,2n) isomeric cross section ratios and the (n,2n) and (n,α) excitation functions for ^{59}Co, Annals of Nuclear Energy 7 (1) (1980) 41 – 46. `doi:https://doi.org/10.1016/0306-4549(80)90005-5`.

[181] N. Otsuka, EXFOR Formats Manual, Tech. Rep. January, International Atomic Energy Agency Nuclear Data Services (2006).
URL `https://www-nds.iaea.org/nrdc/basics/`

[182] L. Adamski, M. W. Herman, A. Marcinkowski, Cross section measurements of the ^{23}Na(n,2n)^{22}Na, ^{58}Ni(n,2n)^{57}Ni and ^{115}In(n,n$'$)^{115m}In reactions, Annals of Nuclear Energy 7 (7) (1980) 397–401. `doi:10.1016/0306-4549(80)90055-9`.

[183] J. Callerame, D. J. Larson, S. J. Lipson, R. Wilson, Cross section of slow neutrons on parahydrogen, Phys. Rev. C 12 (1975) 1423–1427. `doi:10.1103/PhysRevC.12.1423`.

[184] A. Belopolsky, B. Chapman, P. Cock, et al., RPy2, version 2.8 (2017).

[185] M. Berglund, M. E. Wieser, Isotopic compositions of the elements (IUPAC Technical Report), Pure and Applied Chemistry 83 (2) (2011) 397–410. `doi:10.1351/PAC-REP-10-06-02`.

[186] P. E. Koehler, Neutron multiple scattering corrections including extensive realistic simulations of inherent experimental conditions, Nuclear Instruments and Methods in Physics Research 224 (3) (1984) 508 – 518. `doi:https://doi.org/10.1016/0167-5087(84)90042-5`.

[187] T. Taddeucci, R. Haight, H. Lee, et al., Multiple-scattering corrections to measurements of the prompt fission neutron spectrum, Nuclear Data Sheets 123 (2015) 135 – 139, special Issue on International Workshop on Nuclear Data Covariances April 28 - May 1, 2014, Santa Fe, New Mexico, USA. `doi:https://doi.org/10.1016/j.nds.2014.12.024`.

[188] M. Drosg, Dealing with Uncertainties - A Guide to Error Analysis, 2nd Edition, Springer-Verlag, Berlin, 2007. `doi:10.1007/978-3-540-74757-4_7`.

[189] L. P. Geraldo, D. L. Smith, Covariance analysis and fitting of germanium gamma-ray detector efficiency calibration data, Nuclear Instruments and Methods in Physics Research, Section A: Accelerators, Spectrometers, Detectors and Associated Equipment 290 (2-3) (1990) 499–508. `doi:10.1016/0168-9002(90)90569-R`.

[190] E. F. Matthews, A. M. Lewis, L. A. Bernstein, Submitted to Nuclear Instruments and Methods in Physics Research, Section A: Accelerators, Spectrometers, Detectors and Associated Equipment (2020).

[191] D. M. Allen, Mean square error of prediction as a criterion for selecting variables, Technometrics 13 (3) (1971) 469–475. `doi:10.1080/00401706.1971.10488811`.

[192] D. M. Allen, The Relationship Between Variable Selection and Data Agumentation and a Method for Prediction, Technometrics 16 (1) (1974) 125–127. `doi:10.1080/00401706.1974.10489157`.

[193] J. Fox, Applied Regression Analysis and Generalized Linear Models, 2nd Edition, Sage Publications, Thousand Oaks, California, 2008.

[194] N. Fotiades, M. Devlin, R. O. Nelson, T. Granier, Low-spin states in ^{86}Kr from the (n,n') reaction, Physical Review C 87 (4) (2013) 1–6. `doi:10.1103/PhysRevC.87.044336`.

[195] M. Bhat, Nuclear Data Sheets for A = 57, Nuclear Data Sheets 85 (3) (1998) 415–536. `doi:10.1006/ndsh.1998.0021`.

[196] E. Browne, J. Tuli, Nuclear Data Sheets for A = 238, Nuclear Data Sheets 127 (2015) 191–332. `doi:10.1016/J.NDS.2015.07.003`.

[197] R. B. Firestone, T. Belgya, M. Krtička, et al., Thermal neutron capture cross section for ^{56}Fe(n,γ), Physical Review C 95 (1) (2017) 1–11. `doi:10.1103/PhysRevC.95.014328`.

[198] A. Negret, M. Sin, C. Borcea, et al., Cross-section measurements for the ^{57}Fe(n,nγ)^{57}Fe and ^{57}Fe(n,2nγ)^{56}Fe reactions, Physical Review C 96 (2) (2017) 1–12. `doi:10.1103/PhysRevC.96.024620`.

[199] L. A. Bernstein, J. A. Becker, P. E. Garrett, et al., ^{239}Pu(n,2n)^{238}Pu cross section deduced using a combination of experiment and theory, Physical Review C 65 (2) (2002) 216011–216015. `doi:10.1103/PhysRevC.65.021601`.

[200] A. M. Lewis, L. A. Bernstein, T. Kawano, D. Neudecker, Ratio method for estimating uncertainty in calculated gamma cascades, The European Physical Journal A 55 (8) (2019) 141. `doi:10.1140/epja/i2019-12826-y`.

[201] M. Kerveno, C. Borcea, M. Nyman, et al., How to produce accurate inelastic cross sections from an indirect measurement method?, EPJ Nuclear Sciences & Technologies (2018). `doi:10.1051/epjn/2018020`.

[202] R. M. Bahran, et al., Los Alamos National Laboratory Report LA-UR-18-22315, Tech. rep. (2018).

[203] R. Capote, Y.-J. Chen, F.-J. Hambsch, et al., Prompt Fission Neutron Spectra of Actinides, Nuclear Data Sheets 131 (2016) 1–106. `doi:10.1016/j.nds.2015.12.002`.

[204] P. Helgesson, Approaching well-founded comprehensive nuclear data uncertainties: Fitting imperfect models to imperfect data, Ph.D. thesis, Uppsala Universitet (2018).

[205] P. Helgesson, H. Sjöstrand, D. Rochman, Uncertainty-driven nuclear data evaluation including thermal (n,α) applied to ^{59}Ni, Nuclear Data Sheets 145 (2017) 1–24. `doi:10.1016/j.nds.2017.09.001`.

[206] R. Capote, et al., A New Formulation of the Unified Monte Carlo Approach (UMC-B) and Cross-Section Evaluation for the Dosimetry Reaction ^{55}Mn(n,γ)^{56}Mn, in: Reactor Dosimetry: 14th International Symposium, Vol. 9, ASTM International, West Conshohocken, PA, 2012, pp. 179–196.

[207] A. Aravkin, et al., On the estimation of hyperparameters for Empirical Bayes estimators: Maximum Marginal Likelihood vs Minimum MSE, in: Proceedings of the 16th IFAC Symp. Syst. Identif., Elsevier, Brussels, 2012, pp. 125–130.

[208] A. Koning, D. Rochman, Towards sustainable nuclear energy: Putting nuclear physics to work, Annals of Nuclear Energy 35 (11) (2008) 2024–2030. `doi:10.1016/J.ANUCENE.2008.06.004`.

[209] D. Neudecker, R. Capote, H. Leeb, Impact of model defect and experimental uncertainties on evaluated output, Nuclear Instruments and Methods in Physics Research, Section A: Accelerators, Spectrometers, Detectors and Associated Equipment 723 (2013) 163–172. `doi:10.1016/j.nds.2008.11.006`.

[210] A. J. Koning, Bayesian Monte Carlo method for nuclear data evaluation, European Physical Journal A 51 (12) (2015) 1–16. `doi:10.1140/epja/i2015-15184-x`.

[211] S. Ellison, ISO uncertainty and collaborative trial data, Accreditation and Quality Assurance 3 (1998) 95–100. `doi:https://doi.org/10.1007/s007690050197`.

[212] Krishichayan, M. Bhike, W. Tornow, et al., Accurate ^{238}U(n,2n)^{237}U reaction cross-section measurements from 6.5 to 14.8 MeV, Physical Review C 96 (4) (2017) 044623. `doi:10.1103/PhysRevC.96.044623`.

[213] M. B. Chadwick, R. Capote, A. Trkov, et al., CIELO Collaboration Summary Results: International Evaluations of Neutron Reactions on Uranium, Plutonium, Iron, Oxygen and Hydrogen, Nuclear Data Sheets 148 (2018) 189–213. `doi:10.1016/j.nds.2018.02.003`.

[214] Y. Khazov, A. Rodionov, F. Kondev, Nuclear Data Sheets for A = 133, Nuclear Data Sheets 112 (4) (2011) 855–1113. `doi:10.1016/J.NDS.2011.03.001`.

[215] E. Browne, J. K. Tuli, Nuclear Data Sheets for A = 60, Nuclear Data Sheets 114 (12) (2013) 1849–2022. `doi:10.1016/j.nds.2013.11.002`.

[216] T. Kibédi, T. Burrows, M. Trzhaskovskaya, et al., Evaluation of theoretical conversion coefficients using BrIcc, Nuclear Instruments and Methods in Physics Research Section A: Accelerators, Spectrometers, Detectors and Associated Equipment 589 (2) (2008) 202–229. `doi:10.1016/j.nima.2008.02.051`.

Appendix A

EXFOR Parsing Script

```
import os, sys, argparse

def getArgs():
parser = argparse.ArgumentParser(description="intractive exfor parsing")
parser.add_argument("folder", type=str,help="folder to read through")
parser.add_argument("--startwith", type=str, default=None, help="entry to start
    with if not first in folder")
return parser.parse_args()

folder = """C:/Users/amlew/Documents/Programs/x4i/dist/x4i-1.0.3/x4i/data/db/"""


if __name__ == "__main__":

   # read args
   args = getArgs()

   # start in the middle of the file if needed
   if args.startwith is not None:
   start_with = int(args.startwith)
   else:
   start_with = 0

   # figure out which folder
   folder+=args.folder+"/"


   # open files for storage
   general_file = open("../exforvalues/general.txt","a")
```

```
detector_file = open("../exforvalues/detector.txt","a")
other_file = open("../exforvalues/other.txt","a")
sample_file = open("../exforvalues/sample.txt","a")
source_file = open("../exforvalues/source.txt","a")



# loop through files in folder
for filename in os.listdir(folder):
   entry_number = filename.split(".")[0]
   if int(entry_number)<start_with:
   continue
   f = open(folder+filename,"r")
   entry = f.read()
   common = False
   common_section = ""

   bib_info = {
   "REFERENCE " : "",
   "FACILITY  " : "" ,
   "INC-SOURCE " : "",
   "SAMPLE    " : "",
   "METHOD    " : "",
   "DETECTOR  " : "",
   "ERR-ANALYS " : "",
   "TITLE     " : ""
   }

   # split file into subents
   subents = entry.split("ENDSUBENT")

   # read first subent, store values
   key = None
   subents[0] = subents[0].split("\n")
   for line in subents[0]:
      if line[:6] == "COMMON":
         common = True
         common_section += line[:]+"\n"
      elif line[:9] == "ENDCOMMON":
         common = False
      elif common:
         common_section+= line[11:]+"\n"
      elif line[0:4] != "  ":
         if line[0:11] in bib_info:
```

```
          key = line[0:11]
          bib_info[key]+= line[11:]+"\n"
        else:
          key = None
      elif key is not None:
        bib_info[key] += line[11:]+"\n"
      elif key is None:
        continue

    # print error anlysis, get user feedback
    if "No information on source" in bib_info["ERR-ANALYS "]:
      continue
    os.system("clear")
    print("---------------------------")
    print("---------------------------")
    print(entry_number)
    print("---------------------------")
    print("---------------------------")
    print("\n")
    if len(bib_info["ERR-ANALYS "]) ==0:
      print("No error analysis in BIB\n")
    else:
      print(bib_info["ERR-ANALYS "])

    go_on = input("Continue with this entry? (y,n,exit,check) ")
    if go_on=="n" or go_on=="no" or go_on=="N" or go_on=="nn" or go_on=="j":
      print("\n\n")
      continue
    elif go_on == "exit" or go_on == "quit":
      general_file.close()
      detector_file.close()
      other_file.close()
      sample_file.close()
      source_file.close()
      sys.exit()

    # have user return year of reference
    print("\n",bib_info["REFERENCE "])
    year = input("year: ")

    # print the common section in the bib subent
    print(common_section)

    # loop through rest of subents
```

```python
for subent in subents[1:]:
    common = False
    common_section = ""
    subent_info = {
    "REACTION   " : "" ,
    "MONITOR    " : "",
    "ERR-ANALYS " : "",
    "DETECTOR   " : "",
    "INC-SOURCE " : "",
    "SAMPLE     " : "",
    "METHOD     " : ""
    }

    if go_on == "check":
        if "ERR-ANALYS" not in subent:
            print("no errors found, skipping subent\n")
            continue
    subent = subent.split("\n")

    key = None
    for line in subent:
        if line[:6] == "COMMON":
            common = True
            common_section += line[:]+"\n"
        elif line[:9] == "ENDCOMMON":
            common = False
        elif common:
            common_section+= line[:]+"\n"
        elif line[0:4] != "    ":
            if line[0:11] in subent_info:
                key = line[0:11]
                subent_info[key]+= line[11:]+"\n"
            else:
                key = None
        elif key is not None:
            subent_info[key] += line[11:]+"\n"
        elif key is None:
            continue

    print("\n-----------------------")
    print(subent[1].split()[1],"\n")
    print(subent_info["ERR-ANALYS "],"\n")
    go_on = input("Continue with this subentry? (y,n,skip,exit) ")
    if go_on == "n" or go_on == "no" or go_on == "nn" or go_on == "j":
```

```
        continue
    elif go_on =="exit":
        general_file.close()
        detector_file.close()
        other_file.close()
        sample_file.close()
        source_file.close()
        sys.exit()
    elif go_on == "skip":
        continue
    elif go_on == "open":
        os.system("start notepad++ "+folder+filename)

    # print the subent"s common section
    print("\n-------------------------")
    print(common_section)
    print("-------------------------\n")

    # have user input category of uncertainty
    # continues until user supplies "done"
    source = input("\nSource (detector,sample,source,other,print,done): ")

    # for each source, provide information that is relevant
    # and then have the user input the information
    # then print to the file
    while source != "done":
        if source == "detector":
            print("------------------------")
            print(bib_info["DETECTOR "])
            print("------------------------")
            print(subent_info["DETECTOR "])
            print("------------------------")
            print(bib_info["TITLE    "])

            det_type = input("Detctor Type: ")
            uncertainty = input("Uncertainty type: ")
            energy = input("Energy: ")
            value = input("Value: ")

            newline = entry_number+"\t"+year+"\t"+det_type+"\t"+uncertainty+"\t"
            newline += energy+"\t"+value+"\n"
            detector_file.write(newline)
            print("wrote to detector.txt")
```

```
    if source == "sample":
        print("------------------------")
        print(subent_info["REACTION "])
        print("------------------------")
        print(bib_info["SAMPLE  "])
        print("------------------------")
        print(subent_info["SAMPLE  "])
        print("------------------------")

        sample_type = input("Sample Type: ")
        mass = input("Mass: ")
        stability = input("Stablility: ")
        uncertainty = input("Uncertainty type: ")
        value = input("Value: ")

        newline = entry_number+"\t"+year+"\t"+sample_type+"\t"+mass+"\t"
        newline += stability + "\t"+uncertainty+"\t"+value+"\n"
        sample_file.write(newline)
        print("wrote to sample.txt")


    if source == "source":
        print("------------------------")
        print(bib_info["FACILITY "])
        print("------------------------")
        print(bib_info["INC-SOURCE "])
        print("------------------------")
        print(subent_info["INC-SOURCE "])
        print("------------------------")
        print(bib_info["TITLE   "])

        source_type = input("Source Type: ")
        facility = input("Facility: " )
        energy = input("Energy Region: ")
        uncertainty = input("Uncertainty type: ")
        value = input("Value: ")

        newline = entry_number+"\t"+year+"\t"+source_type+"\t"+facility+"\t"
        newline += energy+"\t"+uncertainty+"\t"+value+"\n"
        source_file.write(newline)
        print("wrote to source.txt")

    if source == "other":
        print("------------------------")
```

```
        print(bib_info["FACILITY "])
        print("------------------------")
        print(bib_info["INC-SOURCE "])
        print("------------------------")
        print(subent_info["INC-SOURCE "])
        print("------------------------")
        print(bib_info["METHOD  "])
        print("------------------------")
        print(subent_info["METHOD  "])
        print("------------------------")
        print(bib_info["TITLE   "])

        source_type = input("Source Type: ")
        facility_type = input("Facility Type: ")
        method = input("Method: ")
        energy = input("Energy Region: ")
        uncertainty = input("Uncertainty type: ")
        value = input("Value: ")
        newline = entry_number+"\t"+year+"\t"+source_type+"\t"+facility_type
        newline+= "\t" + method+"\t"+energy+"\t"+uncertainty+"\t"+value+"\n"
        other_file.write(newline)
        print("wrote to other.txt")


    if source == "print":
        print("\n")
        print("--------------------------")
        print(bib_info["ERR-ANALYS "])
        print("--------------------------")
        print(subent_info["ERR-ANALYS "])
        print("--------------------------")
        print(common_section)
        print("--------------------------\n")


    elif source == "exit":
        general_file.close()
        detector_file.close()
        other_file.close()
        sample_file.close()
        source_file.close()
        sys.exit()

    source = input("\nSource: ")
```

Appendix B

EXFOR Data Sets

Table B.1: EXFOR entries used to create the uncertainty value distributions for Chapter 5.

31484	D0615	32691	32690	O1352	14350	32693	D4182	E2051
10844	32706	32675	32595	14162	D4168	14364	32754	13885
31598	D0412	10921	32710	D4148	O1547	14140	23138	10837
32733	32738	10359	10184	13867	D0570	10474	32242	23032
32674	31664	32743	31696	O1736	31616	22752	D6118	30996
D0454	22014	10836	D0446	22205	13901	22870	22751	14341
22091	23033	13996	22939	31433	10238	D4175	10401	31672
12929	D4218	10593	10734	23183	32751	14349	23114	C1805
32678	14149	10421	13841	13597	23204	O1259	13133	33027
32685	C1764	D0562	31615	D0574	32702	31553	32729	D0633
14172	C1742	31654	D4229	22851	14266	O1503	22857	14255
22913	E1934	31695	14041	32717	C1801	D0622	O1694	C1715
D6067	O1512	32692	32740	D4211	32695	23127	32713	32655
10231	D0590	23300	41063	13896	14148	31621	31521	D4241
G3101	22741	31762	31619	D4199	32680	23176	14211	13513
32735	32670	32596	14014	31490	32730	10481	14144	31680
23201	23142	10735	K2293	22969	22935	31627	14154	32734
D4176	10566	22755	23216	12869	D0422	22282	32716	31610
D0455	32714	D0503	31676	13154	10180	10440	23171	32703
O1502	33025	23160	21633	32753	O1796	32746	22655	32677
23149	23034	32653	D4217	31763	D4174	14164	D0282	31628
22494	14352	14147	D4198	D4232	14159	32715	31649	22012
32704	10438	31661	22822	23107	31481	13997	32712	32727
23137	32752	32514	D0357	13787	22392	22309	32701	D4194
D4205	14368	21986	22024	13176	21900	D0631		

Appendix C

Efficiency Calibration Data Set

The calibration standards used in the HPGe work (Chapter 6) and the uncertainties on the data points are detailed here.

Figure C.1: Calibration sources used in the HPGe efficiency calibration work. The ^{288}Th source was not used in the analysis, as the relevant lines were obscured by background and lead scattering gammas in the measurement.

Table C.1: Details about the calibration sources used in the HPGe efficiency calibration work. The uncertainties on each of these values are detailed in Table C.2.

Source	A_0 [kBq]	$t_{1/2}$ [yr]	t [days]
^{241}Am	370	432.6	3085
^{137}Cs	377.4	30.08	2050
^{60}Co	389.2	30.17	2050
^{133}Ba	391.1	10.551	3224
^{152}Eu	352.7	13.517	2493

Table C.2: Experimental data points and their uncertainty components for all of the calibration gamma lines that were used in this work.

E_γ [keV]	Source	δC_{stat} [%]	δA_0 [%]	$\delta\lambda$ [%]	Δt [%]	δB_γ [%]	$\delta\xi$ [%]	δS [%]
59.5409	^{241}Am	0.2	3	0.1	0.5	1.0	0	0
121.7817	^{152}Eu	0.1	1	0.07	0.6	0.6	0	0
244.6974	^{152}Eu	0.3	1	0.07	0.6	0.5	0	0
302.0129	^{133}Ba	0.2	1	0.1	0.5	0.7	0	0
344.2785	^{152}Eu	0.2	1	0.07	0.6	0.8	0	0
356.0192	^{133}Ba	0.1	1	0.1	0.5	0.3	0	0
383.8485	^{133}Ba	0.4	1	0.1	0.5	0.7	0	0
411.1165	^{152}Eu	0.9	1	0.07	0.6	0.6	0	0
443.9606	^{152}Eu	0.7	1	0.07	0.6	0.5	0	0
661.657	^{137}Cs	0.2	1	0.3	0.7	0.2	0	0
778.9045	^{152}Eu	0.5	1	0.07	0.6	0.6	0	0
867.38	^{152}Eu	1	1	0.07	0.6	0.7	0	0
964.057	^{152}Eu	0.6	1	0.07	0.6	0.5	0	0
1085.837	^{152}Eu	0.7	1	0.07	0.6	0.5	0	0
1112.076	^{152}Eu	0.6	1	0.07	0.6	0.6	0	0
1173.228	^{60}Co	0.3	1	0.01	0.07	0.03	0	0
1212.948	^{152}Eu	2.0	1	0.07	0.6	0.7	0	0
1299.142	^{152}Eu	2	1	0.07	0.6	0.7	0	0
1332.492	^{60}Co	0.3	1	0.01	0.07	6E-4	0	0
1408.013	^{152}Eu	0.6	1	0.07	0.6	0.4	0	0
1528.1	^{152}Eu	6	1	0.07	0.6	1.0	0	0

Appendix D

Calibration Source Correlation Matrices

^{133}Ba decays by electron capture to ^{133}Cs. The decay information for ^{133}Ba and level scheme information for ^{133}Cs were obtained from the most recent A = 133 Mass Chain evaluation [214].

^{152}Eu decays by beta minus decay to ^{152}Gd, and by electron capture to ^{152}Sm and. The decay information for ^{152}Eu and level scheme information for ^{152}Gd and ^{152}Sm were obtained from the most recent A = 152 Mass Chain evaluation [73].

^{60}Co decays by beta minus decay to ^{60}Ni. The decay and level scheme information were obtained from the most recent A = 60 Mass Chain evaluation [215].

For all three sources, the internal conversion coefficients were taken from the RIPL-3 database [11]. The BrIcc database [216] provided values that were not available in RIPL. Uncertainties on internal conversion coefficients were neglected in this calculation.

The calculated correlation matrices are shown in Figures D.1, D.2 and D.3, based on 10^6 simulations. The numeric values, rounded to two decimals, are given in Tables D.1, D.2 and D.3.

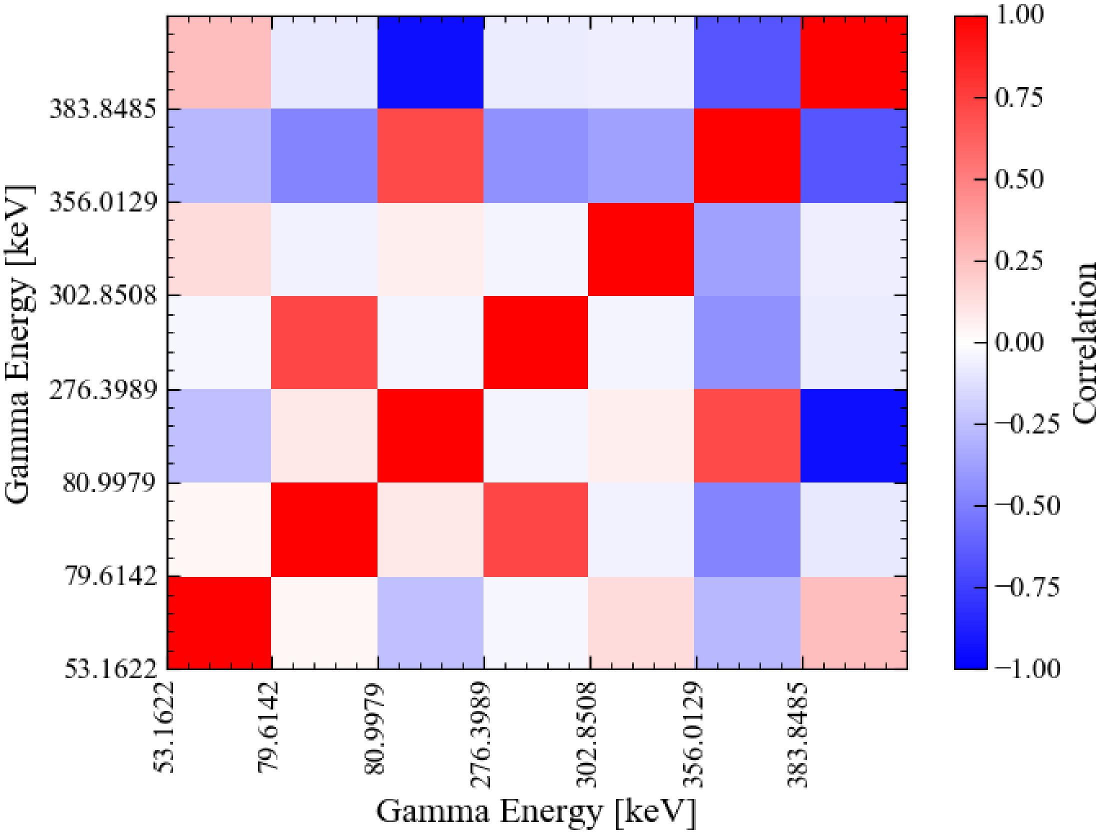

Figure D.1: Correlation matrix for the intensity values of the decay gammas from a ^{133}Ba source that are commonly used for calibration. The correlations are based on a Monte Carlo simulation of 10^6 decays of ^{133}Ba.

Table D.1: Values for the correlation matrix for the intensity values of the decay gammas from a ^{133}Ba source that are commonly used for calibration. The correlations are based on a Monte Carlo simulation of 10^6 decays of ^{133}Ba.

	53.16	79.61	80.99	276.39	302.85	356.01	383.85
53.16	1	0.038	-0.233	-0.032	0.14	-0.27	0.241
79.61	0.038	1	0.091	0.694	-0.051	-0.482	-0.084
80.99	-0.233	0.091	1	-0.068	0.073	0.693	-0.922
276.39	-0.032	0.694	-0.068	1	-0.046	-0.432	-0.076
302.85	0.14	-0.051	0.073	-0.046	1	-0.385	-0.067
356.01	-0.27	-0.482	0.693	-0.432	-0.385	1	-0.639
383.85	0.241	-0.084	-0.922	-0.076	-0.067	-0.639	1

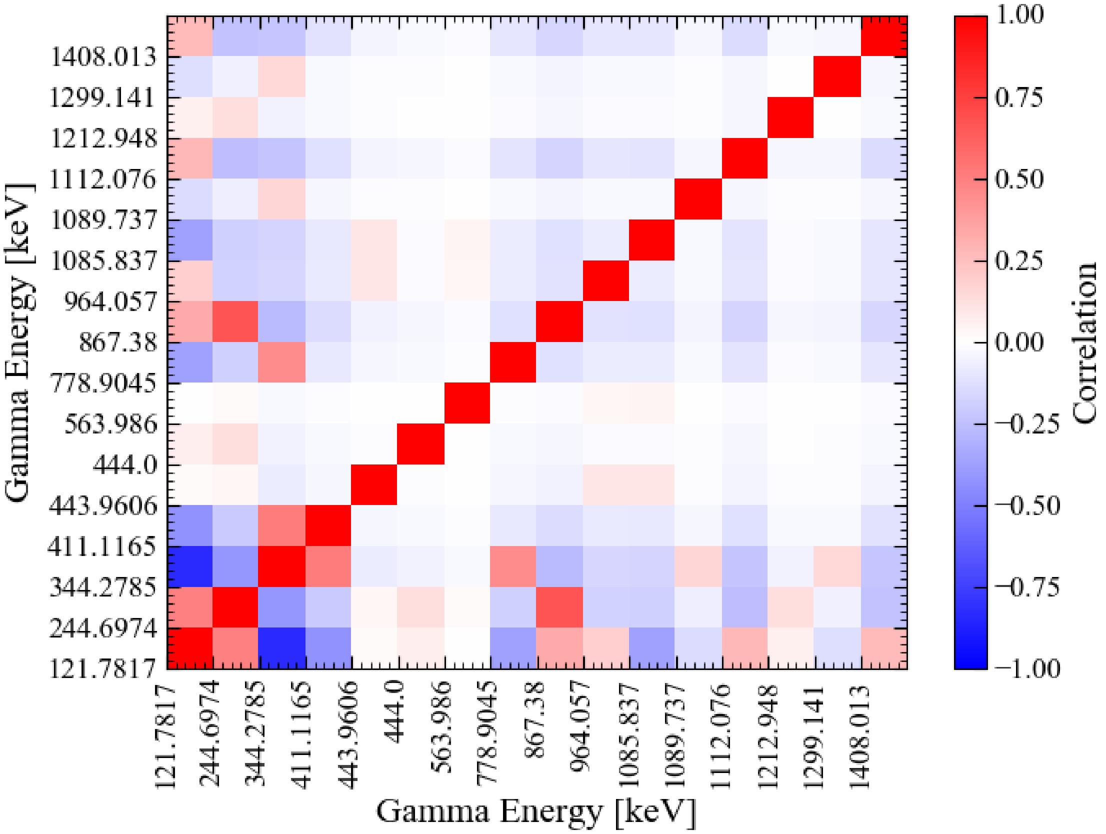

Figure D.2: Correlation matrix for the intensity values of the decay gammas from a ^{152}Eu source that are commonly used for calibration. The correlations are based on a Monte Carlo simulation of 10^6 decays of ^{152}Eu.

Table D.2: Values for the correlation matrix for the intensity values of the decay gammas from a ^{152}Eu source that are commonly used for calibration. The correlations are based on a Monte Carlo simulation of 10^6 decays of ^{152}Eu.

	121.8	244.7	344.3	411.1	443.9	444	563.9	778.9	867.4	964.1	1085	1089	1112	1212	1299	1408
121.8	1	0.49	-0.83	-0.42	0.02	0.06	0.01	-0.37	0.33	0.19	-0.37	-0.14	0.28	0.06	-0.13	0.27
244.7	0.49	1	-0.41	-0.21	0.04	0.13	0.02	-0.18	0.67	-0.17	-0.18	-0.07	-0.25	0.13	-0.06	-0.24
344.3	-0.83	-0.41	1	0.51	-0.07	-0.05	-0.03	0.45	-0.27	-0.16	-0.17	0.16	-0.23	-0.05	0.15	-0.22
411.1	-0.42	-0.21	0.51	1	-0.04	-0.03	-0.02	-0.09	-0.14	-0.08	-0.09	-0.03	-0.12	-0.03	-0.03	-0.11
443.9	0.02	0.04	-0.07	-0.04	1	-0.01	-0.01	-0.03	-0.05	0.09	0.1	-0.01	-0.04	-0.01	-0.01	-0.04
444	0.06	0.13	-0.05	-0.03	-0.01	1	0	-0.02	-0.04	-0.02	-0.02	-0.01	-0.03	-0.01	-0.01	-0.03
563.9	0.01	0.02	-0.03	-0.02	-0.01	0	1	-0.01	-0.02	0.04	0.04	0	-0.02	0	0	-0.02
778.9	-0.37	-0.18	0.45	-0.09	-0.03	-0.02	-0.01	1	-0.12	-0.07	-0.08	-0.03	-0.1	-0.02	-0.03	-0.1
867.4	0.33	0.67	-0.27	-0.14	-0.05	-0.04	-0.02	-0.12	1	-0.12	-0.12	-0.04	-0.17	-0.04	-0.04	-0.16
964.1	0.19	-0.17	-0.16	-0.08	0.09	-0.02	0.04	-0.07	-0.12	1	-0.07	-0.03	-0.1	-0.02	-0.02	-0.09
1085.8	-0.37	-0.18	-0.17	-0.09	0.1	-0.02	0.04	-0.08	-0.12	-0.07	1	-0.03	-0.1	-0.02	-0.03	-0.1
1089.7	-0.14	-0.07	0.16	-0.03	-0.01	-0.01	0	-0.03	-0.04	-0.03	-0.03	1	-0.04	-0.01	-0.01	-0.04
1112.1	0.28	-0.25	-0.23	-0.12	-0.04	-0.03	-0.02	-0.1	-0.17	-0.1	-0.1	-0.04	1	-0.03	-0.04	-0.14
1212.9	0.06	0.13	-0.05	-0.03	-0.01	-0.01	0	-0.02	-0.04	-0.02	-0.02	-0.01	-0.03	1	-0.01	-0.03
1299.1	-0.13	-0.06	0.15	-0.03	-0.01	-0.01	0	-0.03	-0.04	-0.02	-0.03	-0.01	-0.04	-0.01	1	-0.03
1408	0.27	-0.24	-0.22	-0.11	-0.04	-0.03	-0.02	-0.1	-0.16	-0.09	-0.1	-0.04	-0.14	-0.03	-0.03	1

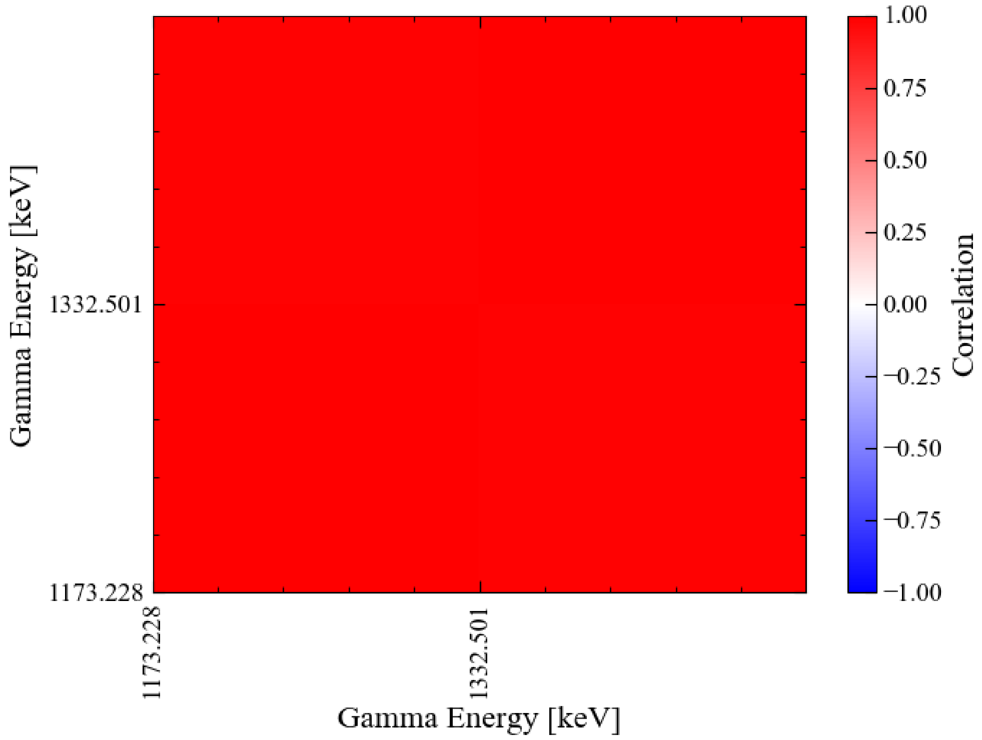

Figure D.3: Correlation matrix for the intensity values of the decay gammas from a ^{60}Co source that are commonly used for calibration. The correlations are based on a Monte Carlo simulation of 10^6 decays of ^{60}Co.

Table D.3: Values for the correlation matrix for the intensity values of the decay gammas from a ^{60}Co source that are commonly used for calibration. The correlations are based on a Monte Carlo simulation of 10^6 decays of ^{60}Co.

	1173.2	1332.5
1173.2	1	0.99
1332.5	0.99	1